Autonomous lung tumor and critical structure tracking using optical flow computation and neural network prediction

by

Peng Thian Troy Teo

A thesis submitted to the Faculty of Graduate Studies of

The University of Manitoba

in partial fulfillment of the requirements for the degree of

DOCTOR OF PHILOSOPHY

Department of Physics & Astronomy

University of Manitoba

Winnipeg, Canada

ABSTRACT

Objectives. The goal in radiotherapy is to deliver adequate radiation to the tumor volume while limiting damage to the surrounding healthy tissue. However, this goal is challenged by respiratory-induced motion. The objective of this work was to identify whether motion in electronic portal images can be tracked with an optical flow algorithm and whether a neural network can predict tumor motion.

Methods. A multi-resolution optical flow algorithm that incorporates weighting based on the differences between image frames was used to automatically sample the vectors corresponding to the motion. The global motion was obtained by computing the average weighted mean from the set of vectors. The algorithm was evaluated using tumor trajectories taken from seven lung cancer patients, a 3D printed patient tumor and a virtual dynamic multi-leaf collimator (DMLC) system. The feasibility of detecting and tracking motion at the field edge was examined with a proof-of-concept implementation that included (1) an algorithm that detected local motion, and (2) a control algorithm that adapted the virtual MLC. To compensate for system latency, a generalized neural network, using both offline (treatment planning data) and online (during treatment delivery) learning, was implemented for tumor motion prediction.

Results and Conclusions. The algorithm tracked the global motion of the target with an accuracy of around 0.5 mm. While the accuracy is similar to other methods, this approach does not require manual delineation of the target and can, therefore, provide real-time autonomous motion estimation during treatment. Motion at the treatment field edge was tracked with an accuracy of -0.4 ± 0.3 mm. This proof-of-concept simulation demonstrated that it is possible to adapt MLC leaves based on the motion detected at the field edges. Unplanned intrusions of external organs-at-risk could be shielded. A generalized network with a prediction error of 0.59 mm, and a shorter initial learning period (compared to previous studies) was achieved. This network may be used as a plug-and-play predictor in which tumor position could be predicted at the start of treatment and the need for pretreatment data and optimization for individual patients may be avoided.

.

ACKNOWLEDGEMENTS

I would like to thank and acknowledge the many special people who have helped me along this journey. Firstly, I am very thankful for my supervisor, Dr. Stephen Pistorius, who has not only provided me with guidance and critical insights, but has always been there to review my work and help me make improvements, either with my presentation skills or logical reasoning. I appreciate his patience in training me to be a capable, independent researcher. In addition, I am grateful that he supports me in taking classes from the computer science department that prove to be useful for my project.

I would like to thank my committee members: Dr. Boyd McCurdy, Dr. Sankar Venkataraman, Dr. Gabriel Thomas and Dr. Ethan Lyn for their advice and support throughout the years. The discussions with Dr. Lyn have always given me a ray of hope for the challenges I encountered. Dr. Venkataraman and Dr. Thomas are always generous with their ideas and suggestions. I thanked Dr. McCurdy for the thorough review of my thesis, and for introducing us, the students, to the other researchers at conference meetings, in particularly, leading to some insightful discussions with Dr. Paul Keall (one of the pioneers in dynamic multileaf collimator tracking).

I am also thankful to Drs. John Lewis, Stephanie Portet, Ching-Kwang Lee and John Readle, who provided reference letters for my scholarship competitions. I would like to acknowledge the financial support from the Natural Sciences and Engineering Research Council of Canada (NSERC)’s PGS-D2 Doctoral Scholarship award, Manitoba Health Research Council Graduate Scholarship award, MITACS- Accelerate Manitoba, CancerCare Manitoba Foundation and the University of Manitoba Scholarship awards.

I would like to extend my deepest appreciation to Dr. YeLin Suh of MDAnderson Cancer Center for making the CyberKnife tumor motion dataset available to this project.

I would also like to acknowledge the assistance from staff physicists Dr. Eric van Uytven and David Sasaki. Dave has always been able to meet our request despite his hectic schedule. Special acknowledgment is also extended to our department administrative officer Alana Dahlin for being our (the students) unofficial counselor and for listening to our problems and worries while always encouraging us to stay positive! Administrative support from Susan Beshta is gratefully acknowledged. I would like to thank Ernie from nuclear electronics for helping us with the actuator and Chad Harris (and his team from the fabrication shop) for fabricating our prototypes. Appreciation is also extended to all the faculty members in Medical Physics Department who taught me and/or who has given me feedbacks to my presentations in journal club, especially Dr. Daniel Rickey, Dr. Harry Ingleby, Dr. Jeff Bews and Dr. Anita Berndt.

I would like to thank the following undergraduate/summer students - Roan Crow, Samantha van Nest, Nadia Alayoubi, Katherine Kehler, Kaiming Guo, Bilal Ahmed and Philip Kawalec, who assisted the project with their experimental and measurement work.

The friendship of fellow students from the lab is appreciated: Krista Chytyk, Tamar, Peishan, Bryan McIntosh, Peter McCowan, Mario, Diego, Jorge Alpuche, Pawel, Ganiyu, Faizal, Mike Hebb, Heather, Riza, Azeez, Parandoush, Princess, Hongwei and Hongyan. Thanks to Bryan for reviewing some of the chapters in this thesis. Friendships of my study buddies and friends outside school are very much appreciated: Jose Mijares Chan, Andrew Schlukbier, Nicole Dionne, Nadia Green, Pon, Chaavz, Anamika, Piotr, Sehajdeep, Deepali, Nelvinder, Manpreet, Mona, Pegah, Dan Troniak and Ailian. I am also thankful to Dr. Ian Whicher for his yoga talk and sharing his perspectives on spirituality, which have been helpful in growing my soul during difficult periods of my journey.

I would also like to thank Delvinder, Amrit and all the members of the University of Manitoba Bison's Bhangra Aerobics Group for introducing Bhangra to me and with which I had the chance to volunteer in various events and to keep fit.

Finally, I am thankful to my family, especially my mom, Helen Sway-Muay Lee, who has always been supportive of my career and academic ventures, and for instilling in me some of the values and perspectives of life.

LIST OF ABBREVIATIONS

AAPM	American Association of Physicist in Medicine
MFPI	Active Matrix Flat Panel Imager
AP	Anterior-posterior
BEV	Beam’s Eye View
CKS	CyberKnife Synchrony
CT	Computed Tomography
DMLC	Dynamic multi-leaf collimator
DQE	Detector Quantum Efficiency
EoE	End-of-exhale
EPID	Electronic Portal Imaging Device
FMEA	Failure Mode and Effect Evaluation Analysis
HoG	Histogram of Gradient
IDRI	Image Database Resource Initiative (IDRI):
IGRT	Image-guided radiotherapy
IGART	Image-guided adaptive radiotherapy
IMRT	Intensity-modulated radiotherapy
INI	Initial frame reference image registration technique
IQR	Interquartile range
KDE	Kernel Density Estimation
kV	kilovoltage
LIDC	Lung Image Database Consortium
LINAC	Linear accelerator

LR	Left-right
MAE	Mean Absolute Error
MLC	Multi-leaf Collimator
MLCpos(ref)	Multi-leaf Collimator reference position
MLP	Multilayer perceptron
MSE	Mean Square Error
MV	Megavoltage
OAR	Organ-at-risk
OPFLOW	Optical flow
PERD	Periodic reference image registration technique
PRV	Planning organ at risk volume
RMSE	Root Mean Square Error
RPM	Real-Time Position Management™ (Varian)
SI	Superior-Inferior
SBRT	Stereotactic body radiation therapy
SEQ	Sequential frame image registration technique
SIFT	Scale Invariant Feature Transform
SVR	Support Vector Regression
VMAT	Volumetric modulated arc therapy

Table of Contents

Chapter 4 Tracking of Target Motion using Global Motion Detected within a Treatment Aperture: A Comparison of Three Approaches Using a Weighted Optical Flow Algorithm and a Virtual DMLC 95

Chapter 6 Prediction of Tumor Trajectory using a Generalized Neural Network coupled with a Sliding Window 173

List of Tables

List of Figures

Chapter 1 Introduction

1.1 Motivation and Rationale

1.1.1 Motivation for motion compensation in radiotherapy

About two-thirds of cancer patients will receive radiation treatment [1]. Radiotherapy consists of locally exposing target tumor cells to ionizing radiation with the aim of causing irreparable damage to their DNA. The goal of radiotherapy treatment is to maximize the dose delivered to the tumor while minimizing the dose delivered to the surrounding normal tissue. In external beam therapy, this is achieved by optimizing the treatment beam profile with the desired outcome for the tumor and normal tissues during the treatment planning stage. However, with tumor and organ motion, the conformity between planned and actual treatment can be compromised. This problem can have a significant impact on lung tumors where motion due to respiration is not accounted for. Organ and tumor motions exist either between fractions i.e. inter-fractions, or during the delivery of a treatment fraction, i.e. intra-fraction.

The American Association of Physicist in Medicine (AAPM) Task Group 76 [2] recommends that respiratory management techniques be considered if (1) motion of greater than 5 mm is observed in any direction, or (2) significant normal tissue sparing (as determined by respective clinics) can be achieved. Otherwise, the extra effort of respiratory management is unwarranted. The 5 mm criterion value may be reduced for special procedures, such as stereotactic body radiotherapy (SBRT), and periodic verification (via imaging) of internal target motion is recommended with the use of external surrogates for tumor motion monitoring. Diaphragm and lung tumor motions of up to 45.9 mm [3] and 66 mm [4] in the superior-inferior (SI) direction have been reported for lung cancer patients undergoing radiation therapy.

The National Comprehensive Cancer Network (NCCN) guidelines for *Non-Small Cell Lung Cancer* (version 3.2014) state, “Respiratory motion should be managed when motion is excessive” [5]. Beam gating and dynamic tumor tracking are recommended for excessive motion [5]. When motion of the integrated target volume is small, “motion-encompassing targeting” is applicable [5].

1.1.2 Motivation for image-guided adaptive radiotherapy with portal images

Population-based treatment margins are currently used to encompass the uncertainties related to motion [6, 7]. Adding treatment margins to cover the uncertainties due to motion ensures a high dose coverage of the target volume. However, this increases the field size and exposes healthy tissues to unnecessary radiation, which would, in turn, increase the risk of radiation-induced side effects [8-12]. In addition to using margins to encompass the errors between planning and treatment delivery, active motion compensation (gating, breathing control, robotic table and dynamic aperture) has been proposed to reduce the deviations between planned and delivered treatment. However, selective activation of treatment delivery, based on a gating signal, increases treatment time. In both gating and breath control, the tumor is never observed directly. Although external surrogates have been used to infer internal target motion, poor correlations were observed for some patients. Motions of the diaphragm and abdominal surface were observed to correlate only for one minute [13]. An instantaneous time shift of up to 0.4 – 0.6 s between a tumor and an external infrared surrogate was observed, and this could induce amplitude mismatches in the range of 2.5 to 4.7 mm [14].

Image-guided adaptive radiotherapy (IGART), which is the subject of this thesis, uses imaging systems to monitor intra-fractional motions (figure 1.1). Treatments would be adapted to compensate for the motions observed. Although various imaging modalities have been used to monitor motions during treatment, the use of MV images from electronic portal imaging devices (EPID) are desirable since the tumor can be tracked directly (in two dimensions) with the treatment beam, and no additional patient dose or external surrogates are involved. However, an EPID has inherently poor contrast, and this poses a challenge for accurate motion tracking [7]. Nevertheless, if a tracking technique can successfully track motions on an MV image, the same technique would have less difficulty in tracking motions on higher contrast images (e.g. kV).

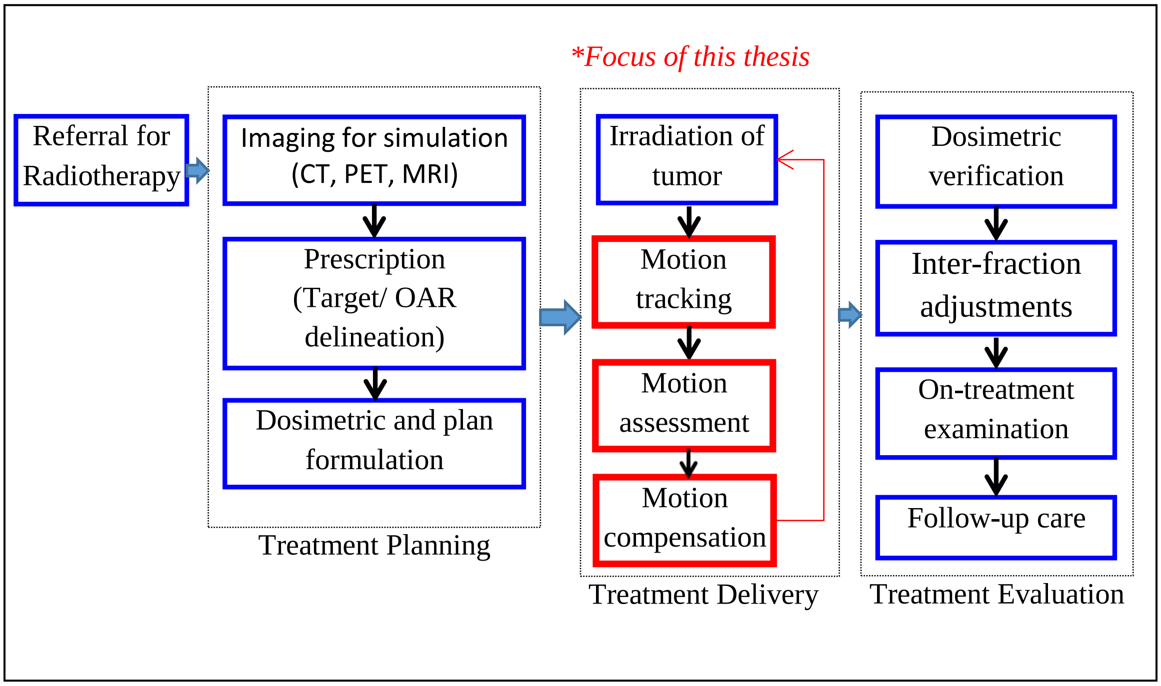

Figure 1.1 : Workflow for radiotherapy incorporating intra-fraction image guidance and adaptation. The focus of this thesis, highlighted in red, involves tracking, predicting and compensating for the motions observed during treatment delivery.

1.1.3 Challenges of markerless tracking

Although various markerless [15-21] and marker-based tracking techniques have been implemented, the use of markers leads to the potential risks of pneumothorax [22] and marker migrations of up to 2.7 cm [23]. Markerless tracking using template matching has been shown to be capable of tracking with an accuracy of 0.5 mm. However, frequent readjustment of the template is required to compensate for the deformation of the lung and tumor shrinkage over the treatment course [24, 25]. Although a multi-region template matching offers flexibility, pre-filtering on a training set is required to identify all of the possible rigid landmarks [19]. While most of the markerless tracking techniques require a pre-defined template or contour to track, optical flow algorithms, [26-29] a pixel-by-pixel algorithm can potentially track motions without a pre-defined template (or contour) or *a priori* knowledge of the object being tracked [26, 27]. The individual optical flow vectors allow motion analysis to be performed at the global level or over a local region. Optical flow techniques have been used to track partially occluded objects from the motion vectors [26], infer structure from motions [27] and track motions at the edges of a field of view [26, 28, 29]. For tumor tracking during radiotherapy, similar problems, such as the partial occlusion of the tumor, due to the MLC leaves or overlapping structures along the beam, are encountered. Unlike template tracking, local optical flow vectors can be used to track an uncontoured external structure which intrudes into the beam's eye view (BEV) in an unplanned way [29].

1.1.4 Motivation for motion monitoring at the field edges

Although the dose limits to the OAR are taken into consideration during treatment planning, this assumes that the setup of the patient is accurate, and patient breathing and tumor/OAR motion during treatment are identical to the pattern delineated during planning. Failure mode and effect analysis (FMEA) have revealed that contouring the OAR, with reported inter-observer deviations of up to 0.9 mm and 8.1 cm for the spinal cord and esophagus respectively [30, 31], could be a potential source of systematic error with a high risk of frequent occurrence [32-35]. In some cases, the use of wrong OAR contours has been reported [16]. The differences between the planning and treatment delivery could alter the proximity between the OAR and the high dose region of the treatment field. In Stereotactic Body Radiation Therapy (SBRT), this is of particular concern due to the steep dose gradient, reduced margin, low-fraction, high dose treatment and intra-treatment patient motion due to the longer treatment duration [36]. The ability to adapt the treatment upon detecting an unplanned intrusion of organ-at-risks into the BEV is becoming more important. With a combination of adaptive beam movement and systematic deviation of the target motion pattern, similar concerns of unintentionally overdosing the OAR have been cited for the CyberKnife system [37].

It has been shown that for most cases, the lung tumor is expected to move similarly to the surrounding OAR since these tumors are embedded in the lung tissue and are forced to follow the lung motion [38]. However, with a wall-seated lung tumor, the lung tumor and the OAR, such as the ribs, can have different motion magnitudes relative to each other [39]. Although breathing adapted radiotherapy and deep inspiration breath hold technique have been shown to minimize motion, some patients were unable to comply with the requirements [40]. With the additional possibilities of setup errors and daily variations in organ motion, it is challenging to consistently maintain the OAR outside of the radiation field [41]. Variation in dose distribution may occur as a result of the surrounding organs moving in and out of the field during respiration [42].

Although studies have been performed to determine the accuracy of MLC leaf pair control for moving target on EPID images [43], detection and tracking of motion close to the leaf edges has, to the knowledge of the author, never been done before. This may be due to the difficulty in identifying the OARs that could potentially intrude into the treatment beam. As a result, current tracking methods, based on *a priori* information such as contour or template matching of the target, might not find an exact match for an unplanned, and partially intruding OAR. The availability of such tools might allow detection of unplanned intrusions of healthy structures into the treatment field.

1.1.5 Motivation for prediction of tumor motion

Due to system latencies and imaging rate constraints in practical systems, the implementation of image-guided adaptive radiotherapy is challenging [44-47]. By the time the aperture reshapes according to the motion detected, the target may have moved out of its tracked position. However, the addition of a prediction model for tumor motion could allow the beam to be positioned at the anticipated tumor location.

Unfortunately, prediction accuracies can be compromised with longer system latencies. This could result in the adapted beam being positioned at a different location compared to the actual tumor. The possibility of the irradiated volume encroaching into the surrounding healthy tissues due to the prediction error could occur. However, this can potentially be detected by monitoring motion at the center and at the edges of the field, which reiterates the motivation presented earlier in section 1.1.5.

1.1.6 Motivation for a generalized neural network

The development of an accurate predictor is challenged by the fact that (1) respiration-induced motions are quasi-periodic and non-stationary and (2) the compromised lung function of cancer patients often leads to irregular breathing patterns. This leads to the requirement of individually optimized prediction models that cater to different patients with different breathing traits. Besides the extra time and resources needed to design the predictor, an individually optimized model can be prone to bias and large errors [48-51]. These models, often trained with pre-treatment data, would require an initial learning period at the beginning of the treatment delivery session, to adapt to the motions observed during treatment delivery. The initial training period requirement would imply that prediction and adaptation of the beam are unlikely to commence immediately at the start of the treatment delivery. Although neural network approaches were shown to predict with higher accuracy in several studies, the complex structure and the lack of universal design guidelines resulted in the implementation of the neural network to be considered as an art rather than a science [52, 53]. The availability of a plug-and-play generalized neural network for tumor motion prediction during treatment delivery is desirable since efforts to individually optimize the models as well as the waiting time prior to making treatment adaptions can be reduced.

1.1.7 Dosimetric impact of using tracking and prediction in adaptive radiotherapy

Commercial, clinical implementations of concurrent tumor irradiation and tracking are limited to the robotic CyberKnife system (Accuray Inc. CA), first reported in 2004 [54], and the Vero gimbaled linac system (Mitsubishi, Japan and BrainLAB AG, Germany) first reported in 2014 [55]. Other systems that follow tumor motion to create a stationary tumor with respect to the treatment beam are limited to research prototypes [56-62]. Using electromagnetically-guided transponder, clinical trial for prostate and lung tumor tracking has been performed with a DMLC system [57, 63]. It is also possible to move the patient couch, which moves the tumor, in order to maintain a stationary tumor with respect to the beam [60, 64-65].

Preliminary results of using a DMLC show a reduction of the gamma failure rate (dose difference at 3%/ 3mm) from 22.5% to 0.2% with tracking and prediction incorporated [44]. In a multi-institutional study involving all the four major real-time adaptive systems (i.e. CyberKnife, DMLC, gimbaled and couch tracking), dose accuracy improves with the mean gamma failure rate (2%/2 mm) decreasing from 15.2% (without adaptation) to 1.6% (with adaptation) [66]. Without adaptation, the mean 3%/3 mm gamma failure rate of 15.2% is higher than the mean failure rate of 2.1% observed for conventional IMRT commissioning where no motion is considered [67]. This implies that motion, when not compensated (i.e., current conventional treatment approach), is a leading error when put in the context of the other dosimetric errors in radiotherapy [66].

In summary, the impact of tumor motion on radiation therapy is significant. Reduction of geometrical uncertainties and its corresponding margins are necessary to mitigate exposure of healthy tissues and OAR to unnecessary radiation. This motivates the use of image guidance and delivery adaptation to compensate for tumor motion. The need for appropriate tools to realize an efficient adaptive system, in turn, motivates us to develop tracking and prediction algorithms that are accurate and robust.

1.2 Thesis Objective

The efficacy of external beam radiotherapy depends on the accuracy of the radiation dose being delivered to the tumor while avoiding damage to the surrounding healthy tissues. A major obstacle to achieving this delivery accuracy is tumor and internal organ motion. The objective of this project is to study the feasibility of using computer vision algorithms, such as the optical flow algorithm, coupled with a prediction model, to automatically track and predict the intra-fractional motion of uncontoured tumor and organs on portal images. This would allow treatment delivery to be modified according to the motions detected. In the process, the susceptibility of the tracking algorithm to the accumulation of position errors will be investigated with an in-house developed virtual DMLC system. Methods to improve the training time and accuracy of the prediction model will be studied.

1.3 Thesis Hypothesis

Based on previous studies examining the current status and challenges associated with image-guided adaptive radiotherapy systems, it is hypothesized that:

i. by using a computer/robotic vision approach such as the optical flow algorithm, the motion of uncontoured tumor can be tracked automatically with an accuracy of 0.5 mm [16, 19] in order to adapt treatment delivery;

ii. motions and intrusions of the critical structure at the edges of the treatment field can be detected and tracked automatically;

iii. system latencies of typical radiotherapy systems can be compensated with a prediction model that is efficient and accurate compared to the existing techniques available for tumor motion prediction [68-77].

1.4 Thesis Overview

To address the above hypotheses, specific aims were determined, and the corresponding developments and outcomes are presented in the thesis as follows:

- **Chapter 2:** A review of the characteristics of tumor motion and its impact on radiotherapy is provided in this chapter. Imaging techniques used to quantify the motion are summarized, and background knowledge on image tracking and neural network prediction are provided.
- **Chapter 3 (specific aim 1 – *To track uncontoured targets with a weighted optical flow algorithm. This work addresses hypothesis (i)*)**: This chapter reports on the development of an approach that automatically tracks the position and inter-frame displacement (i.e. velocity) of an uncontoured moving target on an EPID image, using an image difference weighted optical flow algorithm. The set of image-difference intensities highlights the regions where changes occurred. This varies for subsequent image pairs. Hence, instead of having a fixed threshold for the entire image sequence, an adaptive set of thresholds was obtained automatically. The algorithm was evaluated with patients' digitally reconstructed radiographs (DRR) images and portal images of a phantom moving in an asymmetrical cosine function representing average tumor motion. The tracking accuracy was compared for different breathing frequencies and as a function of target visibility (i.e., contrast-noise-ratio).

- **Chapter 4 (specific aim 2 – *To compare three reference image update techniques for the reduction of tracking errors accumulation. This work addresses hypothesis (i)*)**. Using the weighted optical flow algorithm presented in chapter 3, three techniques of updating the reference image as well as their susceptibility to the accumulation of positional errors were investigated using realistic patient lung tumor motion. In contrast to static tracking [78, 79] presented in chapter 3, dynamic tracking [78, 79] with the adaption of the aperture similar to that of the DMLC system [56, 80] were used in this study. In the first method (INI), the initial frame in the sequence was used as the reference image for the determination of tumor motion in all future images. In the second method (SEQ), the reference image was updated sequentially to the current beam eye's view (BEV) image where the position of the tumor was last determined. In the third method (PERD), the reference image was updated periodically at the end-of-exhale (EoE) of each breathing cycle. These different implementations of the weighted optical flow algorithm were compared using the MV images of a 3D printed lung tumor of a patient as a control for our study. Seven lung patients' tumor trajectories and a virtual DMLC system similar to that of Pepin et. al., [81] was used for tracking and aperture adaptation.
- **Chapter 5 (specific aim 3 – *To track and detect organ intrusion at field edges. This work addresses hypothesis (ii)*)**. This chapter extends the work reported in chapter 3 to investigate the feasibility of using EPID images and local optical flow analysis to track motion at the edges of a treatment field, and using the motion detected to adapt a virtual DMLC system. An optimal cluster size of local optical flow vectors was determined. Techniques to prevent losing track of the intruding object were incorporated in the control algorithms of the virtual DMLC system.

- **Chapter 6 (specific aim 4 – *To implement a neural network for tumor motion prediction. This work addresses hypothesis (iii))*** In this chapter, the systematic design of a neural network to predict tumor motion with a system latency of 650 ms will be presented. Using a mixture of data acquired during the initial period of a tumor trajectory (online), coupled with a generalized model optimized using a diverse patient dataset (offline), the design of a generalized neural network will be presented. Specifically, the average mean square error surface obtained from the prediction response of seven patients' tumor trajectories was used to determine the input data size and number of hidden neurons for the generalized neural network model. With a reduction of error and training time, the possibility of using the neural network as a plug-and-play predictor that does not require optimization with the pre-treatment data of the individual patient is presented.

1.5 Novelty and Contributions

The major contributions (to Science and Engineering) and novelty generated from the work done in fulfilling the four specific aims include:

- **Contribution 1 – tracking uncontoured targets on EPID images.** In tracking a target on portal images, we have shown that by using a dynamic threshold for weighting the optical flow vectors, a markerless, uncontoured target can be tracked with accuracy comparable to other methods [16, 19]. Although the accuracy of our approach is similar to that of other methods, the benefits are that it does not require manual delineation of the target or prior knowledge of the tumor features from a training data set and can, therefore, provide autonomous real-time motion estimation during treatment. The effect of image contrast on optical flow tracking accuracy was reported for the first time. Tracking error decreases as the contrast-noise-ratio (CNR) increases from 4.27 to 5.6. In addition, errors are less dependent on velocity as CNR increases. As CNR increases beyond 5.4, both absolute and relative error approach zero.

This is, to our knowledge, the first study where 1) an uncontoured target is tracked automatically on EPID images using a dynamically weighted optical flow algorithm and 2) the variation of optical flow tracking performance due to changes in EPID CNR is reported.

(*This work was published in the journal of Measurement Science and Technology (IOP Publishing), vol. 24, 074012, 2013, DOI:10.1088/0957-0233/24/7/074012, by the author of this dissertation. The formulation and implementation of the algorithms and the analysis of the results were performed by the author of this dissertation. The experimental work was carried out with the assistance of Roan Crow and Samantha van Nest*).

- **Contribution 2 – reduction of the accumulation of tracking errors**. In tracking patients' tumor trajectory, results demonstrated accumulation of position errors when tracking is performed over a sequence of portal images. The INI method, which uses the initial beams-eye-view (BEV) image as a fixed reference image, is found to be the least prone to the accumulation of position errors. This is followed by the SEQ method, which sequentially updates the reference image with images prior to the incoming image, and the PERD method, which updates the reference image periodically.

  Factors resulting in the accumulation of position errors were identified. They are due to either (1) isolated, or (2) accumulated small inter-frame displacement errors in a similar direction. Potential causes for the inter-displacement errors are attributed to (1) motions that are smaller than the image or tracking resolution; (2) under-estimation of high displacements, a limitation that is common with algorithms that are optimized prior to online tracking.

(*Part of the work was published as a book chapter in vol. 51 of the IFMBE Proceedings series, DOI 10.1007/978-3-319-19387-8_141, and presented at the World Congress on Medical Physics and Biomedical Engineering, June 2015 Canada. The material is also prepared for submission to Medical Physics. The formulation and implementation of the algorithms and the analysis of the results were performed by the author of this dissertation. Further testing of the algorithm on patient traces was performed by Kaiming and Bilal (using an aperture size following the RTOG 0236 guidelines). The experimental work was carried out with the assistance of Nadia Alayoubi and Katherine Kehler*).

- **Contribution 3 – track and adapt the MLCs based on the motions detected at the field edges**. The ability to detect and adapt the treatment field based on motions observed at the edges of a BEV has been demonstrated for the first time. Key processes that are instrumental in this successful implementation have been identified and they include (i) the use of an optical flow algorithm with a 3-by-3 pixel regularization, (ii) monitoring of local optical flow vectors with an optimal cluster size of 9 rows by 10 columns and (iii) formulating an MLC control algorithm with one-frame prediction and buffers incorporated. The buffers are the minimal regions needed to maintain continuous tracking of the intruding structure. The challenges of tracking a small region compared to global motion tracking were identified.

This preliminary proof-of-concept study unveils a unique tool that would allow for (1) intra-fraction monitoring and detection of motion and potential OAR intrusion at the field edges and (2) adaptation of MLC leaves based on the motion detected. The proposed local adaptation technique would be an attractive feature to supplement systems tracking the main target motion.

(*Preliminary results of this work were published in the Journal of Physics: Conf. Series, 489, 012040, 2014, DOI:10.1088/1742-6596/489/1/012040. An extended version is also* *prepared for submission to Medical Physics. The formulation and implementation of the algorithms and the analysis of the results were performed by the author of this dissertation. The experimental work, i.e. image acquisition with patient traces, was carried out with the assistance of Nadia Alayoubi and Katherine Kehler*).

- **Contribution 4 – a generalized neural network that reduces the effort and time required for learning and optimization**). To the best of our knowledge, this work presents the first attempt to use the average mean square error (MSE) error surface obtained from the prediction of different patients' tumor trajectories to determine the parameters of a generalized neural network. Using the first period of the tumor trajectory as a sliding window length, a systematic approach to establishing the values for the parameters of a multi-layer perceptron neural network has been demonstrated for the prediction of tumor motion. An input data length of 35 data samples and 20 hidden neurons were selected for the generalized network. Instead of initializing the weights for every training batch (method 1), inheriting weights from previous training (method 2) improves, on average, the prediction accuracy and computation time. Although the average mean absolute error MAE and MSE of 0.59 mm and 0.83 mm were comparable to other studies [68-71], the initial training period prior to making the first prediction was reduced to an average of 8.8 s, the shortest waiting time compared to previous studies [72-77]. This would allow tracking and treatment adaptation to commence earlier. By eliminating the long waiting time as well as the need to optimize individual networks with pre-treatment data, this neural network could potentially be deployed as a plug-and-play model to predict tumor motions as soon as treatment delivery begins.

  (*An abstract based on the generalized model was selected for presentation (finalist) at the Young Investigator's Symposium at the annual meeting of the Canadian Organization of Medical Physicist (COMP 2016) in St. John's, Newfoundland. Part of the work was published as a book chapter in volume 51 of the IFMBE Proceedings series, DOI:10.1007/978-3-319-19387-8_146, and presented at the World Congress on Medical Physics and Biomedical Engineering, June 2015 Canada. The material is also prepared* *for submission to Medical Physics by the author of this dissertation. The extraction of the tumor traces from the CKS dataset was done by Nadia Alayoubi and Philip*).

- **Contribution 5 – a virtual DMLC system**. Key processes in an image-guided adaptive radiotherapy system, such as accurate tracking of the tumor and rapid adaptation of the treatment beam, make it a challenge to realize these systems physically. The availability of a virtual system, such as the virtual DMLC implemented by Pepin [81] and the VERT 2.9 platform (Vertual Ltd. Hull, UK), would allow a breakdown of these processes to be simulated and verified prior to implementation. By the same token, a novel implementation of a virtual DMLC system was implemented where the positions of the MLCs were updated according to the motion detected. Although negligible latencies are assumed in the current implementation, realistic delays could be incorporated.

References

1. F. J. Berkey, "Managing the adverse effects of radiation therapy", Am Fam Physician. 82(4), 381-388 (2010).
2. American Association of Physicists in Medicine (AAPM), Radiation Therapy Committee, Task Group 76. The Management of Respiratory Motion in Radiation Oncology. Report No. 91. Madison (WI) (2006).
3. P. Giraud, E. Yorke, E. Ford, R. Wagman, G. Mageras, "Reduction of organ motion in lung tumors with respiratory gating", Lung Cancer 51 41-51 (2006).
4. J. Wu, P. Lei, R. Shekhar, H. Li, M. Suntharalingam, W. D'Souza, "Do tumors in the lung deform during normal respiration? An image registration investigation", Int. J. Radiat. Oncol. Biol. Phys. 75 268-275 (2009).
5. National Comprehensive Cancer Network (NCCN) Non-Small Cell Lung Cancer. NCCN Guidelines (version 3.2014). (2014).
6. ICRU Report 62. 1999 Prescribing, Recording and Reporting Photon Beam Therapy, Int. Commission on Radiation Units and Measurements, Bethesda, MD

7. M. van Herk, et al., “The probability of correct target dosage: dose-population histograms for deriving treatment margins in radiotherapy”, Int. J. Radiat. Oncol. Biol. Phys. 47(4), 1121-1135 (2000).

8. B. Emami, “Tolerance of normal tissue to therapeutic radiation”, Reports of Radiotherapy and Oncol. 1, 35-48 (2013).

9. C. K. Glide-Hurst and I. J. Chetty, “Improving radiotherapy planning, delivery accuracy, and normal tissue sparing using cutting edge technologies”, J. Thorac. Dis. 6(4), 303-318 (2014).

10. M. V. Graham, J. A. Purdy, B. Emami, et al., “Clinical dose-volume histogram analysis for pneumonitis after 3D treatment for non-small cell lung cancer (NSCLC)”, Int. J. Radiat. Oncol. Biol. Phys 45, 323-329 (1999).

11. M. Martel, R. Ten Haken, M. Hazuka, et al., “Dose-volume histogram and 3-D treatment planning evaluation of patients with pneumonitis”, Int. J. Radiat. Oncol. Biol. Phys. 28, 575-581, (1994).

12. L. B. Marks et al., “Radiation dose-volume effects in the Lung”, Int. J. Radiat. Oncol. Biol. Phys. 76, S70–S76 (2010).

13. S. S. Vedam, et al., “Quantifying the predictability of diaphragm motion during respiration with a noninvasive external marker”, Med. Phys. 30(4), 505–513 (2003).

14. D. Ionascu, S. B. Jiang et. al., “Internal-external correlation investigations of respiratory induced motion of lung tumors”, Med. Phys. 34(10), 3893- 3903 (2007).

15. M. Orkisz, A. Frery, O. Chapet, F. Mornex and I. E. Magnin, “Attempts to bronchial tumor motion tracking in portal images during conformal radiotherapy treatment”, Comp. Analysis of Images and Patterns (Lect. Notes in Comp. Sci.) 2124, 247–55 (2001).

16. J. Meyer, A. Richter, K. Baier, J. Wilbert, M. Guckenberger and M. Flentje, “Tracking moving objects with megavoltage portal imaging: A feasibility study”, Med. Phys. 33, 1275-1280 (2006).

17. T. Lin, L.I. Cervino, X. Tang, N. Vasconcelos and S. B. Jiang, “Fluoroscopic tumor tracking for image-guided lung cancer radiotherapy”, Phys. Med. Biol. 54, 981-992 (2009)

18. R. Li, J. Lewis, L.I. Cervino and S.B. Jiang, “A feasibility study of markerless fluoroscopic gating for lung cancer radiotherapy using 4DCT templates”, Phys. Med. Biol. 54, N489–N500 (2009).

19. J. Rottmann, M. Aristophanous, A. Chen, L. Court and R. Berbeco, “A multi-region algorithm for markerless beam’s-eye view lung tumor tracking”, Phys. Med. Biol. 55 5585–5598 (2010).

20. Q. Xu, R. Hamilton, R. Schowengerdt, B. Alexander and S. B. Jiang, “Lung tumor tracking in fluoroscopic video based on optical flow”, Med. Phys. 35(12), 5351-5359 (2008).

21. X. Zhang, N. Homma, K. Ichiji, Y. Takai, M. Yoshizawa, “Tracking tumor boundary in MV-EPID images without implanted markers: A feasibility study”, Med. Phys. 42(5), 2510-2523 (2015).

22. N. Kothary, J. Heit, J. Louie, W. Kuo, et. al., “Safety and efficacy of percutaneous fiducial marker implantation for image-guided radiation therapy”, J. Vasc. Interv. Radiol. 20, 235–239 (2009).

23. C. Nelson, G. Starkschall, P. Balter, R. Morice, C. Stevens, and J. Chang, “Assessment of lung tumor motion and setup uncertainties using implanted fiducials”, Int. J. Radiat. Oncol., Biol., Phys. 67(3), 915–923 (2007).

24. M. Chao, Y. Xie, E. Moros, Q. Le and L. Xing, “Image-based modeling of tumor shrinkage in head and neck radiation therapy”, Med. Phys. 37 2351-2358 (2009).

25. A. Pevsner, B. Davis, S. Joshi, et. al. “Evaluation of an automated deformable image matching method for quantifying lung motion in respiration-correlated CT images”, Med. Phys. 33 369-376 (2006).

26. E. Ohn-Bar, S. Sivaraman, and M. Trivedi, “Partially occluded vehicle recognition and tracking in 3D”, IEEE Intelligent Vehicles Symposium IV, 1350–1355 (2013).

27. A. Ramirez, E. Ohn-Bar, and M. Trivedi, “Go with the flow: Improving multi-view vehicle detection with motion cues”, Proc. 22nd Int. Conf. Pattern Recognition, 4140 - 4145 (2014).

28. P. T. Teo, R. Crow, S. van Nest, D. Sasaki and S. Pistorius, “Tracking lung tumor motion using a dynamically weighted optical flow algorithm and electronic portal imaging device”, Meas. Sci. Technol.24, 074012 (15pp) (2013).

29. P. T. Teo and S. Pistorius, “Tissue motion tracking at the edges of a radiation treatment field using local optical flow analysis”, J. of Phys.: Conf. Series, 489 012040 (2014).

30. D. C. Collier, S.S. Burnett, M. Amin, S. Bilton, C. Brooks, A. Ryan, D. Roniger, D. Tran, G. Starkschall, “Assessment of consistency in contouring of normal-tissue anatomic structures”, J. Appl. Clin. Med. Phys. 4(1), 17-24 (2003).

31. F. M. Kong, T. Ritter, D.J. Quint et. al., “Consideration of dose limits for organs at risk of thoracic radiotherapy: Atlas for lung, proximal bronchial tree, esophagus, spinal cord, ribs, and brachial plexus”, Int. J. Radiat. Oncol. Biol. Phys. 81(5), 1442-57 (2011).

32. K. C. Younge, Y. Wang, J. Thompson, J. Giovinazzo, M. Finlay, R. Sankreacha, “Practical implementation of failure mode and effects analysis for safety and efficiency in stereotactic radiosurgery”, Int. J. Radiat. Oncol. Biol. Phys. 91, 1003-1008 (2015).

33. R. P. Manger, A. B. Paxton, T. Pawlicki, and G-Y. Kim, "Failure mode and effects analysis and fault tree analysis of surface image guided cranial radiosurgery", Med. Phys. 42, 2449-2461 (2015).

34. S. Broggi, M. Cantone, A. Chiara, N. Di Muzio, B. Longobardi, P. Mangili, I. Veronese, "Application of failure mode and effects analysis (FMEA) to pretreatment phases in tomotherapy", J. Appl. Clin. Med. Phys. 14(5), 265-277 (2013).

35. F. Yang, N. Cao, L. Young, J. Howard, W. Logan, T. Arbuckle, P. Sponseller, T. Korssjoen, J. Meyer, and E. Ford, "Validating FMEA output against incident learning data: A study in stereotactic body radiation therapy", Med. Phys. 42, 2777 (2015).

36. J. P. Bissonnette, K.N. Franks, T. G. Purdie, D.J. Moseley, J.J. Sonke, D.A. Jaffray, et al., "Quantifying interfraction and intrafraction tumor motion in lung stereotactic body radiotherapy using respiration-correlated cone beam computed tomography", Int. J. Radiat. Oncol. Biol. Phys. 75, 688-695 (2009).

37. M. K. H. Chan, D. L.W. Kwong, E. Tam, A. Tong, S. C.Y. Ng, "Quantifying variability of intrafractional target motion in stereotactic body radiotherapy for lung cancers", J. Appl. Clin. Med. Phys., 14(5), 140-152 (2013).

38. E. Weiss, K. Wijesooriya, S.V. Dill, P.J. Keall, "Tumor and normal tissue motion in the thorax during respiration: Analysis of volumetric and positional variations using 4D CT", Int. J. Radiat. Oncol. Biol. Phys. 67(1), 296-307 (2007).

39. M. Altman, J. Jin, S. Kim, N. Wen, D. Liu, M. Siddiqui, M. Ajlouni, B. Movsas, I. Chetty, "Practical methods for improving dose distributions in Monte Carlo-based IMRT planning of lung wall-seated tumors treated with SBRT", J. Appl. Clin. Med. Phys.13, 4007 (2012).

40. H. D. Nissen and A.L. Appelt, "Improved heart, lung and target dose with deep inspiration breath hold in a large clinical series of breast cancer patients", Radiother. Oncol. 106, 28-32 (2013).

41. R. Méndez, R. Zinkstok, W. Wunderink, R.M. van Os, H. Joosten, Y. Seppenwoolde, P. Nowak, R. Brandwijk, C. Verhoef, J. Jzermans, P. Levendag, B. Heijmen, "Stereotactic body radiation therapy for liver tumors: impact of daily setup corrections and day-to-day anatomic variations on dose in target and organs at risk", Int. J. Radiat. Oncol. Biol. Phys. 75(4), 1201-1208, (2009).

42. G. Li, P. Cohen, H. Xie, D. Low, D. Li and A. Rimner, "A novel four-dimensional radiotherapy planning strategy from a tumor-tracking beam's eye view", Phys. Med. Biol. 57, 7579-7598 (2012).

43. F. Todsaporn, H. Woodruff, P. Rowshanfarzad, D. O'Connor, R. Middleton and P. Greer, "An independent system for real-time dynamic multileaf collimation trajectory verification using EPID", Phys. Med. Biol. 59, 61-81 (2014).

44. B. Cho, P. R. Roulsen, A. Sloutsky, A. Sawant and P. Keall, "First demonstration of combined KV/MV image-guided real-time dynamic multileaf-collimator target tracking", Int. J. Radiat. Oncol. Biol. Phys. 74 859-67 (2009).

45. A. Sawant, R. Venkat, V. Srivastava, D. Carlson, S. Povzner, H. Cattell, and P. Keall, "Management of three-dimensional intrafraction motion through real-time DMLC tracking", Med. Phys. 35, 2050-2061 (2008).

46. D. Ruan and P. Keall, "Dynamic multileaf collimator control for motion adaptive radiotherapy: an optimization approach", Proc. 2011 IEEE Power Engineering and Automation Conf. (PEAM 2011), 100 - 103 (2011).

47. D. Moore, D. Ruan, and A. Sawant, "Fast leaf-fitting with generalized underdose / overdose constraints for real-time MLC tracking", Med. Phys. 43, 465 (10pp.) (2016).

48. G. P. Zhang and V. L. Berardi, "Time series forecasting with neural network ensembles: an application for exchange rate prediction", J. Operational Res. Soc., 52 (6) 652-664, (2001).

49. L. Breiman, "Stacked regressions", Machine Learning, 24, 49-64 (1996).

50. G. Bontempi, "Combination of two estimators" in Handbook Statistical Foundations of Machine Learning. OTexts: Melbourne, Australia. Chap 3.10. https://www.otexts.org/1443 Accessed on 10 April 2016.

51. G. Bontempi, "Model Averaging Approach" in Handbook Statistical Foundations of Machine Learning. OTexts: Melbourne, Australia. Chap 9, https://www.otexts.org/1413 Accessed on 10 April 2016.

52. R. Erenshteyn, R. Foulds, S. Galuska, "Is designing a neural network application an art or a science?", SIGCHI Bulletin, ACM Press. New York, (July 1994).

53. N. Kourentzes and S. F. Crone, "Automatic modelling of neural networks for time series prediction – in search of a uniform methodology across varying time frequencies", Proc. 2nd European Symp. on Time Series Prediction, ESTSP'08, Helsinki, Finland.

54. A. C. Koong, Q. Le, A. Ho, et. al., "Phase 1 study of stereotactic radiosurgery in patients with locally advanced pancreatic cancer", Int. J. Radiat. Oncol. Biol. Phys. 58, 1017–1021 (2004).

55. T. Depuydt, K. Poels, D. Verellen, et al., "Treating patients with real-time tumor tracking using the vero gimbaled linac system: implementation and first review", Radiother. Oncol. 112, 343–351 (2014).

56. A. Sawant, R. Venkat, V. Srivastava, D. Carlson, S. Povzner, H. Cattell, P. Keall, "Management of three-dimensional intrafraction motion through real-time DMLC tracking", Med. Phys. 35(5), 2050 – 2061 (2008).

57. P. Keall, E. Colvill, R. O'Brien, et. al., "First clinical implementation of electromagnetic transponder- guided MLC tracking", Med. Phys. 41(2) 020702 (5pp.) (2014).

58. T. Neicu, H. Shirato, Y. Seppenwoolde and S. B. Jiang, "Synchronized moving aperture radiation therapy (SMART): average tumor trajectory for lung patients", Phys. Med. Biol. 48(5), 587-598 (2003).

59. M. Tacke, S. Nill and U. Oelfke, "Real-time tracking of tumor motions and deformations along the leaf travel direction with the aid of a synchronized dynamic MLC leaf sequencer", Phys. Med. Biol. 52, N505–N512 (2007).

60. I. Buzurovic., K. Huang, Y. Yu, and T.K. Podder, "Robotic approach to 4D real-time tumor tracking for radiotherapy", Phys. Med. Biol., 56 (5) 1299-1320 (2011).

61. NIH/NCI Grant Nos. 5R21CA156068-02, "Lung sparing for SBRT with beam's-eye-view images and real time tumor tracking", Web accessed on July 12th, 2016 (http://fundedresearch.cancer.gov/nciportfolio/search/details;jsessionid=9A257CCF066EDE55236C9D2F83031990?action=abstract&grantNum=5R21CA156068-02&grantID=8298131&grtSCDC=FY%202012&absID=8298131&absSCDC=CURRENT)

62. NIH Clinical Trail NCT02514512, "Lung cancer radiotherapy using realtime dynamic multileaf collimator (MLC) adaptation and radiofrequency tracking (LIGHTSABR)", Trial start date: September 2015. Trial End date: September 2017. Web accessed on July 12th, 2016 (https://clinicaltrials.gov/ct2/show/record/NCT02514512?term=lung+cancer+sydney&recr=Open)

63. WO 2015167980 A1. Real-time Margin Adaptation. US Patent Office. Nov 15 2015.

64. S. Lang, J. Zeimetz, G. Ochsner, M. Schmid Daners, O. Riesterer, S. Klöck, "Development and evaluation of a prototype tracking system using the treatment couch", Med. Phys. 41, 021720 (2014).

65. J. Wilbert, K. Baier, C. Hermann, M. Flentje, M. Guckenberger, "Accuracy of realtime couch tracking during 3-dimensional conformal radiation therapy, intensity modulated radiation therapy, and volumetric modulated arc therapy for prostate cancer", Int. J. Radiat. Oncol. Biol. Phys. 85, 237–242 (2013).

66. G. Ezzell, J. Burmeister, N. Dogan, T. LoSasso, et. al. "IMRT commissioning: multiple institution planning and dosimetry comparisons, a report from AAPM Task Group 119", Med. Phys. 36 5359–5373 (2009).

67. E. Colvill, J. Booth, S. Nill et. al. "A dosimetric comparison of real-time adaptive and non-adaptive radiotherapy: A multi-institutional study encompassing robotic, gimbaled, multileaf collimator and couch tracking", Radiother Oncol. 16 (2016).

68. S. Pollock, D. Lee, P. Keall and T. Kima, “Audiovisual biofeedback improves motion prediction accuracy”, Med. Phys. 40 (4), 041705 (2013).

69. J. H. Goodband, O.C. Haas and J.A. Mills, “A comparison of neural network approaches for online prediction in IGRT”, Med. Phys., 35(3), 1113-1122 (2008).

70. J. Yun, M. Mackenzie, S. Rathee, D. Robinson and B. G. Fallone, “An artificial neural network (ANN)-based lung-tumor motion predictor for intrafractional MR tumor tracking”, Med. Phys. 39 (7), 4423-4433 (2012).

71. P. Verma, J. Wu, M. Langer, I. Das and G. Sandison, “Survey: real-time tumor motion prediction for image-guided radiation treatment”, Computing in Sci. & Engine., 13 (5), 24-35, (2011).

72. J. Rottmann, P. Keall and R. Berbeco, “Markerless EPID image guided dynamic multi-leaf collimator tracking for lung tumors”, Phys. Med. Biol. 58, 4195–4204 (2013).

73. J. Rottmann and R. Berbeco, “Using an external surrogate for predictor model training in real-time motion management of lung tumors”, Med. Phys. 41, 121706 (2014).

74. A. Krauss, S. Nill and U. Oelfke, “The comparative performance of four respiratory motion predictors for real-time tumor tracking”, Phys. Med. Biol. 56, 5303-5317 (2011).

75. M. J. Menten, et. al.,“Comparison of a multileaf collimator tracking system and a robotic treatment couch tracking system for organ motion compensation during radiotherapy”, Med. Phys. 39, 7032 (2012).

76. G. C. Sharp, S. B. Jiang, S. Shimizu, and H. Shirato, “Prediction of respiratory tumor motion for real-time image-guided radiotherapy”, Phys. Med. Biol. 49(3), 425-440, (2004).

77. R. Ernst, A. Drichen, A. Schlaefer, and A. Schweikard, “Evaluating and comparing algorithms for respiratory motion prediction”, Phys. Med. Biol. 58(11), 3911–3929 (2013).

78. C.-K. Wang, M.-Y. Cheng et al., “Design and implementation of a multi-purpose real-time pan-tilt visual tracking system”, Proc. 2004 IEEE Int. Conf. on Control Apps., 1079-1084 (2004).

79. D. Murray and A Basu, “Motion Tracking with an Active Camera”, IEEE Trans. Pattern Analysis and Machine Intelligence 16(5), 449-459 (1994).

80. P. Keall, H. Cattell, D. Pokhrel, S. Dieterich, et al., “Geometric accuracy of a real-time target tracking system with dynamic multileaf collimator tracking system”, Int. J. Radiat. Oncol. Biol. Phys. 65, 1579–1584 (2006).

81. E. W. Pepin, H. Wu and H. Shirato, “Use of dMLC for implementation of dynamic respiratory-gated radiation therapy”, Med. Phys. 40, 101708 (2013).

Chapter 2 Background - Lung Tumor Motion and Its Management with Image-Guidance and Prediction for Radiotherapy

This chapter reviews the impact of tumor motion on the treatment process and the treatment outcome, summarizes the characteristics of typical tumor motion, examines motion-compensating techniques with margins, and compares various imaging techniques for motion quantification. Details of portal imaging, an essential tool for real-time dynamic tumor tracking, are discussed. Theoretical aspects of tracking, image registration and prediction are presented.

2.1 Impact of Motions

2.1.1 Impact of motions during dose calculation and treatment planning

Organ motion produces both random and systematic errors [1]. Random errors manifest as a blurring of the dose distribution while systematic errors shift the cumulative dose distribution relative to the target [1]. The blurring leads to an enlarged beam penumbra at the field edge and thereby to a less conformal dose distribution and potentially poorer target coverage.

According to ICRU 62 [2], setup uncertainties and target motion should be incorporated into the treatment planning with a margin around the clinical target volume (CTV). More specifically, the CTV is extended by the internal margin (IM) accounting for target motion and deformation to form the internal target volume (ITV) (figure 2.1 and table 2.1). However, the definition of these margins, with respect to motion and setup errors, was not specified well [3, 4]. The CTV-PTV margin derived from a population dataset (based on prostate treatment) is given as [4]:

$$\mathrm{Margin}_{ptv} = \alpha\, \Sigma + \beta\, (\sigma - \sigma_p) \tag{2.1}$$

where $\beta\sigma_p$ is the distance between the 95% and 50% isodose surface of the planned dose distribution ($D_{planned}$); β is the distance between the 95% and 50% isodose surface of $D_{blurred}$, the planned dose distribution that has been smeared due to target motion during treatment and setup error; σ is the total standard deviation of all random treatment execution variations (setup error σ_s, target motion σ_m, and the penumbra σ_p), i.e. $\sigma^2 = \sigma_m^2 + \sigma_s^2 + \sigma_p^2$; and Σ is the combined standard deviation of all the systematic errors incurred during preparation and planning, i.e. $\Sigma^2 = \Sigma_m^2 + \Sigma_s^2 + \Sigma_p^2$. To ensure that 90% of the patient population receives a minimum cumulative CTV dose of 95% of the prescribed dose, the margin is given as:

$$\text{Margin}_{ptv} = 2.5\,\Sigma + 1.64\,(\sigma - \sigma_p) \qquad (2.2)$$

Although the concept of a planning organ at risk volume (PRV) was introduced to account for motion and set-up uncertainties of OARs, ICRU-62 does not specify the actions required with PRVs [5-6]. However, in a separate study, a margin of 1.3Σ + /- 0.5σ around a small OAR in low (+) or high (-) dose region [7] is recommended. Adding a treatment margin to cover the limits of motion of the tumor increases the field size, and consequently exposes healthy tissues to unnecessary radiation [3]. However, if the margin is too small, the CTV might not receive sufficient dose in the presence of position and motion uncertainties.

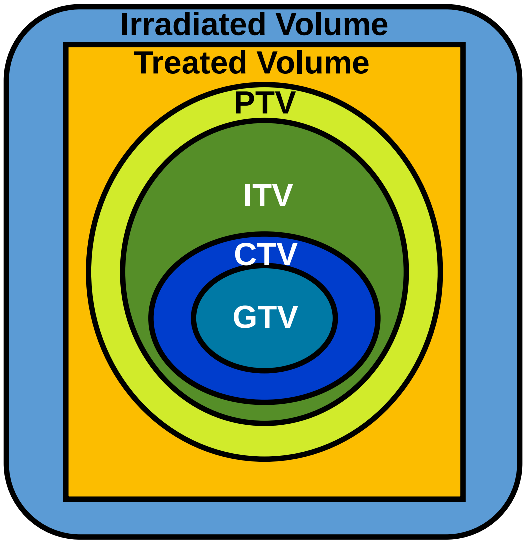

Figure 2.1 : Schematic diagram of the volumes defined by ICRU Report 62 [6].

Table 2.1 : Volumes defined by ICRU Report [6]

Volume	**Definition**
Gross Target Volume (GTV)	Gross content of tumor on planning image
Clinical Target Volume (CTV)	GTV + margin for microscopic disease
Internal Target Volume (ITV)	CTV + internal margin(IM) to encompass motion and deformation
Planning Target Volume (PTV)	ITV + setup margin (SM) to accounts for uncertainties related to setup errors, deliveries, and reproducibility of patient position
Treated Volume	Volume that receives a dose of curative significance (e.g., within the 95% isodose surface)
Irradiated volume	Volume that receives significant dose w.r.t healthy tissue tolerance

2.1.2 Impact of motion during treatment delivery

In addition to using margins to encompass the errors between planning and treatment delivery, active motion compensation (gating and dynamic aperture) has been proposed to reduce the deviations between planned and delivered treatment.

For treatments with dynamic updates of multi-leaves collimators (MLCs), such as IMRT and VMAT, where sections of the field are delivered in a moving sequence, interplay effects between the moving target and surrounding organs with respect to the moving aperture arise [9]. In contrast to image blurring which is due mainly to target motion, the interplay effect is associated with the delivery technique. It causes variations in the dose received by each voxel. However, studies have shown that interplay effect is averaged out with multiple fields as well as overall treatment fractions. When treating lung tumors with IMRT, it has been reported that the maximum dose variation reduces from 30% for one field, to 18% for five fields, and to less than 2% after 30 fractions with five fields [10, 11]. The random nature of the initial phase of the target motion at the beginning of each delivery, and the fact that organ motions are assumed to be random and do not correlate with the treatment delivered for different fractions, [12] helps to average out the interplay effect. This random nature assumption could be compromised when using few fractions, such as in hypofractionated treatments and SBRT.

Compared to sliding-window IMRT treatment, the VMAT/IMAT delivery allows MLCs to move in both directions and allows the gantry to rotate about the target. Both features reduce the effect of interplay. Overall, studies seem to indicate that the risk of underdosing/overdosing the target due to interplay effects is not significant with IMAT treatment [13, 14-15]

2.2 Lung Tumor Motion Measurement Technique and Systems

2.2.1 Direct localization methods

Direct localization of tumors with submillimeter localization accuracies have been reported for both markers and markerless techniques [16]. Using gold seeds with a diameter of 1.5 mm, an accuracy of 0.5mm is achieved when tracked with kV fluoroscopy. Accuracies of 0.5 mm and 0.2 mm have been reported for positron emission radioisotope methods and electromagnetic transponder methods respectively [11]. Using MV portal images, marker and markerless tracking techniques have achieved accuracies of 1 – 2 mm, using tracking techniques such as neural network [17], template matching [18-20], active shape models [21] and optical flow [22] algorithms. Different field of views (FOV) are associated with these direct localization techniques. The large FOV for kV fluoroscopy allows it to view surrounding structures in addition to the tumor, while the other localization techniques are restricted to the tumor. For ultrasound- and magnetic resonance- based localizations, not only are markers not required due to their high contrast, they are also able to provide volumetric imaging of tumor and surrounding OARs. One of the limitations of using markers with MV tracking is the possibility of markers being blocked by the MLCs at certain segments, which limits their direct tracking potential. Correlation and prediction models were built to overcome this occlusion problem [23].

The Calypso 4D localization system uses electromagnetic waves to detect wireless transponders implanted in the tumor of the patient. Sensors measure the emitted magnetic field strength of the transponders to determine the coordinates. The size of the transponders is 1.8mm (diameter) by 8 mm (length) and the implantation process is similar to placing a seed in the prostate. However, the dimension of the transponder and the use of a 14-gauge needle for implantation hinder their application in the lung. The system has a localization frequency of 10 Hz.

2.2.1.1 Direct localization methods - radiographic imaging with portal images

Most of the commercial digital radiographic imaging devices are fabricated in large panel using thin film technology on glass panels (figure 2.2). These devices, which incorporate a matrix of thin-film switches are commonly known as active matrix, flat-panel imagers (AMFPIs) [24] and are used as electronic portal imaging devices (EPIDs), which simply indicates that these imaging panels utilize the therapeutic photon beam as their source of x-rays. The switch in each matrix consists of an amorphous silicon (*a*-Si) photodiode connected to a thin film transistor (TFT). Incident x-rays from the treatment beam are first converted into visible light through a phosphor scintillator. A thin metal plate, usually copper, is typically placed directly above the phosphor to increase photon interactions and therefore improve the sensitivity of the imager. The light is then captured by the array of photodiodes on the *a*-Si substrate. The photodiode converts the incident light into an electric charge. Charges are stored until their release to the read-out electronics [24].

Image artifacts such as the appearance of horizontal lines [25] and vertical and horizontal bands, known as *bandings* [25-27], have been observed with portal images. One of the reasons suggested for the formation of the horizontal lines is the piecing together of smaller imager segments to form the entire image display. These errors are displayed along the grid lines of the sensors [25]. The lack of synchronization between the irradiation pulsing and detector readout have been cited as the other source for the artifacts seen in cine mode portal images [25-27].

Ghosting or *image lag* is another issue [28-29]. In this case, a latent image is formed in subsequent frames due to the trapping of charges within the photodiodes (post-irradiation). One solution would be to continue reading out the charge in the dark field following exposure, include this in the integrated EPID signal, and factor in the lag for all the response collected [28]. The average pixel intensity was observed to increase with field size as well [30].

Low contrast is associated with MV images, and this is because x-ray attenuation is dominated by Compton interactions at MV energies, as opposed to photoelectric interactions at diagnostic energies. The probability of Compton interactions is dependent on the material's electron density, and since anatomical structures generally have relatively small differences in electron density, the image contrast is lower. With a low probability of interaction, the portion of radiotherapy beam that generates a detectable signal in the converter (DQE) is low. Increasing the thickness of the phosphor screen could potentially increase the DQE of EPIDs, at the cost of reduced spatial resolution.

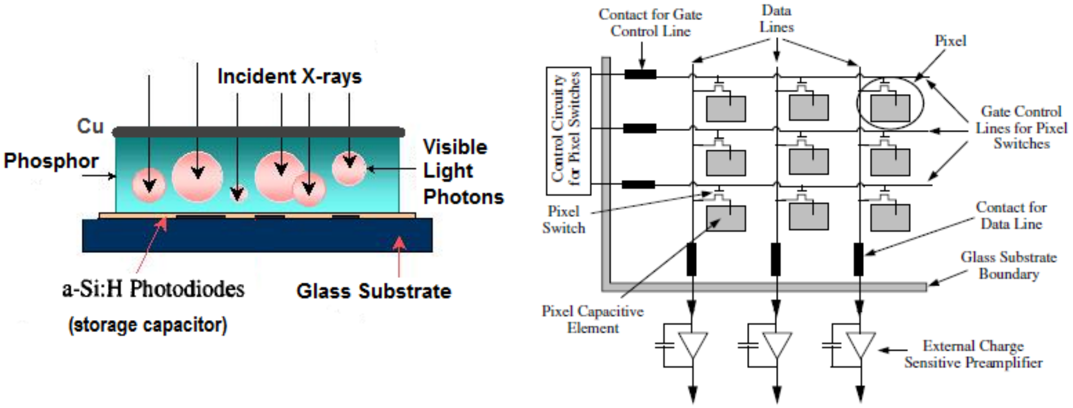

Figure 2.2: (a) Schematic illustration of x-ray interaction with an active matrix, the flat-panel imager (AMFPI) using indirect detection mechanism (Reproduced with permission from http/radonc.ucsf.edu/research_group), (b) a schematic layout of a corner of the AMFPI [24] (Reprint permission requested from AAPM).

2.2.2 Indirect localization methods

Indirect methods use surrogates to infer the spatial position of the tumor. Respiration surrogates can be categorized into two classes: internal surrogates (diaphragm, carina, etc.) and external surrogates (optical skin markers, body surface, tidal volume, etc.).

2.2.2.1 Internal and external surrogates

In using the diaphragm as an internal surrogate for a tumor in the lower lung, an average localization error of 0.8 mm and a correlation of 0.98 was achieved for motion in the superior-inferior (SI) direction [31]. For upper lobe tumors, the carina has been used as a respiratory surrogate with an average localization error of 2–3 mm. The diaphragm, which is easily detectable compared to the carina, incurs a smaller tracking error. For external surrogates, the high correlation between the diaphragm and abdominal surface motion were observed only for one minute [31]. An instantaneous time shift of up to 0.4 – 0.6 sec between the tumor and the external target was observed, and this could induce amplitude mismatches in the range of 2.5 to 4.7 mm [32]. In addition to the potential of drifts in the surrogate, the correlation between tumor motion and abdominal surface motion may fluctuate between patients and treatment fractions [32]. It has been reported that using abdominal surface motion as a surrogate for tumor motion may incur an average error of 5.4 mm [34].

2.2.3 Hybrid of direct and indirect methods

The hybrid monitoring which uses intermittent imaging to verify the position of the tumor inferred by the respiratory surrogate exposes the patients to less radiation. The CyberKnife

Synchrony and systems using kV-MV-RPM [35, 36] use both portal images (direct) and abdominal monitoring (indirect) to monitor tumor motion.

2.3 Tumor Motion Characteristics

Respiration is the dominant factor in causing tumor and organ motions in the abdominal and thorax region. Understanding the breathing patterns and the characteristics of tumor/organ motion helps to devise the appropriate tools to track its motion and account for its effect in radiation therapy.

2.3.1 Respiratory motion and the mechanics of breathing

During inhalation, the diaphragm contracts and the abdomen is forced down and forward. This enlarges the thoracic cavity to create a suction that draws air into the lungs. As the diaphragm relaxes, the elastic recoil of the lung allows air to be exhaled. The internal intercostal muscle lowers the rib cage and reduces the thoracic cavity. The lung is in the most relaxed state (i.e. equilibrium) at the end of exhale. The time taken to inhale is longer than the time taken to exhale. In addition, due to the difference in pressure between the lung and chest wall, the deflating lung volume is less than the inflating lung volume during normal breathing, a phenomenon known as *hysteresis*. The largest lung tumor motion is in the superior-inferior (SI) direction while the smallest motion is in the left-right direction. The magnitude of motion tends to decrease from the lower lobes to the upper lobes of the lungs. Due to the decreased elasticity of the lungs, patients with interstitial fibrosis may encounter shortness of breath and rapid breathing with small amplitudes. The magnitude, period, regularity and baseline of the breathing pattern could vary between planning and treatment sessions. Unlike cardiac motion, the respiratory motion is not necessarily regular (not rhythmic). However, the usage of audio feedback has been shown to improve respiratory reproducibility [3, 37]. The overall reduction in prediction error due to combined audio/visual feedback was 26% ($p < 0.001$) with abdominal wall data and 29% ($p < 0.001$) for diaphragm respiratory data [37].

2.3.2 Lung tumor motion characteristics

The AAPM TG-76 report [3] acknowledged that there is a wide variation in the lung tumor motions observed between studies. The study of tumor motion using the real-time tumor-tracking radiotherapy system (RTRT) developed in Hokkaido [38] has been highlighted in [3] to be the most detailed with two fluoroscopy imagers being used to determine the 3D real-time position of implanted markers on 20 patients during radiotherapy. Images were acquired at 30 frames/s. Hysteresis of 1 to 5 mm has been detected. The average maximum amplitude of 12 ± 2 mm (SI direction) was recorded for tumors located in the lower lobe of the lung and not attached to the chest wall or vertebrae. In another study with 20 patients using the same RTRT system for 4D treatment [39], mean displacements of 10.7 ± 8.6 mm and 8.8 ± 7.0 were recorded in the SI and AP direction respectively. The average velocity of 9.9 ± 5.4 mm/s was also measured [39]. The motions are compared with those measured by the CyberKnife [40] (table 2.2).

A general representation of the tumor trajectory has been given by Seppenwoolde et. al. [39]:

$$S(t) = S(0) - A\,cos^{2n}\left(\frac{2t}{\tau}\right) \tag{2.3}$$

where $S\ (t)$ is the position of the organ at time t, $S\ (0)$ is the position of the organ at expiration, A is the amplitude of motion, $S(0) - A$ is the position at inhalation, τ is the period of motion, and n is the degree of asymmetry of the breathing pattern. This parameterized breathing equation was used to fit the data obtained in [39]. More specifically, the variable n, which models the degree of asymmetry of the motion trajectory, was varied to obtain the best fit in each of the breathing cycles. For 90% of the patients, a value of 1 or 2 for *n* was sufficient to fit all the breathing cycles of the entire motion trajectory. This implies that the underlying shape of breathing motion can be parameterized somewhere between the two curves. For a particular case where the breathing is irregular, an additional range of values of *n* (from 3 to 9) is required for the different cycles in the trajectory [39].

Table 2.2: Summary of the average intrafraction lung tumor displacements.

Source of data	**Nos. of patients**	**SI (mm)**	**AP (mm)**	**LR (mm)**
RTRT 3D treatment [39]	20	5.5 ± 6 (all locations)	2.2 ± 1.9	1.2 ± 0.9
		2 ± 2 [*]		
		12 ± 6 [**]		
RTRT 4D treatment [41]	20	10.7 ± 8.6	8.8 ± 7.0	8.2 ± 6.5
CyberKnife with Synchrony [40]	16	3 ± 2.1 (upper lobe)	2.1 ± 1.4	1.5 ± 1.2
	4	3.2 ± 2 (middle lobe)	1 ± 0.5	1.6 ± 0.8
	7	6.9 ± 3.6 (lower lobe)	3 ± 1.9	2.5 ± 2.9
EM Calypso [42]	7	0.3 (range: -2.1 to 8.1)	0.5 (-1.3 to 9.9) [†]	0.2(-2.3 to 4.8)[†]

[†] *Range of values;* [*]*upper lobe or attached to structures;* [**] *lower lobe or not attached to structures.*

2.3.3 Lung tumor motion and cardiac motion

Applying Fourier analysis to the tumor trajectories, cardiac motions of 1 to 4 mm were detected for seven out of the twenty patients whose tumors were located near the heart [39]. However, motions due to cardiac pulsations are dominant in the lateral direction. While the heart beats at around 1 Hz (60 breaths/min), the average period for the tumor motion was 3.6 ± 0.8 s for that study group [39]. The perturbation of the tumor motion by the heartbeat could potentially affect the adaptation of treatment.

2.3.4 Lung tumor inter- and intra-fraction variations during SBRT treatment

Due to the high dose delivered over few fractions in stereotactic body radiation treatment (SBRT), repeated target localization using image-guided techniques are required [44]. In a study with 28 patients [44], the target delineated from the daily CBCT was manually matched to either the ITV of the reference planning 4DCT or the GTV of the reference helical planning CT. Couch shift was performed if setup error exceeded 3 mm. Further verification of the target location after the couch shift was performed by comparing either the kV CBCT or MV portal imaging with the planning dataset. For MV orthogonal portal imaging (80 fractions), a template of the bony anatomy from the digitally reconstructed radiograph (DRR) of the planning dataset was used as the reference whereas for CBCT, the comparison was made directly with the target from the planning dataset. The authors concluded that:

- mean 3D deviations are 2.2 and 5.3 mm for repeated scans done within and after 34 min of localization. Differences > 11 mm were observed at the end of treatment (> 34 min). It implies that after 34 mins (i.e. the mean and median time from the localization process), variations in intrafraction tumor position increase (i.e. reproducibility decreases). It was inferred that SBRT treatment sessions should ideally be less than ~34 min to ensure that the target is moving as planned. CBCT imaging should be repeated frequently if longer sessions were required,

2.3.5 Baseline drift and average period of lung tumor

The baseline of a tumor motion trajectory, obtained by taking a moving average of the individual motion data, can be considered as the latent, low-frequency component of the tumor motion [45]. In the study by Chan et al. [46], the first 100 s of tumor motion data (recorded with a CyberKnife system) was used to create the reference baseline. A 20 s moving window corresponding to about 5 breathing cycles (average period of 3.6 ± 0.6 s) was then used to derive the baseline for the intra-fraction motion data (figure 2.3). Although the baseline position drifts away from its starting value, it returns closer to its original position by the end of the treatment (figure 2.3). Taking data points at the two extreme ends would exclude the fluctuations in the middle of the treatment, resulting in an underestimation of the intra-fractional variation. Baseline drift in tumor motion was also measured by tracking the centroid of the tumor [47, 48]. Results from the two studies are summarized in Table 2.3. Up to 10% of error in dose can occur as a result of a 5 mm drift [47]. The average breathing period of 3.6 ± 0.6 s measured in [45] is similar to the mean of 3.7 s measured from three other studies [39, 45, 49-50].

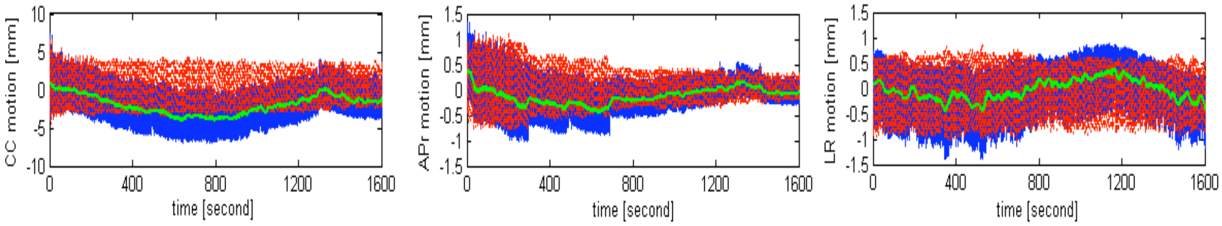

Figure 2.3.: The presence of drift and cyclic motion in the tumor motion (in three directions) of one patient [46]. Green, blue and red lines represent baselines, original, and cyclic motion (the difference between original motion and baseline). Baseline drift extends to -4 mm during treatment before returning to -0.2 mm at the end of treatment.

Table 2.3: Quantification of baseline drifts in tumor motion.

Drift (measured from moving average baseline) [49]	**Percentage of treatment fractions incurring drifts in directions:**		
	SI	**AP**	**LR**
≥ 1 mm	51 %	30 %	15 %
≥ 3 mm	18 %	3 %	2 %
	Average amplitude of drifts		
Drift (measured from tumor centroid) [48]	1.3 ± 5.1 mm	1.4 ± 5.0 mm	0.3 ± 5.5 mm

2.4 Computer Vision for Image-Guided Radiation Therapy

Computer vision, a process that includes the acquisition, retrieval, and interpretation of image contents, can be used to produce decisions for vision-based control systems [51-52]. For image-guided radiation therapy, computer vision has been used to recognize tumor targets [18, 53-54] classify disease stages [55], propagate contours on treatment volume for dose accumulation [56], estimate real-time motion on planar images [16-22], and for real-time treatment adaptation following the motion detected [35-36, 57-58].

2.4.1 Detection and motion tracking – principles and challenges

Two main factors that contribute to the detection and tracking of targets are 1) signal-to-noise ratio and 2) size of the foreground object [59]. In addition, tracking of tumor and marker motion is limited by occlusion, aperture problem, cumulative errors leading to positional drift, losing track of the object, homogenous texture, dynamic background, changes in illumination, motion and jitter of the imaging device, speed of the moving objects relative to image acquisition rate, and inconsistency of object motion [60]. Though most problems can be solved by adding constraints to the tracking process, problems related to the tumor motion are patient-specific. If the motion is slow, the background noise coupled with the regularization constraints imposed on neighboring pixels could overshadow the actual motions. If the speed is higher than the image acquisition rate, a blurred object could reduce the magnitude of motion sensed [60].

2.4.2 Temporal resolution

According to the Nyquist-Shannon Sampling theorem, the tumor/marker position acquisition rate needs to be (at least) twice the maximum frequency of the breathing cycle. The quasi-periodic motion of the tumor with an average period of about 3.7 s, would require the position to be determined every 1.8 s. However, for adaptive image-guided treatment, a real-time the system should be updating the tumor's position at approximately 0.1 - 0.2 s interval (5 -10 Hz) [61-62]. This allows prediction model to be established early during treatment and minimizes tracking (and adaptation) error [61, 62].

2.4.3 Image registration

Tracking is a form of image registration that involves continuously finding correspondence and aligning it with a reference image over a span of time. Image registration can be categorized in terms of intensity, feature, or contour-based approaches. *Intensity-based* methods compare intensity patterns of the entire region of interest via intensity difference or correlation metrics, while *feature-based* methods find correspondence between sparse sets of points representing the region of interest. Knowing the correspondence between a set of features in images, a geometrical transformation is then established to map the target image to the reference image [63]. Features can be edges, contours, or landmark points. An example of a scale and directional invariant feature point is the scale invariant feature transform descriptor (SIFT) [64]. The *contour-based* approaches rely on information at the boundaries of the object. These models are energy-minimization approaches whereby external potentials try to pull an initial curve/spline towards object contours while the internal forces try to constrain the deformation.

The image registration techniques can further be associated with *rigid* or *non-rigid* (deformable) geometric transformations. *Rigid transformations* are linear transformations (e.g. rotation, scaling and translation) and they are global in nature. They cannot model local changes between images [63]. Often, feature-based methods are used when segmentation is involved. However, this implies that the methods are highly dependent on the accuracy of the feature extraction. The intensity-based methods are more robust since they do not rely on a pre-defined set of features that are prone to changes over long image sequences. The generalized framework for image registration is shown in figure 2.4. Since a fixed reference image is required for image registration, studies have shown that the proper selection of a reference image is crucial in avoiding the propagation of errors [65-67]. Dynamic reference images were used to improve the image quality and minimize the deviation between images obtained subsequently in a long sequence [68-69].

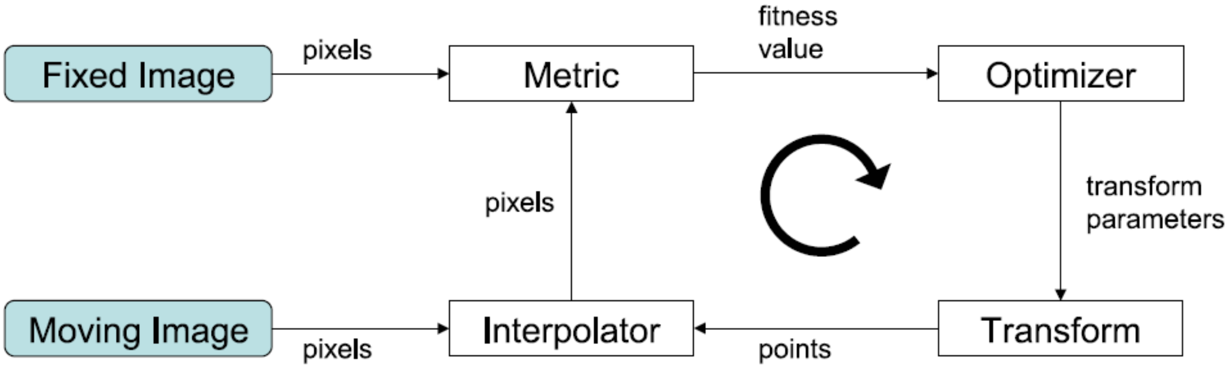

Figure 2.4: Main process in image registration for motion tracking [70].

2.4.4 Optical flow - an example of an intensity-based nonrigid image registration

The optical flow algorithm, which is traditionally used in robotic and automatic machine guidance, is a pixel-by-pixel intensity-based registration technique that eliminates the need for a manual delineation of a rigid template for tracking [22]. Flow vectors corresponding to the apparent velocity and direction of the moving object are computed based on the assumption of a small object displacement and constant illumination over time. Since it uses spatial and temporal intensity differences between images, it has metrics similar to the distance metric (e.g. sum-squared-distance or mean-squared distance). To improve computational speed, a multi-resolution pyramid scheme, where registration is first performed at a coarse resolution level with the images having fewer pixels, is used. In addition to being computationally efficient, this helps to eliminate local minima. The estimated result is then used to initialize registration for the next finer image scale. This process is repeated until image registration is done at the finest (original) scale. A comparison of the optical flow algorithm with other methods in tracking markerless lung tumors on MV EPID images is shown in table 2.4. The same accuracy is observed for both multiple template matching and the optical flow algorithm.

2.5 Prediction Techniques for Real-Time Adaptive Treatment

2.5.1 The need for prediction in radiotherapy

In order to implement adaptive IGRT, the tracking system should be able to perform the following tasks in pseudo real-time: 1) acquire images with a high frame rate, 2) detect and predict the tumor motion to cater for time delays (latency) in delivery adaptation, and 3) alter the treatment beam accordingly. In a detailed analysis, an overall time delay of up to 455 ms can be incurred [57]. This is attributed to image acquisition (200 ms), image reading and saving (150 ms), tumor detection (50 ms), and aperture adjustment (50 ms). For more complex systems, latency may increase to 1400 ms [37]. Since most systems cannot react instantaneously, prediction of future tumor positions ahead of its current position is required for any near real-time adaptive radiotherapy treatment to be successful. Preliminary results showed that beam margins could be reduced by 21% with tracking and prediction. This, in turn, could reduce the mean dose to the surrounding tissue by 10.7% [57].

Table 2.4: Comparison of markerless tumor tracking on MV EPID with different tracking/image registration methods.

Tracking / image registration method	Max. amplitude of tumor motion (mm)	Average tracking error (mm)
Single Template Matching [16]	8 - 10	1.47 ± 0.60
Multiple Template Matching [20]	8 - 10	0.57 ± 0.28
Active Shape Contours [21]	-	1.00 ± 1.00
Dynamically-Weighted Optical Flow [22]	10	0.60 ± 0.20

2.5.2 Categories of prediction algorithms

Existing methods used in predicting respiratory-related tumor motion can be classified into two categories [71-72]: 1) those that utilize a mathematical model to provide inference between its existing data and its estimated response [39, 73-75]; and 2) an empirical approach that uses adaptive filter with signal-processing algorithms to predict future value based on past data [72, 76]. The general class of linear filters, such as the autoregressive moving average (ARMA), belongs to the first category. One potential drawback is their inability to predict samples that are much further away, even if a similar event had happened before. Unlike the model-based approach, adaptive filtering is performed based on the empirical characteristics of the signal itself rather than a fixed model. The adaptive filters adjust their coefficients constantly according to the temporal variation of the signal characteristics as they are collected over time. It is more robust compared to the model-based approach in predicting distant events. Kalman filters, on the other hand, utilize a combination of the source and state (i.e. first category) model coupled with empirical sampling [72].

2.5.3 Comparison of the performance of prediction algorithms in radiotherapy

Various prediction models have been investigated for tracking and predicting tumor motion in radiotherapy. These include linear prediction [77, 78], auto-regressive moving average [79], stationary linear regression [80], sinusoidal modeling [81], adaptive filters [71, 76, 80, 82-84], Kalman filters [77, 85], and neural networks [77, 86-87]. In three of the comparative studies, neural networks have been shown to outperform the other prediction models [77, 88-89]. The first study [77] compares the performance of using linear prediction, neural network and Kalman filtering for latency of up to 1 s. The Kalman filter was unable to fully characterize the state transition matrix with the relatively small amount of data [77]. In the second study [88], a comparison between a linear filter and a neural network shows that for latencies up to 200 ms, the linear filter performs better than neural network. Beyond 200 ms of latency, the neural network outperforms the linear network. In the third study [89], a comparison between four predictors, namely neural networks, linear regression (LR), kernel density estimation (KDE) and support vector regression (SVR) showed that neural networks outperformed the SVR, LR, and KDE by 4%, 9%, and 24%, respectively.

2.5.4 Training, validation and testing methodology

Figure 2.5 (right) depicts the sequence of processing the data for real-time prediction using a sliding window approach (i.e. analyzing a finite length of data sequentially over time). A neural network with a pre-specified architecture is trained on the training set until either the maximum number of training epochs (i.e. iterations) is reached or a negligible improvement in prediction performance was obtained from the validation set. For a neural network model (figure 2.5), while increasing the number of input and hidden nodes would initially reduce the prediction error on the training data, excessive hidden nodes would result in overlearning where the network fit the training data well, but failed to generalize its prediction on unseen validation and test data [90]. Larger errors were observed i) as the prediction horizon increased, ii) during the transitions from inhale to exhale and iii) for irregular motion [71].

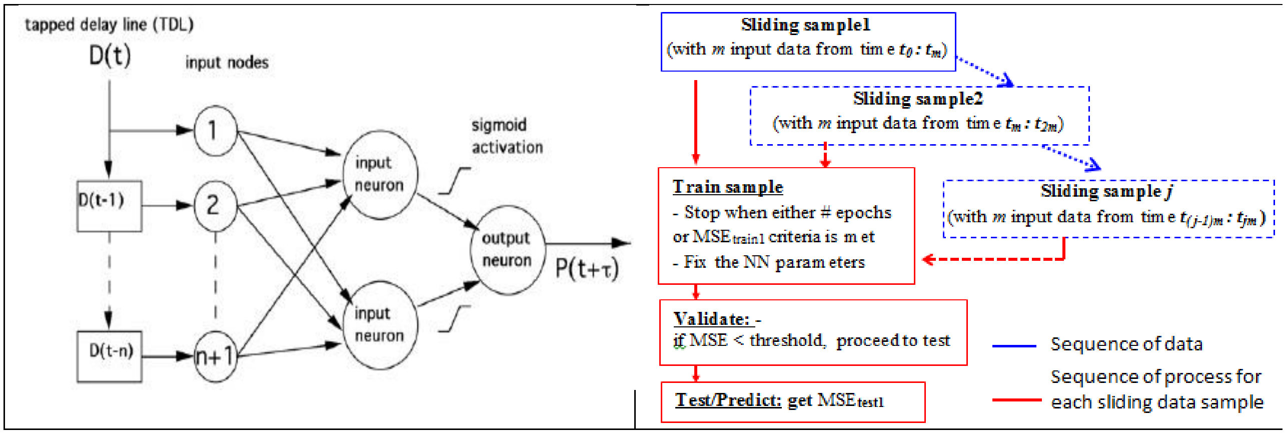

Figure 2.5 : (Left) Structure of a basic neural network; (right) time series prediction using a sliding window approach.

2.5.5 Systems with tumor tracking and prediction for real-time adaptation

In image-guided radiotherapy systems (IGRT), either the aperture of the radiation beam [35-36, 57-58, 91-92] or the patient's couch [93-95] can be adjusted according to the tumor motion detected. The CyberKnife system with a 6-MV LINAC attached to a robotic arm and the DMLC tracking system with electromagnetic transponders [96] are the only clinical system to implement real-time motion tracking and adaptation. However, it suffers from prolonged treatment times due to repeated verifications of tumor position before each beam delivery, and only small tumor volumes can be treated with each beam. Some of the systems that are currently being developed are compared in table 2.5 [35-36, 57-58, 91]. For the system that uses simultaneous kV-MV projection images to obtain the target position, a high degree of beam modulation by MLC leaves often hinders target/surrogate visibility on MV images. In using the RPM signal to build a correlation model, the possibility of amplitude mismatches in the range of 2.5 to 4.7 mm between the internal and external surrogates has to be considered. Given that the machine accuracy of the MV beam isocenter is 0.5 mm (Varian Trilogy), and inter-observer variations in target delineation of ~ 4–10 mm, further effort to reduce error to sub-mm level may yield limited benefits at this time [37].

2.6 Comparing Beam Adaptation (using DMLC) with Gating Techniques

In comparing the DMLC tracking with gating techniques, it has been shown that higher dosimetric accuracy was achieved with gating (0.1% vs. 3.7% ɣ-failure rate) at the expense of treatment efficiency (three times poorer) [97].

2.7 Summary

This chapter provided a review of how tumor motion increases the complexity of lung cancer radiation treatment. Techniques incorporating image-based tracking and prediction are shown to be crucial in monitoring the motion and adapting the treatment to improve therapeutic outcome. Despite the challenges highlighted, several systems that have successfully harnessed both image tracking and prediction capabilities for real-time adaptation have shown promising results.

Table 2.5: Systems incorporating motion tracking and prediction for real-time adaptation of treatment beam.

System	**Geometric accuracy (mm)**		**Dose difference (γ-failure rate) at 3%/ 3mm (%)**	
	With tracking & prediction	**W/out tracking & prediction**	**With tracking & prediction**	**W/out tracking & prediction**
DMLC with simultaneous MV-kV*[57]	0.9 ± 0.5	N.A.	0.2%	22.5%
DMLC with RPM† & simultaneous MV- kV* [35]	< 1.5	3.1–7.6	N.A.	N.A.
DMLC with RPM† & intermittent kV/MV* imaging [36]	0.8 – 1.4	3.1–7.3	N.A.	N.A.
Calypso implanted EM marker with DMLC [91]	0.69 (parallel)	N.A.	0.5%	40.6%
	0.8 (90 deg. to leaf motion)	N.A.		
CyberKnife [58]	≤ 1.5 mm	N.A.	N.A.	N.A.

* Motion determine by a pair of kV/MV-projected 2D positions

† Builds a correlation model with RPM and kV/MV data

N.A. – data not available.

References

1. M. van Herk, “Errors and margins in radiotherapy”, Seminars in Radiation Oncology, 14(1), 52-64 (2004).

2. ICRU-62, “ICRU Report 62 International Commission on Radiation Units Measurements”, Bethesda, MD, USA (1999).

3. American Association of Physicists in Medicine (AAPM), Radiation Therapy Committee, Task Group 76. The Management of Respiratory Motion in Radiation Oncology. Report No. 91. Madison (WI) (2006).

4. M. van Herk, et al., “The probability of correct target dosage: dose-population histograms for deriving treatment margins in radiotherapy”, Int. J. Radiat. Oncol. Biol. Phys. 47(4), 1121-1135 (2000).

5. M. Goitein, “Organ and tumor motion: An overview”, Seminars in Radiation Oncology 14(1), 2-9 (2004).

6. J. A. Purdy, “Current ICRU definitions of volumes: Limitations and future directions”, Seminars in Radiation Oncology 14(1), 27-40 (2004).

7. A. McKenzie, M. van Herk and B. Mijnheer, “Margins for geometric uncertainty around organs at risk in radiotherapy”, Radiother. Oncol., 62, 299-307 (2002).

8. J. J. Sonke, et al., “Adaptive Radiotherapy for Lung Cancer”, Seminar Radiation Oncology, 20, 94-106 (2010).

9. C. X. Yu, D. A. Jaffray and J. W. Wong, “The effects of intra-fraction organ motion on the delivery of dynamic intensity modulation”, Phys. Med. Biol., 43, 91–104 (1998).

10. T. Bortfeld, K. Jokivarsi, M. Goitein, et al., “Effects of intrafraction motion on IMRT dose delivery: Statistical analysis and simulation”, Phys. Med. Biol., 2002, 47, pp. 2203-2220.

11. T. Bortfeld, S. B. Jiang, and E. Rietzel, “Effects of Motion on the Total Dose Distribution”, Seminars in Radiation Oncology, 14(1), 41-51 (2004).

12. S. B. Jiang SB, et al., “An experimental investigation on intra-fractional organ motion effects in lung IMRT treatments”, Phys. Med. Biol., 2003, 48, pp. 1773-1784.

13. L. E. Court, M. Wagar, D. Ionascu, R. Berbeco, and L. Chin, “Management of the interplay effect when using dynamic MLC sequences to treat moving targets”, Med. Phys., 35(5), 1926-1937 (2008).

14. C. L. Ong, et al., “Dosimetric impact of the interplay effect during stereotactic lung radiation therapy delivery using flattening filter-free beams and volumetric modulated arc therapy”, Int. J. Radiat. Oncol. Biol. Phys., 86(4), 743-748 (2013).

15. C. Stambaugh, et al., “Experimentally studied dynamic dose interplay does not meaningfully affect target dose in VMAT SBRT lung treatments”, Med. Phys., 40, 091710 (2013).

16. T. Xu, et al., “Real-time tumor tracking using implanted positron emission markers: concept and simulation study”, Med. Phys., 33(7), 2598–2609 (2006).

17. T. Lin, R. Li, X. Tang, et al., “Markerless gating for lung cancer radiotherapy based on machine learning techniques”, Phys. Med. Biol., 54, 1555–1563 (2009).

18. H. Arimura, et al., “Computerized scheme for automated detection of lung nodules in low-dose computed tomography images for lung cancer screening”, Academic Radiology, vol. 11, no. 6, 617–629 (2004).

19. Y. Cui, et al., “Multiple template-based fluoroscopic tracking of lung tumor mass without implanted fiducial markers”, Phys. Med. Biol., 52(20), 6229–6242 (2007).

20. J. Rottmann, M. Aristophanous, et al., “A multi-region algorithm for markerless beam’s-eye view lung tumor tracking”, Phys. Med. Biol., 55 5585–5598 (2010).

21. Q. Xu, et al., “A deformable lung tumor tracking method in fluoroscopic video using active shape models: a feasibility study”, Phys. Med. Biol., 52(17), 5277–5293 (2007).

22. P. T. Teo et al., “Tracking lung tumor motion using a dynamically weighted optical flow algorithm and electronic portal imaging device”, Meas. Sci. Technol. 24, 074012 (15pp) (2013).

23. R. D. Wiersma, et al., “Use of MV and kV imager correlation for maintaining continuous real-time 3D internal marker tracking during beam interruptions”, Phys. Med. Biol., 54(1), pp.89–103 (2009).

24. L. E. Antonuk, “Electronic portal imaging devices: a review and historical perspective of contemporary technologies and research”, Phys. Med. Biol., 47, R31–R65 (2002).

25. P. Munro and D. C. Bouius, “X-ray quantum limited portal imaging using amorphous silicon flat-panel arrays”, Med. Phys., 25(5), 689-702 (1998).

26. H. C. Woodruff and P. B. Greer, “3D Dose reconstruction: Banding artifacts in cine mode EPID images during VMAT delivery”, J. Phys.: Conf. Ser. (444), 012042 (2013).

27. P. M. McCowan, et al., “An investigation of gantry angle data accuracy for cine-mode EPID images acquired during arc IMRT”, J. Applied Clinical Med. Phys., 15(1), 4507 (2014).

28. L. N. McDermott, et al., “Dose-response and ghosting effects of an amorphous silicon electronic portal imaging device”, Med. Phys., 31, 285–295 (2004).

29. M. C. Kirby et al., “Developments in electronic portal imaging systems”, Bri. J. Radiology, S50–S65 (2006).

30. S. L. Berry et al., “A field size specific backscatter correction algorithm for accurate EPID dosimetry”, Med. Phys., 37(6), 2425-34 (2010).

31. S. S. Vedam, et al., “Quantifying the predictability of diaphragm motion during respiration with a noninvasive external marker”, Med. Phys., 30(4), 505–513 (2003).

32. D. Ionascu, S. B. Jiang et. al., “Internal-external correlation investigations of respiratory induced motion of lung tumors”, Med. Phys., 34(10), 3893- 3903 (2007).

33. J. D. Hoisak, J.D., et al., “Prediction of lung tumor position based on spirometry and on abdominal displacement: accuracy and reproducibility”, Radiother Oncol, 78(3), 339–346 (2006).

34. S. Ahn, et al., “A feasibility study on the prediction of tumor location in the lung from skin motion”, Br J Radiol, 77(919), 588–596 (2004).

35. B. Cho, et al., “Real-time target position estimation using stereoscopic kilovoltage/megavoltage imaging and external respiratory monitoring for dynamic multileaf collimator tracking”, Int. J. Radiat. Oncol. Biol. Phys., 79(1), 269-278 (2011).

36. B. Cho, et al., “Experimental investigation of a general real-time 3D target localization method using sequential kV imaging combined with respiratory monitoring”, Phys. Med. Biol., 57(22) pp.7395-7407 (2012).

37. S. Pollock et al., “Audiovisual biofeedback improves motion prediction accuracy”, Med. Phys., 40 (4), 041705 (2013).

38. T. Kimet et al., “Audiovisual biofeedback improves diaphragm motion reproducibility in MRI”, Med. Phys., 39 (11), 6921-6928 (2012).

39. Y. Seppenwoolde, H. Shirato, et al., “Precise and real-time measurement of 3D tumor motion in lung due to breathing and heartbeat, measured during radiotherapy”, Int. J. Radiat. Oncol. Biol. Phys., 53, pp.822–834 (2002).

40. S. Dieterich and Y. Suh, "Tumor motion ranges due to respiration and respiratory motion characteristics", in H. Urschel (Eds.): Treating Tumors that Move with Respiration, Springer, chap. 1.4 (2007).

41. H. Shirato, et al., "Speed and amplitude of lung tumor motion precisely detected in four-dimensional setup and in real-time tumor-tracking radiotherapy", Int. J. Radiat. Oncol. Biol. Phys., 64(4), pp.1229-1236 (2006).

42. P. Shah, P. A. Kupelian, B. J. Waghorn et al., "Real-time tumor tracking in the lung using an electromagnetic tracking system", Int J Radiation Oncol Biol Phys, 2013, 86(3), 477-483.

43. B. Cho, et al., "First demonstration of combined kV/MV image-guided real-time dynamic multileaf-collimator target tracking", Int. J. Radiat. Oncol. Biol. Phys., 74(3), 859-867 (2009).

44. T. G. Purdie, et al., "Respiration correlated cone-beam computed tomography and 4DCT for evaluating target motion in Stereotactic Lung Radiation Therapy", Acta. Oncol., 45(7), 915-922 (2006).

45. M. W. Kissick and T. R. Mackie, "Task Group 76 Report on 'The management of respiratory motion in radiation oncology", Med. Phys, 33, 3874–3900 (2009).

46. M. Chan, et al., "Quantifying variability of intrafractional target motion in stereotactic body radiotherapy for lung cancer", J Appl Clin Med. Phys., 14(5), 140–152 (2013).

47. S. R. Chaudhari, et al., "Dosimetric variances anticipated from breathing induced tumor motion during tomotherapy treatment delivery", Phys. Med. Biol., 54, 2541–2555 (2009).

48. J. F. Gauthier, et al., "Characterization of lung tumors motion baseline using cone-beam computed tomography", Med. Phys., 39(11), pp.7062-7070 (2012).

49. Y. Suh, S Dieterich, et al., "An analysis of thoracic and abdominal tumor motion for stereotactic body radiotherapy patients", Phys. Med. Biol., 53(13), 3623–3640 (2008).

50. Y. Seppenwoolde, "Treatment precision of image-guided liver SBRT using implanted fiducial markers depends on marker–tumor distance", Phys. Med. Biol., 56(17), 5445–5468 (2011).

51. M. Sonka, et al., "Image Processing, Analysis, and Machine Vision", Thomson. ISBN 0-495-08252-X (2008).

52. C. Antonio et al., "Decision forests for computer vision and medical image analysis", Springer, (2013).

53. A. El-Baz, et al., “Computer-Aided Diagnosis Systems for Lung Cancer: Challenges and Methodologies”, Int J of Biomed Imag. Article ID 942353, 46 pages (2013).

54. K. Suzuki, F. Li, S. Sone, and K. Doi, “Computer-aided diagnostic scheme for distinction between benign and malignant nodules in thoracic low-dose CT by use of massive training artificial neural network”, IEEE Trans. Medical Imaging 24(9), 1138–1150 (2005).

55. M. Chao, “Image-based modeling of tumor shrinkage in head and neck radiation therapy”, Med. Phys. 37, 2351–2358 (2010).

56. G. G. Zhang, et al., “The use of 3D optical flow method in mapping of 3D anatomical structure and tumor contours across 4D CT data”, J. Appl. Clin. Med. Phys. 9, 59–69 (2008).

57. B. Cho, et al., “First demonstration of combined kV/MV image-guided real-time dynamic multileaf-collimator target tracking”, Int. J. Radiat. Oncol. Biol. Phys. 74(3), 859-867 (2009).

58. W. Kilby, J. R. Dooley et. al. “The CyberKnife robotic radiosurgery system in 2010”, Technology in Cancer Research and Treatment, 9(5), 433-452 (2010).

59. G. Sharp et. al, “Implications of Detection Theory”, in M. Murphy (Eds.): Adaptive Motion Compensation in Radiotherapy, CRC Press, chap. 2.3 (2012).

60. S. H. Shaikh, N. Chaki, and K. Saeed, “Moving Object Detection Using Background Subtraction”, Springer, chap. 2 (2014).

61. Q. Ren et al., “Adaptive prediction of respiratory motion for motion compensation radiotherapy”, Phys. Med. Biol. 52(22), 6651–6661 (2007).

62. P. R. Poulsen, B. Cho, A. Sawant, D. Ruan, P. Keall, “Detailed analysis of latencies in image-based dynamic MLC tracking”, Med Phys. 37, 4998-5005 (2010).

63. A. Goshtasby., “2-D and 3-D Image Registration for Medical, Remote Sensing, and Industrial Applications”, Wiley (2005).

64. Lowe, D. G., “Distinctive image features from Scale-Invariant Keypoints”, Int. J. Comp Vision 60, 91-110 (2004).

65. L. Matthews, T. Ishikawa et al., “The template update problem”, IEEE Trans Pattern Analysis and Machine Intelligence 26(6), 810-815 (2004).

66. X. Xiao, A. Ferro et. al., “Adaptive reference image set selection in automated X-Ray inspection”, J. of Electrical and Computer Engineering Article ID 794526, 7 pages (2014).

67. L. Huckvale, et al., “Reference image selection for difference imaging analysis”, MNRAS, 442, 259-272 (2014).

68. L. Gui and J. Seiner, “An image pattern tracking Algorithm for time-resolved measurement of mini- and micro-scale motion of complex object”, Algorithms 2, 533-549 (2009).

69. P. T. Teo et al., “Drift correction techniques in the tracking of lung tumor motion”, World Congress on Med. Phys. and Biomedical Engineering, 4 pages (2015).

70. M. Vila, A. Bardera, M. Feixas and M. Sbert, “Tsallis mutual information for document classification”, Entropy, 13, 1694-1707 (2011).

71. M. Murphy, et al. “Adaptive filtering to predict lung tumor breathing motion during image-guided radiation therapy”, Proc. 16th Int. Congress on Computer-assisted Radiology Surgery (CARS 2002), 539-544 (2002).

72. M. J, Murphy, “Tracking moving organs in real time”, Semin. Rad, Oncol. 14, (1), 91-100 (2004).

73. R. Colgan, J. R. McClelland, D. McQuaid et. al., “Planning lung radiotherapy using 4D CT data and a motion model”, Phys. Med. Biol. 53 (20), 5815-5830 (2008).

74. J. R. McClelland, A. Chandler, J. Blackall, S. Tarte et. al., “A continuous 4D motion model from multiple respiratory cycles for use in lung radiotherapy”, Med. Phys. 33 (9), 3348-3358 (2006).

75. T. Neicu, H. Shirato, Y. Seppenwoolde and S. B Jiang, “Synchronized moving aperture radiation therapy (SMART): average tumor trajectory for lung patients”, Phys. Med. Biol. 48, 587-598 (2003).

76. M. Isaksson, J. Joakim, and M. Murphy, “On using an adaptive neural network to predict lung tumor motion during respiration for radiotherapy applications”, Med. Phys. 32, 3801-3812 (2005).

77. G. C. Sharp et al., “Prediction of respiratory tumor motion for real-time image-guided radiotherapy”, Phys. Med. Biol. 49(3), 425–440 (2004).

78. H. Shirato et al., “Physical aspects of a real-time tumor-tracking system for gated radiotherapy”, Int. J. Radiat. Oncol. Biol. Phys. 48(1), 1187–1195 (2000).

79. Q. Ren et al., “Adaptive prediction of respiratory motion for motion compensation radiotherapy”, Phys. Med. Biol. 52(22), 6651–6661 (2007).

80. N. Riaz et al., “Predicting respiratory tumor motion with multi-dimensional adaptive filters and support Vector Regression”, Phys. Med. Biol. 54(19), 5735–5748 (2009).

81. S. Vedam et al., “Predicting respiratory motion for four-dimensional radiotherapy”, Med. Phys. 31, 2274–83 (2004).

82. M. J. Murphy, “Using neural networks to predict breathing motion”, Proc. 7th Int’l Conf. Machine Learning and Applications, IEEE Press 528–532 (2008).

83. M. J. Murphy and D. Pokhrel, “Optimization of an adaptive neural network to predict breathing”, Med. Phys. 36(1), 40–47 (2009).

84. A. Sahih et al., “Bilinear filter approach for internal and external respiratory motion modelling and prediction”, Proc. 16th Int’l Conf. System Engineering (ICSE2006), IEEE CS Press 425–430 (2006).

85. D. Putra et al., “Prediction of tumor motion using interacting multiple model filter”, Proc. 3rd IET Int’l Conf. Medical Signal and Information Processing (MEDSIP), CP520, 1–4 (2006).

86. J.H. Goodband, O.C. Haas, and J.A. Mills, “A comparison of neural network approaches for online prediction in IGRT”, Med. Phys. 35(3), 1113–1122 (2008).

87. M. Kakar et al., “Respiratory motion prediction by using the adaptive neuro fuzzy inference system (ANFIS)”, Phys. Med. Biol. 50(19), 4721–4728 (2005).

88. M. Murphy and S. Dieterich, “Comparative performance of linear and nonlinear neural networks to predict irregular breathing”, Phys. Med. Biol. 51, 5903-5910 (2006).

89. A. Krauss, S. Nill and U. Oelfke, “The comparative performance of four respiratory motion predictors for real-time tumor tracking”, Phys. Med. Biol. 56, 5303-5317 (2011).

90. P.T. Teo et al., “Application and parametric studies of a sliding window neural network for respiratory motion predictions of lung cancer patients”, World Congress on Med. Phys. and Biomed Engineering, 4 pages (2015) (Submitted).

91. A. Krauss, et al., “Electromagnetic real-time tumor position monitoring & dynamic multileaf collimator (DMLC) tracking using a Siemens 160 MLC: geometric & dosimetric accuracy of an integrated system”, Int. J. Radiat. Oncol. Biol. Phys. 79, 579–587 (2011).

92. T. Depuydt, K. Poels, D. Verellen, et al., “Treating patients with real-time tumor tracking using the vero gimbaled linac system: implementation and first review”, Radiother Oncol 112, 343–351 (2014).

93. I. Buzurovic., K. Huang, Y. Yu, and T.K. Podder, "Robotic approach to 4D real-time tumor tracking for radiotherapy", Phys. Med. Biol. 56 (5), 1299-1320 (2011).

94. S. Lang, J. Zeimetz, G. Ochsner, M. Schmid Daners, O. Riesterer, S. Klöck, “Development and evaluation of a prototype tracking system using the treatment couch”, Med. Phys. 41, 021720 (2014).

95. J. Wilbert, J. Meyer, K. Baier, M. Guckenberger, C. Herrmann, R. Hob, C. Janka, L. Ma, T. Mersebach, A. Richter, M.l Roth, K. Schilling, and M. Flentje, “Tumor tracking and motion compensation with an adaptive tumor tracking system (ATTS): System description and prototype testing”, Med. Phys. 35, 3911- 3921 (2008).

96. P. Keall, E. Colvill, R. O’Brien, J. Ng, P. Poulsen, T. Evade, A. Kneebone and J. Booth, “First clinical implementation of electromagnetic transponder- guided MLC tracking”, Med. Phys. 41(2), 020702 (5pp.) (2014).

97. M. Falk, T. Pommer, et. al., “Motion management during IMAT treatment of mobile lung tumors — A comparison of MLC tracking and gated delivery”, Med. Phys. 41 (10), 101707 (2014).

Chapter 3 Tracking Lung Motion Using a Dynamically Weighted Optical Flow Algorithm and Electronic Portal Imaging Device

This chapter presents the feasibility of using a computer vision algorithm and electronic portal images to track the motions of a tumor-like target from a breathing phantom. This approach was also applied to track uncontoured tumor motion observed on patient DRR images. This work is based on material that was published in the Journal of Measurement Science and Technology (IOP Publishing), vol. 24, 074012, 2013, DOI:10.1088/0957-0233/24/7/074012, by the author of this dissertation.

Abstract

Purpose: This chapter investigates the feasibility and accuracy of using a computer vision algorithm and electronic portal images to track the motion of a tumor-like target from a breathing phantom.

Methods: A multi-resolution optical flow algorithm that incorporates weighting based on the differences between frames was used to obtain a set of vectors corresponding to the motion between two frames. A global value representing the average motion was obtained by computing the average weighted mean from the set of vectors. The tracking accuracy of the optical flow algorithm as a function of breathing rate and target visibility was investigated. Synthetic images with different contrast-to-noise ratios (CNR) were created, and motions were tracked.

Results: The accuracy of the proposed algorithm was compared against potentiometer measurements giving average position errors of 0.6 ± 0.2 mm, 0.2 ± 0.2 mm and 0.1 ± 0.1 mm with average velocity errors of 0.2 ± 0.2 mm/s, 0.4 ± 0.3 mm/s and 0.6 ± 0.5 mm/s for 6, 12 and 16 breaths/min motions respectively. The cumulative average position error reduces more rapidly with the greater number of breathing cycles present in higher breathing rates. As the CNR increases from 4.27 to 5.6, the average relative error approaches zero, and the errors are less dependent on the velocity. When tracking a tumor on patient DRR images, a high correlation was obtained between the dynamically weighted optical flow algorithm, a manual delineation process and a centroid tracking algorithm.

Conclusions: While the accuracy of our approach is similar to that of other methods, the benefits are that it does not require manual delineation of the target and can, therefore, provide accurate real-time motion estimation during treatment.

3.1 Introduction

Diaphragm and lung tumor motions of up to 45.9 mm [1] and 33 mm in the superior-inferior (SI) direction [2] have been reported for lung cancer patients undergoing radiation therapy respectively. The rotation and deformation of lung tumors are small, and it has been shown that its motion may be adequately modeled using translation only [2]. In conventional radiation therapy, a margin around the tumor is used to account for its trajectory of motion for planning purposes [3]. Although this procedure enhances the tumor control probability (TCP), the normal tissue complication probability (NTCP) is increased as a result. Real-time monitoring of target motion is part of the overall long-term objective of image-guided adaptive radiotherapy (IGRT) that aims to improve the TCP while minimizing NTCP; i.e. improving the overall therapeutic ratio of radiotherapy [4].

Several techniques have been developed which seek to improve dose delivery to the treatment region in the presence of motion. Such techniques fall into two main categories: gating or dynamic adaptation of the treatment beam. Gating techniques rely on the fulfillment of predetermined conditions in order for the treatment beam to be activated. A common method for estimating the position of the internal tumor is to track an external marker fixed to the patients' chest via infrared camera images [1]. During treatment beam delivery, the radiation beam is turned on when the external marker passes through a spatial window defined during the treatment planning stage. While breath coaching improves the correlation between internal and external markers, deviations of 10 mm can still exist for some patients [5]. In addition, the relative position of the external reference may change with respect to the tumor during treatment; and without adjusting the gating window, the purpose of external marker tracking is defeated. Gating techniques also typically increase treatment times since the beam is only conditionally activated. Throughout the course of radiation treatment, a tumor can change in size and orientation. Treatment based on a fixed margin, defined during the initial planning stages, could result in errors if an automatic deformable tracking algorithm is not used. Thus, adopting real-time tracking and dynamic adaptation will improve system accuracy and efficiency.

Various computer vision-based techniques [6] have been proposed for tracking objects. These methods often aim at finding and learning the best features for tracking across different image settings [7]. Some of the advanced features include: histograms of gradients (HoG) [8], the spatial density of objects [9], and key points derived from the scale invariant feature transform (SIFT detector) [10]. Models capable of learning these features in a supervised [11] and unsupervised approach [12] have been developed. To track these features over different images, a general representation is required. This can only be acquired with an extensive training dataset.

One of the objectives of the proposed method is to avoid the requirements of any a priori information, such as the contour of a tumor or features acquired from training images. Although the optical flow algorithm [13-15] uses a less robust feature, i.e., temporal and spatial variation of pixel intensity, it does not require extensive training images required by the learning models. This work evaluates the use of a multi-layer (i.e. multi-resolution) adaptive threshold optical flow algorithm to track uncontoured lung tumors.

3.1.1 Tracking techniques on portal images

Portal images can be acquired in real time using an electronic portal imaging device (EPID) placed distal to the patient which detects the photon beam exiting the patient. Such images are conventionally used for patient setup correction, where a small dose of radiation is administered prior to the treatment session to correct for the position of the patient when compared to the planned treatment. These images can be used for real-time tumor tracking, which in turn may be used to dynamically adapt the treatment.

Several markerless methods have been proposed for online tracking of tumors with EPID. Most of these methods require either prior knowledge of the target object or segmentation of the target, such that the delineated contours on the initial image can be used for tracking on subsequent images. The active shape [16] and neural network method [17, 18] require training data sets while the use of similarity measures such as the normalized cross correlation and normalized mutual information between the EPID images require a reference 4D-CT template [19]. Although template matching [20-22] is capable of tracking to within 0.5 mm, frequent readjustment of the template is required to compensate for the deformation of the lung and tumor shrinkage over the treatment course [23, 24]. Although a multi-region template matching offers flexibility, pre-filtering on a training set is required to identify all the possible rigid landmarks [22].

In most studies, the gold standard used to verify the accuracy of the tracking algorithm is based on a clinician’s manual delineation of the tumor to calculate the pixel shift. However, manual delineation results in inter-observer variations of over 2.8 mm [23, 25].

It has been shown that the robustness of a Proportional-Integral-Differentia (PID) based controller can be increased by incorporating velocity information in the control process [26]. Although the velocities of typical clinical tumors have been determined [27, 28], none of the image tracking publications have dealt explicitly with the accuracy of tracking the velocities of an uncontoured tumor.

3.1.2 Optical flow tracking technique

Optical flow tracking is a method which tracks apparent motion of image intensity using the temporal and spatial gradients. Various implementations of the optical flow algorithm have been used to track organ and tumor motion. Since the change of each pixel can be represented by an optical flow vector, it offers the potential to track the motion of a deformable object where a rigid template might not find an exact match [29]. Optical flow has been used to track the pixel displacement of a segmented tumor contour from fluoroscopic video images [30]. 3D optical flow algorithms [31, 32] are used to map the displacements of contoured voxels across a four-dimensional computed tomography (4D CT) data set. Those studies compared the automatic tracking of the segmented tumor with that of a clinician’s manual delineation for different phases of the breathing cycle.

Most optical flow algorithms impose a smoothness constraint [13] or a neighborhood propagation regularization criteria [14, 15]. As a result, the optical flow vectors propagate beyond the motion edges, their magnitude decays slowly, and the boundary information is blurred. The average optical flow velocity obtained will also be lower as a result of the inclusion of the decaying optical flow components. Although object segmentation and classification procedures have been used to provide better object boundary detection, most require a priori information of the image properties. Due to the low contrast of the tumor in megavoltage portal images and the scattering of the photon beam with surrounding tissues, the accurate detection of motion with small magnitudes is challenging because it has been difficult to find a meaningful threshold for the optical flow vectors that separates small motion from random noise [22, 23].

3.1.3 Accuracy of tracking as a function of marker visibility

It has been shown that: 1) the accuracy of tracking a moving target improves as the contrast-to-noise ratio (CNR) of the marker increases; 2) the CNR of a moving marker decreases as the speed of the marker increases; 3) the CNR of a stationary marker can be improved by integrating and averaging over image frames; and 4) CNR increases as the size of the marker increases [34]. The typical maximum range of CNR for a clinical portal image was given as 5 to 10 [35]. To evaluate the accuracy of the proposed tracking algorithm as a function of marker visibility, the CNR for the phantom target was assessed, and images with a range of CNR close to 5 were generated and used for tracking.

This chapter evaluates the accuracy of an approach that automatically tracks the position and velocity of an uncontoured moving target on an EPID image sequence, using an average image-difference weighted optical flow algorithm. The set of image-difference intensities highlights the regions where changes occurred. This varies for subsequent image pairs. Hence, instead of having a fixed threshold for the entire image sequence, an adaptive set of thresholds was obtained automatically [36, 37]. The accuracy of the tracking was compared to the measurements obtained from a potentiometer attached to the actuator of the phantom's target. Instantaneous velocity and cumulative position errors were obtained, and the mean position error over the entire radiation duration was assessed. The average position error over a breathing cycle was compared for breathing rates of 6, 12 and 16 breaths/min. The tracking accuracy of the optical flow algorithm as a function of target visibility (i.e. CNR) was analyzed.

3.2 Methods and Materials

3.2.1 Optical flow tracking algorithm

A multi-resolution (also known as a multi-layer or an image pyramid) optical flow algorithm was implemented. Velocity vectors from a coarser decomposed image were used to initialize the optical flow computation for a higher resolution level, allowing tracking of larger displacements to be performed with greater accuracy than a single resolution approach [38-40]. In the proposed approach, a small group of reliable flow vectors was obtained from a set of absolute image-difference intensities [3, 37]. The array of difference values was used to weight the optical flow vectors. The average optical flow velocity was determined from the array of weighted vectors.

The mathematical formulation for obtaining the optical flow vectors $\boldsymbol{v}_{opt}$ (pixels/frame) is provided in this section [13, 38-40]. The formulation relies on two basic assumptions. The first assumes that the intensity I of the moving object along the x and y coordinates remains constant between frames acquired at time t i.e. [13]:

$$I(x, y, t) = I(x + \partial x, y + \partial y, t + \partial t) \tag{3.1}$$

This implies that the object has a similar contrast between the two image frames. By assuming small motions of dx and dy between consecutive frames, the right-hand side of (3.1) can be expanded using first-order Taylor series to get

$$I(x, y, t) + \frac{\partial I}{\partial x} v_x + \frac{\partial I}{\partial y} v_y + \frac{\partial I}{\partial t} + higher\ order\ terms \tag{3.2}$$

Substituting (3.2) to (3.1) yields the optical flow constraint equation:

$$\frac{\partial I}{\partial x} v_x + \frac{\partial I}{\partial y} v_y + \frac{\partial I}{\partial t} = 0 \tag{3.3}$$

where (v_x, v_y) are the optical flow velocity vectors and ($\frac{\partial I}{\partial x}, \frac{\partial I}{\partial y}$) are the image gradients along x and y directions, respectively. $\frac{\partial I}{\partial T}$ is the rate of change of brightness per image frame. Equation (3.3) does not have a unique solution since there is only one equation and two unknowns. The Lucas-Kanade implementation [38] of the optical flow algorithm solves this problem by creating an over-determined system using a local regularization approach where a small neighborhood / window of pixels is assumed to have the same velocity.

To implement a multi-layer optical flow for a given image pair, two individual Gaussian pyramids each comprising of three image resolution levels are constructed for each image [38]. Using the raw image (i.e. the basic layer), each subsequent image in the higher-level is obtained by (1) convolving the lower layer image with a Gaussian kernel and (2) removing every even-numbered row and column in the convolved image. As a result, an image with a coarser resolution and down-sampled by a factor of one-quarter of the area of the previous layer is obtained at each subsequent (i.e. higher) level image. The optical flow velocity vector is first obtained between two subsequent images with a coarser resolution (at the higher level). The resulting velocity vector is then used as an initial guess (g_x^L, g_y^L) in a least mean squares estimate to recursively solve for (v_x, v_y) by minimizing the image matching error function between two images. This process solves for the velocity vector of each pixel in that layer, and this value is subsequently used as an initial guess for the next layer L of analysis in which the pixel size is reduced to a finer resolution. This analysis continues for three different pixel size levels, and allows for the algorithm to accurately track larger motions. The image matching error function can be defined for layer L as [38-40]:

$$\varepsilon^L\left(d_x^L, d_y^L\right) = \sum_{x=r_x^L-w_x}^{r_x^L+w_x} \sum_{x=r_y^L-w_y}^{r_y^L+w_y} \left(I_1^L(x,y) - I_2^L(x+g_x^L+d_x^L, y+g_y^L+d_y^L)\right)^2 \tag{3.4}$$

where (r_x, r_y) is the position vector describing the location of an image point at coordinates (x, y), (I_1^L, I_2^L) is the intensity at position (x, y) in images *1* and *2* respectively, $(\mathrm{w}_\mathrm{x}, w_y)$ describe the size of the regularization window along x and y axes of the image plane, $(d_x^L,\ d_x^L)$ is the displacement of a pixel from image *1* to image *2*, and can be written as the velocity vector:

$$(d_x^L,\ d_x^L) = v^L = \begin{pmatrix} v_x^L \\ v_y^L \end{pmatrix} \tag{3.5}$$

For a given resolution level L, letting

$$(I_{11}(x,y) = I_1^L(x,y) \tag{3.6}$$

$$(I_{22}(x,y) = I_2^L(x\ + g_x^L, y + g_y^L) \tag{3.7}$$

$$(\delta I(x,y) = I_{11}(x,y) - I_{22}(x,y) \tag{3.8}$$

$$v = \binom{v_x}{v_y} = v^L \tag{3.9}$$

allow equation (3.4) to be written as:

$$\varepsilon(\boldsymbol{v}) = \varepsilon[v_x \quad v_y] = \sum_{x=r_x-w_x}^{r_x+w_x} \sum_{y=r_y-w_y}^{r_y+w_y} \left(I_{11}(x,y) - I_{22}\big(x + v_x, y + v_y\big)\right)^2 \tag{3.10}$$

The derivative of $\varepsilon(v)$ with respect to *v* is:

$$\frac{\partial \varepsilon(\boldsymbol{v})}{\partial \boldsymbol{v}} = \sum_{x=p_x-w_x}^{p_x+w_x} \sum_{x=p_y-w_y}^{p_y+w_y} \left(I_{11}(x,y) - I_{22}\big(x + v_x, y + v_y\big)\right) . \begin{bmatrix} \frac{\partial I_{22}}{\partial x} & \frac{\partial I_{22}}{\partial y} \end{bmatrix} \tag{3.11}$$

It can be written as:

$$\frac{1}{2} \frac{\partial \varepsilon(\boldsymbol{v})}{\partial \boldsymbol{v}} \approx Av - b \tag{3.12}$$

with

$$A = \sum_{x=r_x-w_x}^{r_x+w_x} \sum_{y=r_y-w_y}^{r_y+w_y} \begin{bmatrix} I_x^2 & I_x I_y \\ I_x I_y & I_x^2 \end{bmatrix} \tag{3.13}$$

$$b = \sum_{x=r_x-w_x}^{r+w_x} \sum_{y=r_y-w_y}^{r_y+w_y} \begin{bmatrix} \delta I. I_x \\ \delta I. I_y \end{bmatrix} \tag{3.13}$$

where (I_x, I_y) are the image derivatives with respect to x and y-direction, $\delta I(x,y) = I_{11}\,(x,y) - I_{22}\,(x,y) = \,|I_t\,(x,y)|$, is the modulus of the image derivative with respect to time, and $\delta I.I_x$ is the dot product of the two derivatives (i.e. I_t and I_x).

At the optimum,

$$\left.\frac{\partial \varepsilon(v)}{\partial v}\right|_{\boldsymbol{v=v_{opt}}} = [0 \quad 0] \tag{3.14}$$

which results in solving the relation:

$$Av_{opt} - b = 0 \tag{3.15}$$

$$v_{opt} = A^{-1}b \tag{3.16}$$

With k being the iterative index, the second image I_{22} is related to the previous estimated displacement $\boldsymbol{v}^{k-1}$ by:

$$I_{22}{}^{k}(x,y) = I_{22}\left(x + \boldsymbol{v}_{\boldsymbol{x}}^{k-1}, y + \boldsymbol{v}_{\boldsymbol{y}}^{k-1}\right) \tag{3.17}$$

Letting $n^k = \left[n_x{}^k \quad n_y{}^k\right]$ to be the new residual pixel motion, the error function epsilon can be written as:

$$\epsilon^k(n^k) = \epsilon\left(\left[n_x{}^k \quad n_y{}^k\right]\right) \tag{3.18}$$

$$\epsilon^k(n^k) = \sum_{x=p_x-w_x}^{p_x+w_x} \sum_{x=p_y-w_y}^{p_y+w_y} \left(I_{11}(x,y) - I_{22}\left(x + n_x, y + n_y\right)\right)^2$$

the optimal residual motion vector can be obtained by solving (from equation (3.16)):

$$n^k = A^{-1}b^k \tag{3.19}$$

where

$$b^k = \sum_{x=p_x-w_x}^{p_x+w_x} \sum_{x=p_y-w_y}^{p_y+w_y} \left(\begin{bmatrix} \delta I^k . I_x \\ \delta I^k . I_y \end{bmatrix} \right) \tag{3.20}$$

and the k^{th}image difference is expressed as:

$$\delta I^k(x, y) = I_{11}(x, y) - {I_{22}}^k(x, y) \tag{3.22}$$

With $I_x(x, y)$and $I_y(x, y)$ computed prior to the iterative process, matrix A remains constant throughout the iteration. The only update in the iterations is from b^k which accounts for the residual difference after the image is translated by v^{k-1}. Hence, both n^k and v^k will be updated with a new b^k:

$$v^k = v^{k-1} + n^k \tag{3.23}$$

For the first iteration, $v^{k=1}$is set to [0 0]. In subsequent iterations, v^k will be fed back and used as an initial guess for the next iteration step. The iteration will stop when either the computed residual motion n^L converges (< 0.05), or the maximum number of iterations is reached. In our implementation, the maximum iteration was set to 10. The iteration process will be performed at each layer *L*. A regularization window of 9-by-9 pixels was used in our implementation.

The modulus of image intensity differences between two successive image frames can be considered as a 2D map of weightings, i.e. $W_{i,j} = |I_{t0}(x, y)|$. Multiplying the weightings with each element (i, j) of the 2D array of optical flow vectors results in a 2D array of weighted optical flow solutions. To determine the average global motion, the weighted mean velocity $\langle v_{weighted} \rangle$ (pixels/frame) was computed with:

$$\langle v_{weighted} \rangle = \frac{\sum_{i,j} W_{i,j} . v_{opt}}{\sum_{i,j} W_{i,j}} \tag{3.24}$$

The velocity of the actual target v_{algo} (mm/s) calculated from two image frames was determined from:

$$v_{algo} = \langle v_{weighted} \rangle (IRes)(IRate)(InvMag) \tag{3.25}$$

where *IRes* (mm/pixel) and *IRate* (frames/s) are the resolution and image acquisition rate of the EPID respectively; and *InvMag* is the inverse magnification ratio, i.e. ratio of the distance from the source to the moving target to the distance from the source to EPID. The EPID used had an image resolution of 0.391 mm/pixel and an image acquisition rate of 7.5 frames/s. The displacement d_{algo} (mm) of the calibration target between two frames was given by:

$$d_{algo} = \langle v_{weighted} \rangle (IRes)(InvMag) \tag{3.26}$$

Integrating the changes in displacement and directions between pairs of consecutive frames provides an estimate of the accumulated target motion over time. However, residual errors incurred in the computation of motion between consecutive image frames can accumulate constructively over time [41]. The computed position of the target and the cumulative position error plot were used to analyze the errors compared to potentiometer measurements.

To estimate the number of layers required in the multi-resolution algorithm, the entire image was synthetically translated by 10 pixels, corresponding to the simulated motion of 20.6 mm/s. The simulated motion was higher than the average lung tumor motion associated with breathing. Three iterations were used to compute the optical flow velocities at each image resolution level. Simulations were performed on a 2.2 GHz Intel Core Duo 2 system with 3 GB RAM.

3.2.2 Breathing phantom's target motion

To evaluate the accuracy of the algorithm, a calibrated potentiometer (ETI Systems LCP12) was attached to the linear actuator of a Radiology Support Devices (RSD) RS-1500 Breathing Phantom. The calibration target, used to represent a tumor, was a 30 mm^3 cube of attenuating material provided by the phantom manufacturer. This target was attached to a linear actuator (figure 3.1) which was used to mechanically drive the target. The motion which the target executes was described by the following asymmetrical cosine function [28]:

$$S(t) = S(O) - Acos^{2n}\left(\frac{2t}{\tau}\right) \tag{3.21}$$

where $S(t)$ (mm) is the position of the organ at time t, $S(0)$ (mm) is the position of the organ at expiration, A (mm) is the amplitude of motion, τ (s) is the period of motion, and n is the degree of asymmetry of breathing pattern. In this work, $n=2$ was used [42]. The target was driven with an amplitude of 11.5 mm, a value chosen to represent typical lung tumors displacements [27]. The breathing rate was initially set at 12 breaths/min. Tracking of motion with periodicities of 6 and 16 breaths/min were performed to investigate the tracking performance outside the average patient tumor motion of 12 breaths/min. The increase in the numbers of breaths per minute corresponds to a rapid transition between the inhaling and exhaling phases.

The National Instrument LabView software and USB-6009 Data Acquisition Suite were used to control the motion characteristics of the linear actuator. A second LabView interface was used to measure the resistance of the attached potentiometer which was linearly proportional to the extension of the actuator arm. The velocity was obtained by taking the derivative of the recorded position function with respect to time.

3.2.3 Image acquisition

The tumor target placed at a distance of 100 cm from the source was irradiated using a Varian Linac 2100iX 6 MV beam at a dose rate of 600 MU/min. The radiation field size was 9.1 cm by 8.2 cm, measured at the target level (i.e., the isocenter). At the EPID level, (142.3 cm from the source) this would translate to an irradiation area of 12.9 cm by 11.7 cm. Within this area, a smaller window measuring 9.2 cm by 7.0 cm (235 pixels by 178 pixels) was selected for our region of image analysis. This field of view that covers the motion of the target was selected at the center of the EPID. The parameters for the setup shown in figure 3.1(a) are given in table 3.1. The image sequence (figure 3.1(b)), in DICOM format, was imported into Matlab and converted to a double-precision image (with intensity value ranging from 0 to 1) for processing.

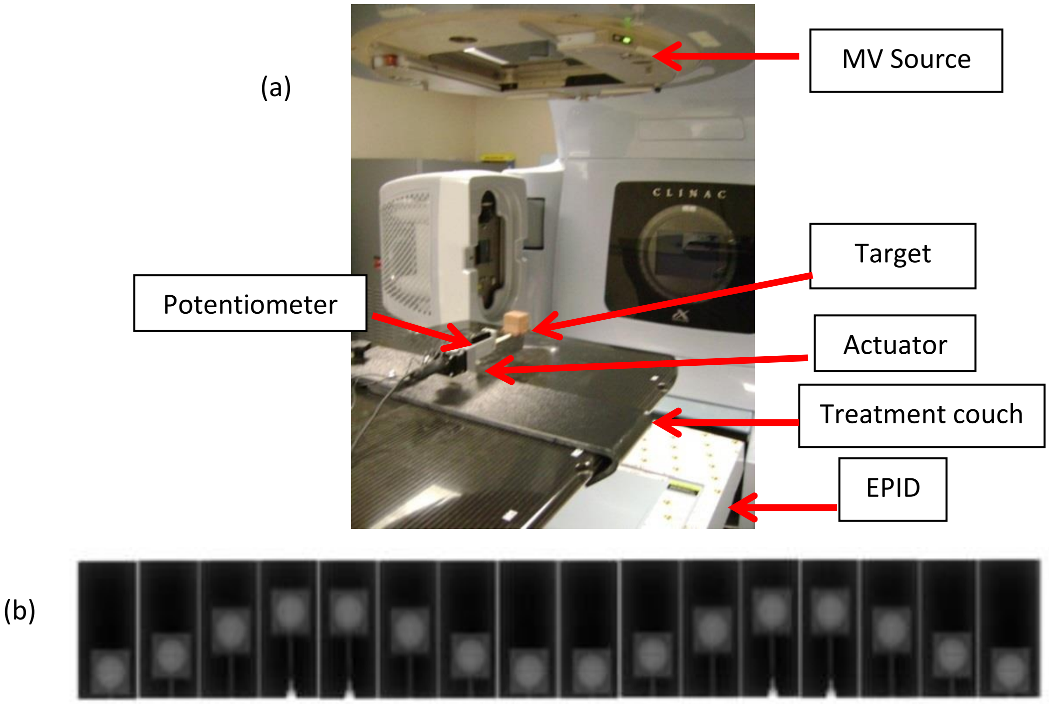

Figure 3.1 : (a) Actuator and treatment couch setup; (b) image sequence showing the motion of the target.

Table 3.1 : Parameters for measurement set-up.

Setup Parameters	**Reference Values**	**Dimensions at EPID**
Mid-line of Target (isocenter)	100 cm from source	n/a
Imager	142.3 cm from source	n/a
Radiation field length	9.1 cm @ isocenter	12.9 cm
Radiation field width	8.2 cm @ isocenter	11.7 cm
Target block dimension	3.0 cm × 3.0 cm	4.3 cm × 4.3 cm
Target motion amplitude (superior- inferior)	1.2 cm	1.7 cm
Image region of interest (length)	235 pixels @ EPID	9.2 cm
Image region of interest (width)	178 pixels @ EPID	7.0 cm

3.2.4 Evaluation of results

3.2.4.1 Tracking accuracy compared with potentiometer

The potentiometer data was recorded at time intervals of 0.1 s. The data from the tracking algorithm was limited by the imaging frame rate of 7.5 frames/sec, which was equivalent to sampling at time intervals of 0.133 s. Linear interpolation was performed on the potentiometer data to yield a set of velocities with the same time intervals as those obtained from the algorithm. Synchronization of the potentiometer and image data were performed by 1) incorporating a triggering pulse sequence in the programmed motion, and 2) setting time equals zero for both potentiometer readings and optical flow tracking as the end of the triggering pulse.

For the linear potentiometer, a maximum linearity tolerance of 0.5% was associated with a maximum extension of 12 mm. The error associated with the data acquisition is negligible as the NI USB-6009 data acquisition card has a timing resolution of 10^{-9} s and a precision of 100 parts per million.

To evaluate the algorithm's tracking accuracy as a function of time, the data was analyzed in several ways. The first method utilized a histogram to analyze the distribution of the errors (differences) between velocity measured by the potentiometer and that determined by the algorithm. The histogram data was fitted with a normal distribution and the average, and standard deviation was determined for the entire error population derived from tracking 234 image frames. In the second method, a linear regression analysis was used to determine the correlation of the velocity obtained from the potentiometer and algorithm. The third method involves sampling the entire image sequence into individual breathing cycles to obtain the sample mean and standard deviation of errors per breathing cycle. The maximum average error was then determined from the sample mean. The cumulative position error ε_s (mm) at time t (s) was evaluated by taking the recurrent sum of the previous position error $\varepsilon_s(t-1)$ and the product of the current velocity error ε_v (mm/s) multiplied by the time interval Δt(s), i.e.:

$$\varepsilon_s(t) = \varepsilon_s(t-\Delta t) + [\varepsilon_v(t) * \Delta t] \tag{3.22}$$

where $\varepsilon_v = v_{potentiometer} - v_{algo}$ Dividing the cumulative position error with the continuous time variable resulted in the cumulative average position error over time. The cumulative position error plot was used to detect the instantaneous position error while the cumulative average position error plot revealed the mean position error over time.

3.2.4.2 Tracking accuracy as a function of marker visibility and velocity

The CNR between the target and background region (figure 3.2(a)) defined by:

$$CNR = \frac{\bar{I}_{target} - \bar{I}_{background}}{\sigma_{background}} \tag{3.23}$$

was assessed for an image sequence of 234 frames (figure 3.2(b)). $\bar{I}_{target}$ and $\bar{I}_{background}$ are the mean pixel intensities of the target and background region respectively and $\sigma_{background}$ is the standard deviation of the intensities in the background region. Images were acquired with a 6 MV beam at a dose rate of 600 MU/min. Since the random variations between image frames were small, averaging of the image frames did not increase the range of the CNR (figure 3.2(c)). To achieve a broader range of CNR, images with similar noise distribution but different CNR were artificially generated. This was done by selecting an image with a CNR closest to the mean value of the 234-image sequence, and scaling each pixel values in the target region uniformly to obtain CNR of 4.27 to 5.57. Translations of 1 to 10 pixels corresponding to target motions of 2.1 mm/s to 20.6 mm/s (at isocenter) were simulated on each of the images. The optical flow algorithm and image processing procedures were then applied to track the motion. Errors relative to the simulated target speed (mm/s) were determined.

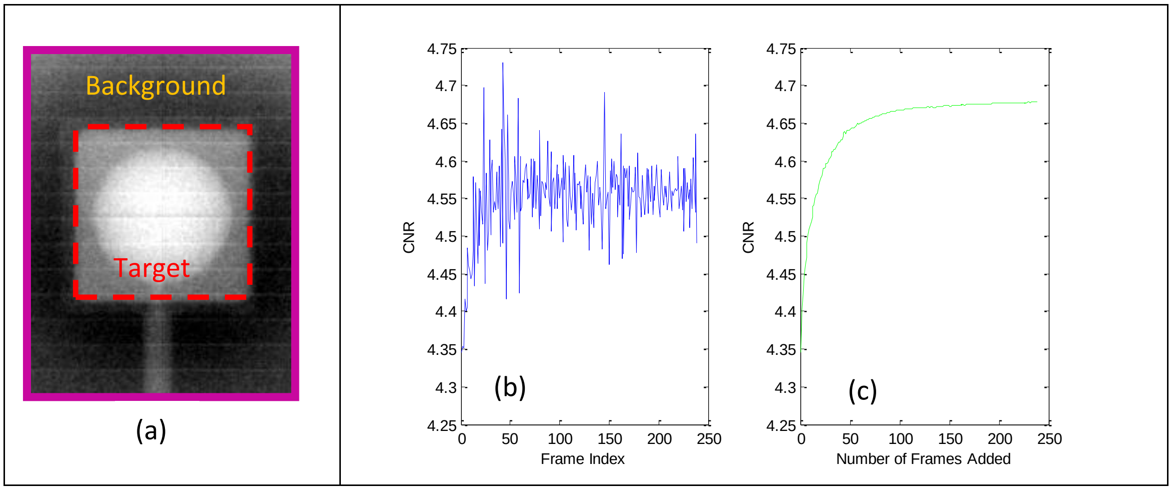

Figure 3.2 : (a) Region within the red box is defined as the target while the region outside of it is defined as the background; (b) CNR of the target determined for individual images; (c) integrated and averaged images over 234 frames. Since the random variations between image frames were small, averaging of the image frames did not increase the range of the CNR.

3.2.4.3 Tracking accuracy with patient images

In our preliminary experiment, a sequence of fluoroscopic video (figure 3.3) was acquired following the method described in [6]. A total of ten digitally reconstructed radiographs (DRRs) corresponding to ten breathing phases of the patient were used for tracking evaluation. Similar to a recent study [30, 43], ten tumor positions were manually delineated by a clinician. For comparison, the average of four manual delineations was used for each breathing phase. In addition, a centroid tracking algorithm [44], based on the segmentation between the foreground and the background (and finding the center of the segmented region), was adapted and used as an additional source of comparison. The three methods were compared using the Pearson Correlation Coefficient.

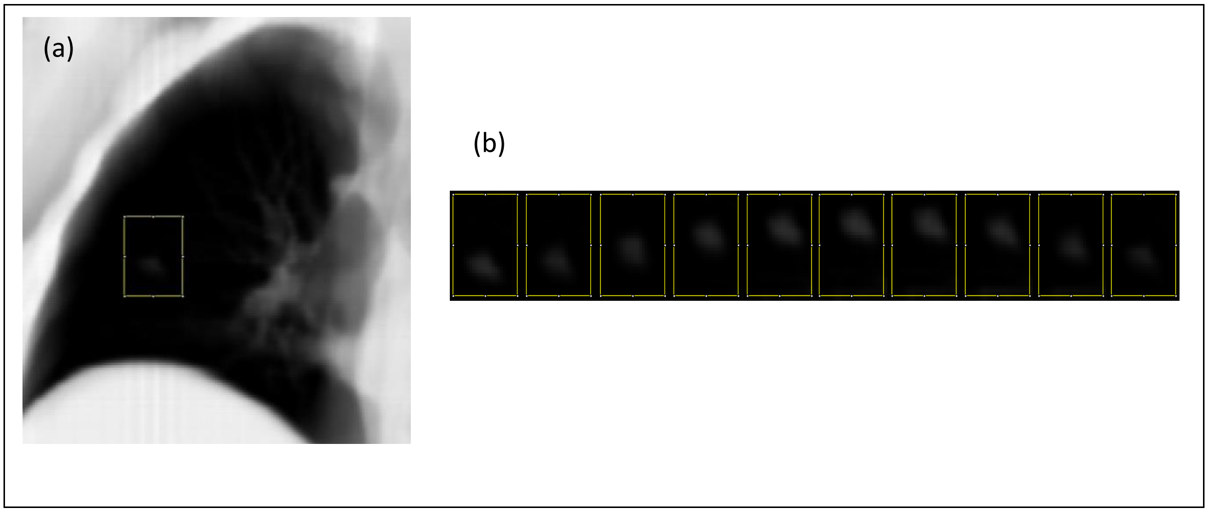

Figure 3.3 : (a) A lung patient's DRR image; (b) sequence of the uncontoured tumor motion for the 10 breathing phases.

3.3 Results

3.3.1 Simulated image translation

Figure 3.4 depicts the simulated image translation and the computed optical flow vectors overlaid on the normalized image difference plot. The vector field plot in figure 3.4(c), illustrates that although the entire image has been translated by 10 pixels, regions with strong contrast generate a denser vector field plot compared to regions with homogeneous intensity.

Figure 3.5 depicts the histogram distribution of the optical flow velocity vectors for the simulated 10 pixels image translation for one to four multi-resolution layers. The left column illustrates the histogram for the horizontal vectors while the right column depicts the vertical motion vectors. With the actuator programmed to move only in the vertical direction, the horizontal vectors were expected to have a mean amplitude distribution centered at zero. For the vertical motion vectors, the peak at the zero amplitude is due to the zero motion recorded from the homogeneous regions while the peak at an amplitude of -10 pixels/frame reflects the simulated image translation. As the number of layers for the multi-resolution algorithm increases from one to three, the peak of the histogram distribution corresponding to the simulated vertical translation increases in height. The location of the dominant peak of the distribution does not change significantly beyond three layers. Average computation times of 7.52 s, 8.85 s, 9.76 s and 10.1 s were obtained for one to four layers respectively. The three-layer multi-resolution algorithm was an effective tradeoff between accuracy and computation efficiency for the desired range of motion tested.

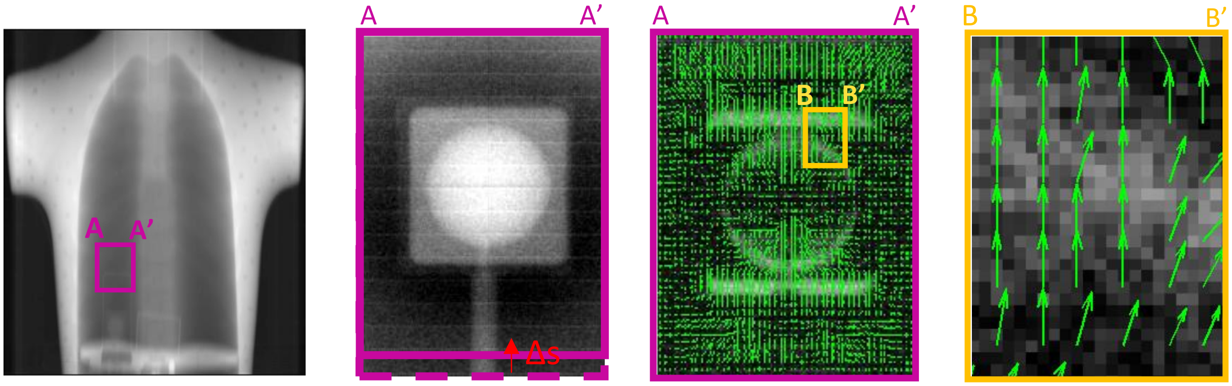

(a) (b) (c) (d)

Figure 3.4 : (a) Location of the target with respect to the phantom; (b) simulated translation of the entire window with Δs=10pixels; (c) computed optical flow vectors superimposed on the normalized difference image; (d) a zoom-in view of the optical flow vectors.

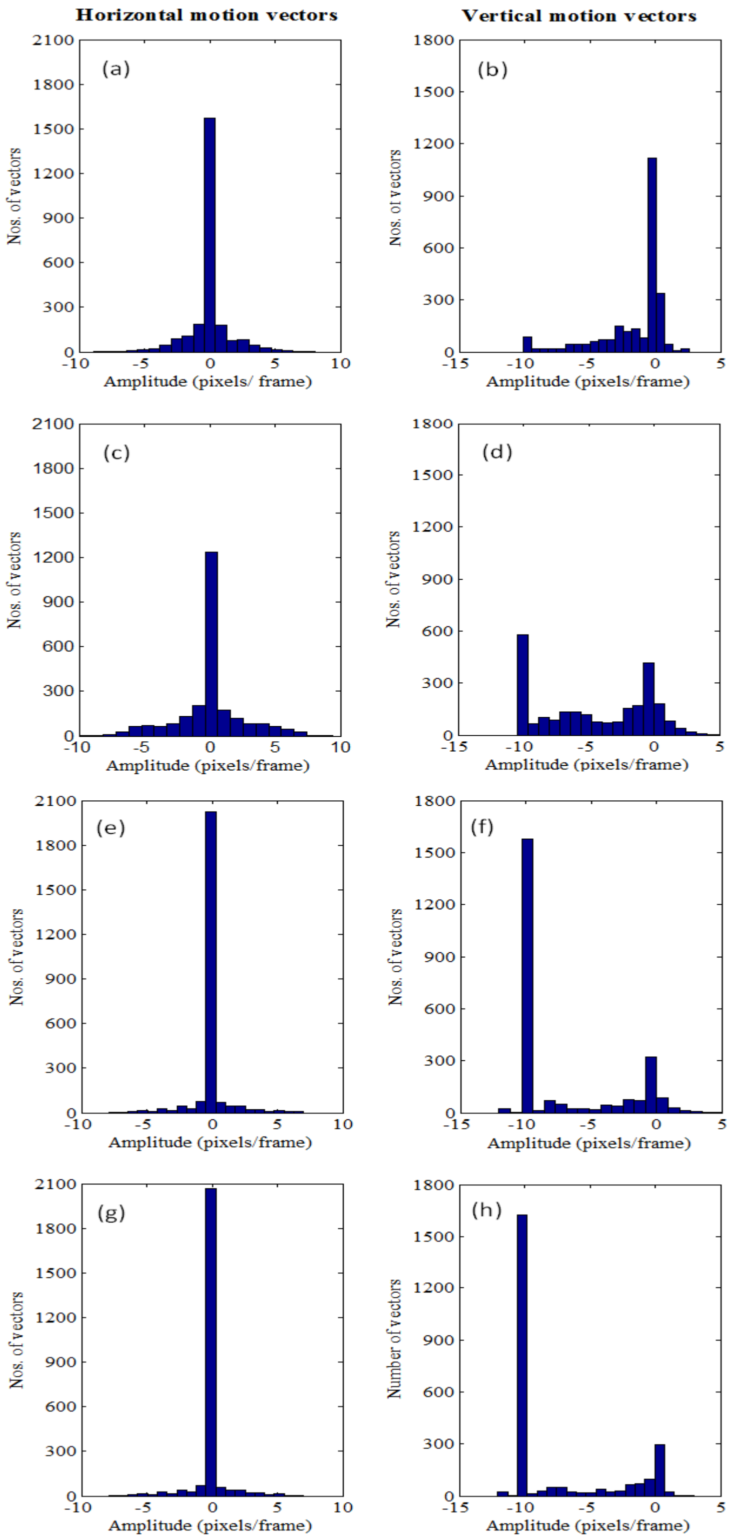

Figure 3.5 : Histogram for horizontal (*left*) and vertical (*right*) optical flow vectors computed with (a)-(b) 1 layer; (c)-(d) 2 layers;(e)-(f) 3 layers and (g)-(h) 4 layers of the multi-resolution algorithm. The simulated motion is 10 pixels.

3.3.2 Tracking accuracy compared with potentiometer

3.3.2.1 Target moving at 12 breaths/min (clinical average)

The velocity trajectory shown in figure 3.6(a) was obtained after computing the optical flow for a 234-image sequence and using the conversion provided by equation (3.25). The vertical axis represents the velocity detected between two frames while the horizontal axis represents the equivalent time index between the frames. A maximum velocity of 10 mm/s was measured by the potentiometer. The errors between the potentiometer and the computed velocity vary around a mean of zero. When the actuator target was in the extension phase (i.e., in the positive velocity direction), the positive and negative errors correspond to underestimation and overestimation of the computed velocity respectively. When the target was retracting (velocity is negative), the positive and negative errors correspond to overestimation and underestimation, respectively, of the computed velocity. Maximum and average velocity errors of 1.2 mm/s and 0.4 ± 0.3 mm/s were obtained for the entire sequence. The corresponding cumulative position error is shown in figure 3.6(b).

Figure 3.7(a) depicts the velocity errors fitted with a normal distribution. A mean of 0 bounded by a 95% confidence interval of (-0.05, 0.05) mm/s and a standard deviation of 0.55 mm/s was obtained. The linear regression analysis between the measured and computed velocities (figure 3.7(b)) fitted with a $y = ax + b$ gives $a = 0.97$ and $b = 0$ bounded by 95% prediction bounds of (0.96, 0.98) and (-0.04, 0.05) respectively. A goodness-of-fit analysis returns a root mean square error of 0.5 mm/s.

The computed velocity profile for each breathing cycle (period of 5 s) shown in figure 3.8(a) was compared with the potentiometer result and the mean, and standard deviation of errors per breathing cycle are plotted in figure 3.8(b). A maximum average velocity error of 1.1 ± 0.6 mm/s per breathing cycle is observed.

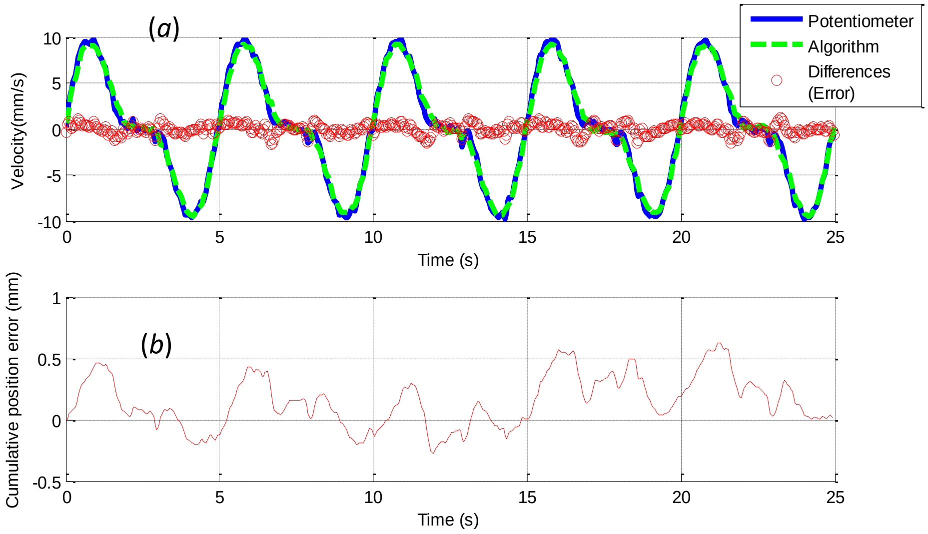

Figure 3.6 : (a) Velocities (mm/s) of the target computed using the optical flow algorithm and measured by the potentiometer. The velocity errors were obtained by subtracting the computed velocity from the measured velocity. The computed results were obtained by analyzing a sequence of 234 images. (b) Cumulative position error (mm) obtained by summing previous position error with the product of the current velocity error and its current time interval (refer to equation (3.21))

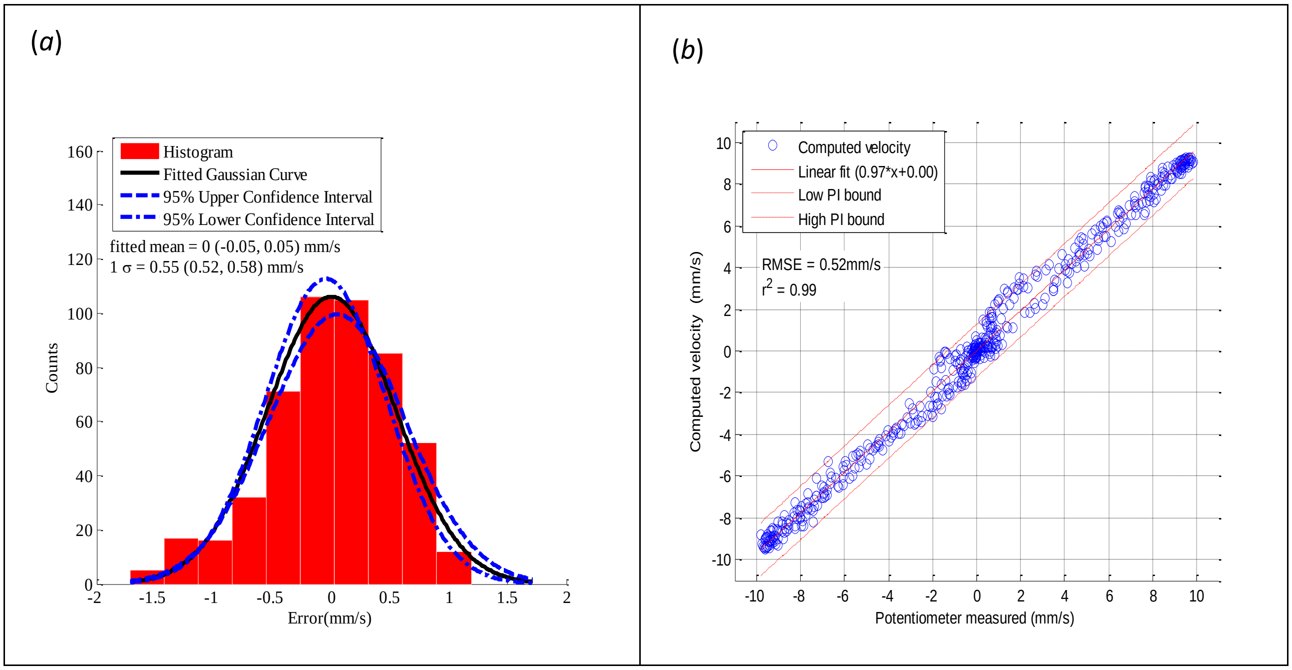

Figure 3.7 : (a). Distribution of the differences (error) between the computed and potentiometer measured velocity. The mean of the distribution occurs at 0 bounded by (-0.05, 0.05) mm/s 95% confidence interval with 1 standard deviation of 0.55 mm/s; (b) linear regression analysis to determine the correlation of measured velocities with that detected by the optical flow algorithm.

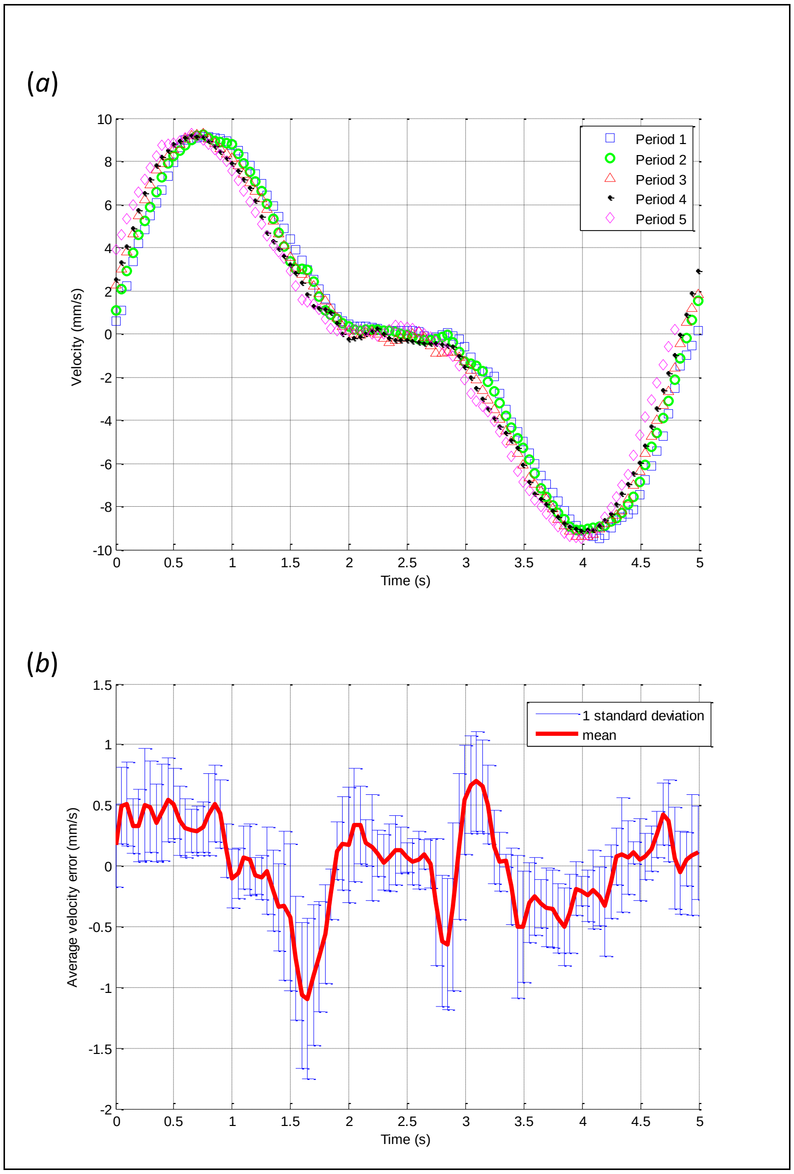

Figure 3.8 : Velocity profile of an average breathing cycle with a period of 5 s for a 12 breaths/min motion - (a) overlay of the computed velocity profiles of each period; (b) average and one standard deviation of the differences (error) between the computed and potentiometer measured velocity. A maximum (absolute) average velocity error of (1.1 ± 0.6) mm/s per breathing cycle was observed at 1.7s.

3.3.2.2 Target moving at 6 and 16 breaths/min

Results for tracking motion with 6 breaths/min are presented in figure 3.9. The maximum velocity of 5 mm/s was measured (figure 3.9(a)). During the first 5 s where the velocity plot is positive (extraction phase of the actuator), a mean positive error of 0.1 ± 0.3 mm/s corresponds to an underestimation of the computed velocity. In the next 5 s where the velocity is negative, a mean negative error of -0.06 ± 0.22 mm/s indicates underestimation of the computed velocity during the retraction of the target. The algorithm underestimated the true velocity in both phases. Similar trends of underestimation during the extraction and retraction of the target were observed for the other periods. Overall, a maximum and average velocity error of 0.9 mm/s and 0.2 ± 0.2 mm/s respectively were obtained for the entire image sequence. For the cumulative position errors at 6 breaths/min (figure 3.9(b)), all the errors were positive. For the 16 breaths/min motion, a maximum and average velocity error of 2.3 mm/s and 0.6 ± 0.5 mm/s were obtained for the entire image sequence respectively. In contrast to the 12 and 16 breaths/min, only positive errors were observed for the 6 breaths/min motion. The cumulative average position errors decrease more quickly over time for 12 and 16 breaths/min motions than the 6 breaths/min motion. The larger number of breathing cycles from the faster breathing motion helps to average out the errors.

In analyzing the correlation between the computed and measured velocities, correlation coefficients of 0.95 and 0.97 bounded with a 95% prediction interval of (0.94, 0.96) and (0.96, 0.98) were obtained for 6 and 16 breaths/min respectively. Using a similar analysis shown in figure 3.8, maximum average errors of 0.4 ± 0.4 mm/s and 1.5 ± 0.6 mm/s per breathing cycle were obtained for 6 and 16 breaths/min motions respectively.

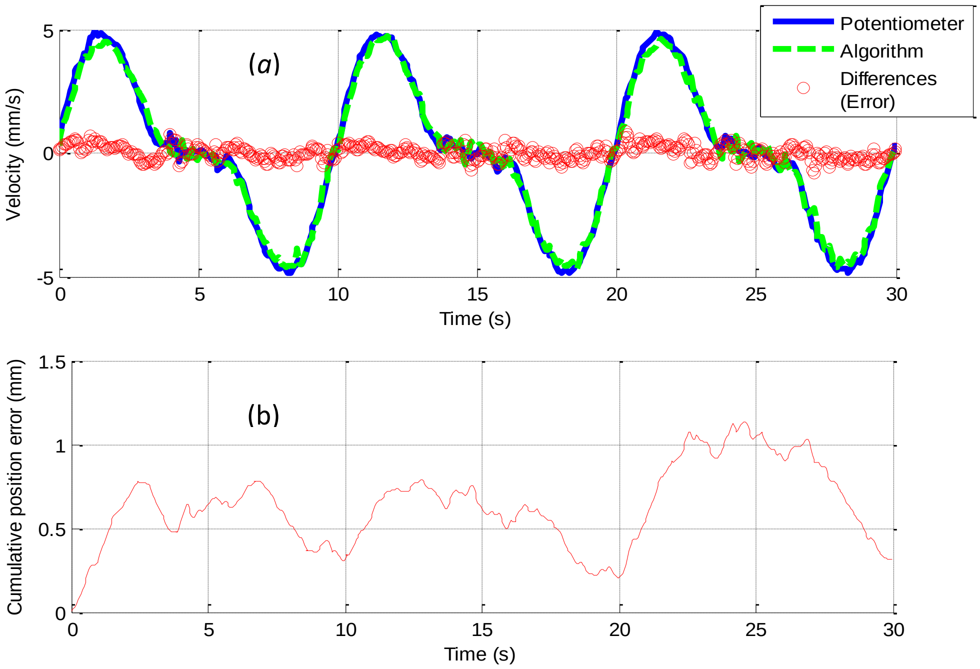

Figure 3.9 : Comparison of (a) velocity profiles and (b) cumulative position errors for 6 breaths/min.

3.3.2.3 Accumulated target positions

Figure 3.10 compares the positions computed from the algorithm (summing d_{algo} obtained from equation (3.26)) with those measured by the potentiometer. Maximum displacements of 11.5 mm were measured by the potentiometer for the three breathing rates. For 6 breaths/min (figure 3.10(a)), underestimations of the computed positions were observed when the actuator was fully extended. This is supported by the analysis of the velocity error (figure 3.9(a)) provided in section 3.3.2.2, where underestimation is more common than overestimation in the computed velocity during the extraction and retraction phases of all periods. However, since the underestimation of the velocity is smaller during the retraction of the target (as mentioned in section 3.3.2.2), instead of returning to the initial starting position, the target retracts further to a negative-valued position at the end of each period. Maximum position errors of 1.1 mm, 0.6 mm and 0.7 mm, and average position errors of 0.6 ± 0.2 mm, 0.2 ± 0.2 mm, 0.1 ± 0.1 mm were obtained for 6, 12 and 16 breaths/min motion, respectively.

Using a similar analysis shown in figure 3.8, maximum average errors of 0.6 ± 0.4 mm, 0.4 ± 0.2 mm and 0.2 ± 0.1 mm per breathing cycle were obtained for 6, 12 and 16 breaths/min motions respectively.

A summary of the overall tracking performance compared to potentiometer results is provided in table 3.2. The error analysis proves to be consistent as it is observed that the maximum average errors (obtained from an average breathing cycle), is in between the maximum errors and the average errors obtained from an entire image sequence. Generally, as the breathing rate increases, the velocity errors increase while the position errors decrease. This apparent contradiction is explained in the Discussion (section 3.4).

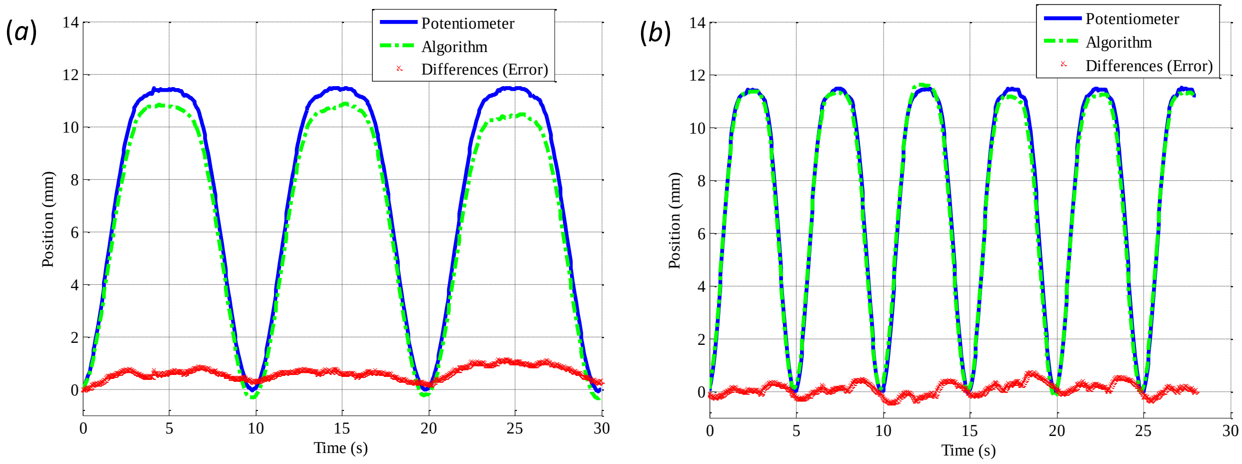

Figure 3.10 : (a)-(b) Position of actuator accumulated from the detected inter-frame displacement for 6 and 12 breaths/min respectively.

Table 3.2 : Summary of tracking results compared with potentiometer measurements.

	6 breaths/min†	12 breaths/min†	16 breaths/min†
Max velocity error (mm/s)	0.9	1.2	2.3
Max position error (mm)	1.1	0.6	0.7
Average velocity error (mm/s)	0.2 ± 0.2	0.4 ± 0.3	0.6 ± 0.5
Average position error (mm)	0.6 ± 0.2	0.2 ± 0.2	0.1 ± 0.1
Maximum average velocity error over a breathing cycle (mm/s)	0.4 ± 0.4	1.1 ± 0.6	1.5 ± 0.6
Maximum average position error over a breathing cycle (mm/s)	0.6 ± 0.4	0.4 ± 0.2	0.2 ± 0.1
Correlation coefficient *	0.95 (0.94, 0.96)	0.97 (0.96, 0.98)	0.97 (0.96, 0.98)

*Correlation coefficient between computed and measured velocity with 95% prediction interval.
†Maximum velocities of 5, 10 and 12.5mm/s were measured for 6, 12 and 16 breaths/min respectively.
(For all errors, the absolute values are reported, i.e. without the sign).

3.3.3 Tracking accuracy as a function of CNR

Figure 3.11(a) and (b) graphs the absolute and relative error of the computed velocity versus the simulated velocity for images with different CNR. A CNR of 4.58 corresponds to the image without contrast enhancement. In both plots, the error reduces as CNR increases. While the absolute error decreases from an average of 1.2 ± 0.7 mm to an average of 0 ± 0.1 mm, the corresponding relative error decreases from 11.2 ± 1.2 % to 0.3 ± 0.3 % as the CNR increases from 4.27 to 5.6. In addition, as CNR increases, errors are less dependent on velocity. At low CNR, the absolute errors (figure 3.11(a)) increase with velocity. However, this corresponds to a reduction when measured in terms of relative error (figure 3.11(b)). Despite a decrease in the relative error, a higher level of uncertainty is observed as the simulated velocity increases. With CNR of 4.58, the absolute errors for the simulated velocities are in the same range as those obtained when making the comparison with potentiometer measurements (table 2.2). A similar trend of increasing velocity errors as the velocity increases was observed when compared with potentiometer measurements.

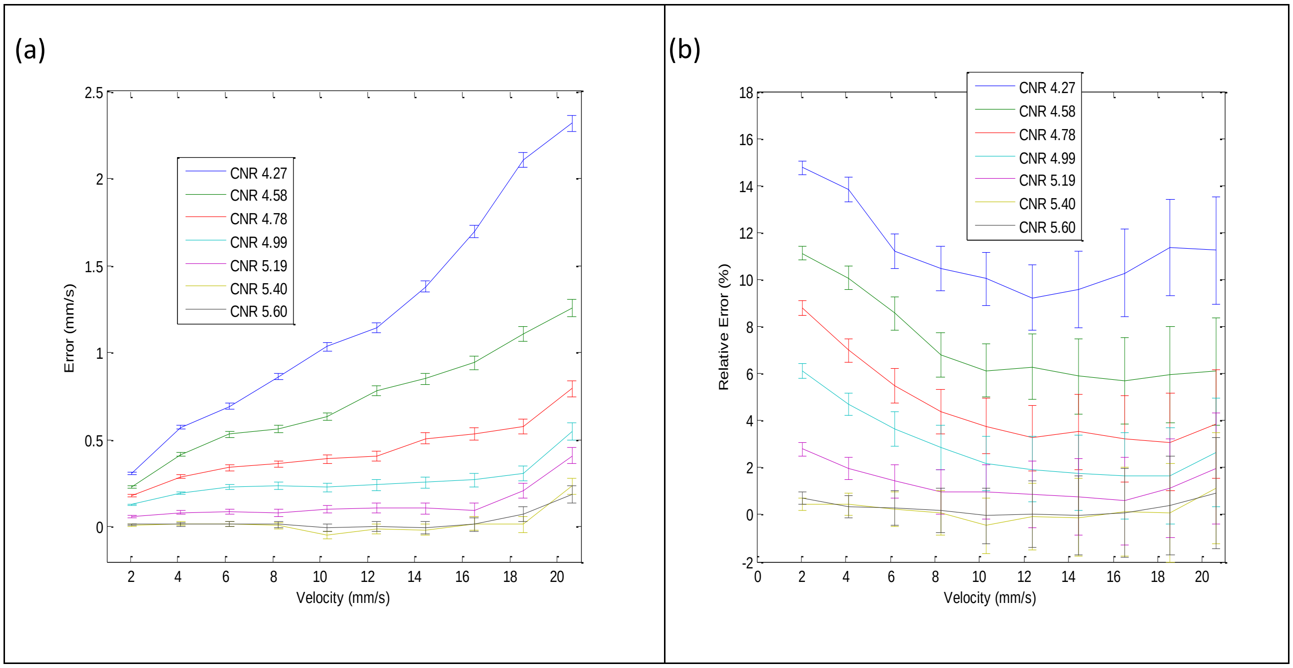

Figure 3.11 : (a) Absolute and (b) relative error versus simulated velocity for images with different target CNR. In both plots, higher errors are associated with low CNR.

3.3.4 Tracking accuracy with patient images

Figure 3.12 compares the performance of the three methods (i.e. optical flow, centroid tracking, and manual delineation) in tracking the tumor motion shown in the patient DRR images (figure 3.3b). From frame 1 to frame 6, the tumor is observed to be traveling in a negative direction. This corresponds to the upward motion of the tumor (inhalation of the lung) observed in the respective image sequence shown in figure 3.3. Beyond frame 6, the tumor travels in the opposite direction that corresponds to the exhalation of the lung. Minimum velocity is observed in frame 6 when the breathing transits from inhalation to exhalation. The error bars for optical flow and centroid tracking algorithm were computed by considering the localization error due to imaging uncertainty. For manual delineation, the uncertainty includes both interobserver deviations and the imaging uncertainty. The piecewise (Pearson) correlation reports a correlation that is greater than 0.95 for the magnitude and 0.97 for the direction between all methods with a p-value lower than 0.001 in all cases.

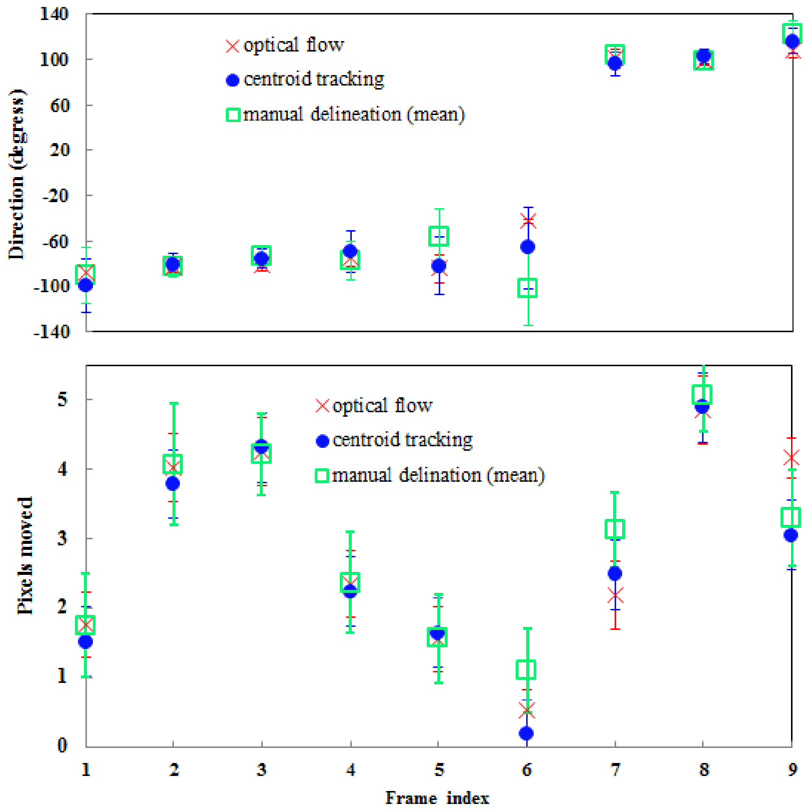

Figure 3.12 : Comparison of tracking performances in terms of (a) direction and (b) magnitude of velocity (pixels moved per frame) of tumor motion for patient images shown in figure 3.3. The negative direction from frame 1 to frame 6 corresponds to the upward motion of the tumor (patient inhalation) observed in the respective images in figure 3.3. Minimum velocity is observed in frame 6 when the breathing transits from inhalation to exhalation.

3.4 Discussions

From the comparison with potentiometer measurements (table 3.2), it is observed that the velocity error generally *increases* with higher breathing rates while the position error *decreases* with higher breathing rates. This contradiction in the trend of the errors can be explained as follows:

i) Higher breathing rates are associated with greater maximum velocities. With these greater maximum velocities, larger errors are incurred due to the limitations of the algorithm. This is supported by the simulation results shown in figure 3.11(a).

ii) At the same time, the *decrease* in position error with faster breathing pace is due to the position error of the actuator being a cumulative sum of the displacement errors between image frames. Similar to the velocity errors, underestimation, and overestimation of displacement exists between image frames. With more breathing cycles, the cumulative effects of the displacement errors get averaged out frequently, resulting in smaller cumulated position errors. This could occur only when the displacement errors, similar to velocity errors, are cyclical and bounded as opposed to monotonically increasing. The above analysis regarding the higher rate of error cancellation for the faster breathing pace is supported by the rapid decrease of the cumulative average position error. Another possible reason for the small position errors is due to the fact that the cumulative displacement errors simply do not have as much time to build up during the shorter breathing cycles.

Given a longer duration of radiation, the position error magnitude is likely to get eliminated for the slower breathing rate.

The magnitude of errors obtained from the comparison with potentiometer measurements is in the same range as those obtained with the simulated velocity. The maximum range of CNR for clinical portal images is around 5 to 10 [35]. From the acquired image sequence of our anthropomorphic phantom target, the average CNR of the images is around 4.56. In the absence of published literature on the typical CNR of lung / lung tumors for MV portal images, simulation is performed to create images having a range of CNR values. To provide an estimate of how the tracking accuracy would deviate from our present study of using an anthropomorphic phantom, a set of images was created with CNR values varying around 4.56 (i.e. from 4.27 to 5.6). From the results, higher tracking errors are observed to be associated with images having a lower CNR (i.e. 4.27-4.75). As CNR increases beyond 5.4, both absolute and relative error approach zero. The smaller errors (obtained from the simulated images with CNR > 5.4) compared to the results of tracking the target over the acquired image sequence are as expected since the mean CNR of the acquired image sequence is about 4.56. This study provides a first attempt to estimate the variation of optical flow tracking performance due to changes in EPID CNR. The variation of the CNR was simulated by changing the contrast of the target. Acquisition of clinical images with a wider range of contrast as well as verification of the tracking accuracy of these images would be carried out in the future.

In conventional radiotherapy, an ITV would be required to accommodate the typical motion of a tumor [27]. With tracking, the radiation beam can be delivered to conform to the moving target. Based on the average maximum position error of our tracking algorithm (1 mm), and assuming that the motion is dominant in the superior-inferior direction, the elimination of the ITV could reduce the normal tissue irradiated by approximately 9.5 mm. The 1 mm positional tracking error could be added to the setup error margin. For a 5 cm diameter (stage T2) [45] lung tumor, this would reduce the V_{20} (% of lung volume receiving at least 20 Gy of radiation dose) by approximately 200 cm^3 (~6%) [46]. This corresponds to a 6% reduction in radiation-induced pneumonitis [47].

Using template matching to track the motion of a phantom moving at 10.5 breaths/min resulted in an average position tracking error of 0.57 ± 0.28 mm for a maximum displacement of 10mm [22]. In comparison, an average tracking error of 0.4 ± 0.2 mm per breathing cycle was established for our algorithm with a target moving at 12 breaths/min over a maximum displacement of 11.5 mm. Our results are thus similar to those using template matching. However, the ground truth used for those benchmarks was based on a clinician's manual delineation of the target trajectory throughout the entire image sequence. The average manual delineation uncertainty was quoted as 0.51 ± 0.19 mm, and the accuracy of tracking algorithms based on manual delineation is therefore limited by the variability in the manual delineation process itself [24]. This is to our knowledge the first study where 1) an uncontoured target is being tracked automatically on EPID images, and 2) an independent measurement is used to establish the accuracy of a tracking algorithm.

In most of the previous EPID target-tracking studies [17-22], the variation in the tracking accuracy for different breathing rates was not fully studied. By using a programmable phantom, the accuracy of our proposed motion tracking algorithm, with different breathing rates, has been established. A multi-template approach [22] is more accurate than the single-template tracking method proposed in [20] because the multiple smaller templates (3 templates) are able to account better for the deformation of targets when the average is taken over a larger number of samples. In our algorithm, the average optical flow value is computed from individual pixel motion. This represents a larger number of samples compared to the multi-template approach. In addition, the matching error between the tumor and template increases when the tumor deforms over the treatment course [23]. Hence, instead of having a fixed template for the entire image sequence, an adaptive set of thresholds utilizing the image-difference weighting is incorporated in our tracking. This caters to fluctuations in the image intensity of the surrounding tissue during breathing. Our method, which operates at a pixel-by-pixel level, has the potential of being more sensitive in detecting the motion of a tumor than a template delineated approach which is based on a human's visual capability to differentiate between a markerless tumor and its background.

With a global averaging approach, the algorithm assumes that the motion detected from the beam's eye view is that of a tumor target. Any intrusion of surrounding structures moving in a different direction will affect the accuracy of the tracking results. Detection and discrimination of optical flow vectors due to intruding structures will be studied in future work. The prediction of the target position to compensate for system lag in modifying the treatment beam will be built upon the accuracies established in this paper.

3.5 Conclusions

This work establishes the accuracy of using an optical flow algorithm to track a tumor-like motion in a clinical treatment machine. By comparing the tracking of our algorithm with a potentiometer measurement, average position errors of 0.6 ± 0.2 mm, 0.2 ± 0.2 mm and 0.1 ± 0.1 mm and average velocity errors of 0.2 ± 0.2 mm/s, 0.4 ± 0.3 mm/s and 0.6 ± 0.5 mm/s are obtained for 6, 12 and 16 breaths/min motion, respectively. This tracking approach has smaller positional errors for faster breathing rates even though the velocity errors are larger. This is because the average error reduces with the increased number of breathing cycles present at higher breathing rates. Tracking errors were found to be strongly dependent on the velocity at low CNR.

Previous studies exhibited large errors when using optical flow algorithms to detect object motion on EPID imaging [33]. This study has shown that by using a dynamic threshold for weighting the optical flow vectors, an EPID can be used to obtain accurate motion. This study has also shown that when the algorithm was used to track a tumor on patient DRR images, the tracking performance of our algorithm was statistically similar to that of both a manual delineation process and a centroid tracking algorithm. Although the accuracy of our approach is similar to that of other methods, it has the benefits of not requiring manual delineation of the target or prior knowledge of the tumor features from a training data set and can, therefore, provide accurate real-time motion estimation during treatment.

References

1. P. Giraud, E. Yorke, E. C. Ford, R. Wagman, G. S. Mageras, H. Amols, C. C. Ling and K. E. Rosenzweig, “Reduction of organ motion in lung tumors with respiratory gating”, Lung Cancer 51, 41-51 (2006).

2. American Association of Physicists in Medicine (AAPM), Radiation Therapy Committee, Task Group 76. The Management of Respiratory Motion in Radiation Oncology. Report No. 91. Madison (WI) (2006).

3. ICRU Report 62. “Prescribing, Recording and Reporting Photon Beam Therapy”, Int. Commission on Radiation Units and Measurements, Bethesda, MD (1999).

4. D. Verellen, M. De Ridder, N. Linthout, K. Tournel, G. Soete and G. Strome, “Innovations in image-guided radiotherapy”, Nature Reviews Cancer 7, 949-960 (2007).

5. S. Hunjan, G. Starkschall, K. Prado, L. Dong and P. Balter, “Lack of correlation between external fiducial positions and internal tumor positions during breath-hold CT”, Int. J. Radiat. Oncol. Biol. Phys. 76, 1586-1591 (2010).

6. A. Vedaldi and B. Fulkerson, “VLFeat: An open and portable library of computer vision algorithms”, http://www.vlfeat.org/ (2008).

7. A. Yilmaz, O. Javed and M. Shah, “Object tracking: A survey”, ACM Comput. Surv. 38, 4, Article 13 (2006).

8. N. Dalal and B. Triggs, “Histograms of Oriented Gradients for Human Detection Proc.”, Int. Conf. Computer Vision & Pattern Recognition (CVRP’05) 886-893 (2005).

9. M. Rodriguez, I. Laptev, J. Sivic and J. Y. Audibert, “Density-aware person detection and tracking in crowds”, Proc. Int. Conf. on Computer Vision (ICCV’11) 2423-2430 (2011).

10. D. G. Lowe, “Distinctive image features from scale-invariant keypoints”, Int. J. Computer Vision 60, 91-110 (2004).

11. S. Avidan, “Support vector tracking”, IEEE Trans. Pattern Analysis and Machine Intelligence 26, 1064-1072 (2004).

12. D. Stavens and S. Thrun. “Unsupervised Learning of Invariant Features Using Video Proc.”, Int Conf. Computer Vision and Pattern Recognition (CVPR’10) 1649-1656 (2010).

13. B. K. P. Horn and B. G. Schunck, “Determining optical flow”, Artificial Intelligence 17, 185-204 (1981).

14. A. Singh, “An estimation-theoretic framework for image-flow computation”, Proc. of ICCV 1992, CVGIP: Image Understanding (Osaka, Japan) 56, 168-177 (1990).

15. J. N. Pan and Y. Q. Shi, “A kalman filter for improving optical flow accuracy along moving boundaries”, SPIE Proceedings Visual Communications and Image Processing 2308, 638-649 (1994).

16. Q. Xu, R. J. Hamilton, R. A. Schowengerdt and S. B. Jiang, “A deformable lung tumor tracking method in fluoroscopic video using active shape models: a feasibility study”, Phys. Med. Biol. 52, 5277-5293 (2007).

17. T. Lin, R. Li, X. Tang, J. G. Dy and S. B. Jiang, “Markerless gating for lung cancer radiotherapy based on machine learning techniques”, Phys. Med. Biol. 54, 1555-63 (2009).

18. T. Lin, L. I. Cervino, X. Tang, N. Vasconcelos and S. B. Jiang, “Fluoroscopic tumor tracking for image-guided lung cancer radiotherapy”, Phys. Med. Biol. 54, 981-92 (2009).

19. R. Li, J. Lewis, L. I. Cervino and S. B. Jiang, “A feasibility study of markerless fluoroscopic gating for lung cancer radiotherapy using 4DCT templates”, Phys. Med. Biol. 54, N489-N500 (2009).

20. H. Arimura, Y. Egashira, Y. Shioyama, K. Nakamura, S. Yoshidome, S. Anai, S. Nomoto, H. Honda, H. Toyofuku, Y. Higashida, Y. Onizuka and H. Terashima, “Computerized method for estimation of the location of a lung tumor on EPID cine images without implanted markers in stereotactic body radiotherapy”, Phys. Med. Biol. 54, 665-77 (2009).

21. B. Cho, P. R. Roulsen, A. Sloutsky, A. Sawant and P. J. Keall, “First demonstration of combined KV/MV image-guided real-time dynamic multileaf-collimator target tracking”, Int. J. Radiat. Oncol. Biol. Phys. 74, 859-67 (2009).

22. J. Rottmann, M. Aristophanous, A. Chen, L. Court and R. Berbeco, “A multi-region algorithm for markerless beam’s-eye view lung tumor tracking”, Phys. Med. Biol. 55, 5585-98 (2010).

23. M. Chao, Y. Xie, E. Moros, Q. Le and L. Xing, “Image-based modeling of tumor shrinkage in head and neck radiation therapy”, Med. Phys. 37, 2351-8 (2010).

24. A. Pevsner, B. Davis, S. Joshi, A. Hertanto, J. Mechalakos, E. Yorke, K. Rosenzweig, S. Nehmeh, Y. E. Erdi, J. Humm, S. Larson, C. Ling and G, “Evaluation of an automated deformable image matching method for quantifying lung motion in respiration-correlated CT images”, Med. Phys. 33, 369-76 (2006).

25. D.J. Moseley, E. A. White, K. L. Wiltshire, T. Rosewall, M. B. Sharpe, J. H. Siewerdsen, J. P. Bissonnette, M. Gospodarowicz, P. Warde, C. N. Catton and D. A. Jaffray, “Comparison of localization performance with implanted fiducial markers and cone-beam computed tomography for on-line image-guided radiotherapy of the prostate”, Int. J. Radiat. Oncol. Biol. Phys. 67, 942–53 (2007).

26. G. Ellis and R. D. Lorenz, “Comparison of motion control loops for industrial applications”, Proc. IEEE 34th IAS Annual Meeting 2599–605 (1999).

27. H. Shirato, K. Suzuki, G. C. Sharp, K. Fujita, R. Onimaru, M. Fujino, N. Kato, Y. Osaka, R. Kinoshita, H. Taguchi, S. Onodera and K. Miyasaka, “Speed and amplitude of lung tumor motion precisely detected in four-dimensional setup and in real-time tumor-tracking radiotherapy”, Int. J. Radiat. Oncol. Biol. Phys. 64, 1229-36 (2006).

28. Y. Seppenwoolde, H. Shirato, K. Kitamura, S. Shimizu, M. van Herk, J. V. Lebesque and K. Miyasaka, “Precise and real-time measurement of 3D tumor motion in lung due to breathing and heartbeat, measured during radiotherapy”, Int. J. Radiat. Oncol. Biol. Phys. 53, 822-34 (2002).

29. K. O. Noe, B. D. Senneville, U. V. Elstrom, K. Tanderup and T. S. Sorensen, “Acceleration and validation of optical flow based deformable registration for image-guided radiotherapy”, Acta. Oncologica 47, 1286 -93 (2008).

30. Q. Xu, R. J. Hamilton, R. A. Schowengerdt, B. Alexander and S. B. Jiang, “Lung tumor tracking in fluoroscopic video based on optical flow”, Med. Phys. 35, 5351-60 (2008).

31. T. Guerrero, G. Zhang, T. C. Huang and K. P. Lin, “Intrathoracic tumor motion estimation from CT imaging using the 3D optical flow method”, Phys. Med. Biol. 49, 4147–61 (2004).

32. G. G. Zhang, T. C. Huang, T. Guerrero, K. P. Lin, C. Stevens, G. Starkschall and K. Forster, “The use of 3D optical flow method in mapping of 3D anatomical structure and tumor contours across 4D CT data”, J. Appl. Clin. Med. Phys. 9, 59-69 (2008).

33. M. Orkisz, A. Frery, O. Chapet, F. Mornex and I. E. Magnin, “Attempts to bronchial tumor motion tracking in portal images during conformal radiotherapy treatment Computer Analysis of Images and Patterns”, Lecture Notes in Computer Science 2124/2001, 247-55 (2001).

34. J. P. Osmond, H. M. Zin, E. J. Harris, G. Lupica, N. M. Allinson and P. M. Evans, “Imaging of moving fiducial markers during radiotherapy using a fast, efficient active pixel sensor based EPID”, Med. Phys. 38, 6152-59 (2011).

35. T. Radcliffe, R. Rajapakshe and S. Shalev, “Pseudocorrelation: A fast, robust, absolute, grey-level image alignment algorithm”, Med. Phys. 21, 761-70 (1994).

36. P. L. Rosin, “Thresholding for change detection”, Comp. Vision Image Understanding 86, 79-95 (2002).

37. J. C. Sosa, J. A. Boluda, F. Pardo and R. Gomez-Fabela, “Change-driven data flow image processing architecture for optical flow computation”, J. Real-Time Image Proc. 2, 259-70 (2007).

38. B. D. Lucas and T. Kanade, “An iterative image registration technique with an application to stereo vision”, Proc. 7th Int. Joint Conf. on Artificial Intelligence 674-9 (1981).

39. J. Y. Bouguet, “Pyramidal Implementation of the Lucas Kanade Feature Tracker Technical report”, Intel Corporation Microprocessor Research Labs (2000).

40. J. Marzat, Y. Dumortier and A. Ducrot, “Real-time dense and accurate parallel optical flow using CUDA”, Proc. 17th Int. Conf. Central Europe Comp. Graphics, Visualization Comp. Vision (WSCG) Czech Republic 105-11 (2009).

41. I. Nagai and Y. Tanaka, “Localization and Error Correction for Mobile Robot with an Image Sensor”, Proc. SICE-ICASE Int. Joint Conf. Busan, Korea 5373-7 (2006).

42. R. George, S. S. Vendam, T. D. Chung, V. Ramakrishnan and P. J. Keall, “The application of the sinusoidal model to lung cancer patient respiratory motion”, Med. Phys. 32 2850-61 (2005).

43. W. Y. Lin, S. F. Lin, S. C. Yang, S. C. Liou, R. Nath and W. Liu, “Real-time automatic fiducial marker tracking in low contrast cine-MV images”, Med. Phys. 40 117151-12 (2013).

44. G. Bradski, “The OpenCV library”, Dr. Dobb’s Journal of Software Tools 120-6 (2000).

45. A. Nair, M. J. Klusmann, K. H. Jogeesvaran, S. Grubnic, S. J. Green and I. Vlahos, “Revisions to the TNM staging of non-small cell lung cancer: rationale, clinicoradiologic implications, and persistent limitations”, Radiographics 31 215-38 (2011).

46. C. Ding, C. H. Chang, J. Haslam, R. Timmerman and T. Solberg, “A dosimetric comparison of stereotactic body radiation therapy techniques for lung cancer: robotic versus conventional linac-based systems”, J. Appl. Clin. Med. Phys. 11(3) 212-24 (2010).

47. L. B. Marks, S. M. Bentzen, J. O. Deasy, F. M. Kong, J. D. Bradley, I. S. Vogelius, I. El Naqa, J. L. Hubbs, J. V. Lebesque, R. D. Timmerman, M. K. Martel and A. Jackson, “Radiation dose-volume effects in the lung”, Int. J. Radiat. Oncol. Biol. Phys. 76 S70-6 (2010).

Chapter 4 Tracking of Uncontoured Target using Global Motion Detected within a Treatment Aperture: A Comparison of Three Approaches Using a Weighted Optical Flow Algorithm and a Virtual DMLC

This chapter compares the performance of a weighted optical flow algorithm (developed in chapter 3) implemented with three different reference image update techniques. The accuracy and susceptibility of each algorithm to the accumulation of positional errors was compared using a virtual DMLC and a printed patient tumor as a control. Part of the work was published as a book chapter in volume 51 of the IFMBE Proceedings series, DOI 10.1007/978-3-319-19387-8_141, and presented at the World Congress on Medical Physics and Biomedical Engineering, June 2015 Canada. The material is also prepared for submission to Medical Physics by the author of this dissertation.

Abstract

Purpose: To improve the efficacy of radiation treatment, accurate tracking of the target, during treatment, is desirable. This work investigates the feasibility of tracking a markerless, uncontoured target using the motion detected within a treatment aperture. Tracking was achieved using a weighted optical flow algorithm, implemented using three different techniques for updating the reference image. The accuracy, and susceptibility of each algorithm to the accumulation of position errors, were compared using a virtual DMLC and a 3D printed patient tumor as a control.

Methods: Images of target motion with ranges of between 4.6 mm to 15.8 mm (peak-to-peak) taken from the breathing patterns of seven lung cancer patients were acquired using an

amorphous silicon portal imager (AS1000, Varian, Palo Alto, CA) at ~7.5 frames/s. A weighted optical flow algorithm was used to track the motion with three different reference image registration techniques. The first technique (INI) used the initial irradiated field as a fixed reference image to determine the target motions for each new incoming image. In the second technique (SEQ), the reference image was updated sequentially by the (previous) image acquired just prior to the current irradiated field. The motion was computed by accumulating the changes between sequential pairs of images, acquired over the treatment delivery. The last method (PERD), periodically updated the reference image at the end-of-exhale (EoE) of each breathing cycle. Motion between the EoE was with respect to the current reference, and the motion between consecutive EoE were computed with sequential updates of the reference images. The slope of the position and velocity profiles were used to automatically detect the EoE. A virtual Dynamic Multi-Leaf Collimator (DMLC) system was implemented to simulate the adaptation of the treatment aperture based on the motion detected. The accuracies of the algorithms were compared using a printed patient tumor as a control.

Results: When using realistic tumor motion, position errors were observed to accumulate during the tracking of the target motion over an MV EPID image sequence. The INI method was the least prone to accumulation of position errors, followed by the SEQ and PERD method. Mean absolute errors of 0.16 mm, 0.32 mm and 0.38 mm and precisions of 0.32 mm, 0.68 mm, and 0.79 mm were obtained for the INI, SEQ and PERD methods respectively. Overall, the INI approach performs the best with the smallest error and is the most robust against the accumulation of position errors. Position errors were observed to accumulate from either (1) a single error in the displacement, or (2) a series of small constructively-added inter-frame displacement errors.

Conclusions: A weighted optical flow algorithm implemented with three different reference image registration techniques was shown to successfully track a markerless, uncontoured target using the global motion computed inside the treatment aperture. Although the errors are comparable to other tracking methods, the proposed method does not require a tumor template or contour for tracking.

4.1 Introduction

The management of intra-fractional tumor and organ motion is important to the efficacy of radiation therapy. Respiratory-induced tumor motion in the lung could potentially result in the under-treatment of the tumor and over-dosing of healthy tissues. Although margins have been used to encompass tumor motion during beam delivery, the surrounding healthy tissues are exposed to unnecessary radiation.

Clinical implementations of concurrent tumor irradiation and tracking is limited to the robotic CyberKnife system from Accuray Inc., CA. [1, 2]. Other systems that track the tumor motion and adapt the aperture to create a stationary tumor with respect to the treatment beam are limited to research prototypes [3-5]. A clinical trial for prostrate tumor tracking has been performed using an electromagnetically-guided transponder with a DMLC system. [6] Key processes in these adaptive systems such as accurate tracking of the tumor and rapid adaptation of the treatment beam make it a challenge to realize these systems physically. The availability of a virtual system, such as the VERT 2.9 platform (Vertual Ltd. Hull, UK), would allow a breakdown of these processes to be simulated and verified before implementing it clinically.

The use of MV images from electronic portal imaging devices (EPID) to monitor motion is desirable since the tumor can be tracked directly with the residual treatment beam and no additional patient dose or external surrogates are involved. However, EPID has inherently poor contrast, and this poses a challenge for accurate motion tracking [7]. Although various markerless [7-13] and marker-based tracking algorithms have been implemented, the use of markers suffers the potential risks of pneumothorax [14] and marker migration of up to 2.7 cm has been reported [15].

While most of the markerless tracking techniques require a pre-defined template or contour to track [7-13], optical flow algorithms [16-19], which are pixel level algorithms, can potentially track motions without a manually-delineated template or extensive learning with a *priori* data [16, 17]. The individual optical flow vectors allow motion analysis to be performed at the global level or over a local region. These features enable it to: detect a partially occluded object from the motion vectors [16], infer structure from motions [17] and track unplanned intrusions into the field of view [16, 17, 19]. For tumor tracking during radiotherapy, similar problems, such as the partial occlusion of the tumor, due to the MLC leaves or overlapping structures along the beam, is encountered. Unlike template tracking, local optical flow vectors could be used to track partially occluded targets and uncontoured external structures which intrude into the irradiated field in an unplanned way [19].

In previous work by Xu *et. al.,* [12], to track markerless tumor motion, a two-stage process was used. A contour is delineated on a reference image and an optical flow algorithm is used to track the edges represented by the contour. To eliminate uncertainties in the optical flow vectors computed, template matching is then performed around the tumor position estimated from the optical flow algorithm. In contrast, our previous work tracked uncontoured tumor motion with sequential image pairs using a weighted optical flow algorithm to emphasize regions that provide accurate optical flow vectors [18]. In that work, it was assumed that with proper patient setup, the irradiated field would encompass the tumor in the initial frame and the average global motions detected in subsequent images were due to the movement of the main target.

However, with sequential tracking over long image sequences, tracking errors tend to accumulate. When these errors accumulate constructively, a drift in the tracked position occurs, as observed in medical images [12, 20-23], as well as images for non-medical applications [24, 25]. The accumulation of position errors was insignificant while tracking a tumor moving with a theoretical (i.e. asymmetrical cosine) function on MV images [18]. However, while using the same optical flow algorithm to track motion obtained from a patient's tumor trajectory, the accumulation of position errors due to the uneven cancellation of errors was noticeable [23]. Although image registration with a reference image could eliminate the accumulation of tracking errors, the image quality of the reference image is key to avoiding any systematic errors for all subsequent image comparisons [25]. In addition, changes in the background and object shape could render the initial frame that was defined from a distant location obsolete when compared to subsequent images [11, 24-25]. Hence, techniques using periodic reference image update have been proposed to mitigate both the accumulation of tracking errors associated with sequential image tracking as well as the systematic error of using a poor image reference defined from the initial frame of an image sequence [24-25].

This work is an extension of our previous works where a weighted optical flow algorithm was used to autonomously track the average global motion of a markerless, uncontoured lung tumor on electronic portal images [18]. In contrast to static tracking [26, 27] presented in our previous work [18, 19] and by Xu *et al.* [12], dynamic tracking [26, 27] with the adaption of the aperture [5, 28] was used for this study. The images used therefore reflect the beam's eye view (BEV) for the treatment

Three techniques for updating the reference image as well their susceptibility to the accumulation of positional errors were investigated. In the first method (INI), the initial frame in the sequence was used as the reference image for the determination of tumor motion in all future images. In the second method (SEQ), the reference image was updated sequentially to the previous image where the position of the tumor was last determined. In the third method

(PERD), the reference image was updated periodically at the end-of-exhale (EoE) of each breathing cycle. These different implementations of the weighted optical flow algorithm were compared using the MV images of a 3D printed lung tumor of a patient as a control for our study. A virtual DMLC system similar to that presented by Pepin *et al*. [29] was implemented to model the tracking and update of the aperture, for the tumor trajectories of seven lung cancer patients.

4.2 Methods and Materials

4.2.1 Brief review of weighted optical flow algorithm

A summary of our previous work on using the weighted optical flow algorithm to track tumor motion is provided in this section. The algorithm assumes that the intensities for the corresponding pixels between two images remain constant and motion between two images is small in order to be tracked accurately. Our implementation, which aims to track a target without a template or contour, utilizes a two-stage process. Firstly, the optical flow vectors were obtained using a multi-resolution scheme to provide tracking over the required distance. A 9-by-9 pixel window was used to provide a region necessary to support the computation of valid optical flow vector using the Lucas-Kanade local least squares approach [30]. Secondly, an average weighting based on the image differences was used to select the vectors corresponding to the motion observed in the non-homogeneous regions. An accuracy of 0.6 mm was obtained for tracking a 30 mm (average diameter) target moving with a maximum peak-to-peak distance of 10 mm.

4.2.2 Virtual dynamic multi-leaf collimator (virtual DMLC)

In this work, the focus is on comparing the algorithm’s tracking performance using different reference MV images for registration. To eliminate the impact of latency due to the adaptation of the MLC leaves, a virtual DMLC system with infinite maximum leaf speed and acceleration similar to that proposed by Pepin et. al. [29] was implemented in MATLAB (The MathWorks Inc, MA). Virtual MLC leaves with a width of 5mm at the isocenter (18 pixels on the EPID at 140 cm from the source) were used to form a circular treatment aperture. The MATLAB code for the creation of a virtual DMLC aperture based on a given diameter and width of the MLC is available for download [31].

4.2.3 Weighted optical flow algorithm implementation with different reference image update

4.2.3.1 Using the initial image as a fixed reference image *(INI)*

In the INI method, all incoming images were registered directly with the initial frame of the image sequence, *IM*(1). The optical flow algorithm was applied to determine the inter-frame displacements between all subsequent images and the first image *IM*(1). (figure 4.1). For the i^{th} image *IM*(i)., the position of the center of the aperture $Pos_{aperture}$and target Pos_{target} along the superior-inferior (SI) direction can be written as:

$$Pos_{aperture}(i) = \begin{cases} P_0 & i = 1,2 \\ P_0 + \sum_{i}^{n} OF_{INI}(i-2)\,; & i \geq 3 \end{cases} \tag{4.1}$$

$$Pos_{target}(i) = P_0 + \sum_{i}^{n} OF_{INI}(i-1)\,; \qquad i \geq 2 \tag{4.2}$$

where $OF_{INI}(i-1)$ is the optical flow displacement between *IM(1)* and *IM(i)*, $P_0 = Pos_{aperture}(1)$ is the position of the center of the aperture for the first (and second frame) and *n* is the number of frames in the image sequence. For the present study, it was assumed that the target was positioned at the isocenter and the first image was acquired with the center of the target and the center of the aperture at isocenter, i.e. $Pos_{target}(1) = Pos_{aperture}(1) = P_0 = 0$. As a proof-of-concept, the target was programmed to move in the superior-inferior (SI) direction. As a result, the position was measured from inferior (negative) to superior (positive). This formulation can be extended to include motion in the other directions. A detailed derivation using a mathematical induction process is presented in the supplementary materials.

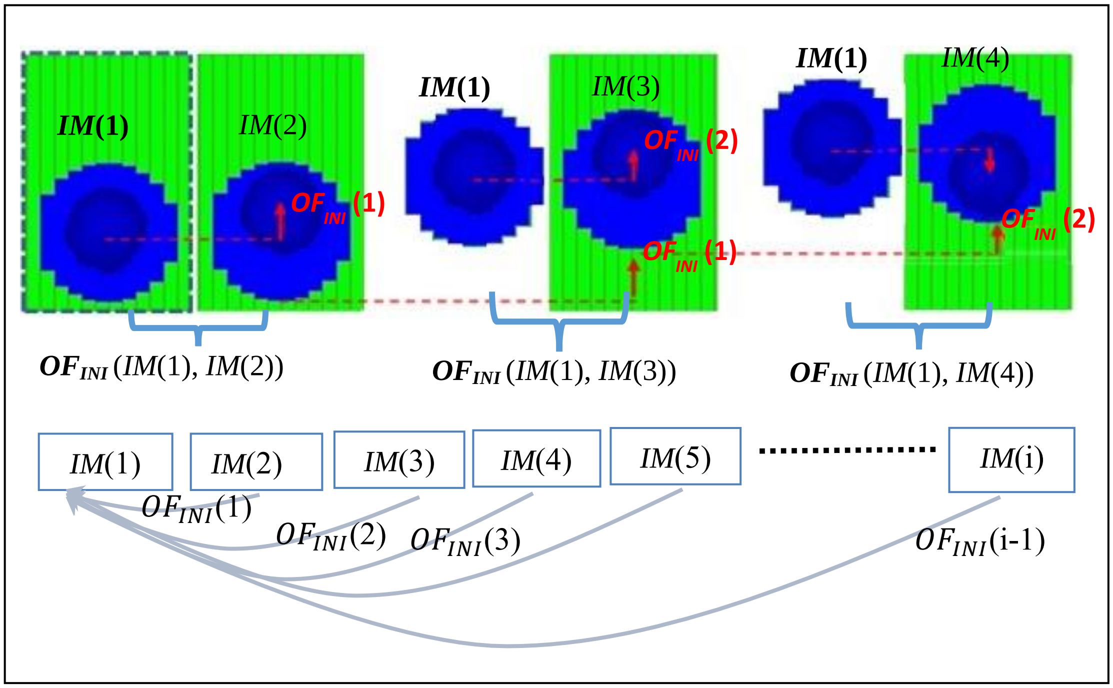

Figure 4.1 : A schematic depiction of weighted optical flow tracking using a virtual DMLC and an initial image as a fixed reference image for subsequent motion computation (INI). In this method, all incoming images (*IM*(2), *IM*(3), etc.) were registered directly with *IM*(1) to calculate inter-frame displacements using the optical flow algorithm.

4.2.3.2 Sequential reference image update (SEQ).

In the second method (SEQ), the first irradiated field of the sequence was initially used as the reference image. Following the acquisition of a new image, the motion between the new image and the reference image was calculated. Once the motion was determined, the new image becomes the reference image for the next optical flow calculation (figure 4.2). The position of the aperture $Pos_{aperture}$ and target Pos_{target} in image *IM*(*i*) were updated cumulatively and are given as:

$$Pos_{aperture}(i) = \begin{cases} P_0 & i = 1,2 \\ P_0 + \sum_{i}^{n} OF_{SEQ}(i-2)\,; & i \geq 3 \end{cases} \tag{4.3}$$

$$Pos_{target}(i) = P_0 + \sum_{i}^{n} OF_{SEQ}(i-1)\,; \qquad i \geq 2 \tag{4.4}$$

where $OF_{SEQ}(i-1)$is the optical flow displacement between image *IM*(*i* -1) and image *IM*(*i*), and $P_0$and *n* are defined in equations (4.1) and (4.2).

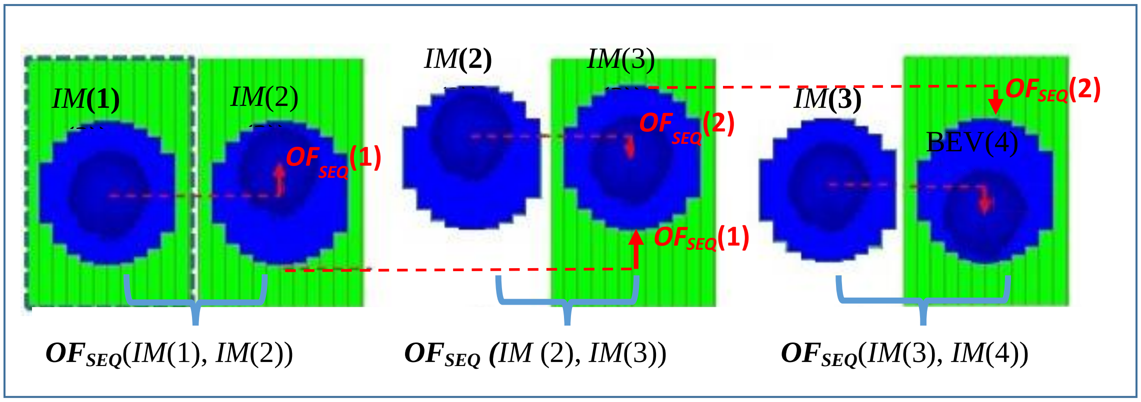

Figure 4.2 : A schematic depiction of the motion tracking using the sequential reference image update method (SEQ). In this approach, the first image of the sequence *IM*(1) was initially used as the reference. Following the acquisition of a new image *IM*(2), the motion between the new image and the reference image was calculated. Once the motion was determined, *IM*(2) becomes the new reference image for the next optical flow calculation with *IM*(3).

4.2.3.3 Periodic reference image update (PERD)

The third method (PERD) used a combination of sequential reference image registration and periodic registration with an ‘anchor’ [21] reference image (figure 4.3). The anchor image was obtained at the end-of-exhale (EoE) of each breathing cycle where image registration was performed between the previous reference $IM_{Ref}(m\text{-}1)$ and image $IM(i)$ acquired at EoE, where m is the index of EoE occurrences in the breathing trace. After registration with the previous reference image, the new image at the EoE was assigned as the new reference for the following breathing cycle. The position of the target in the new breathing cycle obtained with sequential image registration was calculated using Pos_{target_Ref} as the new reference position determined at EoE. The reason for selecting the EoE to update the reference image is because the tumor position is most re-producible during EoE [32].

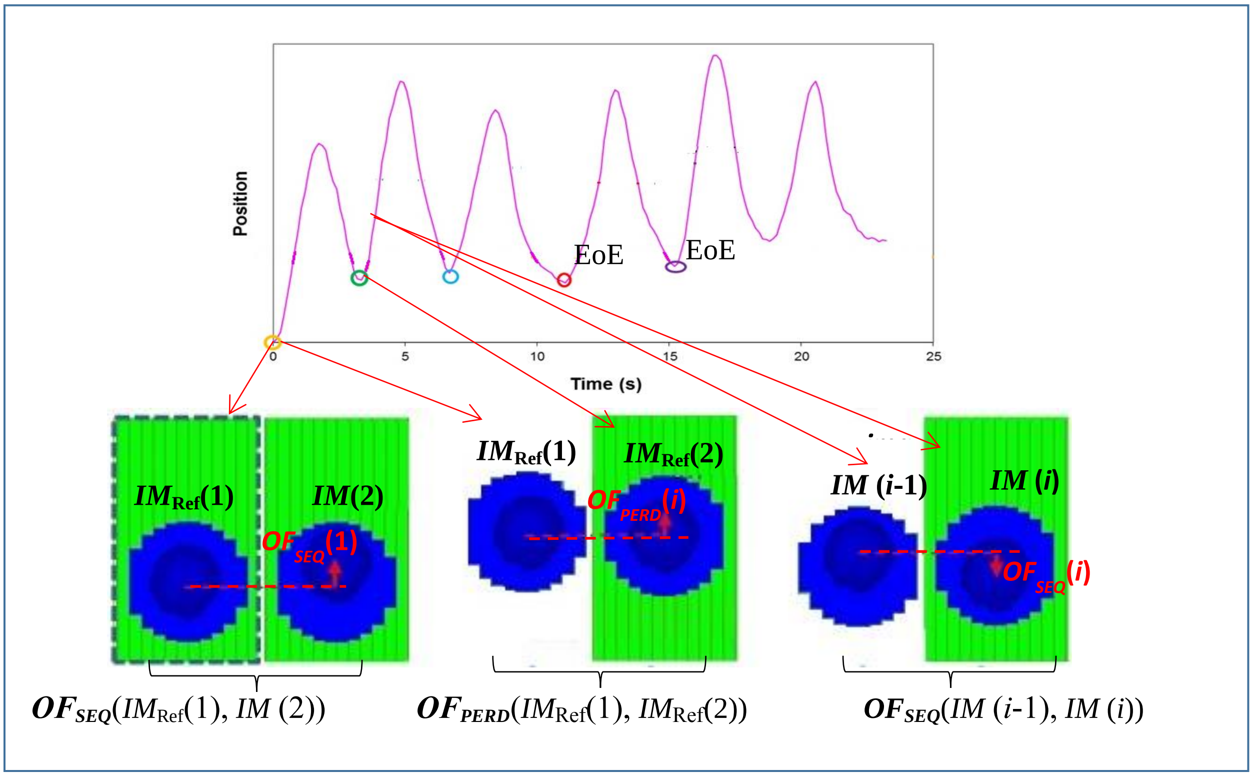

Figure 4.3 : A schematic depiction of motion tracking using a periodic reference image update method (PERD). This method uses sequential reference image registration (SEQ) within each breathing cycle. At the end of each breathing cycle (EoE), a new reference image, for example, $IM_{\text{Ref}}(2)$ was created by calibrating this image with the previous reference image $IM_{\text{Ref}}(1)$. The position of the target in the new breathing cycle (obtained with sequential image registration) was calculated using the new reference position determined at the EoE.

In between EoE, the position of the treatment aperture $Pos_{aperture}$ and target Pos_{target} at image $IM(i)$ can be expressed as:

$$Pos_{aperture}(i) = \begin{cases} P_0 & i = 1,2 \\ Pos_{apertureRef}(m) + \sum_{i=1}^{n} OF_{SEQ}(i-2) & m \geq 1, i \geq 3 \end{cases} \qquad (4.5)$$

$$Pos_{target}(i) = Pos_{aperture}(i) + \sum_{i=1}^{n} OF_{SEQ}(i-1) \qquad i \geq 2 \qquad (4.6)$$

At EoE, the new m^{th} reference position of the target $Pos_{target\_Ref}(m)$ as well as its position $Pos_{target}(i)$ with respect to the EPID image sequence were given by:

$$Pos_{targetRef}(m) = Pos_{aperture}(i) + OF_{PERD}(m-1) \qquad m \geq 1, i \geq 2 \tag{4.7}$$

$$Pos_{target}(i) = Pos_{targetRef}(m) \qquad m \geq 1, i \geq 2 \tag{4.8}$$

where $OF_{PERD}(m-1)$ is the optical flow displacement obtained between the previous reference image $IM_{\text{Ref}}(m-1)$ and $IM_{\text{Ref}}(m)$. The displacement of the target $Disp_{target\_Ref}$ at EoE measured with respect to its position in the previous *IM* image ($i-1$) is determined from:

$$Disp_{targetRef}(m) = Pos_{targetRef}(m) - Pos_{target}(i-1) \qquad m \geq 1, i \geq 2 \tag{4.9}$$

The current position of the aperture $Pos_{aperture}$ in image *IMi* will be assigned as the new reference position for the aperture:

$$Pos_{apertureRef}(m) = Pos_{aperture}(i) \qquad m \geq 1, i \geq 2 \tag{4.10}$$

The aperture $Pos_{aperture}$ in the immediate image *IM(i*+1) following the reference calibration will be updated with the displacement $Disp_{targetRef}$ determined at the new reference position:

$$Pos_{aperture}(i+1) = Pos_{apertureRef}(m) + Disp_{targetRef}(m) \qquad m \geq 1, i \geq 2 \tag{4.11}$$

By updating the reference image at each EoE, a new reference image was obtained for each breathing cycle.

The determination of the EoE was achieved autonomously by using the higher order derivatives of the position trajectory of the tumor, such as the inter-frame displacement (velocity) and acceleration. The tumor was assumed to be at the EoE when the following conditions were met. Firstly, using a moving window of four inter-frame displacements $Disp_{target}$ and assuming that the exhale phase was associated with negative inter-frame displacement, an EoE was considered to have occurred two frames earlier when the previous third and fourth inter-frame displacements were negative while the current and previous inter-frame displacements were non-negative:

$$Disp_{target}(i-a)\begin{cases} < 0 & a = 3.4 \\ \geq 0 & a = 1, 2 \end{cases} \qquad i \geq 4 \tag{4.12}$$

where $Disp_{target}(i-1)$ is the optical flow displacement between image $IM(i$ -1) image and $IM(i)$. The window of data serves as a filter to remove the impact of random noise. Secondly, assuming that deceleration is associated with exhale and acceleration is associated with inhale, then EoE could have potentially occurred two frames earlier when:

$$Disp_{target}(i-a) - Disp_{target}(i-b)\begin{cases} < 0 & (a,b) = (3{,}4), \\ \geq 0 & (a,b) = (1, 2), \end{cases} \qquad i \geq 5 \tag{4.13}$$

In other words, using the four data points, EoE was detected when the first two displacements and acceleration were positive (or zero) while the other two respective data were negative. Although a larger moving window could be used to filter out the noise, it would delay the adjustment of the reference to two frames after the EoE.

4.2.4 Evaluation

The techniques were evaluated by tracking the motion of a printed 3D lung tumor phantom projected on MV images (refer to figure 4.4). The 3D printed tumor, obtained from the CT image of patient #64 of the Lung Image Database Consortium (LIDC) [33] has an average diameter of 27mm. It is not connected to the lung wall or to any major bronchi, which made it easier to isolate and convert to an .STL (Stereo lithography) file for fabrication. The tumor was fabricated using a Solidoodle2 (Solidoodle LLC,NY) printer with Acrylonitrile Butadiene Styrene (ABS) as its filament material. Following the guidelines of the Radiation Therapy Oncology Group (RTOG) 0236 as well as the adaptation of the margin suggested by Colvill *et al.*, [34] a margin of 5 mm was added around the tumor to provide a Planning Target Volume (PTV) of 37 mm. Due to the finite width of the MLC leaves, a circular aperture with a diameter of 40 mm (144 pixels with EPID at 140 cm) comprising of eight columns of 5 mm MLC leaves were implemented in our virtual DMLC system (described in Section 4.2.2).

Motion trajectories (SI direction) representing the average clinical tumor motion (represented by an asymmetrical cosine function [35]), and from seven cancer patients measured by the CyberKnife [36], were used to drive the actuator supporting the 3D tumor. The characteristics of these motion traces, which were selected to represent a diverse patient tumor motion, are shown in table 4.1. In addition to the maximum peak-to-peak position, velocity and acceleration, the frequency of each motion trace was characterized by the dominant frequency component of their respective frequency spectrum. MV EPID (AS-1000) images were acquired in continuous acquisition mode with the tumor and EPID positioned at 100 cm and 140 cm respectively from the source of a Varian Clinac linear accelerator delivering a 6MV beam at 600 MU/min. The EPID imager has a resolution of 0.39mm/pixels and an acquisition frame rate of 7.5 frames/s. An average of 200 images was collected for each motion trace. The motions estimated from these images (using the algorithm) were compared with the motions of the actuator obtained from a potentiometer attached to it and the position errors (tracking – potentiometer readings) were recorded. The accuracy of each method was obtained by taking the mean position difference (and the standard deviation) for all the patients. The precision of each method was estimated by taking the width of the central 68% of the distribution of position differences after normalizing each distribution to its mean error.

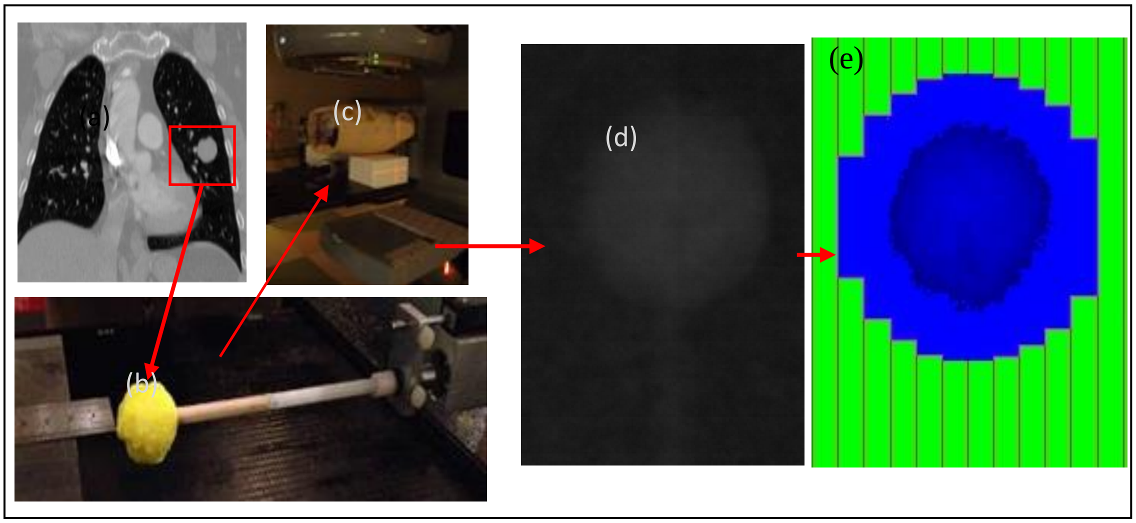

Figure 4.4 : Setup and control for the comparison of the three different implementations of the algorithm: (a) Tumor model obtained from patient #64 in the LIDC database; (b) a 3D tumor printed with Acrylonitrile Butadiene Styrene material; (C) irradiation with Varian Linac; (d) acquisition of MV EPID images; (e) implementation of a virtual DMLC to follow the motion of a tumor (MV image enhanced for display).'.

Table 4.1 : Characteristics of the tumor motions (SI direction) of seven CyberKnife patients

Patient	**Max Position * (mm)**	**Max Displacement (mm/frame)**	**Max Acceleration (mm/s^2)**	**Dominant Frequency (Hz)**
1	7.9	1.4	50.5	0.42
2	9.2	1.6	27.0	0.42
3	9.5	1.6	32.6	0.43
4	15.8	2.6	50.6	0.26
5	4.6	0.6	19.1	0.26
6	8.0	1.4	35.4	0.21
7	8.7	1.2	18.6	0.20

**Amplitude of motion*

4.3 Results

Figure 4.5(a) to (g) depicts the inter-frame displacement (mm/frame), position (mm), displacement error (mm/frame) and position error (mm) for patients 1 to 7 respectively. Accumulation of displacement errors resulting in a drift (in the position) was observed for the trajectories of patient 1, 3, 5 and 7 tracked using the SEQ method. The drifts were observed at time > 11.5 s and time > 14s for patients 1 and 3 respectively. For patient 5, the drifts were observed in between 15s – 20 s. For patient 7, the drift occurred at time > 10 s. For the PERD method, discrete deviations of the inter-frame displacements are observed more frequently compared to the other two methods. These isolated events manifested as distinct shifts in the estimated displacement value away from the expected value. The shifts, reflected in the corresponding displacement error plots, are due to the re-calibration of the target's position at EoE. However, some displacement shifts are observed in between EoEs. These shifts are due to spurious detections of the EoEs. These spurious detections cause the reference position to be updated using images that are apart from those at EoE. As an example, from the position error plot shown in figure 4.5(c) (patient 3), there is an accumulation (in the negative direction) of the position error from 13.7 s to 15 s. This is caused by a spurious update of the reference position at 13.7 s, indicated by a distinct shift in the displacement error plot. However, a re-calibration of the target position at the subsequent EoE is observed (with a jump in the position error) at time t = 15 s. This re-calibration at the EoE eliminates the accumulation of the position error for the following cycle.

The mean position errors for each patient are shown in table 4.2, and the distributions of these errors are shown in figure 4.6. It is observed that the INI method yields the smallest position errors compared to the SEQ and PERD methods. For SEQ method, the largest mean and spread of position errors is from patient 7. Patient 7 has the lowest dominant frequency and lowest maximum acceleration. For the PERD approach, tumor motions with higher dominant frequency (patients 2 and 3) are observed to have larger errors (figure 4.6).

The mean and standard deviation of the position errors obtained from the seven patients were used to determine the accuracies of each method. The precision of each method was estimated using the central 68th percentile of each distribution shown in figure 4.7. Table 4.3 provides the accuracy, precision and mean absolute error of each method. The INI method outperformed the other two methods with the smallest mean absolute error (0.16 mm) and the smallest spread of error (0.32 mm). This performance is followed by the SEQ and PERD methods.

(a) Patient 1

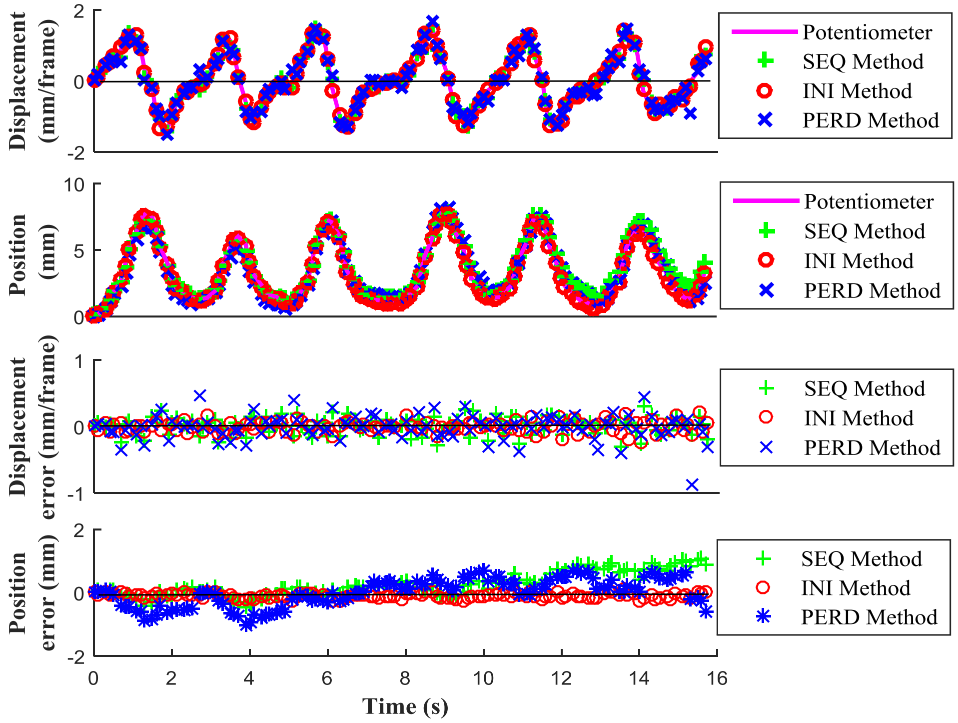

(b) Patient 2

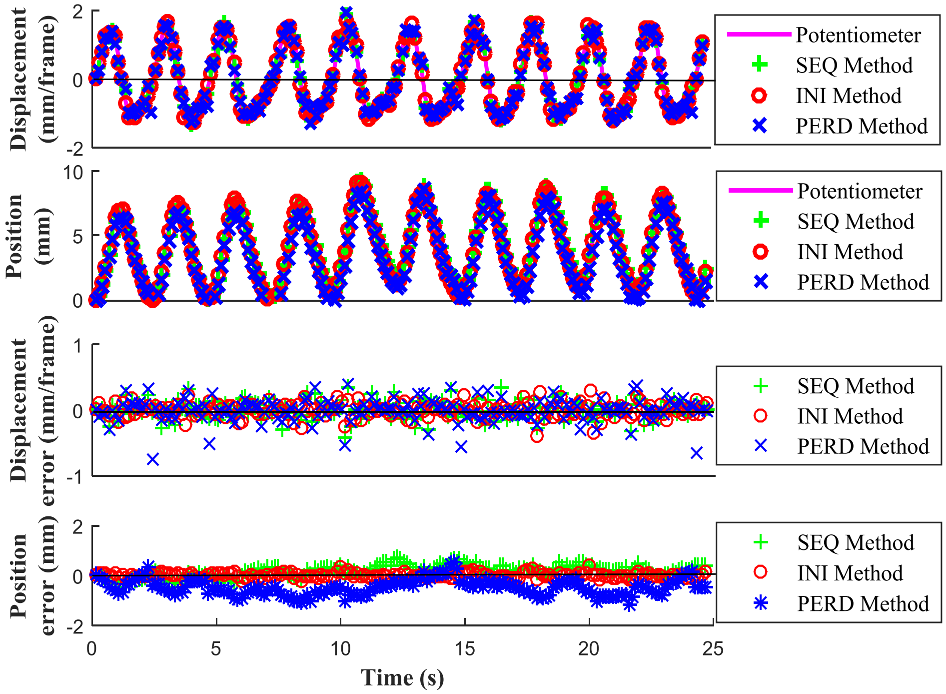

(c) Patient 3

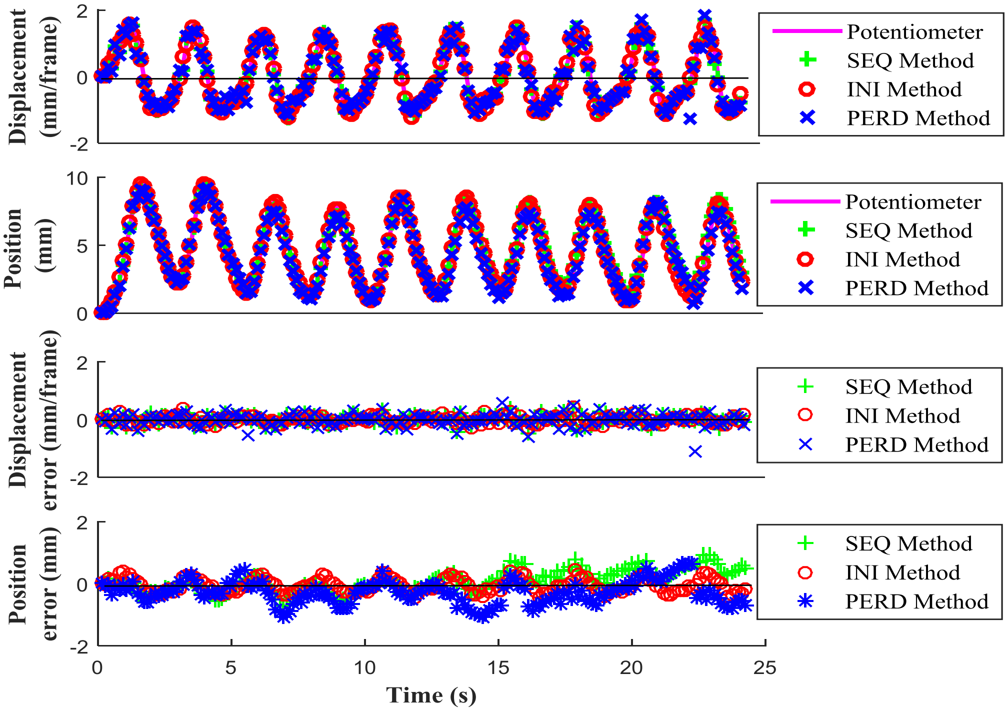

(d) Patient 4

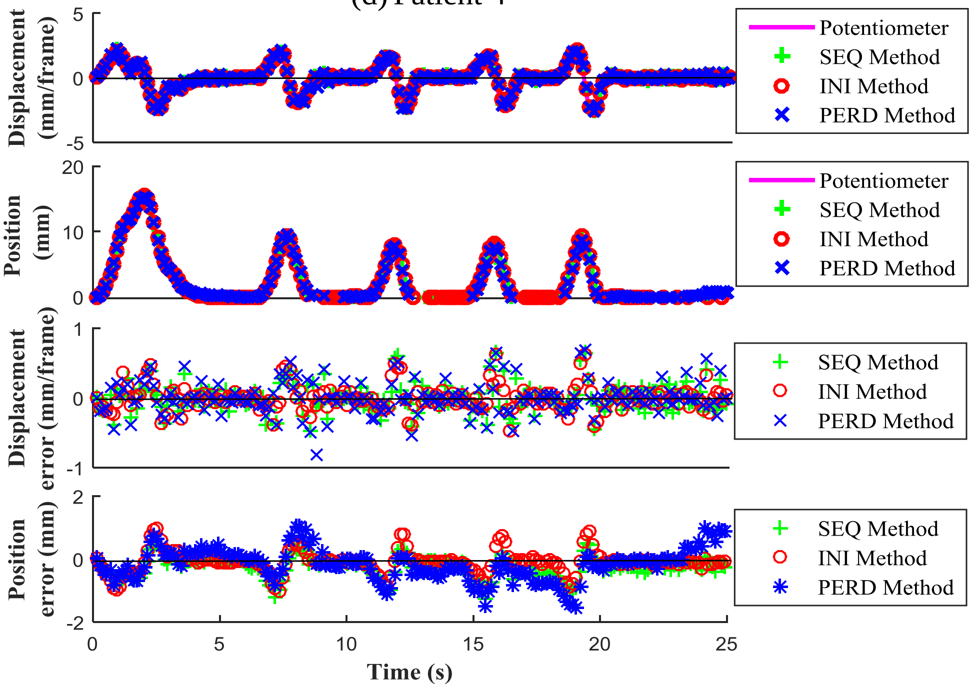

(e) Patient 5

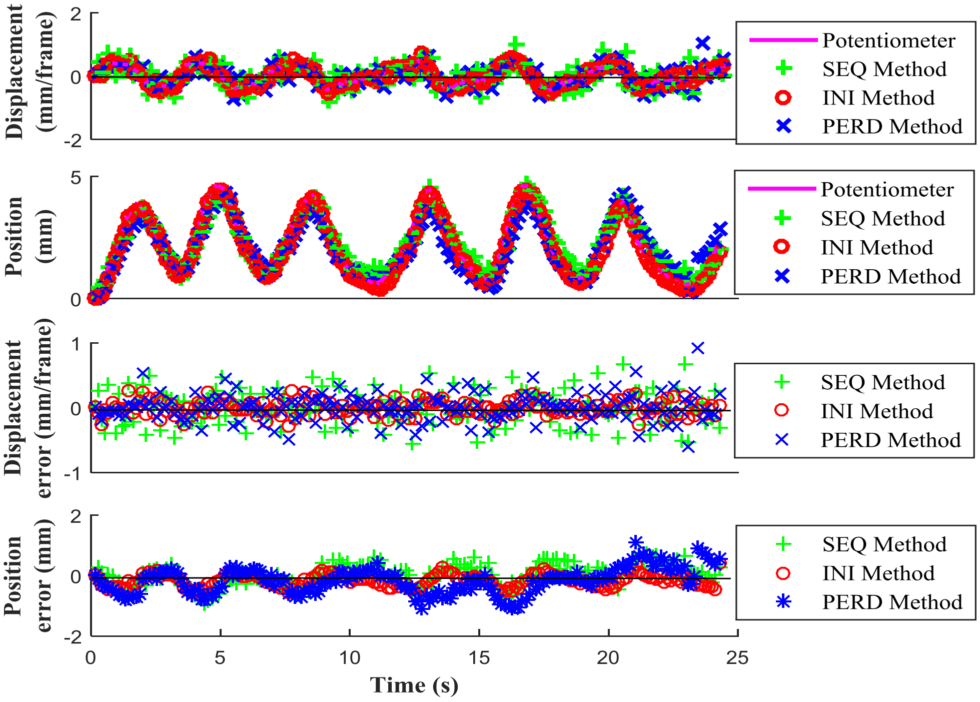

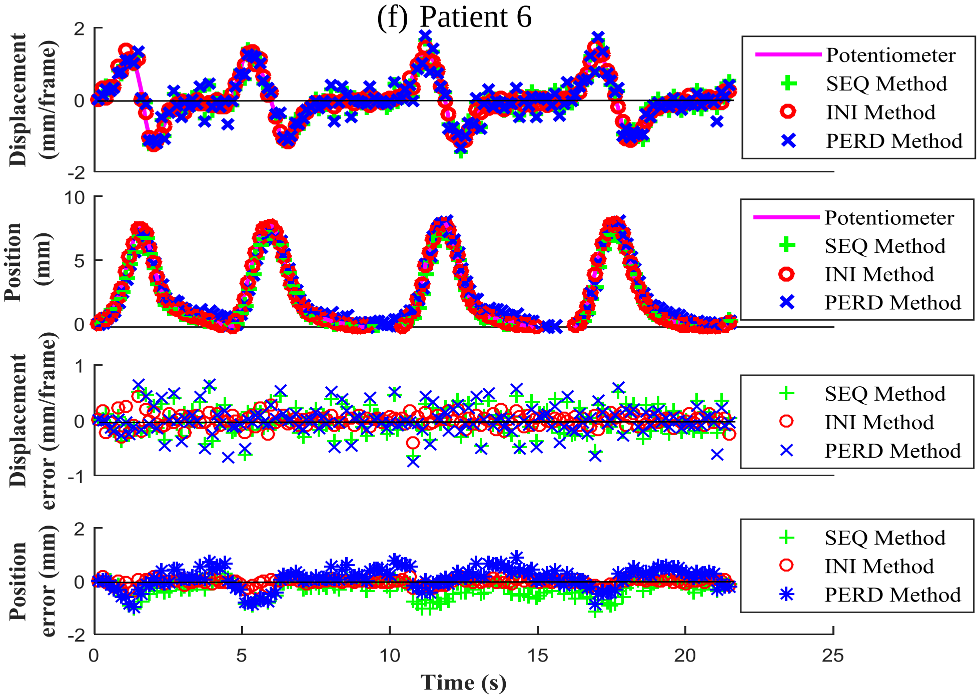
(f) Patient 6

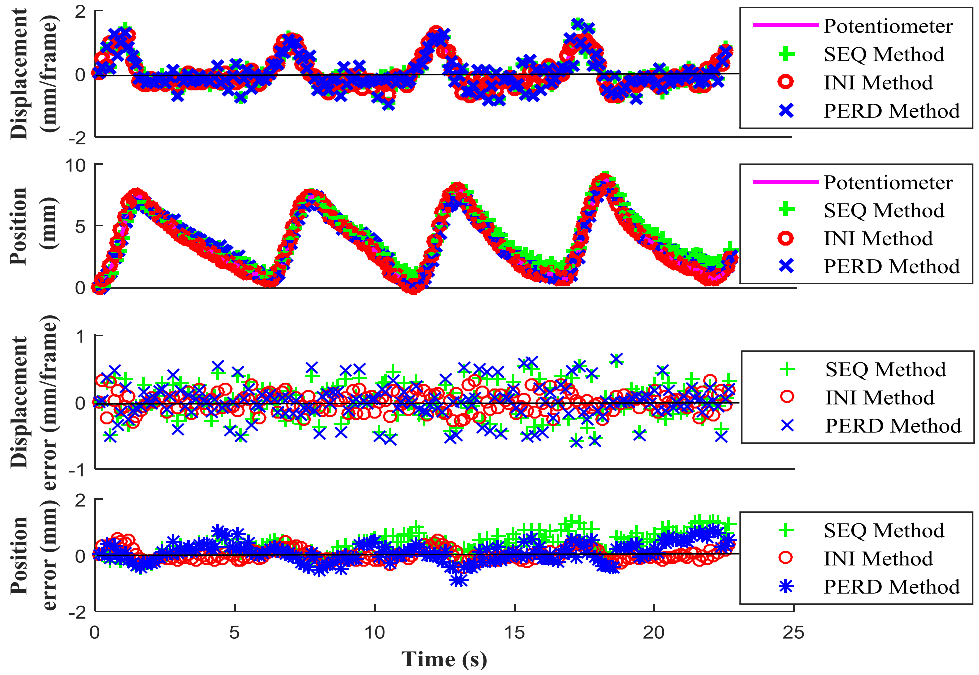
(g) Patient 7

Figure 4.5 : The inter-frame displacement, position, displacement error and position error profiles of patients 1 through 7 ((a)-(g)) estimated using (i) initial image as a fixed reference image (INI), (ii) with a sequential (SEQ) and (iii) a periodic (PERD) update of reference image.

Table 4.2 : Mean position errors ± the central 68% of the error distribution for three different implementations of the weighted optical flow algorithm with patients 1 through 7.

	Mean position errors (mm)		
	INI Method	**SEQ Method**	**PERD Method**
Patient 1	-0.01 ± 0.08	0.25 ± 0.37	0.00 ± 0.43
Patient 2	0.01 ± 0.10	0.16 ± 0.25	-0.48 ± 0.31
Patient 3	-0.05 ± 0.22	0.07 ± 0.35	-0.27 ± 0.37
Patient 4	-0.09 ± 0.34	-0.26 ± 0.33	-0.16 ± 0.54
Patient 5	-0.16 ± 0.20	-0.01 ± 0.36	-0.18 ± 0.43
Patient 6	-0.03 ± 0.11	-0.30 ± 0.31	0.09 ± 0.39
Patient 7	0.01 ± 0.20	0.39 ± 0.38	0.10 ± 0.34

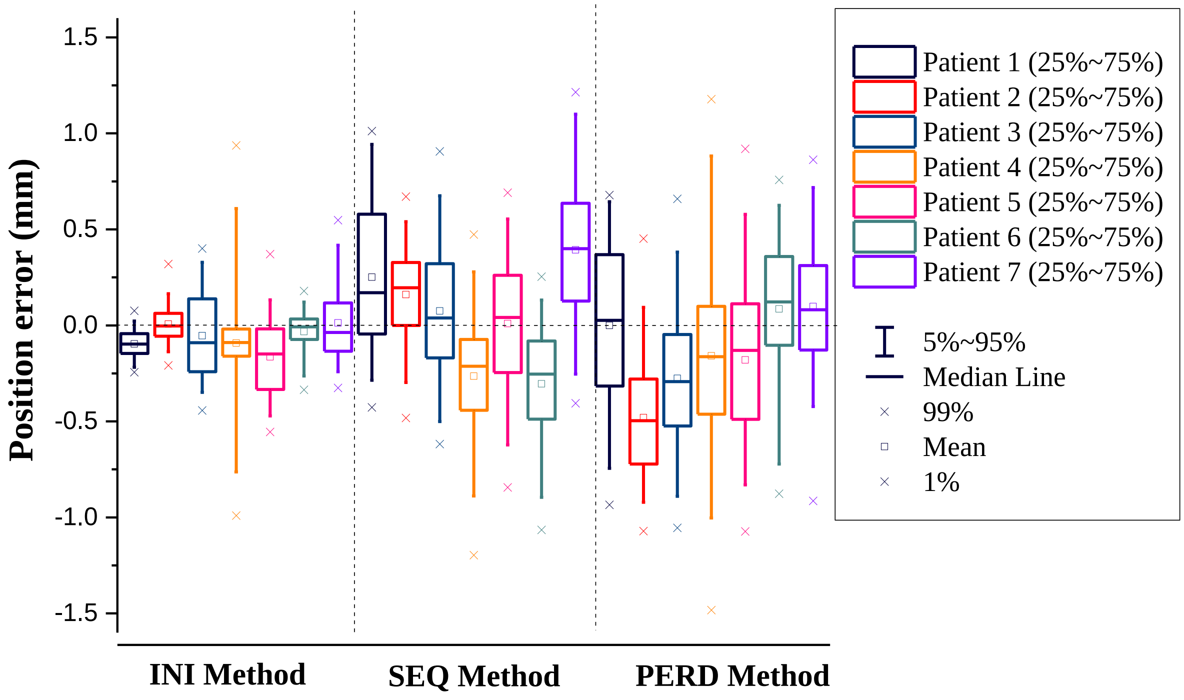

Figure 4.6 : Position errors of the seven patients obtained using three different implementations of the weighted optical flow algorithm.

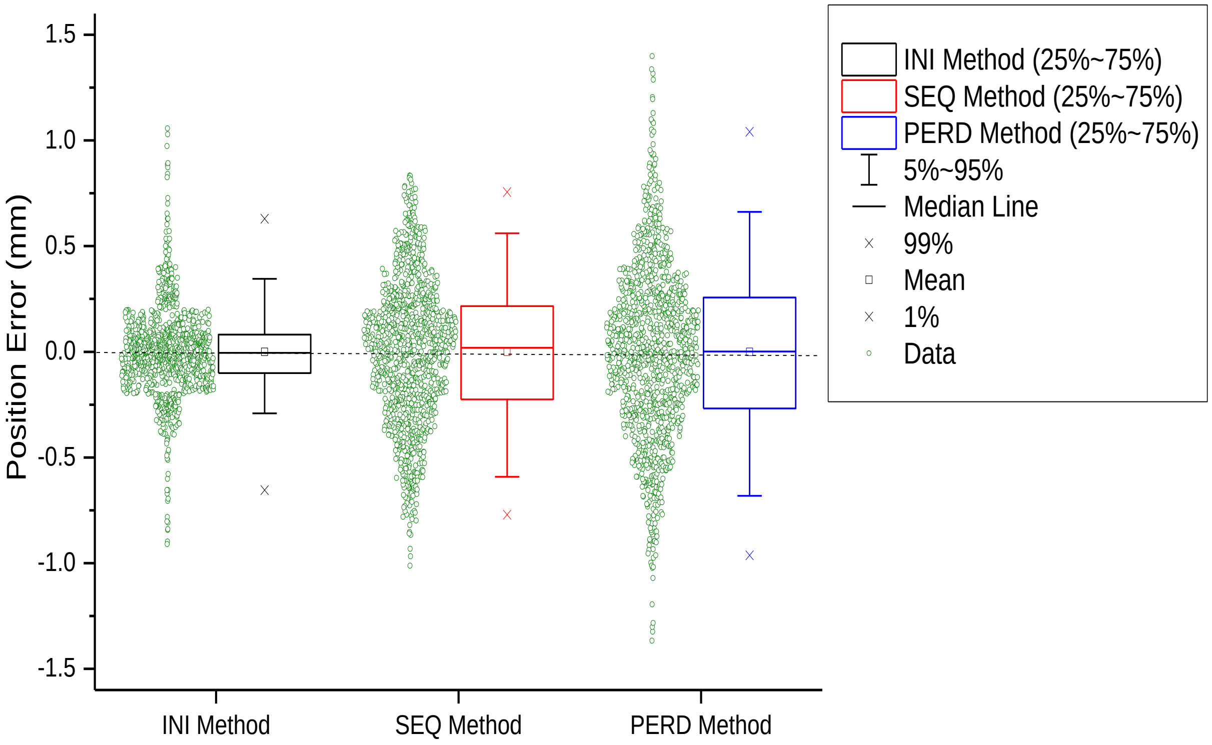

Figure 4.7 : The distribution of the position errors for each method

Table 4.3 : The overall performance of three tracking methods quantified by the accuracy (mean position error ± 1 standard deviation of all patients), precision (the width of the central 68% of the distributions shown in figure 4.7) and the mean absolute position error.

	INI	**SEQ**	**PERD**
Mean ± 1 Std. (mm)	-0.06 ± 0.21	0.04 ± 0.41	-0.14 ± 0.45
Distribution Width (mm)	0.32	0.68	0.79
Mean Abs. Error (mm)	0.16	0.32	0.38

4.4 Discussion

4.4.1 Analysis of results

From the patient cohort, there are two distinct groupings based on the dominant frequency component. While patients 1-3 have a higher dominant frequency than patients 4-7 this does not appear to affect the tracking results. Instead, it is observed that the position errors were due either to (1) an error in the inter-frame displacement or (2) the accumulation of small inter-frame displacement errors in the same direction. These errors could be present in all the three methods of image registration. Since the PERD method uses periodic calibration at EoEs, it is the most susceptible to type (1) error. In particular, the spurious detection of EoEs cause image registration and position calibration to be performed in between the actual EoEs (highlighted in section 3). As a result, the aim of calibrating the position while the velocity is at its minimal within a breathing cycle was not achieved. Hence, in addition to the errors incurred using sequential image tracking in between EoEs, errors were incurred due to the spurious detection of EoEs when using the PERD method. The combination of errors due to sequential and periodic reference image registration resulted in the PERD method having the largest position error.

Errors are a combination of systematic uncertainties and random effects. The systematic uncertainties are in turn a complex function of the position, velocity and acceleration of the object being tracked. In some cases, errors appear to be correlated with the position. In previous work, it has been shown that it is a complex relationship with smaller displacement resulting in larger fractional errors in position [18]. In other cases, errors are seen to accumulate in one or the other directions, primarily in the positive direction due to the under-estimation of the displacement in the negative direction. The integration of the random displacement errors can also result in accumulation of positional errors. In previous work, it was shown that as the number of breathing cycle increases, the accumulation of random errors was reduced. Position drift resulting from the accumulation of tracking errors is a known issue in medical imaging modalities [21-22], as well in other non-medical imaging applications [24-25]. Further investigations are required.

Some of the common causes of the isolated inter-frame displacement error are (1) motions that are smaller than the image resolution [21,37] and (2) the underestimation of large displacements that are beyond the parameters of the tracking algorithm. In the current work, the three-layer optical flow algorithm is capable of tracking motions with magnitudes similar to those observed from the seven patients. As a result, the inter-frame displacement error is likely due to motions that are smaller than the image resolution rather than the under-estimation of the large displacements. This could potentially be mitigated by integrating motion from multiple image frames, an approach that has also shown success in reducing position drift [38]. However, the optimal number of image frames required for the integration requires further studies.

4.4.2 Limitations in the estimation of the EoEs

For the PERD method, additional errors were incurred when determining and updating the reference periodically (as described in Section 4.4.1). The current implementation uses the change of slope in the position and the inter-frame displacement to determine the EoE of each cycle. This implementation requires a moving window to monitor the change in slope and to minimize the impact of noise. Although a larger moving window could be used to filter out the noise, the detection and adjustment of the reference position at EoE would be delayed, potentially reducing treatment accuracy. In the current implementation, a moving window of four data points was used, and the EoE would be detected when the slope of the velocity and acceleration derived from the first two images are different from the next two data points. This implementation implies that any update of the new reference image will only happen two frames after EoE. This update could potentially introduce errors when the adjustment occurs at higher velocities [39] causing abrupt changes in the inter-frame displacement as observed in our results (as described in section 4.3). Since a prediction algorithm would be employed in practice to compensate for system latency, this prediction could be used to predict the EoE in each breathing cycle. The position errors for the PERD method could be reduced by calibrating the reference position at the predicted EoE positions, eliminating the two frame delay.

4.4.3 Image quality of the reference image and its impact

In tracking the micro-scale motion of insect body parts with a high-speed digital imaging system (i.e. 10,000 frames/s), it has been shown that a good quality reference image is essential if the tracking drift is to be minimized [25]. Our previous study has demonstrated that the tracking accuracy of the optical flow is affected by the contrast-to-noise ratio of the image. To reduce the blurring of the target, the reference image should ideally be selected when there is little motion in the MV images. Therefore, in our PERD implementation, the reference images were updated at the EoE and for our INI implementation, the initial reference image was selected at the beginning of the target motion. It should be noted that the stationary target observed in the initial frame is a result of our experimental setup, i.e. acquiring the initial image at the beginning of the actuator motion. For clinical applications, the acquired initial frame might not correspond to a slow moving target. Thus, further verification of the impact on the INI method would be required. The determination of EoE in the PERD implementation was performed autonomously and was thus subject to the accuracy of the EoE-finding algorithm. Future improvements could include methods to assess the quality of an incoming image before assigning it as a reference.

Since the mean intensity of the x-ray image changes with the variation of the volume of the chest (with the optimal image quality being obtained at the EoE), Berbeco *et al.* [40] have shown that it can be used as an approach to automatically determine the EoE. Although the use of an initial frame as a reference image assumes that the background does not change rapidly, background information can be assessed from prior knowledge (e.g. treatment planning data or images obtained during patient setup) and could be suppressed if necessary [27, 41]. In our experiment, the INI method avoids using intermediate image frames where the image quality could be inferior to the initial frame acquired with the object moving at low velocity. Further verification on the fluctuations of the quality of the reference image and its effects on the different methods are required.

4.4.4 Comparison between dynamic vs. static tracking

The accuracies (mean absolute position errors) of 0.16 mm, 0.32 mm and 0.38 mm with a precision of 0.26 mm, 0.50 mm, and 0.60 mm for the INI, SEQ and PERD methods, respectively, are within the accuracies (i.e. 0.6 ± 0.2 mm) obtained for static tracking, i.e. without adapting the aperture [11, 18]. The difference between the previous work and the current work which uses a DMLC system is akin to static versus a dynamic tracking, respectively [26, 27]. In static tracking, the aperture, and field of view (FOV) does not move (e.g., tracking using the kV images of a LINAC). A large FOV is required to capture the full extent of the target motion. Tracking of the target using direct registration with the initial frame would be challenging since it is necessary to handle the maximum displacement of the target motion. In dynamic tracking, the aperture follows the target and the distance to be tracked between the constantly updated FOVs is small compared to static tracking using a fixed FOV. Thus, dynamic tracking with a conformal aperture is less likely to encounter challenges associated with tracking large inter-frame displacements. In contrast to the large FOV used for static tracking, the small FOV of dynamic tracking ensures that the optical flow velocities are mainly due to the motion of the target rather than the background. This would explain for the smaller tracking error observed in our current work with dynamic tracking compared to previous work on static tracking [11, 18]. Unlike static tracking where errors are solely due to image registration, in dynamic tracking, errors could incur from image registration and adjustment of the aperture. However, in the current work, aperture update was implemented with the virtual DMLC and no mechanical aperture adjustment errors were present.

4.4.5 Comparison with other tracking methods

Although the accuracy of our current weighted optical flow algorithm is comparable with other methods, such as template matching [8-11], our method does not aim to track a contour or template since soft tissues, including tumor, do not have a well-defined boundary on MV images. The ability to track without a template was achieved by computing the optical flow map to capture all motions (i.e. the global motion) within the aperture and giving greater weights to vectors near the non-homogeneous motion region, an approach that is similar, but more ‘global’ than tracking the boundaries of a moving tumor [13]. Although our method has a similar assumption that the tumor is the only target in the aperture [13], tracking of multiple targets is feasible with local clusters of optical flow vectors [16,17,19]. The dosimetric benefits of tracking the global motion of an uncontoured target outweigh the impact of the errors associated with our methods, as verified with other tracking systems having similar magnitudes of error [33, 42, 43].

4.4.6 Future extensions of our work

Although the current work has shown that using an initial frame as the reference image yields a higher tracking accuracy, in this work, a fixed aperture similar to a conformal treatment delivery was assumed. For IMRT and VMAT applications where the treatment aperture is optimized to meet certain dose constraints, the SEQ approach, which updates the reference image sequentially, provides for greater similarity between the two apertures. The similarities allow common regions to be established rapidly for the optical flow computation. Extending our experiment to IMRT and VMAT type of treatments will be performed in the future.

Although data for seven patients with diverse motion characteristics were used in this study, further studies using a larger dataset size with various tumor shapes, deformations, trajectories with baseline shift, and image quality are required to confirm our preliminary observations. Like most studies that use cine mode to acquire EPID images, the memory limitation of a clinical LINAC limits the maximum number of high resolution images that can be acquired to about 200 [44, 45]. With a frame rate of 7.5 frame/s, this amounts to about 27 s of treatment time, which is short compared to typical treatment time of around 4 min. Given the possible accumulation of position errors, proposed algorithms should be validated over a longer image sequence, a task that will be included in our future work.

Besides the CyberKnife system and three other research prototypes that track tumor motion with the treatment beam and adapts treatment delivery [3, 5, 34], the virtual DMLC implemented in our study [31] could serve as a rapid verification/simulation for tracking and adaptation of treatment beams. In particular, it would be extended to simulate the tracking and adaptation of aperture based on the intrusion of external critical organs into the irradiated field, a validation for some of the preliminary results demonstrated by our group [19].

4.5. CONCLUSIONS

Tracking of tumor motion was implemented with a weighted optical flow algorithm using three different approaches to update the reference image. Results highlighted the possibility of accumulating position errors during the tracking of the target on MV EPID images using patient-driven tumor trajectories. The INI method which uses the initial irradiated field as a fixed reference image is the least prone to accumulation of position errors. The INI method is followed by the SEQ method, which sequentially updates the reference image to the image frame prior to the incoming image, and the PERD method, which updates the reference image periodically. The performance of the algorithms is also reflected in the mean absolute errors of 0.16 mm, 0.32 mm and 0.38 mm and precisions of 0.32 mm, 0.68 mm, and 0.79 mm for the INI, SEQ and PERD methods, respectively (mean absolute position errors of INI < SEQ < PERD). It should be noted that the INI method assumes that the initial reference image was selected at the beginning of the target motion. We observed that the position errors are due to either (1) a single error in the displacement, or (2) accumulation of small inter-frame displacement errors in a similar direction. Adaptation of the aperture to follow the tumor motion was realized with a virtual DMLC system and its performance was validated with seven patient tumor motions. With a tracking accuracy that is comparable to other tracking methods, the proposed weighted optical flow algorithm coupled with the use of the initial image as a fixed reference image can be used to track markerless, uncontoured tumors with minimal accumulation of position errors.

References

1. A. Schweikard, H. Shiomi, J. Adler, “Respiration tracking in radiosurgery”, Med Phys 31, 2738–2741 (2004).

2. M. J. Murphy, “Tracking moving organs in real time”, Semin. Radiat. Oncol. 14, 91–100 (2004).

3. T. Neicu, H. Shirato, Y. Seppenwoolde and S. B. Jiang, “Synchronized moving aperture radiation therapy (SMART): average tumour trajectory for lung patients”, Phys. Med. Biol. 48(5), 587-598 (2003).

4. M. Tacke, S. Nill and U. Oelfke, “Real-time tracking of tumor motions and deformations along the leaf travel direction with the aid of a synchronized dynamic MLC leaf sequencer”, Phys. Med. Biol. 52, N505–N512 (2007).

5. A. Sawant, R. Venkat, V. Srivastava, D. Carlson, S. Povzner, H. Cattell, P. Keall, “Management of three-dimensional intrafraction motion through real-time DMLC tracking”, Med. Phys. 35(5), 2050 – 2061 (2008).

6. P. Keall, E. Colvill, R. O’Brien, J. A. Ng, P R Poulsen, T. Eade, A. Kneebone, and J. Booth, “First clinical implementation of electromagnetic transponder- guided MLC tracking”, Med. Phys. 41(2) 020702 (5pp.) (2014).

7. M. Orkisz, A. Frery, O. Chapet, F. Mornex and I. E. Magnin, “Attempts to bronchial tumor motion tracking in portal images during conformal radiotherapy treatment”, Comp. Analysis of Images and Patterns (Lect. Notes in Comp. Sci.) 2124, 247–55 (2001).

8. J. Meyer, A. Richter, K. Baier, J. Wilbert, M. Guckenberger and M. Flentje, “Tracking moving objects with megavoltage portal imaging: A feasibility study”, Med. Phys. 33, 1275-1280 (2006).

9. T. Lin, L.I. Cervino, X. Tang, N. Vasconcelos and S.B. Jiang, “Fluoroscopic tumor tracking for image-guided lung cancer radiotherapy”, Phys. Med. Biol. 54, 981-992 (2009)

10. R. Li, J. Lewis, L.I. Cervino and S.B. Jiang, “A feasibility study of markerless fluoroscopic gating for lung cancer radiotherapy using 4DCT templates”, Phys. Med. Biol. 54, N489–N500 (2009).

11. J. Rottmann, M. Aristophanous, A. Chen, L. Court and R. Berbeco, “A multi-region algorithm for markerless beam’s-eye view lung tumor tracking”, Phys. Med. Biol. 55, 5585–5598 (2010).

12. Q. Xu, R. Hamilton, R. Schowengerdt, B. Alexander and S. B. Jiang, “Lung tumor tracking in fluoroscopic video based on optical flow”, Med Phys. 35(12), 5351-5359 (2008).

13. X. Zhang, N. Homma, K. Ichiji, Y. Takai, M. Yoshizawa, “Tracking tumor boundary in MV-EPID images without implanted markers: A feasibility study”, Med. Phys. 42(5), 2510-2523 (2015).

14. N. Kothary, J. Heit, J. Louie, W. Kuo, B. Loo, Jr., A. Koong, D. Chang, D. Hovsepian, D. Sze, and L. Hofmann, “Safety and efficacy of percutaneous fiducial marker implantation for image-guided radiation therapy”, J. Vasc. Interv. Radiol. 20, 235–239 (2009).

15. C. Nelson, G. Starkschall, P. Balter, R. Morice, C. Stevens, and J. Chang, “Assessment of lung tumor motion and setup uncertainties using implanted fiducials”, Int. J. Radiat. Oncol., Biol., Phys. 67(3), 915–923 (2007).

16. E. Ohn-Bar, S. Sivaraman, and M. Trivedi, “Partially occluded vehicle recognition and tracking in 3D”, IEEE Intelligent Vehicles Symposium IV, 1350–1355 (2013).

17. A. Ramirez, E. Ohn-Bar, and M. Trivedi, “Go with the flow: Improving multi-view vehicle detection with motion cues”, Proc. 22nd Int. Conf. Pattern Recognition (ICPR), 4140 - 4145 (2014).

18. P. T. Teo, R. Crow, S. van Nest, D. Sasaki and S. Pistorius, “Tracking lung tumour motion using a dynamically weighted optical flow algorithm and electronic portal imaging device”, Meas. Sci. Technol. 24, 074012 (15pp) (2013).

19. P. T. Teo and S. Pistorius, “Tissue motion tracking at the edges of a radiation treatment field using local optical flow analysis”, J. of Phys.: Conf. Series, 489 012040 (2014).

20. E. J. Harris, N. R. Miller, J. C. Bamber, J. R. N. Symonds-Tayler, and P. M. Evans, “Speckle tracking in a phantom and feature-based tracking in liver in the presence of respiratory motion using 4D ultrasound”, Phys. Med. Biol. 55(12), 3363–3380 (2010).

21. T. P. O’Shea, J. C. Bamber, and E. J. Harris, “Temporal regularization of ultrasound-based liver motion estimation for image-guided radiation therapy”, Med. Phys. 43 (1), 455-465 (2016).

22. M. Bell, B. Byram, E. Harris, P. Evans and J. C. Bamber, “In vivo liver tracking with a high volume rate 4D ultrasound scanner and a 2D matrix array probe”, Phys. Med. Biol. 57, 1359–1374 (2012).

23. P. T. Teo, K. Guo, N. Alayoubi, K. Kehler, S. Pistorius, “Drift correction techniques in the tracking of lung tumor motion”, Proc. IFMBE World Congress on Med. Phys. and Biomed. Eng. 51, 575-578 (2015).

24. W. Li, D. Cosker and M. Brown, “An anchor patch based optimization framework for reducing optical flow drift in long-picture sequences”, Proc Asian Conf Comp Vision (CVMA), 112-125 (2013).

25. L. Gui and J. M. Seiner "An image pattern tracking algorithm for time-resolved measurement of mini- and micro-scale motion of complex", Algorithms, 2, 533-549 (2009).

26. C-K. Wang, M-Y. Cheng *et al.*, "Design and implementation of a multi-purpose real-time pan-tilt visual tracking system", Proc. 2004 IEEE Int. Conf. on Control Apps., 1079-1084 (2004).

27. D. Murray and A Basu, "Motion Tracking with an active camera", IEEE Trans. Pattern Analysis and Machine Intelligence 16(5), 449-459 (1994).

28. P. Keall, H. Cattell, D. Pokhrel, S. Dieterich, *et al.*, "Geometric accuracy of a real-time target tracking system with dynamic multileaf collimator tracking system", Int. J. Radiat. Oncol. Biol. Phys. 65, 15 79–1584 (2006).

29. E. W. Pepin, H. Wu and H. Shirato, "Use of dMLC for implementation of dynamic respiratory-gated radiation therapy", Med. Phys. 40, 101708 (2013).

30. B. D. Lucas and T. Kanade, "An iterative image registration technique with an application to stereo vision", Proc. 7th Int. Joint Conf. on Artificial Intelligence 674-9 (1981).

31. Matlab code for the implementation of a virtual DMLC system. Accessed on June 26th 2016. https://www.dropbox.com/sh/1kpbrwibbff00zp/AAB9zOUsah9I75QWNvHrZIR2a?dl=0

32. V. Boldea, G. C. Sharp, S. B. Jiang and D. Sarrut, "4D-CT lung motion estimation with deformable registration: Quantification of motion nonlinearity and hysteresis", Med. Phys. 35:1008-1018 (2008).

33. S. G. Armato G. McLennan, L. Bidaut L, G. F. McNitt-Gray, et. al., "The Lung Image Database Consortium (LIDC) and Image Database Resource Initiative (IDRI): A completed reference database of lung nodules on CT scans", Med. Phys. 38(2), 915–931 (2011).

34. E. Colvill, J. Booth, S. Nill, M. Fast, J. Bedford, U. Oelfke, M. Nakamura, P. Poulsen, E. Worm, R. Hansen, T. Ravkilde, J. S. Rydhög, T. Pommer, P. Munck af Rosenschold, S. Lang, M. Guckenberger, C. Groh, C. Herrmann, D. Verellen, K. Poels, L. Wang, M. Hadsell, T. Sothmann, O. Blanck, and P. Keall. "A dosimetric comparison of real-time adaptive and non-adaptive radiotherapy: A multi-institutional study encompassing robotic, gimbaled, multileaf collimator and couch tracking", Radiother Oncol. 119, 159–165 (2016).

35. Y. Seppenwoolde, H. Shirato, K. Kitamura, S. Shimizu, M. van Herk, J. V. Lebesque and K. Miyasaka, "Precise and real-time measurement of 3D tumor motion in lung due to breathing and heartbeat, measured during radiotherapy", Int. J. Radiat. Oncol. Biol. Phys. 53 822-834 (2002).

36. Y. Suh, S. Dieterich, B. Cho B, and P. Keall, "An analysis of thoracic and abdominal tumour motion for stereotactic body radiotherapy patients", Phys. Med. Biol. 53, 3623–3640 (2008).

37. T. Brox and J. Malik, “Large displacement optical flow: descriptor matching in variational motion estimation”, IEEE Trans Pattern Analysis & Machine Intelligence 33, 500 – 513 (2011).

38. H. Badino, A. Yamamoto, and T Kanade, “Visual odometry by multi-frame feature integration”, Proc., 2013 IEEE International Conference on Computer Vision Workshops (ICCVW), 222-229 (2013).

39. S. Yip, J. Rottmann and R. Berbeco, “The impact of cine EPID image acquisition frame rate on markerless soft-tissue tracking”, Med. Phys. 41, 061702 (7pp) (2014).

40. R. I. Berbeco, H. Mostafavi, G. C. Sharp and S. B. Jiang, “Towards fluoroscopic respiratory gating for lung tumours without radiopaque markers”, Phys. Med. Biol. 50, 4481-4490 (2005).

41. R. Tanaka, S. Sanada, K. Sakuta and H. Kawashima, “Improved accuracy of markerless motion tracking on bone suppression images: preliminary study for image-guided radiation therapy”, Phys. Med. Biol. 60, N209–N218 (2015).

42. H. Shirato, S. Shimizu, K. Kitamura et. al., “Four-dimensional treatment planning and fluoroscopic real-time tumor tracking radiotherapy for moving tumor”, Int. J. of Radiat. Oncol. Biol. Phys. 48, 435–442 (2000).

43. M. J. Menten, M Guckenberger, C. Herrmann, A. Kraub, S. Nill, U. Oelfke, J. Wilbert, “Comparison of a multileaf collimator tracking system and a robotic treatment couch tracking system for organ motion compensation during radiotherapy”, Med Phys. 39, 7032-7041 (2012).

44. P. M. McCowan, D. Rickey, P. Rowshanfarzad, P. B. Greer, W. Ansbacher, and B. M. McCurdy, “Investigation of gantry angle data accuracy for cine-mode EPID images acquired during arc-IMRT”, J. App. Clin. Med. Phys. 15(1), (2014).

45. J. Adamson and Q. Wu, “Independent verification of gantry angle for pre-treatment VMAT QA using EPID”, Phys. Med. Biol. 57(20), 6587-6600 (2012).

Chapter 5 Adaptive Treatment Delivery with Real-Time Organ-At-Risk (OAR) Intrusion Detection and Avoidance – a Proof-of-Concept Study with Electronic Portal Images and an Optical Flow Algorithm

This chapter presents a method to detect motion at the edges of a treatment field using local clusters of vectors computed from the optical flow algorithm presented in chapter 3. Part of the work was published in the Journal of Physics: Conf. Series, 489, 012040, 2014, DOI:10.1088/1742-6596/489/1/012040. The material is also prepared for submission to Medical Physics by the author of this dissertation.

Abstract

Purpose: The increase of high-dose, low-fraction treatments makes it more important to adapt the treatment immediately upon detecting an unplanned intrusion of healthy tissues or organs-at-risk (OAR) into the treatment field. In this work, a method to detect motion at the edges of a treatment field is proposed. This motion could be due to either a moving aperture encroaching on an external (outside the planned treatment region) OAR or an external OAR that is moving into the irradiated field. The detection of local motion at the field edges is used to adapt the multileaf collimator (MLC) to shield the intruding OAR from unnecessary radiation. The hypothesis that motion can be reliably detected, and the MLC leaves could be adapted accordingly was tested. A simulation framework using an adaptive virtual MLC, coupled with patient tumor motion was created. This work, which focuses on the local motion detection and adaptation at the edges of the treatment field, is an extension of previous studies into tracking the motion of a tumor target.

Methods: This proof-of-concept implementation includes (1) an algorithm that detects and tracks the motion at the edges of a treatment field and (2) a control algorithm that adapts the virtual MLC based on the motion detected. An optimal cluster size of local vectors that resulted in the smallest tracking error at the edges was determined by a parameter sweep. The algorithm was evaluated with a phantom programmed to move in a sinusoidal fashion and with tumor motion data of five lung cancer patients. The motions were recorded with an electronic portal imaging device (EPID). To simulate an external object intruding into the treatment field, a duplicate of the image sequence was flipped and concatenated to the original image sequence so that the intruding object would travel at the same velocity but in opposite directions to the target. The adaptation of the MLC was simulated by moving the edge of the image frame.

Results: In tracking a structure moving with an asymmetric cosine function having velocities of 0 to 10 mm/s and an intrusion depth of 10 mm, an optimal cluster size of 9-by-9 vectors was found to provide the smallest average absolute position error of 0.3 mm. A strong linear correlation between the adapted MLC leaves and the actual OAR position was observed with a slope of 0.98 and an offset of -0.4 mm. In evaluating the algorithm with patient data, a mean position tracking error of -0.4 ± 0.3 mm and a precision of 1.1 mm were obtained.

Conclusions: This proof-of-concept simulation illustrates that it is possible to adapt MLC leaves based on the motion detected at the edges of the irradiated field and demonstrates that it would be feasible to shield an unplanned intrusion of an external object or OAR into the treatment field. The results provide motivation to combine global adaptation of the treatment field (due to the motion of the main target) with local adjustments at the edges to avoid unexpected intrusions.

5.1 Introduction

5.1.1 Tumor motion and adaptive radiotherapy

Tumors and OARs can move with respiration at various anatomical sites. Under these circumstances, it can be a challenge to ensure that sufficient radiation dose is delivered to the tumor while avoiding damage to the surrounding healthy tissues. Several techniques have been proposed to mitigate the impact of respiratory motion. These techniques include respiratory gating, margin expansion, and breath control [1]. However, gating and breath control increase treatment time, while margin expansion increases the volumn of the surrounding healthy tissues being irradiated. Adaptive radiotherapy incorporating real-time tracking with beam adaptation has been proposed to improve efficiency and reduce toxicity [2]. In Dynamic Multi-leaf Collimator (DMLC) systems, the leaf positions are dynamically modified to follow the motion of the target, thereby reducing the size of the treatment field [2-4]. To minimize the effects of errors in the correlation between internal and external surrogates, cine mode Electronic Portal Imaging Device (EPID) images have been used to track motion during beam delivery without additional radiation to the patient [4-5]. Various marker-less techniques have also been proposed for real-time tracking of targets with EPID images [5-8]. However, most of these tracking methods require either prior knowledge of the target or segmentation of the target, such that the delineated contours on the initial image can be used for tracking on subsequent images. These methods often assume negligible target deformations. To ensure sufficient radiation is delivered to the tumor, these methods emphasize tracking the motion of the tumor.

5.1.2 Healthy tissue and OAR monitoring

In radiation therapy, the emphasis has been placed on tracking the main clinical target within the irradiated field. However, it has been shown that discrepancies in the dose distribution of the target and normal tissues can arise if the delivery of intensity modulated radiation therapy (IMRT) disregards the motion of surrounding tissue [9,10]. The planning organ at risk volume (PRV) has been introduced to account for the uncertainty associated with the OAR motion. However, limitations exist [11]. Although the dose limits to the OAR are taken into consideration during treatment planning, this assumes that the setup of the patient is accurate, and patient breathing and tumor/OAR motion during treatment are identical to the pattern delineated during planning. Failure mode and effect analysis (FMEA) has revealed that contouring the OAR, with reported inter-observer deviations of up to 2.9 cm and 7.6 cm for the esophagus and heart respectively [12,13] could be a potential source of systematic error with a high risk of frequent occurrence [14,16]. Challenges in contouring the OAR as well as the use of wrong OAR contours have been reported [13,16]. The differences between the planning and treatment delivery could alter the proximity between the OAR and the high dose region of the treatment field. The error in estimating the OAR position is of particular concern in Stereotactic Body Radiation Therapy (SBRT) due to the steep dose gradient, reduced margin, low-fraction, high dose treatment and intra-treatment patient motion due to the longer treatment duration [17,18]. "No-fly zones" [18] have been proposed for central tumors abutting the proximal bronchial tree, and functional avoidance radiotherapy has been proposed to avoid the functional portion of the lung [19]. The efficacies of these regimes are dependent on the ability to monitor both the target and the surrounding healthy tissues during treatment delivery. In addition, the ability to adapt the treatment upon detecting an unplanned intrusion of healthy tissues into the irradiated field is becoming more important. With a combination of adaptive beam movement and systematic deviation of the target motion pattern, similar concerns of unintentionally overdosing the OAR have been cited for the CyberKnife system [20].

For most cases, it has been shown that a lung tumor is expected to move similarly to the surrounding OARs since these tumors are embedded in the lung tissue and are forced to follow the lung motion [21]. However, with a chest wall-seated tumor in the lung, the lung tumor and the OAR, such as the ribs, can have different motion magnitudes relative to each other [22]. During the irradiation of the mammary tissues of breast cancer patients, the ipsilateral lung and heart are also often exposed to non-negligible dose [23]. For patients with cancer in the left breast, it has been shown that the left anterior descending artery (LAD) can have larger intra-fractional motion than the heart and left ventricle (LV). The errors in the irradiated volume of the LAD (as a result of the intra-fractional motion) are larger than the errors in the irradiated volume of the heart and LV [23]. These errors are larger than the errors due to the contouring uncertainties. Thus, the ability to avoid the LAD during treatment delivery could be crucial in reducing radiation-induced cardiac diseases. Although breathing adapted radiotherapy and deep inspiration breath hold techniques have been shown to reduce cardiac exposure, some patients were unable to comply with the requirements [23]. Setup errors and daily variations in organ motion, make it more difficult to consistently maintain the OAR outside of the radiation field [25]. Variation in dose distribution may occur as a result of the surrounding organs moving in and out of the field during respiration [26].

Although studies have been performed to determine the accuracy of MLC leaf-pair control for a moving target on EPID images [27], detection, and tracking of motion close to the leaf edges has to the knowledge of the authors, never been examined before. The lack of previous studies may be due to the difficulty in identifying the OARs that could potentially intrude into the treatment beam. As a result, current tracking methods based on apriori information such as contour or template matching [5,6] of the target might not find an exact match for an unplanned, partially intruding OAR.

5.1.3 Global and local motion tracking with optical flow

The optical flow process can be perceived as a pre-processor to tracking whereby a motion vector is initially derived for each pixel. In conventional optical flow tracking, some form of segmentation is required to associate individual vectors with the objects spatially and temporally. In real-time applications, manual delineation to associate them with the corresponding targets is impossible and autonomous ways to associate the vectors with the moving objects are required. The Scale Invariant Feature Transform (SIFT) flow uses a group of SIFT local features to associate the object with the flow vectors [28], while the Histograms of Gradients (HoG) approach uses distribution profiles of the local vectors to track the object in an image sequence [28]. However, learning algorithms are often needed to train and recognize these local features on subsequent images. An average-weighted multi-resolution optical flow algorithm with a 9-by-9 pixel regularization has been previously used to automatically track the global motion of a tumor target with an accuracy of 0.4 ± 0.2 mm [30, 31]. A preliminary attempt to detect local motion at the edges of a treatment field was performed by partitioning the edges of the treatment field into horizontal and vertical grids, creating clusters of 9-by-9 optical flow vectors [31]. The average value of the clustered vectors provides the detection of motion at the edges of the field. The 9-pixel width corresponds to the width of a 2.5 mm MLC when projected to the EPID at 140 cm from the source.

Recent studies have used EPID images for dosimetric evaluation (and detecting incidents in radiotherapy [19, 32-33]. This paper extends our work on optical flow tracking of a tumor to investigate the feasibility of using local optical flow analysis to track unplanned intrusions / motion at the edges of a treatment field [30-31]. A virtual DMLC system was used to study the feasibility of adapting the MLC to take the detected motion into account. This motion, which is assumed to be caused by the OARs (intended to remain outside the treatment field), could be due to either (a) an external OAR moving into a static treatment field (figure 5.1(a), or (b)) an adaptive aperture encroaching onto a stationary object (figure 5.1(b)). As a proof-of-concept, an external OAR moving into a static field (figure 5.1(a)) will be used to demonstrate the feasibility of the proposed method. Detection and potential adaptation to shield the intruding OAR (figure 5.2) are assumed to be based on rectifying the geometric abnormalities detected at the edges. The accuracy of this control algorithm was tested using simulated object intrusions with sinusoidal as well as patient tumor motion patterns. Techniques to prevent losing track of the intruding object were incorporated to cater for a change in the direction of intrusion as well as a change in the velocity when compared to the anticipated motion derived from the previous pair of image frames. Our previous work demonstrating the ability to track the tumor motion has been reported already and hence is beyond the scope of this paper [30]. The current work focuses on whether it is feasible to use optical flow techniques to make minor adjustments to the treatment field based on detected motion at the edges of the field. The concept of detecting an object as it enters or leaves the field of view is similar to a pan-zoom-tilt (PZT) camera system [35-36], and an obstacle detection system for autonomous vehicle [37-38]. The proposed technique in this study aims to supplement existing DMLC tracking systems which track the main target, by tracking motion at the field edges to detect unplanned OAR intrusions. Tracking motion, and adapting the field as the OAR enters into the treatment field, shields the OAR. By adapting the aperture as the

OAR subsequently leaves the treatment field, ensures that deviations from the treatment plan are minimized.

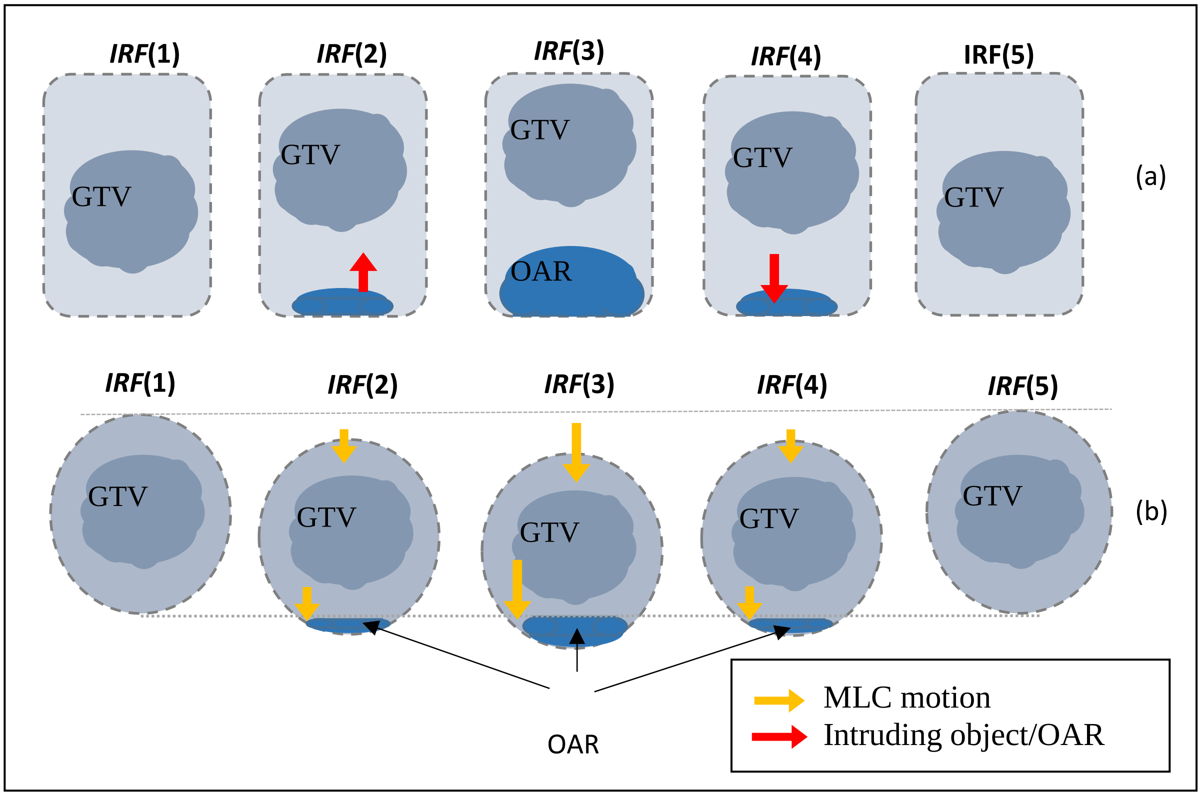

Figure 5.1 : Examples of potential unplanned OAR intrusion into the irradiated field (IRF) for (a) conformal (non-adaptive) and (b) dynamic conformal MLC treatment settings. For (a), the external moving object/OAR intrudes into a static field periodically, and for (b) a stationary OAR intrudes into the irradiated field that is following the motion of a tumor.

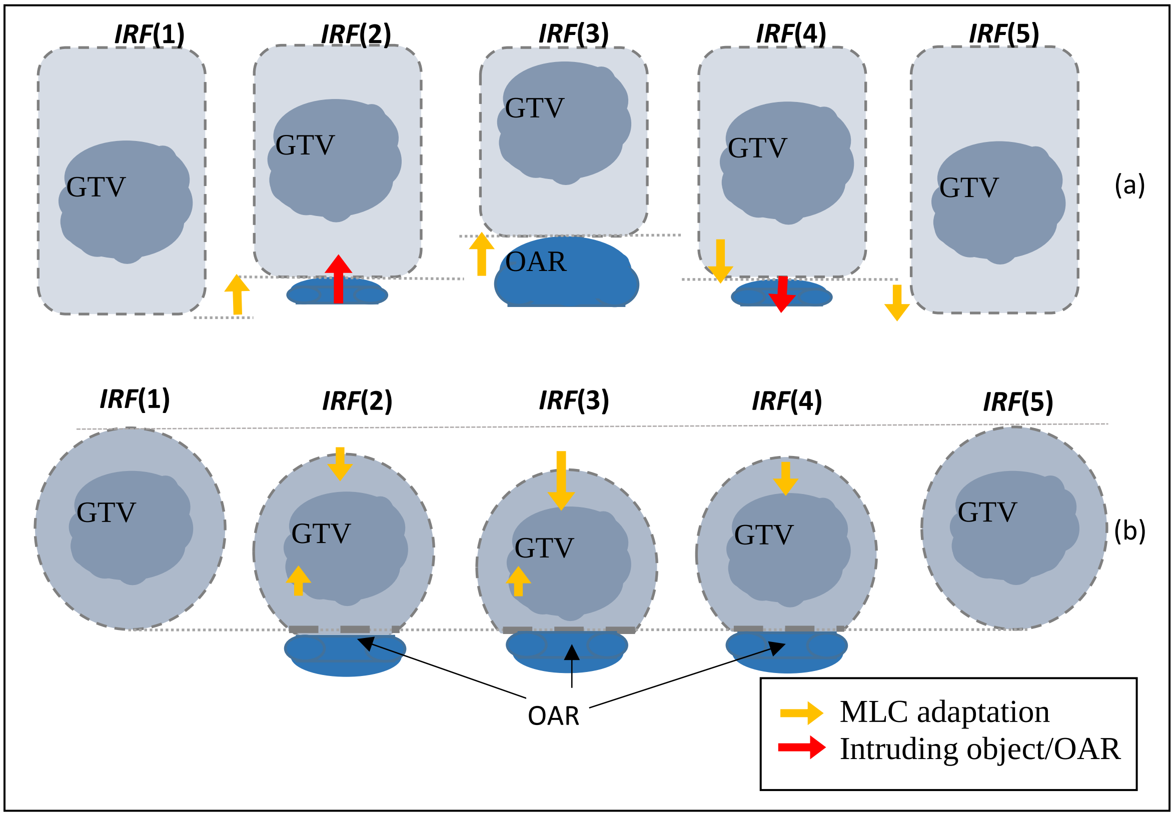

Figure 5.2 : Possible intra-fraction adaptations of treatment field based on the intrusions of OAR detected at the edges of the irradiated field (IRF) for (a) conformal (non-adaptive) and (b) dynamic MLC treatment settings as shown in figure 5.1

5.2 Methods and Materials

5.2.1 Overall process of motion detection and MLC leaves adaption

The flowchart of the proposed intra-fractional adaptation of the MLC leaves based on the motion detected and tracked at the edges of a treatment field is shown in figure 5.3. The major tasks of this OAR intrusion–avoidance system are: (1) estimation of motion using optical flow computation between two images [30]; (2) formation of local clusters of vectors at the edges of the optical flow map [31]; (3) analysis of each cluster adjacent to an MLC leaf; (4) updating the position of the intruding object/OAR observed at the edge of each MLC leaf; (5) predicting the position of the intruding object/OAR in the next frame based on the motion observed in the previous pair of image frames; (6) determine the buffers (i.e. the difference between the position of the intruding OAR and the MLC placement) needed and (7) adapting the MLC leaves for the next image frame. The details of these steps are described in the following sections, and an example of the treatment situation considered in our study is shown in figure 5.4.

5.2.2 Algorithm for motion estimation

The optical flow algorithm was applied to consecutive image frames to detect and track motions within the treatment aperture. A neighborhood (i.e. window) surrounding a pixel was used to obtain the solution for the optical flow constraint equation using the local least squares method proposed by Lucas-Kanade *et a*l. [39]. Since a uniform window size was applied to all the pixels in the entire image, the pixels at the edges of an image frame did not have a symmetrical neighborhood of pixels to support the computation, and the optical flow could not be computed in these regions. In our previous work [30], a 3-layer multi-resolution optical flow algorithm with 9-by-9 pixel regularization was used, and it resulted in 4 rows of pixels at the edges of the images where no optical flow vectors could be computed. In this work, a similar optical flow algorithm was used but with a 3-by-3 pixel regularization which reduced the number of rows of pixels without optical flow vectors to one. The regularization scheme and its impact on the edge intrusion tracking accuracy were evaluated.

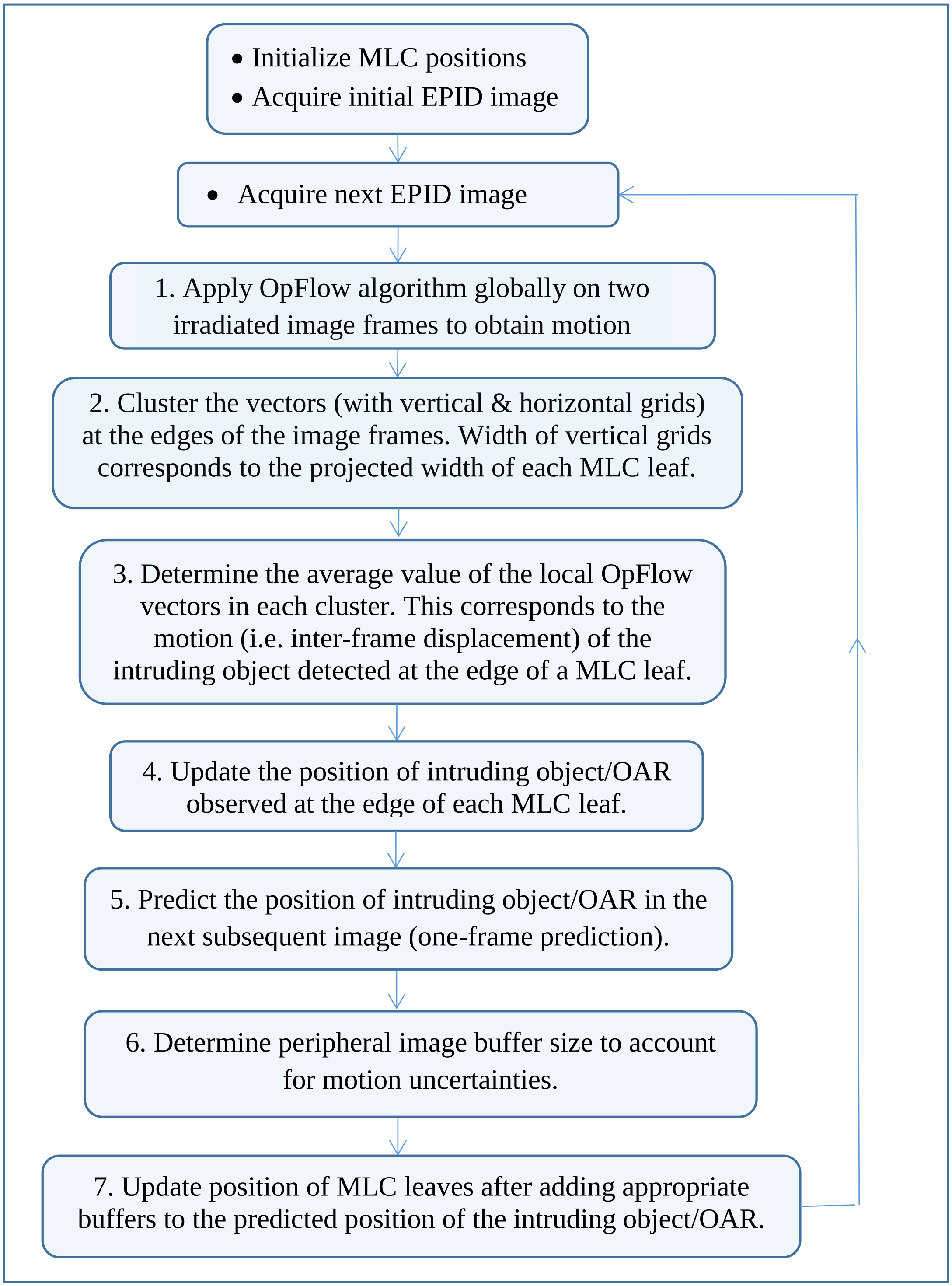

Figure. 5.3. : Flowchart of the main process of adapting the MLC leaves according to the local optical flow (OpFlow) vectors detected at the edges of an irradiated field (IRF).

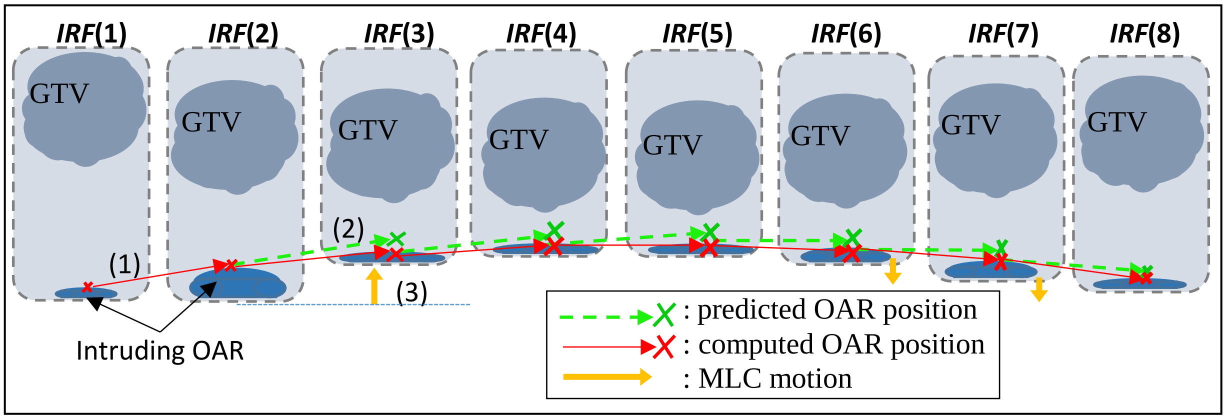

Figure 5.4 : An example of the scenario considered for our proof-of-concept study in adapting the MLC leaves based on the intrusions of an OAR detected at the edge of a treatment field (IRF). Steps involve in adapting the treatment field to shield the OAR include: (1) calculating the OAR position with local analysis of motion vectors at the edges, (2) using this motion to predict the position of the OAR in the next image frame, and (3) repositioning the MLC to follow the predicted OAR position, including a buffer space.

5.2.3 Deriving a common region from two different image sizes as a result of treatment field adaptation

To compute an optical flow map, two images of a similar size were required for comparison. However, with the adjustment of the position of the MLC leaves, the size and shape of the two images under comparison varied accordingly. Where the detected motion at the edge indicated an intrusion of the external structure into the irradiated field, the MLC leaves would be adjusted in a similar inward direction, hence reducing the size of the radiation field and also the irradiated volume. A common region *S* between the previous image and the new image formed by the MLC shape would be constrained by the current edges of the smaller field. For the case where the object leaves the irradiated field, the MLC would be extended beyond the previous boundary, creating a larger irradiated field. The optical flow map was computed with the smaller common region *S* bounded by the previous position of the MLC leaves instead of its newly expanded position. The details of the mathematical analysis are included in the supplementary materials.

5.2.3.1 Local optical flow analysis

In analyzing the local motions near the edges of the treatment field shown in figure 5.5(a), the optical flow map derived from tracking motion between two consecutive images was partitioned with vertical and horizontal grids near the edges, creating clusters of optical flow vectors. The number of columns of pixels (and corresponding vectors) in a cluster was determined from the width of an MLC leaf projected onto the EPID level. The EPID was placed at 140 cm from the source, resulting in a projected width of 3.5 mm for a 2.5 mm MLC leaf. With an EPID resolution of 0.391mm/pixel, a 9-pixel wide column corresponding to the width of the MLC leaf was used for each l cluster (figure 5.5). By varying the number of rows of pixels (and corresponding vectors) within a cluster, different motion estimates were obtained by taking the mean and standard deviation of the vectors bounded by the vertical and horizontal grids. The optimal number of rows of vectors was determined by comparing the estimated position with a known motion profile of the intruding OAR.

5.2.4 Algorithm for the adaptation of MLC based on intrusion of OAR

5.2.4.1 Tracking an intruding OAR

Assume that the initial treatment field planned without motion adaption is bounded by an initial MLC position *MLCpos*(*ref*) at one of the field edges. Any objects outside of the planned treatment field are assumed to be potential organs-at-risk (OARs). The intrusion of OARs into the treatment field, as observed in subsequent EPID images, would generate a set of positive optical flow vectors pointing inwardly towards the center of the treatment field (figure 5.5(a)). The irradiated field that observes the initial intrusion of the OAR would have its image frame number and MLC position indexed as k = 1 and *MLCpos*(*ref*) respectively. Further intrusion would result in the accumulation of the inter-frame displacements obtained from the mean local optical flow values $\widehat{OF}_L(k)$ (pixels) between image frame *k* and *k* +1, where *k* is the image frame counter when the OAR is present within the irradiated field (figure 5.5). The OAR position OAR_{In_BEV} can be expressed as:

$$OAR_{In\_BEV}(k) = \begin{cases} 0 & k = 1 \\ OAR_{In\_BEV}\,(k-1) + \widehat{OF}_L(k) & k > 1 \end{cases} \qquad \begin{matrix} (5.1a) \\ (5.1b) \end{matrix}$$

where $\widehat{OF}_L(k)$ and $OAR_{In\_BEV}(k)$ are defined as positive from the field edge in the direction pointing into the field.

As with any tracking method, position errors can accumulate. To minimize these errors, the position of the OAR was re-initialized for every image frame where the accumulated OAR position $OAR_{In\_BEV}(k)$ or MLC leaf position $MLCpos(k)$ was beyond the initial reference MLC leaf position *MLCpos*(*ref*).

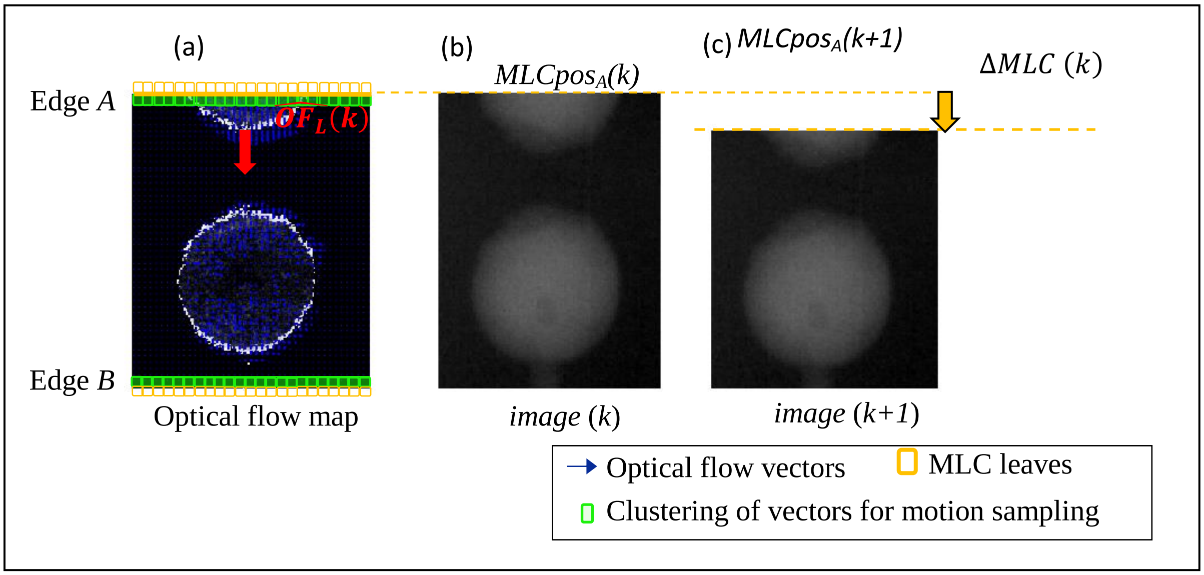

Figure 5.5 : Schematic diagram showing adaptation of MLC to shield the intruding object/OAR with (a) computation and detection of motion $\widehat{\boldsymbol{OF}_{\boldsymbol{L}}}(\boldsymbol{k})$ at the edges of an irradiated field and moving the MLC leaves from (b) $MLCpos_A(k)$ in image(k) to (c) $MLCpos_A(k+1)$ in image(k+1) with a displacement $\Delta \boldsymbol{MLC}(\boldsymbol{k})$. The MLC leaves are represented by a straight edge. Grids (green color) at the edges of the field correspond to the local motion sampling region for each MLC leaf.

5.2.4.2 One-frame prediction of OAR position and the placement of MLC

An idealized virtual DMLC system was assumed whereby the MLC leaves would adapt based on motion detected at the edges of the BEV. Delays due to image acquisition and motion computation typically encountered in practical systems were not considered in this study. The positioning of the MLC was based on the local motion $\widehat{OF_L}(k)$ between two prior, consecutive images, which served as a prediction of the OAR position in subsequent images (figure 5.4). This assumes that the motion of the intruding OAR does not change drastically so that the target can always be tracked. The predicted position of the intruding OAR was given by:

$$Predicted\ OAR_{In\_BEV}(k+1) = \ OAR_{In\_BEV}(k)\ \pm\ \widehat{OF}_L(k) \qquad k > 1 \tag{5.1}$$

where k, $\widehat{OF}_L(k)$ and $OAR_{In\_BEV}(k)$ are defined in equation (1). However, unlike tracking of the main target that is predominantly present in the irradiated field, intrusions at the edges have a relatively small mass to track over a short period of time. Instead of moving the MLCs to the predicted position of the OAR, spatial buffers were added to increase the area of OAR observed in the EPID image and therefore prevent losing track of the OAR (buffers illustrated in figure 5.4). Although a large buffer would ensure that the OAR can be tracked at all times, this would expose a larger portion of the OAR to unnecessary radiation. Hence, the size of the buffer is a trade-off between tracking the OAR versus exposing the OAR to unnecessary radiation. The design of the buffer takes into consideration (1) the OAR intruding slower than predicted (2) the OAR changing direction or (3) the OAR leaving the irradiated field faster than the predicted. The likelihood of losing track the OAR is highest during these three scenarios. The buffer for these three displacement regions, namely, the region with (1) positive displacements $(\widehat{OF}_L(k) > background)$; (2) near zero displacements $(\widehat{|OF_L(k)|} < background)$; and (3) negative displacements $(\widehat{OF}_L(k) < -background)$ were calculated as follows:

$$buffer(k+1) = \begin{cases} 1, & \widehat{OF}_L(k) >\ background \qquad \text{(5.2a)} \\ -background + 1, & \widehat{|OF_L(k)|} < background \qquad \text{(5.3b)} \\ -lookAhead\ buffer + 1, & \widehat{OF}_L(k) < -background \qquad \text{(5.3c)} \end{cases}$$

where the *lookAhead buffer* = 2 pixels and the background = 1/2 pixel (at EPID level), which is equivalent to 0.14 mm at the isocenter. The background was determined from the average value of the vectors obtained from two image frames where no motion was present. Both $\widehat{OF}_L(k)$ and $lookAhead\ buffer$ are defined as positive in the direction pointing inwards to the irradiated field from the respective field edges. Hence, the *-background* and *-lookAhead buffer* would expand the MLC leaves outward from the center of the treatment field. In addition to the buffers, one pixel was added to all three regions of displacement to compensate for the one row of missing motion vectors due to the non-symmetrical neighborhood encountered with a 3-by-3 pixel regularization at the edges of the optical flow map. This would leave the 'adaptive component' of the buffer, associated with the three displacement categories, at between 0 and 2 pixels. When the motion computed is larger than the *background* (i.e. OAR intruding towards the center of the irradiated field), the MLC was positioned with a buffer, defined by equation (5.2a), away from the center of the predicted OAR position. For the case when the local optical flow $\widehat{OF}_L(k)$ has a magnitude smaller than the *background*, the leaves will be positioned with a buffer defined by Eq. (5.2b) away from the predicted OAR position to anticipate for a possible change in direction of the intruding OAR. The *background* was used as a threshold to identify motion uncertainty. As the OAR moves away from the center of the irradiated field towards the field edge, a *lookAhead buffer* was added to the predicted position of the OAR (equation 5.3(c)), in order to avoid losing track of the OAR. This buffer allows the MLC to move faster than the predicted MLC motion. Although a consistent buffer following the one used for negative displacement (three pixels) can be utilized throughout for all the regions, smaller buffers used in the other displacement categories were found to reduce exposure to the OAR while maintaining continual tracking. The MLC leaves (see figure 5.2) are defined in the following manner:

$$MLCpos_A(k) > MLCpos_B(k) \tag{5.3}$$

and the MLC leaves were positioned according to:

$$MLCpos_A(k+1) = Predicted\ OAR_{In\_BEV}(k+1) - buffer(k+1) \tag{5.5a}$$

$$MLCpos_B(\ k+1) = \ Predicted\ OAR_{In\_BEV}(k+1)\ + buffer(k+1) \tag{5.5b}$$

where $MLCpos_{A,B}(k)$ adheres to the standard geometrical definition given by [40].

To prevent the MLC from tracking an OAR past the planned MLC position (i.e. when the OAR is leaving the field), a limit which prevented tracking beyond the initial reference position was imposed. When the calculated positions of the leaves are beyond their initial reference position (*MLCpos*(*ref*) in image k = 1), the MLC positions at the respective edges (*Edges A and B*, refer to figure 5.5 (a)) will be reset to their original positions, i.e.

$$MLCpos_{A,B}(k) = \ MLCpos_{A,B}(ref) \tag{5.6}$$

5.2.5 Simulation and measurement setup

5.2.5.1 Determine optimal vector cluster size with sinusoidal motion tracking

In the experimental setup, CT images from the lung tumor of Patient #64 of the Lung Image Database Consortium [41] were used to create a 3D tumor (figure 5.6 (a)). The 3D printed tumor, fabricated with Acrylonitrile Butadiene Styrene (ABS) material, has a mass of 8.1 ± 0.1 g, a diameter ranging from 25.5 ± 0.5 mm to 28.5± 0.5 mm and a volume of 9.2 cm^3 (using an average radius of 13 mm). The 3D printed tumor (figure 5.6 (c)) was attached to the linear actuator of a Radiology Support Devices RS-1500 Breathing Phantom and placed at a distance of 100 cm from the source. It was programmed to move with an asymmetrical cosine function having a maximum displacement of 10 mm in the superior-inferior (SI) direction and a maximum velocity of 10 mm/s as previously described [30, 31]. The National Instrument LabView software package and USB-6009 Data Acquisition Suite were used to control the motion characteristics of the linear actuator. A second LabView interface was used to measure the resistance of the attached potentiometer (figure 5.6) which was linearly proportional to the extension of the actuator arm. The target was irradiated using a Varian 2100iX Clinac, 6 MV beam at a dose rate of 600 MU/min with a field size of 9.1 cm by 8.2 cm (i.e. at the isocenter). The field size corresponds to an irradiated area of 12.7 cm by 11.5 cm at the EPID (140 cm from the source). About 200 sequential EPID images, each with an image resolution of 0.391mm/pixel, were acquired at a frame rate of 7.5 frames/s. The motion detected with the optical flow algorithm, i.e. $\widehat{OF}_L(k)$, was converted from pixels/frame to mm for comparison with the position recorded by the potentiometer. Optical flow algorithms with a regularization of 3-by-3 pixels and 9-by-9 pixels were used to compute the motion vectors. A parametric study to determine the optimal cluster size of local vectors was performed at the edges of the field.

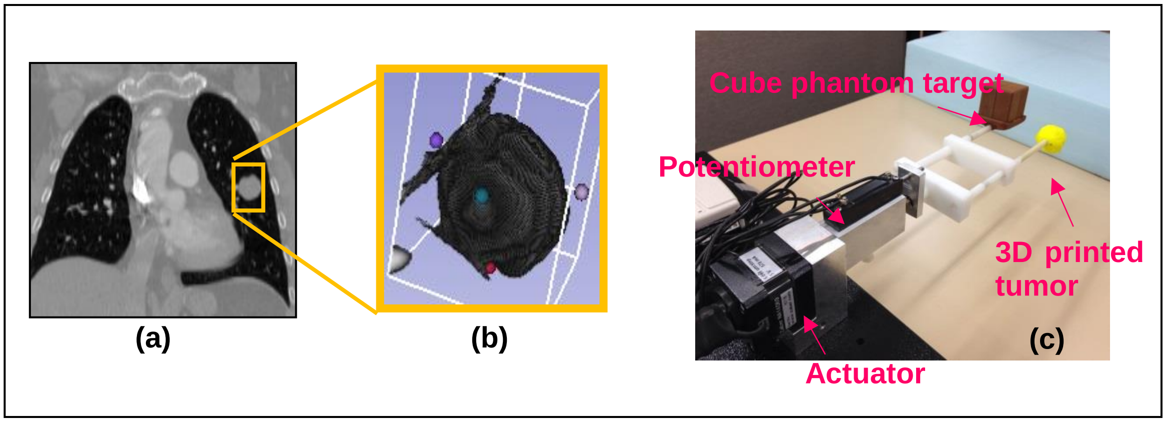

Figure 5.6 : (a) Coronal view of the volumetric CT data set of Patient 64 from the LIDC-IDRI database; (b) corresponding tumor volume for 3D printing, and c) setup for MV beam irradiation.

5.2.5.2 Simulation of the intrusion of an OAR into an irradiated field

Since the lung phantom only supported moving the tumor target, OAR motion intruding into the treatment field was simulated using image processing techniques. These techniques will be described in this section (figure 5.7). For the case of the asymmetrical cosine motion, a smaller window of 7.4 cm by 5.5 cm (about 265 pixels by 197 pixels with EPID @140 cm from source) encompassing the motion of the target was cropped from the radiated region to approximate the field size of a conformal field treatment. A duplicate of this cropped image sequence was flipped and concatenated to the original such that the two targets traveled in the opposite direction with the same velocity (figure 5.7). A new irradiated field was created that included the concatenated image in such a way that the duplicated target would intrude periodically into the field synchronously with the original target motion. In this way, the accuracy of tracking the intrusion was estimated by comparing the computed motion at the beam edges with the motion of the tumor measured by the potentiometer.

In this study, a rectangular field was assumed. This rectangular field was bound by virtual MLC leaves aligned in parallel to the direction of the main target motion. The image width of 197 pixels (with EPID @140 cm from source) was bound by 22 MLC leaves each having a width of 2.5 mm (i.e. 9 pixels). In our previous study [31], a cube phantom was used for both the target and the intruding object. Since the intruding object had a straight edge, the motion detected at the edge of each of these MLC leaves was expected to be similar. Thus, motion analysis was performed at the edge of only one of the MLC leaves (i.e. the center leaf along the field edge), and this representative motion was used to adapt the entire field edge consisting of all the individual MLC leaves (figure 5.5). Future implementation beyond this proof-of-concept study will have the individual leaves conformed around the 3D patient tumor, and subsequent local adaptations will be performed using individual leaves.

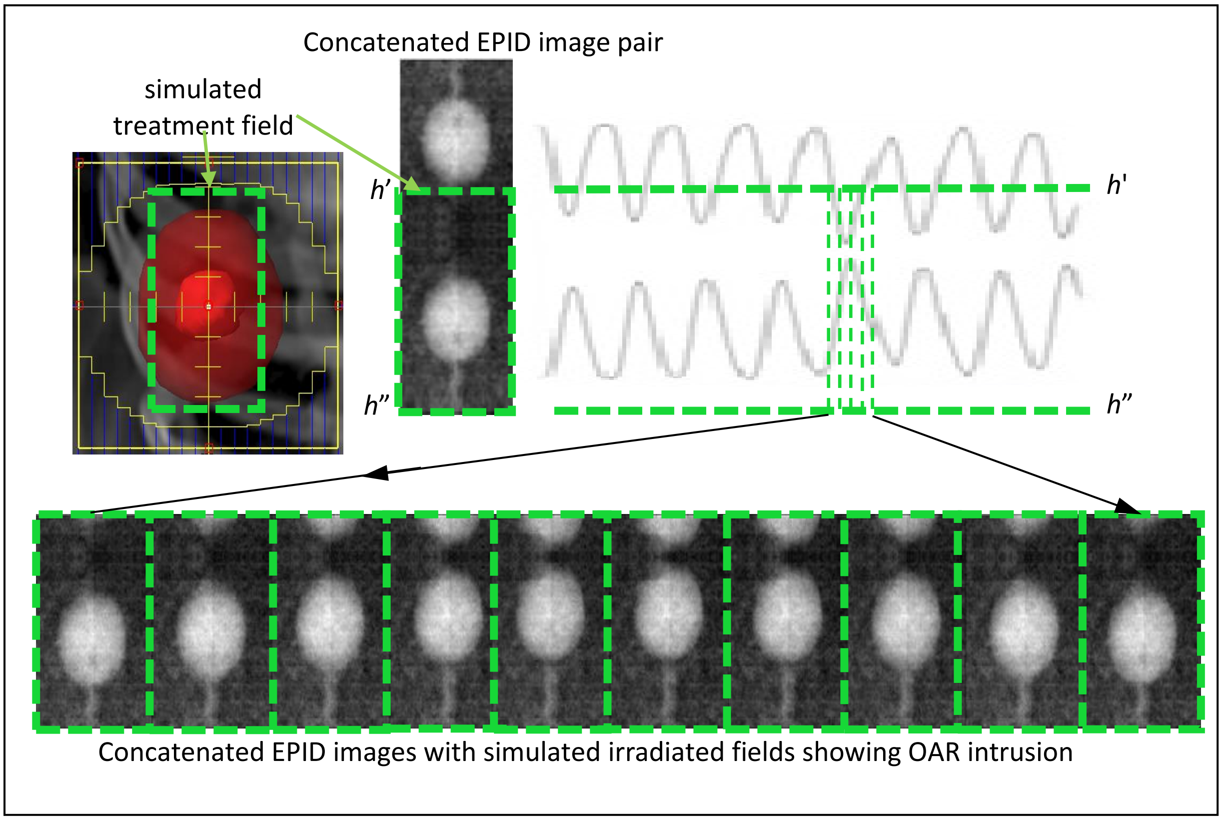

Figure 5.7 : Simulation of an OAR intruding at the edges of the irradiated fields.

With a fixed column width of 9 pixels to emulate an actual 2.5 mm MLC leaf width, the number of rows of pixels between horizontal grids was varied to determine the optimal cluster size of vectors for tracking intrusion at the edges. By averaging the differences between the computed and potentiometer results across the entire motion trajectory (intrusion and retraction), mean tracking errors for each cluster size were obtained.

The adaptation of the virtual MLC leaves and hence the changes in the field edges were simulated by updating the cropped region of the image matrix. However, since the optical flow vector provides sub-pixel motion detection, the edges of the cropped region might not necessarily align to a pixel. This limitation in our simulation was overcome by expanding the cropped image region to the nearest pixel away from the field center.

5.2.5.3 Evaluation of the robustness of the algorithm with patient data

The 3D printed tumor (figure 6(c)), attached to the linear actuator, was programmed to move according to five patients' tumor motions obtained from the CyberKnife Synchrony (CKS) dataset [42]. About 200 EPID images were acquired for each patient's trace. Duplicated sets of the image were rotated and concatenated with the original sequence to simulate the intrusion of a circular structure into the irradiated field. A similar window width of 5.5 cm and a length encompassing the respective tumor motion of each patient trace was cropped from each image to simulate the radiation field size.

5.3 Results

5.3.1 Optimal cluster size of vectors for intrusion detection with MLC adaptation

Figure 5.8 depicts the mean position errors with one standard deviation obtained with different cluster sizes (i.e. different number of rows in the cluster region) for computing optical flow vectors at the field edge. Since the possibility of losing track of an intruding OAR is large when the intruding OAR changes its direction (i.e. at maximum intrusion), the errors at this location (maximum intrusion) were plotted to evaluate the robustness of the buffer size chosen. The intruding OAR was moving according to an asymmetrical cosine function. Figure 5.8 (a) and figure 5.8 (b) depicts the results obtained with 3-by-3 and 9-by-9 regularization in the optical flow computation respectively. The position errors obtained with 3-by-3 regularization remain relatively stable for a range of row cluster sizes (from seven to thirteen rows) as compared to the results using a 9-by-9 regularization (figure 5.8 (b)). Smaller errors were obtained using the 3-by-3 regularization due to fewer missing rows of vectors at the edge of the optical flow map. From figure 5.8 (a), a minimal mean position error of 0.0 ± 0.4 mm was obtained for a cluster size of nine rows of pixels. Hence, cluster sizes of nine rows of vectors together with an optical flow regularization of 3-by-3 pixels were used to optimize local motion analysis.

5.3.2 Tracking accuracies for a simulated OAR moving with an asymmetrical cosine function representing average tumor motion

Figure 5.9 (a) plots the actual (obtained from the potentiometer) and computed inter-frame displacements (i.e. velocities) of the intruding OAR moving in an asymmetrical cosine pattern. Results were obtained using an optical flow algorithm with a 3-by-3 pixels regularization and a local cluster of 10 rows by 9 columns of vectors. Integrating the displacements over time provides the actual and computed positions of the intruding OAR shown in figure 5.9 (b). The updating of the MLC leaf positions was assumed to be instantaneous, and the MLC positions (averaged over five positions samples) are plotted in figure 5.9 (b) for comparison. These positions are plotted with zero magnitude representing the initial reference MLC leaf position *MLCpos*(*ref*) that detects the first incidence of intrusion into the field. Figure 5.9 (c) plots the differences between the computed OAR position and the MLC position with respect to the actual position of the intruding OAR obtained from the potentiometer. From figure 5.9 (b) and figure 5.9 (c), it is observed that in most cases, the MLC positions are further away from the actual and computed OAR positions. The difference in position is expected since a buffer was incorporated in the algorithm to prevent losing track of the OAR. Table 1 provides a summary of the differences observed in figure 5.9 (c). The computed OAR positions have an average absolute difference of about

0.3 mm while a larger difference of 0.6 mm, due to the use of a buffer, is observed for the MLC position when compared to the actual OAR position measured by the potentiometer. The negative, mean errors of -0.1 ± 0.3, -0.1 ± 0.4 and -0.5 ± 0.6 indicate that on average, the computed, predicted and MLC leaf positions are trailing behind the actual position (i.e. measured by a potentiometer) of the intruding OAR, as measured with respect to *MLCpos*(*ref*).

Figure 5.10 compares the correlation between the computed OAR positions with a) actual position (given by the potentiometer) of the intruding OAR (figure 5.10 (a) and (b)) predicted OAR position (figure 5.10 (b), and (c)) MLC positions (figure 5.10 (c)). For case (a), the linear regression depicts a slope of 1.06 bounded by (1.05, 1.08) 95% prediction interval and a negative offset of -0.17 mm bounded by 95% prediction interval of (-0.22, -0.11) mm. For case (b), the slope reduces to 1.03 (1.02, 1.05) with an offset of -0.12 (-0.22, - 0.04), and for case (c), a slope of 0.98 (0.96, 1.00) with an offset of -0.4 (-0.50, -0.29) depicts the linear regression between the MLC leaf positions and the computed OAR positons. The larger RMSE in figure 5.10 (c) is attributed to the buffer added to the predicted motion of the OAR.

The histogram in Figure 5.11 provides a breakdown of the position errors (computed - actual position of OAR) for three different velocity ranges of the computed OAR velocities: a) negative, i.e. the intruded OAR retracts away from the center of the irradiated field with $\widehat{OF}_L(k)$ < -0.1 mm/s; (b) zero, i.e. $|\widehat{OF}_L(k)|$ < 0.1 mm/s; and (c) positive, i.e. OAR intrudes towards the center of the irradiated field with $\widehat{OF}_L(k)$ > 0.1 mm/s. With negative velocities (figure 5.11 (a)), the position errors are mostly negative (i.e. the computed position under-estimates the actual position). Since position errors are measured with respect to the initial reference position *MLCpos*(*ref*), negative errors imply that the actual positions of the OAR are further into the irradiated field than its computed positions during retraction. With positive velocities (figure 5.11 (c)), both negative and positive errors will occur.

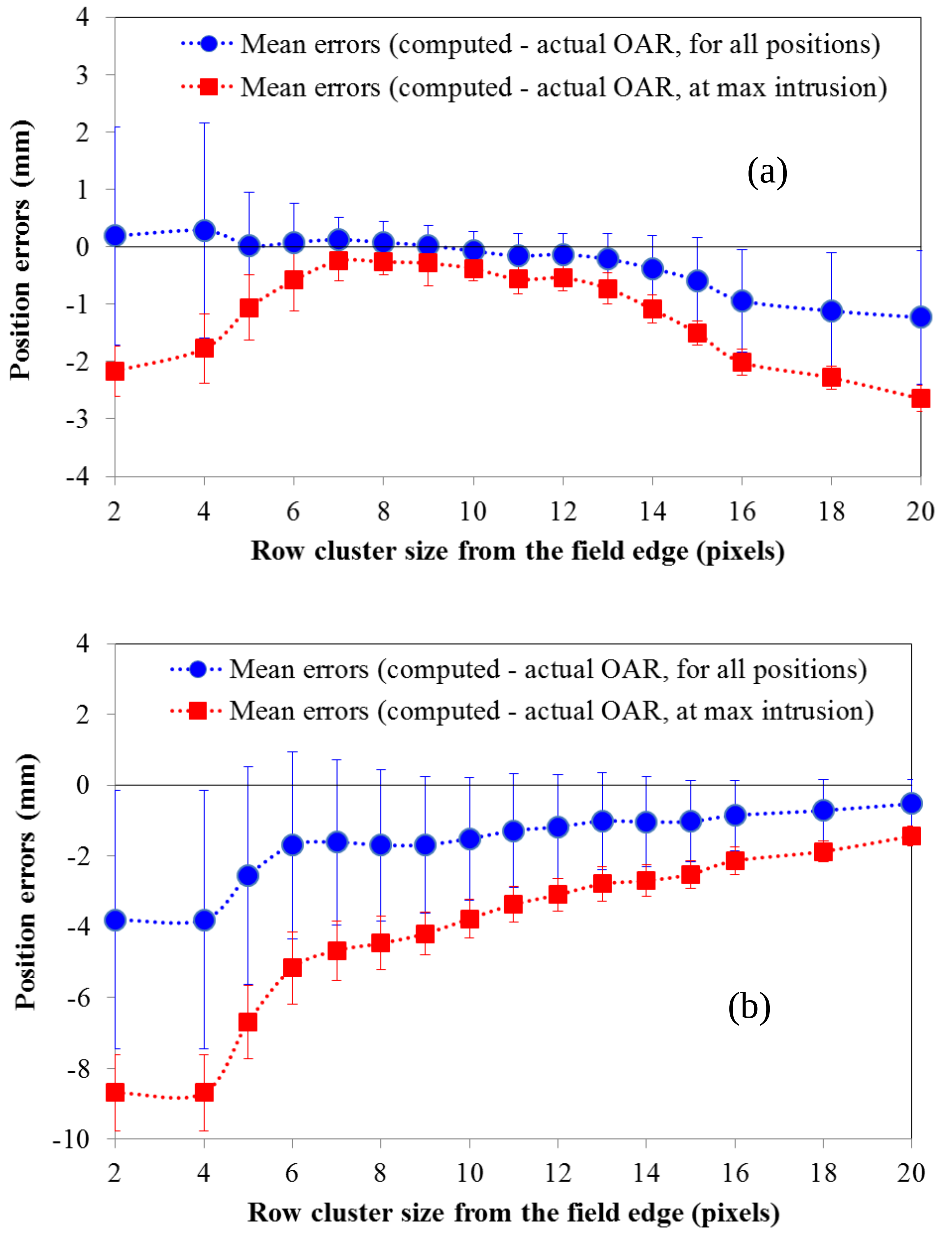

Figure 5.8 : Mean position errors with one standard deviation obtained with different cluster sizes (i.e., numbers of rows from the field edge) for optical flow vector analysis. (a) 3-by-3 and (b) 9-by-9 pixel regularization were employed for the optical flow computation. As the OAR phantom intrudes with varying inter-frame displacements, the MLC leaves were adapted accordingly. Differences (errors) between the computed (tracked) and the actual position of the OAR phantom were obtained. By averaging the errors from all the images across the entire motion trajectory (intrusion and retraction), mean errors for each cluster size were obtained.

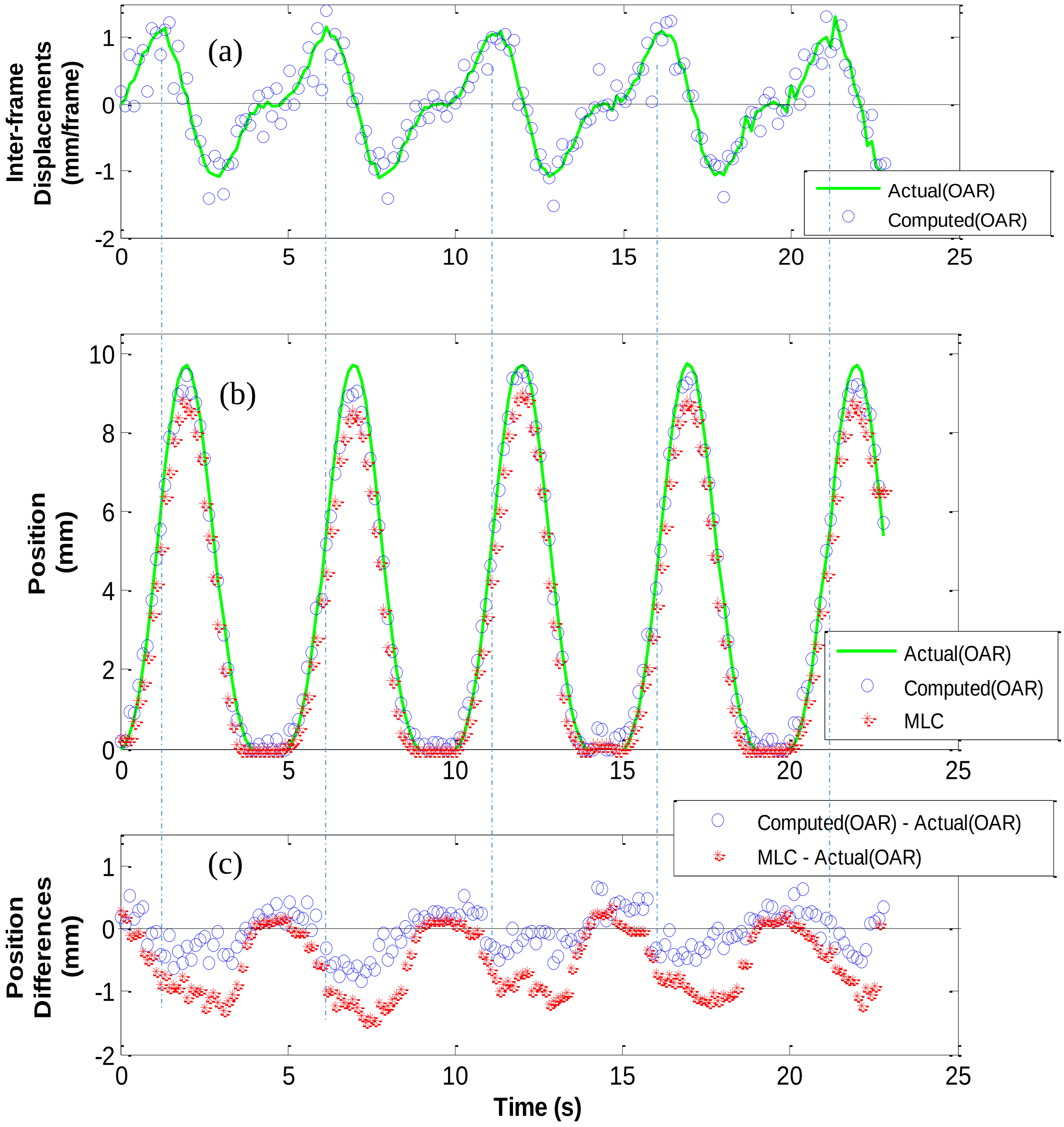

Figure 5.9 : Comparison of the actual (from the potentiometer) and computed (a) inter-frame displacements and (b) position of the intruding OAR. The position of the MLC, assuming instantaneous adaptation, is included in (b). (c) The plot of the differences between the computed OAR and MLC positions with respect to the actual OAR positions. The relationship between the approximate onset of negative position difference and the maximum inter-frame displacement in each cycle are shown by the vertical dash lines drawn at locations where maximum inter-frame displacement is encountered.

Table 5.1 : Summary of the distribution of differences (compared to the actual OAR motion) obtained in the benchmarking process of tracking intrusion moving according to a mathematical function representing average patient tumor motion.

Differences	Mean absolute	Mean	25 percentile	Median	75 percentile
Inter-frame displacement (computed - actual OAR, mm/frame)	0.2 ± 0.1	0.0 ± 0.2	- 0.1	0.0	0. 15
Position (computed – actual OAR, mm)	0.3 ± 0.2	- 0.1 ± 0.3	- 0.3	- 0.1	0. 2
Position (MLC – actual OAR, mm)	0.6 ± 0.5	- 0.5 ± 0.6	- 0.9	- 0.5	0.0

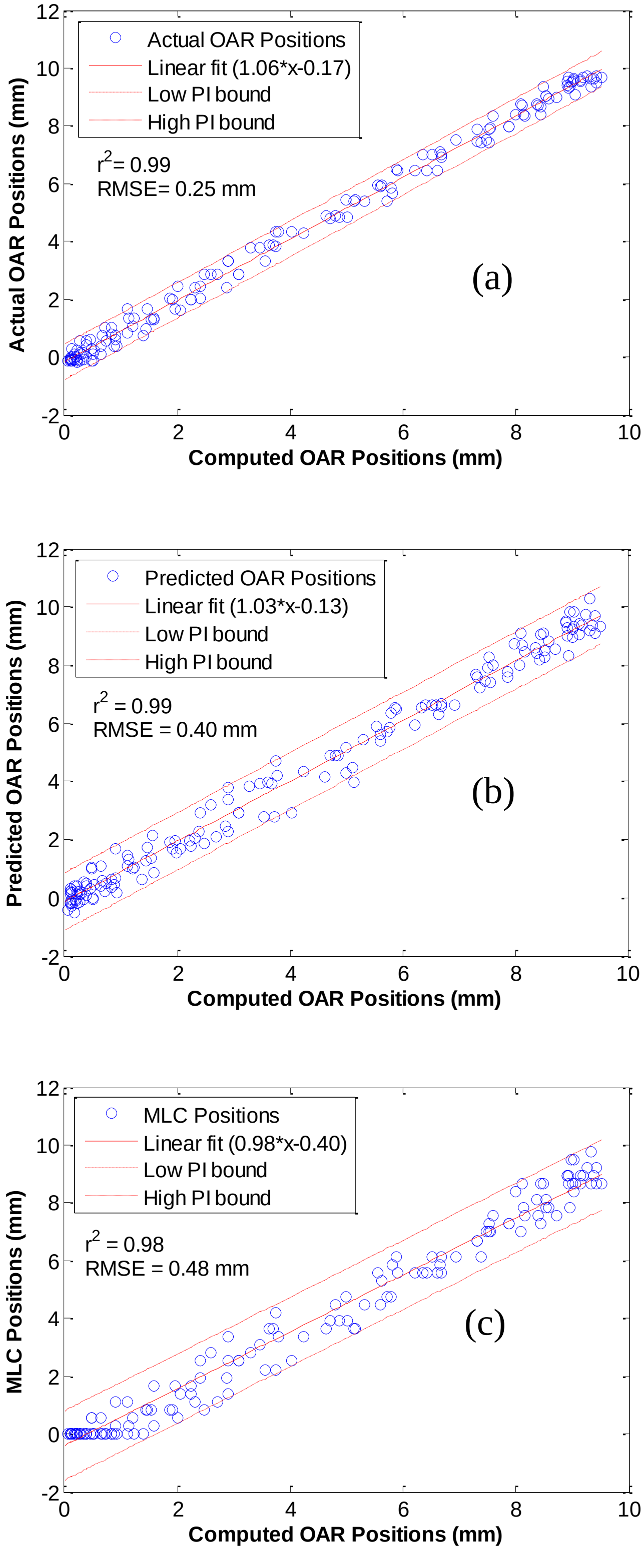

Figure 5.10 : Linear regression plot showing the correlation between the computed OAR positions with a) the actual OAR, b) predicted OAR and c) MLC leaf positions.

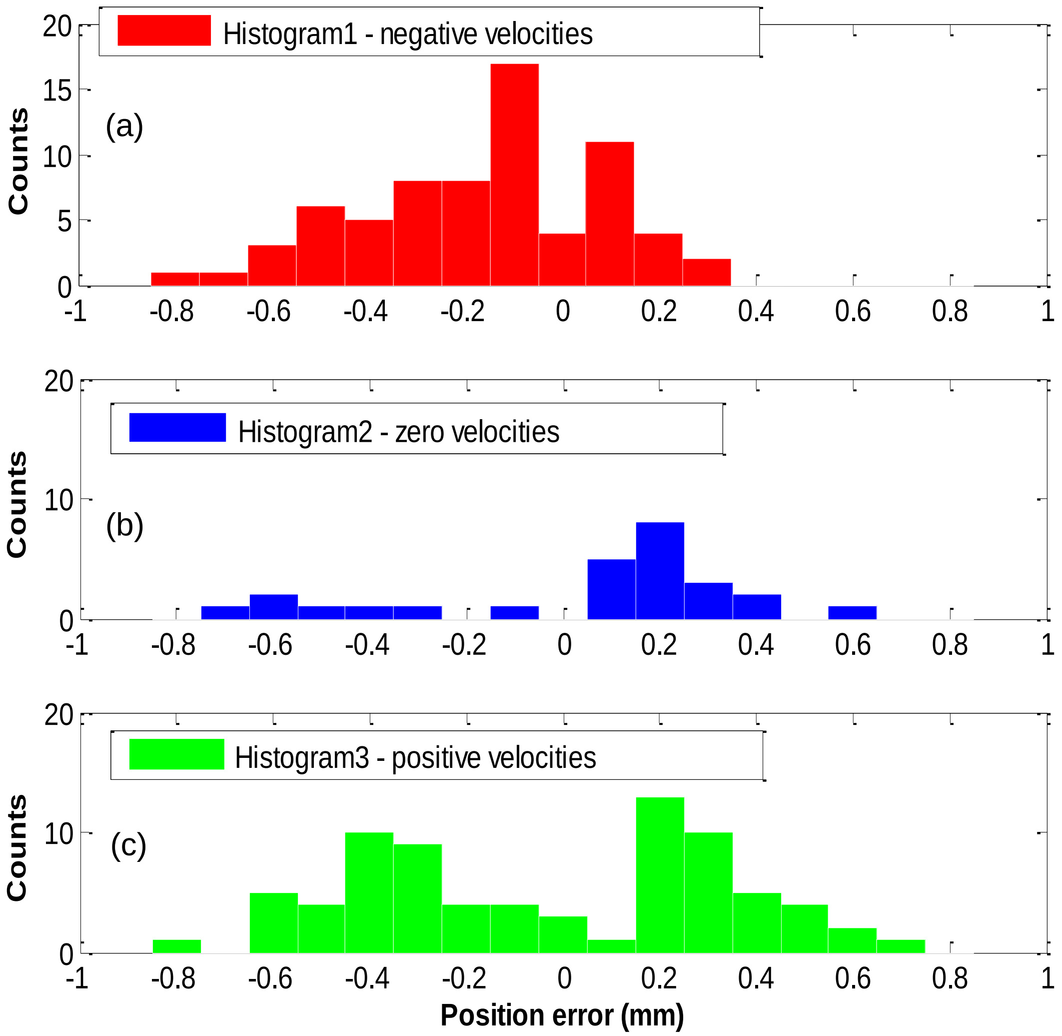

Figure 5.11 : Histograms of position errors (computed- actual position of OAR) for three computed velocity ranges of the OAR: (a) negative i.e. $\widehat{\boldsymbol{OF_L}}(\boldsymbol{k})$ (mm/s) < -0.1 mm/s; (b) zero, i.e. $|\widehat{\boldsymbol{OF_L}}(\boldsymbol{k})|$ < 0.1 mm/s; and (c) positive, i.e. $\widehat{\boldsymbol{OF_L}}(\boldsymbol{k})$ > 0.1 mm/s.

5.3.3 Accuracies of tracking an OAR intruding with patient tumor motions

Since a strong correlation was observed between the computed OAR and MLC positions, subsequent analysis was performed only on the tracking accuracy of the OAR. Figure 5.12 plots the actual position, computed position, and differences (i.e. error) when tracking an external

OAR intruding into the simulated irradiated field following the tumor motions of five lung cancer patients. As observed from patients 2, 4 and 5, the error increases when the intrusion is at its maximum, i.e. during the transition between intrusion into the irradiated field and retracting towards the field edge. Overall, the largest error was observed from Patient 2 whereby in addition to the spikes in the tracking error in the 3rd and 7th cycle, consistent position error at the end of the retraction phase contributes to drift in the tracking. The distributions of the tracking errors for all the patients are compared in the boxplots shown in figure 5.13 and a summary is provided in table 5.2. The higher frequency of motion exhibited by patients 1 and 2 resulted in a larger average and a wider distribution of position errors compared to the lower frequency motion exhibited by patients 3, 4 and 5. An overall tracking accuracy of -0.4 ± 0.3 mm was obtained by taking the average and one standard deviation of the position errors of all the patient data. By normalizing the offset of all the mean position errors and selecting the central 68th percentile of the entire error distribution, a precision of 1.1 mm is obtained with the proposed method of tracking intrusions. The negative mean position errors observed in all patients indicate, on average, the method underestimates the computed positions.

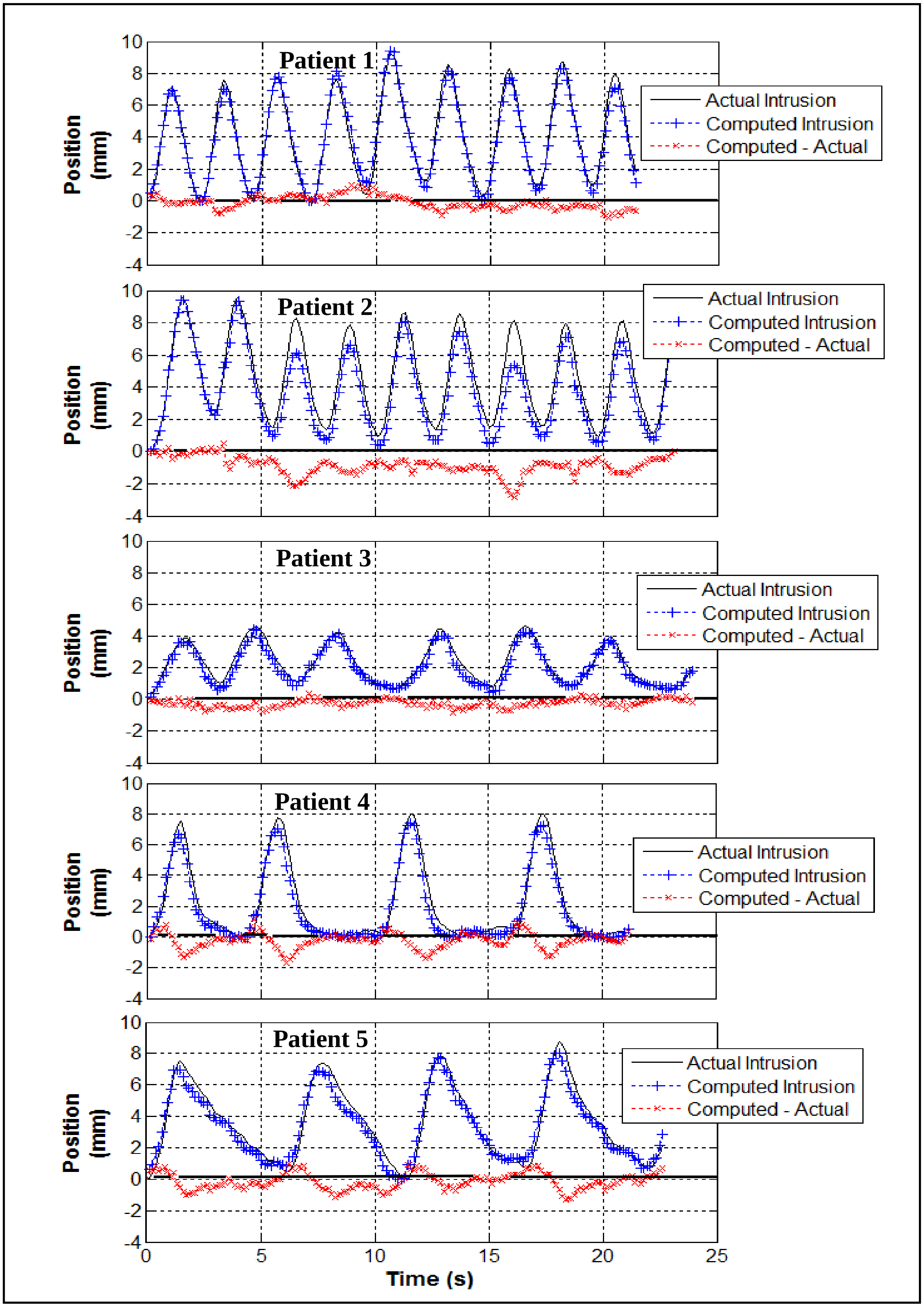

Figure 5.12 : Actual and computed (i.e. tracked) trajectory of external object/OAR intruding into the BEV following the tumor motions of five lung cancer patients.

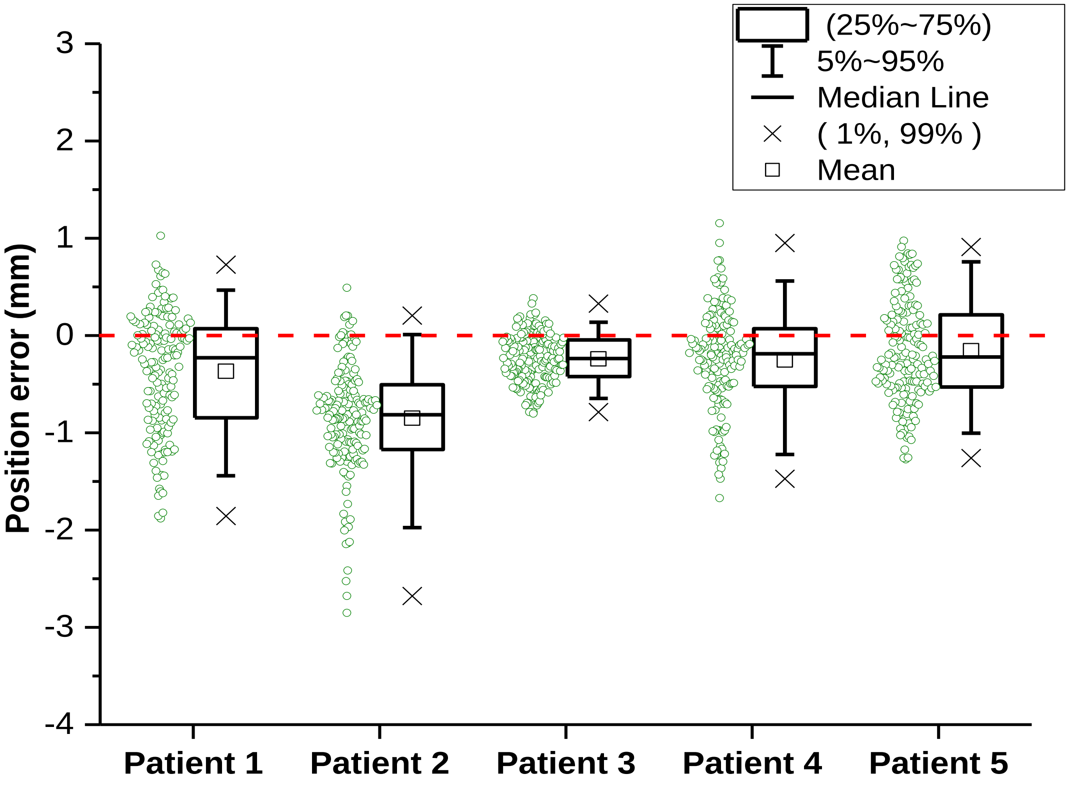

Figure 5.13 : Boxplot shows the distribution of position errors incurred from tracking a simulated OAR intruding into the radiation field following the tumor motions of five lung cancer patients.

Table 5.2 : Summary of the position errors (computed-actual) obtained from tracking a curved-edge structure/OAR intruding the intruding into the radiation field with patient tumor motions.

Error Statistics (mm)	Patient 1	Patient 2	Patient 3	Patient 4	Patient 5
Mean	-0.4	-0.9	-0.2	-0.3	-0.2
Std. dev.	0.6	0.6	0.3	0.5	0.5
25th percentile	-0.8	-1.2	-0.4	-0.5	-0.5
Median	-0.2	-0.8	-0.2	-0.2	-0.2
75th percentile	0.1	-0.5	0.0	0.1	0.2
Max. absolute	1.9	2.9	0.8	1.7	1.3
	All patients				
Accuracy (mm)	-0.4 ± 0.3				
Precision (mm)	1.1				

5.4 Discussions

Figure 5.8(a) and figure 5.8(b) show that 3-by-3 pixel regularization resulted in smaller errors than 9-by-9 pixel regularization. The smaller errors were a result of the smaller number of missing rows of vectors at the edges of the irradiated field when 3-by-3 pixel regularization was used. Although 9-by-9 regularization was previously shown to provide reliable global tracking of the main target [30, 31], for local detection and tracking of intrusions at the edges, smaller regularization yields greater accuracy. In a practical implementation, parallel computation of the optical flow using two different regularization schemes could be applied to global tracking of the main target and local tracking at the edges of the irradiated field.

From table 5.1, a mean absolute difference of 0.6 mm was obtained when comparing the MLC positions with the actual OAR positions. This error encompasses both tracking and prediction error of 0.3 mm. The remaining errors would have been attributed to the differences between the MLC positions and the actual OAR positions.

The linear regression plots in figure 5.10(b) and 5.10(c) have offsets of 0.13 mm and 0.40 mm in the correlation of the predicted OAR position and MLC position with respect to the computed OAR positions, respectively. The difference in the offsets is about 0.3 mm. This offset seems consistent with the single row of pixels (0.28 mm) used in the non-adaptive buffer to compensate for the missing row of vectors at the edge of the field. Comparing figures 5.9 (a), 5.9 (b) and 5.9 (c), the computed OAR position starts to under-estimate its actual position near the peak of the inter-frame displacement during the intrusion phase (i.e. positive displacement). Under-estimation implies that the computed OAR position intrudes less inwardly into the irradiated field, i.e. located nearer to the initial MLC edge *MLCpos*(*ref*). Since position errors (computed –

actual OAR positions) are measured with respect to the initial reference position *MLCpos*(*ref*), negative errors would have been incurred. Hence, during the intrusion phase, a combination of positive (before the peak of displacement) and negative position errors are observed in figure 5.11 (a). Under-estimation would peak at the positions where the intrusion is at its maximum as observed in figure 5.9 (b). The accumulation of the position errors in the retraction phase causes the computed position of the OAR to be nearer to *MLCpos*(*ref*), thereby increasing the negative position errors as supported by the histogram shown in figure 5.11 (a). The accumulation of position errors would account for the difference in the error distributions between figure 5.11 (a) and 5.11 (c).

As a result of momentarily losing track of the OAR during intrusion (i.e. positive displacements (figure 5.9(a)), instances of zero displacement, are observed during. The impact of tracking during intrusion is minimal as compared to losing track when the OAR retracts and exits the radiation field. The lesser impact (during intrusion) is due to the fact when a zero displacement is detected momentarily during the intrusion, the algorithm is designed to retract the MLC leaves and expand the analysis region with an added buffer (equation 5.2(b)), so as to re-capture the frontal edge of the intruding structure in the irradiated field. Furthermore, the probability of the intruding structure making an abrupt reversal is small versus a gradual transition. In most cases, as long as the OAR continues to intrude into the irradiated field, it (i.e. the OAR) will appear in the subsequent image frame. However, during retraction, any increase in velocity compared to the velocity predicted from previous images could potentially see the MLC adapting less than the motion of the retracting structure (i.e. the edge of the partially intruded OAR), thereby losing track of it. For these reasons, different buffers were applied when tracking an intruding versus a retracting OAR. Ultimately, the buffer size is a trade-off between the amount of healthy tissue/OAR exposed to radiation and the need to maintain constant tracking of the intruding OAR. To maintain tracking of the OAR, a buffer with two rows of pixels was initially implemented for both intrusion and retraction of OAR. However, since the impact of losing track during intrusion is minimal, the buffer size was reduced to one row of pixels with the benefits of shielding more, healthy tissue.

When compared to the tracking of the global motion of the main target [28], similar limitations of the algorithm exist when tracking high velocities. The uncertainty in tracking at the edges is greater than when tracking a central tumor (0.3 ± 0.3 mm vs. 0.2 ± 0.2 mm). The inaccuracies in tracking the OAR may be attributed to the use of a 3-by-3 pixel regularization in the current optical flow algorithm and the need to add buffers to prevent losing track of the OAR. The buffers cause the MLC leaves to move either behind or ahead of the OAR during intrusion and retraction respectively. As a result, sampling of the local motion vectors at the edges of the MLC leaves might not coincide with frontal edges of the OAR where contrast is high. The motion vectors could have been sampled from the homogeneous region of the OAR where their magnitudes are less reliable [30].

The above analysis of the limitations and accuracies of the algorithm was performed in the benchmarking process with a sinusoidal motion. Extending the work to track to track more realistic motion using patient traces provides verification of the robustness of the algorithm for tracking motion with different characteristics. From the results of the patient studies shown in figure 5.12 and table 5.2, the higher frequency motions exhibited by patients 1 and 2 incur a larger average position error compared to the lower frequency motions exhibited by patients 3, 4 and 5. For higher frequency motion the number of intrusions is higher and as a result, there is a higher chance of incurring errors compared to the low-frequency motions with fewer intrusions.

This scenario is different from that of tracking the global motion where the target is always present in the image. For global tracking, the higher frequency motions are observed to incur smaller position errors [30].

In analyzing the spikes in the tracking errors observed during the 3rd and 7th breathing cycle of patient 2 (refer figure 5.12), the presence of banding artifacts was observed at the edge of the affected images. Banding artifacts are stripes of light and dark regions spanning across the entire width of an EPID image and are due to the interaction between the irradiation pulses and the EPID image readout [43]. The fluctuation in intensity violates one of the assumptions of the optical flow algorithm for accurate tracking. The variations in image quality can pose a challenge for local motion analysis that monitors over a small region of interest. Possible solutions include 1) incorporating methods to handle banding artifacts [43] and 2) tracking with robust SIFT features [28] instead of using the intensity-based optical flow algorithm.

The tracking errors would have a minimal impact on the dosimetry of the main target. As shown in the benchmarking study of tracking the sinusoidal motion, any over-estimation would result in momentary loss of tracking, which prevents the MLC leaves from advancing further than the OAR. Any under-estimation of the motion would imply that a portion of the intruding OAR would not be shielded. Overall, the potential benefits of adapting the MLC to shield the OAR would outweigh the impact of the associated error (about 1 mm).

In this study, the intrusions were simulated with motions represented by tumor trajectories. These intrusions emulate either 1) a stationary OAR intruding into the treatment field that is following the motion of a tumor, or 2) a moving OAR that is intruding into the irradiated field periodically. The intrusions at the field edges were simulated with a non-overlapping intruding

OAR. However, in practical situations, the OAR could intrude and overlap with either the target or the margins required for effective treatment. Continuous adaptation to shield the intruding OAR could encroach into the treatment regions that could compromise local tumor control probability (TCP). It is envisioned that a weighting between treating the main target and the amount of adaptation required to avoid the OAR would be needed, which itself warrants a separate study. However, preliminary works of adapting the beam to different margins during treatments have already been proposed [44, 45]. Since the local adaptations could introduce deviations to the treatment delivery compared to the treatment plans, its dosimetric impact, and treatment outcome would require further detailed studies.

Although MV images have been known to suffer from low contrast, the accuracy of tracking motions with images of clinical contrast-to-noise ratio have been studied and could be accounted for in practical applications [30]. As long as there is motion in the image, the optical flow algorithm, which provides pixel-by-pixel motion estimation, has been known to detect the "structure from motion" [46], despite the low contrast. Alternatively, our proposed method can be used to track motions of implanted seeds that have a higher contrast.

An ideal dynamic MLC system was assumed whereby the MLC leaves would adapt to every subsequent image. For practical realization, mechanical constraints of the MLC leaf, delay due to image processing and acquisition, and optimization and fitting of the MLC leaves to conform to the shape and dosimetric plan of the target have to be factored into the system [47-50].

Without adapting the MLC leaves, the intrusion detection mechanism itself can be applied to provide intra-fraction verification of unintended exposure of healthy tissues/OAR to radiation during treatment. Further tracking of the intrusion could provide the duration and the cumulative radiation dose of each unintended exposure. Another alternative application could be to use the OAR tracking as a real-time safety monitoring method, whereby the treatment is terminated when an unplanned intrusion is observed. With treatment such as VMAT and IMRT, a potential method of treatment verification involves comparing the treatment images with the DRR of the planned treatment field [51]. Following this technique, structures that intrude into the treatment field at the edges will be detected by our proposed method when making a comparison with the planned treatment field. Subsequent adaption of the field edges could be pursued for real-time rectification.

This work focuses on detecting local motions at the edges and adapting the MLC leaves accordingly. Tracking of the global motion due to the main target has been well studied by other research groups [2-8], as well as in our previous work [30] and hence, has not been repeated in this paper. We have demonstrated the capability of the algorithm in tracking rigid-body objects intruding with clinically realistic velocities and motion profiles using data from five patients, and a simple rectangular treatment field bound by a bank of MLC leaves on a straight edge. The next logical step would be to track both the global motion of the main target as well as intrusions at the edges of a clinical treatment field instead of the simulated rectangular field. With a smaller field size, it would be interesting to compare the difference between the global and local motions at the edges. A complete solution that combines an adaptive aperture [2-4] (i.e. adapting the leaves according to the global motion) with local correction at the edges to avoid OAR intrusion (i.e. the work presented here) is also currently being studied and will be reported in the future. The results are promising and to the best of our knowledge, this is a first attempt to determine local motion at the edge of an irradiated field, in particularly, to track a partially intruding OAR next to an MLC leaf's edge and adapt the leaf according to the motion detected.

5.5 Conclusions

The ability to detect and adapt the treatment field based on motions observed at the edges of an irradiated field has been demonstrated. The optical flow algorithm was optimized using 3-by-3 pixel regularization, a cluster of 9 rows by 9 columns of local vectors and a control algorithm with one-frame prediction and buffers. A virtual DMLC system was used to evaluate how closely an MLC could follow the tumor motion. In the benchmarking process (i.e. OAR moving according to a mathematical function), the average absolute position error of 0.3 mm was obtained in tracking intrusions with a maximum velocity of 10 mm/s and a maximum displacement of 10 mm representing average clinical tumor motion. A strong correlation ($r^2 \geq 0.98$) was observed between the MLC leaves and computed OAR positions. The algorithm was further evaluated using realistic motions obtained from five lung cancer patients. A mean position tracking error of -0.4 ± 0.3 mm and a precision of 1.1 mm were obtained when tracking the intrusion while adapting the MLC leaves to spare the OAR. These errors are small in comparison to the typical organ motion while limiting the exposure of the OAR to less than 0.5 mm.

This preliminary proof-of-concept study unveils a unique tool that would allow for (1) intra-fraction monitoring and detection of motion and potential OAR intrusion at the field edges and (2) adaptation of MLC leaves based on the motion detected. Challenges of local motion tracking using a small region of optical flow vectors have been highlighted. The proposed local adaptation technique would be an attractive feature to supplement systems tracking the main target motion.

References

1. American Association of Physicists in Medicine (AAPM), Radiation Therapy Committee, Task Group 76. The Management of Respiratory Motion in Radiation Oncology. Report No. 91. Madison (WI) (2006).

2. P. Keall, V. Kini, S. Vedam and R. Mohan, “Motion adaptive x-ray therapy: a feasibility study”, Phys. Med. Biol. 46, 1–10 (2001).

3. P. Keall, H. Cattell, D. Pokhrel, S. Dieterich, K.H. Wong, M. J. Murphy, S. Vedam, K. Wijesooriya and R. Mohan, “Geometric accuracy of a real-time target tracking system with dynamic multileaf collimator tracking system”, Int. J. Radiat. Oncol. Biol. Phys. 65, 1579–1584 (2006).

4. J. R. McClelland, S. Webb, D. McQuaid, D. M. Binnie and D. J. Hawkes, “Tracking ‘differential organ motion’ with a ‘breathing' multileaf collimator: magnitude of problem assessed using 4D CT data and a motion-compensation strategy”, Phys. Med. Biol. 52(16), 4805-4826 (2007).

5. J. Meyer, A. Richter, K. Baier, J. Wilbert, M. Guckenberger and M. Flentje, “Tracking moving objects with megavoltage portal imaging: A feasibility study”, Med. Phys. 33, 1275-1280 (2006).

6. J. Rottmann, M. Aristophanous, A. Chen, L. Court and R. Berbeco, “A multi-region algorithm for markerless beam’s-eye view lung tumor tracking”, Phys. Med. Biol. 55 5585–5598 (2010).

7. T. Lin, L. I. Cervino, X. Tang, N. Vasconcelos and S. B. Jiang, “Fluoroscopic tumor tracking for image-guided lung cancer radiotherapy”, Phys. Med. Biol. 54, 981-992 (2009)

8. R. Li, J. Lewis, L. I. Cervino and S. B. Jiang, “A feasibility study of markerless fluoroscopic gating for lung cancer radiotherapy using 4DCT templates”, Phys. Med. Biol. 54, N489–N500 (2009).

9. S. Webb, “The effect on IMRT conformality of elastic tissue movement and a practical suggestion for movement compensation via the modified dynamic multileaf collimator (dMLC) technique”, Phys. Med. Biol. 51, R403-R425 (2006).

10. R. McMahon, L. Papiez and G. Sandison, “Relative motion of tumors and normal tissue during dynamic MIC tracking delivery”, Australas. Phys Eng. Sci. Med. 30 (4), 331-336 (2007).

11. J. C. Stroom and B. J. Heijmen, “Limitations of the planning organ at risk volume (PRV) concept”, Int. J. Radiat. Oncol. Biol. Phys. 66(1), 279-286 (2006).

12. D. C. Collier, S.S Burnett, M. Amin, S. Bilton, C. Brooks, A. Ryan, D. Roniger, D. Tran and G. Starkschall, “Assessment of consistency in contouring of normal-tissue anatomic structures”, J. Appl. Clin. Med. Phys. 4(1), 17-24 (2003).

13. F. M. Kong, T. Ritter, D. J. Quint, S. Senan, L. E. Gaspar, R. U. Komaki, C. W. Hurkmans, R. Timmerman, A. Bezjak, J. D. Bradley, B. Movsas, L. Marsh, P. Okunieff, H. Choy and W. J. Curran Jr., “Consideration of dose limits for organs at risk of thoracic radiotherapy: Atlas for lung, proximal bronchial tree, esophagus, spinal cord, ribs, and brachial plexus”, Int. J. Radiat. Oncol. Biol. Phys. 81(5), 1442-57 (2011).

14. K.C. Younge, Y. Wang, J. Thompson, J. Giovinazzo, M. Finlay and R. Sankreacha, “Practical implementation of failure mode and effects analysis for safety and efficiency in stereotactic radiosurgery”, Int. J. Radiat. Oncol. Biol. Phys. 91, 1003-1008 (2015).

15. R.P. Manger, A.B. Paxton, T. Pawlicki, and G-Y. Kim, “Failure mode and effects analysis and fault tree analysis of surface image guided cranial radiosurgery”, Med. Phys. 42, 2449-2461 (2015).

16. F. Yang, N. Cao, L. Young, J. Howard, W. Logan, T. Arbuckle, P. Sponseller, T. Korssjoen, J. Meyer, and E. Ford, “Validating FMEA output against incident learning data: A study in stereotactic body radiation therapy”, Med. Phys. 42, 2777 (2015).

17. J. P. Bissonnette, K.N. Franks, T. G. Purdie, D. J. Moseley, J. J. Sonke, D.A. Jaffray, L.A. Dawson and A. Bezjak, “Quantifying interfraction and intrafraction tumor motion in lung stereotactic body radiotherapy using respiration-correlated cone beam computed tomography”, Int. J. Radiat. Oncol. Biol. Phys. 75, 688-695 (2009).

18. J. Haseltine, A. Rimner, D. Gelblum, A. Modh, K. Rosenzweig, A. Jackson, E. Yorke and A. Wu, “Fatal complications after stereotactic body radiation therapy for central lung tumors abutting the proximal bronchial tree”, Pract Radiat Oncol. 6(2), e27-e33 (2016).

19. Y. Vinogradskiy, L. Shubert, Q. Diot, T. Waxweiller, P. Woo, R. Castillo, E. Castillo, T. Guerrero, C. Rusthoven, L. Gaspar, B. Kavanagh and M. Mifton, “Regional lung function profiles of stage I and III lung cancer patients: An evaluation for functional avoidance radiation therapy”, Int. J. Radiat. Oncol. Biol. Phys. 95(4), 1273-1280 (2016).

20. M. K. H. Chan, D. L.W. Kwong, E. Tam, A. Tong and S. C. Y. Ng, “Quantifying variability of intrafractional target motion in stereotactic body radiotherapy for lung cancers”, J. Appl. Clin. Med. Phys., 14(5), 140-152 (2013).

21. E. Weiss, K. Wijesooriya, S. V. Dill and P. J. Keall, “Tumor and normal tissue motion in the thorax during respiration: Analysis of volumetric and positional variations using 4D CT”, Int. J. Radiat. Oncol. Biol. Phys. 67(1), 296-307 (2007).

22. M. Altman, J. Jin, S. Kim, N. Wen, D. Liu, M. Siddiqui, M. Ajlouni, B. Movsas and I. Chetty, “Practical methods for improving dose distributions in Monte Carlo-based IMRT

planning of lung wall-seated tumors treated with SBRT", J. Appl. Clin. Med. Phys.13, 4007 (2012).

23. H. D. Nissen and A. L. Appelt, "Improved heart, lung and target dose with deep inspiration breath hold in a large clinical series of breast cancer patients", Radiother. Oncol. 106, 28-32 (2013).
24. O. El-Sherif, E. Yu, I. Xhaferllari and S. Gaede, "Assessment of intrafraction breathing motion on left anterior descending artery dose during left-sided breast radiation therapy", Int. J. Radiat. Oncol. Biol. Phys. 95(3), 1075-1082, (2016).
25. R. Méndez, R. Zinkstok, W. Wunderink, R.M. van Os, H. Joosten, Y. Seppenwoolde, P. Nowak, R. Brandwijk, C. Verhoef, J. Jzermans, P. Levendag and B. Heijmen, "Stereotactic body radiation therapy for liver tumors: impact of daily setup corrections and day-to-day anatomic variations on dose in target and organs at risk", Int. J. Radiat. Oncol. Biol. Phys. 75(4), 1201-1208, (2009).
26. G. Li, P. Cohen, H. Xie, D. Low, D. Li and A. Rimner, "A novel four-dimensional radiotherapy planning strategy from a tumor-tracking beam's eye view", Phys. Med. Biol. 57, 7579-7598 (2012).
27. F. Todsaporn, H. Woodruff, P. Rowshanfarzad, D. O'Connor, R. Middleton and P. Greer, "An independent system for real-time dynamic multileaf collimation trajectory verification using EPID", Phys. Med. Biol. 59, 61-81 (2014).
28. L. Ce, J. Yuen and A. Torralba, "SIFT flow: dense correspondence across scenes and its applications", IEEE Trans. Pattern Analysis Machine Intelligence, 33, 978-994 (2011).
29. N. Dalal, and B. Triggs, "Histograms of oriented gradients for human detection", IEEE Conf. Proc. Comp. Vision and Pattern Recognition, CVPR 2005. (2005).
30. P. T. Teo, R. Crow, S. van Nest, D. Sasaki and S. Pistorius, "Tracking lung tumor motion using a dynamically weighted optical flow algorithm and electronic portal imaging device", Meas. Sci. Technol. 24, 074012 (15pp) (2013).
31. P. T. Teo and S. Pistorius, "Tissue motion tracking at the edges of a radiation treatment field using local optical flow analysis", J. of Phys.: Conf. Series, 489 012040 (2014).
32. P. McCowan, E. Van Uytven, T. Van Beek, G. Asuni, B. McCurdy, "An in vivo dose verification method for SBRT–VMAT delivery using the EPID", Med. Phys. 42(12), 6955-6963 (2015).
33. B. McCurdy, K. Luchka, S. Pistorius, "Dosimetric investigation and portal dose image prediction using an amorphous silicon electronic portal imaging device", Med. Phys. 28(6), 911-924 (2001).

34. C. Bojechko, M. Phillps, A. Kalet and E. Ford, “A quantification of the effectiveness of EPID dosimetry and software-based plan verification systems in detecting incidents in radiotherapy”, Med. Phys. 42, 5363-5369 (2015).

35. S. Calderara, R. Vezzani, A. Prati and R. Cucchiara, "Entry edge of field of view for multi-camera tracking in distributed video surveillance”, Proc. IEEE Conf. on Advanced Video and Signal Based Surveillance. 93-98 (2005).

36. K. Gupta and A. V. Kulkarni, "Implementation of an automated single camera object tracking system using frame differencing and dynamic template matching”, Proc. 2007 Int. Conf. on Systems, Computing Sciences and Software Engineering (SCSS), 245-250 (2007).

37. Z. Ying, D. Comaniciu, M. Pellkofer and T. Koehler, "Passing vehicle detection from dynamic background using robust information fusion”, Proc. 7th IEEE Conf. Intelligent Transportation Systems, 564-569 (2004).

38. D. Comaniciu, Y. Zhu, M. Pellkofer and T. Koehler, “System and method for detecting a passing vehicle from dynamic background using robust information fusion”, US Patent 7248718 B2, 2007.

39. B. D. Lucas and T. Kanade, “An iterative image registration technique with an application to stereo vision”, Proc. 7th Int. Joint Conf. on Artificial Intelligence 674-679 (1981).

40. Radiotherapy equipment – Coordinates, movements and scales. IEC 61217 Ed. 2.0 International Electrotechnical Commission. (2011).

41. S. G. Armato, G. McLennan, L. Bidaut, M. McNitt-Gray, C. Meyer, A. Reeves et al., “The Lung Image Database Consortium (LIDC) and Image Database Resource Initiative (IDRI): A completed reference database of lung nodules on CT scans”, Med. Phys. 38(2), 915–931 (2011).

42. Y. Suh, S. Dieterich, B. Cho B, and P. Keall, “An analysis of thoracic and abdominal tumor motion for stereotactic body radiotherapy patients”, Phys. Med. Biol. 53, 3623–3640 (2008).

43. P. M. McCowan, D. W. Rickey, P. Rowshanfarzad, P. B. Greer, W. Ansbacher and B. M. McCurdy, “An investigation of gantry angle data accuracy for cine-mode EPID images acquired during arc IMRT”, J. Appl. Clin. Med. Phys. 15, 4507 (2014).

44. J. Rottmann, P. Keall and R. Berbeco, “Real-Time Personalized Margins”, AAPM 56th Annual Meeting, Med. Phys. 41, 474 (2014).

45. C. Coolens, S. Webb, H. Shirato, K. Nishioka and P. M. Evans, “A margin model to account for respiration-induced tumor motion and its variability”, Phys. Med. Biol. 53, 4317–4330 (2008).

46. D-J Lee, P. Merrell, B. Nelson and Z. Wei, "Multi-frame structure from motion using optical flow probability distributions", Neurocomputing 72, 1032-1041 (2009).

47. A. Sawant, R. Venkat, V. Srivastava, D. Carlson, S. Povzner, H. Cattell, and P. Keall, "Management of three-dimensional intrafraction motion through real-time DMLC tracking", Med. Phys. 35, 2050-2061 (2008).

48. D. Ruan and P. Keall, "Dynamic multileaf collimator control for motion adaptive radiotherapy: an optimization approach", Proc. 2011 IEEE Power Engineering and Automation Conf. (PEAM 2011), 100 - 103 (2011).

49. E. Wisotzky, R. O'Brien and P. J. Keall, "A novel leaf sequencing optimization algorithm which considers previous underdose and overdose events for MLC tracking radiotherapy." Med. Phys. 43, 132 (5pp.) (2016).

50. D. Moore, D. Ruan, and A. Sawant, "Fast leaf-fitting with generalized underdose / overdose constraints for real-time MLC tracking", Med. Phys. 43, 465 (10pp.) (2016).

51. J. Bryant, J. Rottmann, J. H. Lewis, P. Mishra, P. Keall, and R. Berbeco, "Registration of clinical volumes to beams-eye-view images for real-time tracking", Med. Phys. 41, 121703 (2014).

Chapter 6 Prediction of Tumor Trajectory Using a Generalized Neural Network Coupled with a Sliding Window

In this chapter, a systematic design of a neural network using a mixture of online data acquired during the initial period of the tumor trajectory, coupled with a generalized model optimized using a group of patient data (obtained offline) is presented. This neural network could be used to predict the tumor and/or critical structure motions detected using the algorithms presented in chapters 3-5. Part of the work was published as a book chapter in volume 51 of the IFMBE Proceedings series, DOI:10.1007/978-3-319-19387-8_146, and presented in the World Congress on Medical Physics and Biomedical Engineering, June 2015 Canada. An abstract based on the generalized model was selected for presentation at the Young Investigator's Symposium (finalist) at the annual meeting of the Canadian Organization of Medical Physicist (COMP 2016) in St. John's, Newfoundland. The material is also prepared for submission to Medical Physics by the author of this dissertation.

Abstract

Purpose: Accurate prediction of intra-fraction lung tumor motion is required to compensate for system latency in image-guided adaptive radiotherapy systems. The purpose of this study includes finding an optimal prediction model that (1) has a short learning period so that prediction and adaptation can commence as soon as the treatment begins, and (2) requires minimal re-optimization for individual patients. Specifically, the feasibility of predicting tumor position using a mixture of online data (intra-fraction) acquired from the initial period of the lung tumor trajectory, coupled with a generalized model optimized using a group of patient data

(obtained offline) is examined. The efficiencies and accuracies of using inherited vs. randomly initiated weights to initialize training for each sliding window (training batch) are compared.

Methods: A 3-layer perceptron neural network was implemented to predict tumor motion over a prediction horizon of 650 ms. The backpropagation algorithm was used for training with a sliding temporal window of samples as input while weight matrices were updated using a batch gradient descent approach. Seven 1-minute lung tumor motion samples in the superior-inferior direction were selected from a CyberKnife dataset to represent abrupt, fast and average circumstances of breathing. The data were sampled at a rate of 7.5 Hz (0.133 s) to emulate the frame rate of an electronic portal imaging device (EPID). To determine the optimal parameters of the network, the sliding window length was set to be equivalent to the first breathing cycle detected from each trajectory. Next, performing a parametric sweep, an averaged error surface of mean square error (MSE) with input data size and number of hidden neurons as parameters was obtained from the prediction responses of the seven patients. One pair of input data size and number of hidden neurons was selected as parameters for the generalized neural network model based on the MSE score while maintaining a parsimonious model. Using the generalized model, the prediction accuracies for the seven patients were evaluated while including data from an 8th patient as a leave-one-out scheme for cross-validation. To reduce training time, instead of using random weights to initialize learning (method 1), weights inherited from previous training batches (method 2) were used to predict tumor position in each sliding window. Accuracies and efficiencies of using both methods were compared.

Results: An input data size of 35 samples (4.6 s) and 20 hidden neurons was selected for the generalized neural network. An average sliding window length of 29 samples (3.9 s) was used. The average initial learning period prior to the availability of the first predicted tumor position is 8.8 s. With an average mean absolute error of 0.59 mm and an average computation time of 0.02 s, method 2 yields lower errors and faster computation. The average root-mean-square-error of 0.83 mm is comparable to results published in previous studies. Prediction errors are mainly due to the irregular periodicities between cycles. The errors for the leave-one-out cross-validation sample are within the range of errors observed from the other trajectories.

Conclusions: A network with a relatively short initial learning time was achieved. Its accuracy is comparable to previous studies. This network could be used as a plug-and-play predictor in which (a) tumor positions can be predicted as soon as treatment begins and (b) the need for pretreatment data and optimization for individual patients can be avoided.

6.1 Introduction

6.1.1 Challenges and criteria for the implementation of prediction in adaptive radiotherapy

Human respiration motion signals are considered as semi-periodic and non-stationary. The signals exhibit variations in trend, frequency, and baseline over time [1]. The variations imply that the prediction accuracy is limited to the near term as its accuracy diminishes over longer time spans [2]. Hence, a good prediction model should be 1) robust to both regular and irregular breathing patterns; 2) able to recover rapidly from random inputs and abrupt changes such as sneezing and coughing, and 3) able to adjust its parameters quickly using a minimal amount of input data gathered during a patient’s treatment.

In order to use a neural network to predict tumor motion, optimization of the network and measurement of its performance must be performed by (1) offline learning with pre-treatment data, or (2) online learning during the initial periods of the treatment delivery. In both approaches, the optimal network model is often selected with its parameters optimized according to the tumor trajectories of the individual patients. Challenges exist in using the individually optimized models trained with either offline or online learning.

With offline learning using pre-treatment data, the motions learned during training could be different to the motions observed during treatment delivery. Inter-fractional variations of >3mm in tumor position relative to the first pre-treatment cone beam CT scan have been noted in 60% of subsequent treatment fractions [3]. This could introduce systematic errors between the predicted motion which is based on the learned weights (from previous fractions) and the motion observed during treatment. Hence, the network needs to adapt to motion observed during treatment. Training periods ranging from 12 s to 80 s have been used to determine the optimal parameters of the neural network [4].

With online learning, given the complexity of the network design and the changing nature of the tumor trajectory, the network will take longer to train if offline training is not available before it is capable of making its first prediction. This would imply that adaption of treatment to compensate for tumor motion can only occur after this initial ‘waiting period’. Despite these challenges highlighted in both methods, the individually optimized neural network models are prone to biases and large errors when compared to a generalized model [5-8]. The generalized neural network trained with diverse motion patterns would require less adaptation that could reduce both initial and subsequent training durations.

6.1.2 Design considerations for using a neural network as a predictor for tumor motions

The prediction performance of a neural network depends on (1) the characteristics of the data, (2) presentation of the data to the training model, (3) the training scheme and (4) the architecture of the neural network model [1, 5, 9-10]. While the characteristics of the data describe the amplitude, trends, cyclic and other underlying components of the tumor trajectory (refer to [1]), the presentation of data would involve the selection of appropriate input data and sliding window length. The learning algorithms and the number of training epochs are associated with the overall learning scheme of the model while the architecture of the network is dependent on the size of the hidden layers, the number of hidden neurons and the types of activation functions. The number of hidden neurons is a tradeoff between the inabilities to learn with few neurons versus poor generalization capability with an excessive number of neurons. Changes of data over time could render an optimal model obsolete. Due to the numerous design considerations, the trial-and-error approach in determining the optimal parameters, and the lack of a universal design guidelines, the design of a neural network has often been considered as an art rather than an exact science [11-13].

To avoid problems associated with finding the optimal neural network model, a model averaging approach which combines a diverse range of predictors has been used to realize a model that is less susceptible to bias and large errors [5-9]. By combining predictors, the prediction performance may be better than using an individually optimized model [5-9]. In addition, the model averaging approach avoids the tediousness of fine-tuning the parameters to optimize an individual model [5]. The most common form of model averaging is realized via an ensemble of neural networks with each of the networks trained using different algorithms, structures, and initial weights [5, 13-15]. The outcomes from these individual networks are then used to make a collective forecast.

To ensure that a neural network can be used to predict the underlying motion, the principle of model parsimony should be adhered to. This rule-of-thumb suggests that given a variety of models with different structures and complexity that fit the data, the network with the smallest / most compact structure should be adopted to avoid overfitting [16, 17].

In this work, the concept of using an averaged model while adhering to the principle of parsimony will be explored [17]. Systematic design of the neural network using a mixture of data acquired during the initial period of the tumor trajectory, coupled with a generalized model optimized using diverse patient data will be presented. Specifically, the average mean square error surface obtained from seven patients will be used to determine the input data size and number of hidden neurons for the generalized neural network model. Modifications to the design of the neural network include (a) integration of the tumor position obtained during delivery into the design parameter of the neural network; (b) incorporation of prediction outcome from different patients to determine the parameters of a generalized NN; and (c) reduction of error and training time using inherited weights from previous training batches. The possibility of using the neural network as a plug-and-play model that does not require optimization from the pre-treatment data of individual patients will be tested.

6.2 Methods and Materials

6.2.1 Proposed neural network model

A multilayer perceptron neural network model was implemented with 3 layers, namely input (l =1), hidden (l = 2) and output layer (l =3) (figure 6.1). For the current time series forecast application, the input layer consists of x input nodes that represent a vector of historical data. The hidden layer consists of k hidden nodes to serve as the learning and memory for the neural network. $\Theta^{(1)}$ is the weight matrix from the input layer to the hidden layer, and $\Theta^{(2)}$ is the weight matrix from the hidden to the output layer. The output layer sums and weights the outcome from the hidden nodes and produces the value y predicted in the future horizon through a single output node. Multiple output nodes could be used for multi-step predictions.

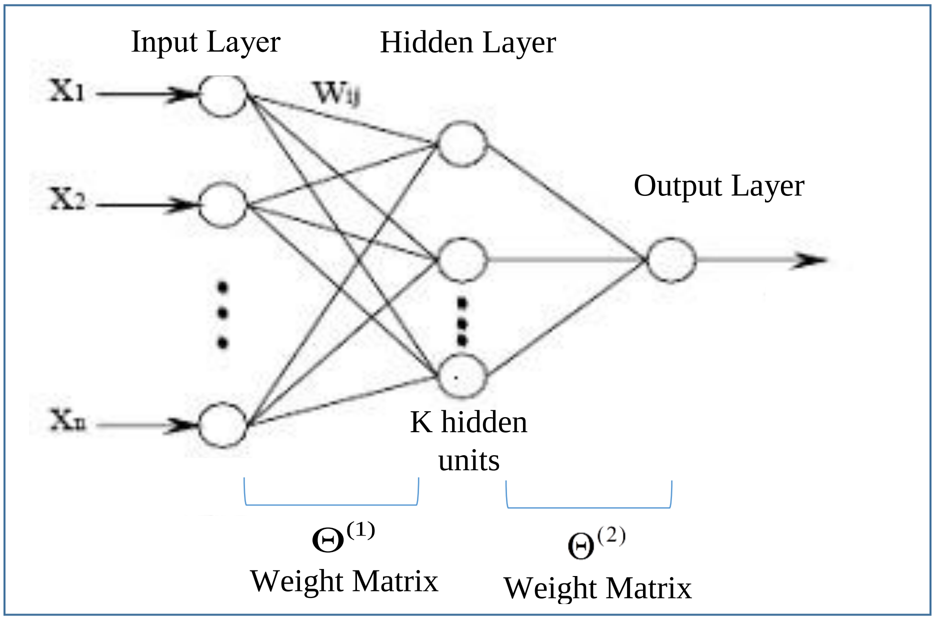

Figure 6.1 : A three layer neural network model.

6.2.2 Learning algorithm using backpropagation with gradient descent

The backpropagation algorithm [18-23] was used for learning. The algorithm consists of forward and backward passes. In the forward pass, the data from each input node is multiplied by the weights connecting between the input nodes to all the hidden nodes. The weights are coefficients that model the connection between the neurons/ nodes. At the input of each hidden node the multiplied values from the different input nodes are summed to produce a value z. An activation function is applied to the summed data prior its exit from the hidden node. The activation function maps the summed data to a bounded, non-linear range of values. At the output node, the summed data from all the hidden nodes is compared to the targeted value y (i.e. acquired tumor position from an electronic portal imaging device).

In the backward pass, the difference between the targeted and predicted value is propagated from the output layer back to the hidden and input layers respectively. In each layer, the difference between the backpropagated and forward output value of each node is determined. The gradient of these differences (i.e., error) with respect to the changes in the weights are established (for each node). Using a gradient descent approach, the weights associated with each node are adjusted to reduce their respective errors. The weight values are refined iteratively using different sets of training data presented to the network. Training will terminate when the error threshold or the maximum number of training epochs is reached.

The use of the gradient descent method to search for the combination of weights that minimizes the error function requires the computation of the gradient of the error function for each iteration. To ensure the differentiability and continuity of the error function, a sigmoid function of the form

$$\mathrm{g}(z) = \frac{1}{1+e^{-z}} \tag{6.1}$$

was used as the activation function on the neural nodes, where z represents the summed value at the input of each node in the hidden and output layers. The corresponding gradient of the activation function has the form

$$\mathrm{g}'(z) = g(z)(1-g(z)) \tag{6.2}$$

A batch gradient descent to update the weight matrices of the network was used in this work [21]. In the forward pass, the matrix for the input values to the hidden nodes in the hidden layer ($l = 2$) can be expressed as

$$z^{(2)} = \Theta^{(1)}x \tag{6.3}$$

where $\Theta^{(1)}$ is the matrix for all the weights between the input and hidden layers. After applying the activation function to the summed input, the activated output from the hidden nodes can be represented in a matrix

$$a^{(2)} = g(z^{(2)}) \tag{6.4}$$

The activated values in the matrix are transmitted from the hidden layer to the output layer (l =3). The summed value at the output node is given as

$$z^{(3)} = \Theta^{(2)}a^{(2)} \tag{6.5}$$

where $\Theta^{(2)}$ is the matrix for all the weights between the hidden and output layers. By definition, the sigmoid function maps data from (-infinity, infinity) to (0, 1). However, there is no guarantee that for our application the data is from 0 to 1. Therefore, the activation function was not applied to the output layer. The squared error, i.e. overall cost function *J* in the output layer (*l* =3) can be expressed as

$$J = \frac{1}{2}\left(z^{(3)} - y\right)^2 \tag{6.6}$$

where y are the actual output values and the factor of ½ is a value applied to simplify the function's derivative. The expression will later be multiplied by a learning rate, and hence it does not matter if a constant coefficient is introduced now. The goal is to minimize J as a function of the weights Θ. This requires the determination of the error derivative with respect to the weights. The weights can then be updated by an amount proportional to the rate at which the error changes as the weight is changed. The iterations of the gradient descent algorithm updates according to:

$$\Theta = \Theta - \alpha \frac{\partial J}{\partial \Theta} \tag{6.7}$$

where α is the learning rate.

The backward pass begins by letting the error sensitivity term $\delta^{(3)}$ with respect to the input $z^{(3)}$ of each activation function, be represented by (in the output layer, *l* =3)

$$\delta^{(3)} = \frac{\partial J}{\partial z^{(3)}} = (z^{(3)} - y)\ . \tag{6.8}$$

$\delta^{(3)}$ indicates the sensitivity of the network error with respect to changes in the input of each activation function. The error term in the hidden layer can be calculated using the chain rule:

$$\delta^{(2)} = \frac{\partial J}{\partial z^{(2)}} = \frac{\partial J}{\partial z^{(3)}} \frac{\partial z^{(3)}}{\partial a^{(2)}} \frac{\partial a^{(2)}}{\partial z^{(2)}} \tag{6.9}$$

among which

$$\frac{\partial J}{\partial z^{(3)}} = \delta^{(3)},$$

$$\frac{\partial z^{(3)}}{\partial a^{(2)}} = \Theta^{(2)},$$

$$\frac{\partial a^{(2)}}{\partial z^{(2)}} = g'(z^{(2)}) \tag{6.10}$$

Substituting equation (6.10) into equation (6.9) and using the chain rule derivation above allows the error on the hidden layer to be expressed as:

$$\delta^{(2)} = (\Theta^{(2)})^T \delta^{(3)} * g'(z^{(2)}) \tag{6.11}$$

Since the input value $z^{(l+1)}$ to the hidden nodes in layer (l + 1) is related to the weights and activation in the preceding layer through the relation

$$z^{(l+1)} = \Theta^{(l)} a^{(l)} \tag{6.12}$$

the gradient of the cost function with respect to the weights can be expressed as

$$\begin{aligned}\frac{\partial J}{\partial \Theta^{(l)}} &= \frac{\partial J}{\partial\left(\Theta^{(l)} a^{(l)}\right)}\left(a^{(l)}\right)^T \\ &= \frac{\partial J}{\partial z^{(l+1)}}\left(a^{(l)}\right)^T \\ &= \delta^{(l+1)}\left(a^{(l)}\right)^T\end{aligned} \tag{6.13}$$

Finally, the weights can be updated by

$$\begin{aligned}\Theta^{(l)} &= \Theta^{(l)} - \alpha \frac{\partial J}{\partial \Theta^{(l)}} \\ &= \Theta^{(l)} - \alpha \delta^{(l+1)}\left(a^{(l)}\right)^T\end{aligned} \tag{6.14}$$

where α is the learning rate. The change of weights can be simplified as:

$$\Delta\Theta^{(l)} = -\alpha \frac{\partial J}{\partial \Theta^{(l)}} \tag{6.15}$$

After sufficient training iterations, a set of optimal weights Θ can be obtained that minimizes the cost function J, and these weights are used to predict future tumor positions.

6.2.3 Data acquisition

The goal is to use different tumor trajectories to test the ability of the prediction algorithm. We are concerned with various contributors to lung tumor motion. These include the amplitude, rate, shape, and consistency of the patient’s breath as well as the tumor location within the lungs/thoracic cavity, the health of the tissue in the lungs, and any unexpected change in breathing such as a cough or sigh. Different speeds and sudden variations in the tumor motion may present different circumstances that will affect the accuracy of target tracking.

The CyberKnife Synchrony (CKS) dataset provides the raw data used by the system in tracking the position of tumors at various sites [24]. The CKS method measures motion of external surrogates (light emitting optical fibers tracked by an infrared camera) and periodically determines the actual position of the tumor (with images of implanted gold fiducials) to test and update the correlation model. Due to system noise, these traces are smoothed out by the CKS team in their analysis of the patient data. They use a first-order low-pass Butterworth filter to smooth the data in each dimension. Thirty lung tumors, over 105 fractions, are included. Twenty-eight of these fractions have been imported and analyzed for this experiment. Considering the ranges of amplitude, breathing rate, and shape of the recorded traces, 1 minute of tumor motion data in the superior-inferior (S-I) direction of seven patients were selected to represent fast, slow and average circumstances of breathing rate and amplitude. Some trajectories were chosen since they included an abrupt change in breathing pattern (a cough or sigh, for example) and some represent a lack of consistency in the overall trace. The data were sampled at a rate of 7.5 Hz to emulate the frame rate of the Varian AS500 electronic portal imaging device. The characteristics of these traces are summarized in table 6.1.

6.2.4 Partitioning of data for training using a sliding window approach

The neural network model was trained with a sliding window scheme shown in figure 6.2 [25-32]. The stages of sliding window learning include: (1) initial learning with a finite set of training data; (2) testing the model by making predictions for a defined prediction horizon; (3) sliding the training window forward to obtain a new model with the updated training data; (4) using the new model to make a subsequent prediction; and (5) repeating the sliding window process till all data are predicted. The learning scheme shown in figure 6.2 depicts a first-in-first-out data sequence with a sliding window of length L encompassing the output of the training, validation, and testing samples. The data are the tumor positions acquired during treatment delivery.

Table 6.1 : Characteristics of the tumor trajectories (S-I direction) of seven patients observed over a duration of 1 min.[†]

Lung tumor trajectories	Breaths per min., Groupings	Range of Amplitudes (mm)	Max. Acceleration[*] (mms^{-2}), Rank	General Description
P1	24, 1	4-8	-43.9, 2	Irregular peak and trough positions
P2	25, 1	7-9	-38.4, 4	Regular shape and period
P3	24, 1	6-10	-38.5, 3	One larger breath
P4	17, 2	4-16	73.8, 1	High acceleration, one deep inhale followed by an irregular period
P5	15.5, 2	2-4	-10.3, 7	Irregular peaks and troughs positions
P6	12, 3	7-8	-30.9, 5	Irregular period
P7	11, 3	8-9	-20.6, 6	Non-symmetry between inhale and exhale.

[*] Maximum acceleration was determined by the peak magnitude of acceleration in the 1-minute trace. The positive or negative sign indicates the direction of change in velocity.

[†] The characteristics of the tumor trajectories are different from those presented in table 4.1.

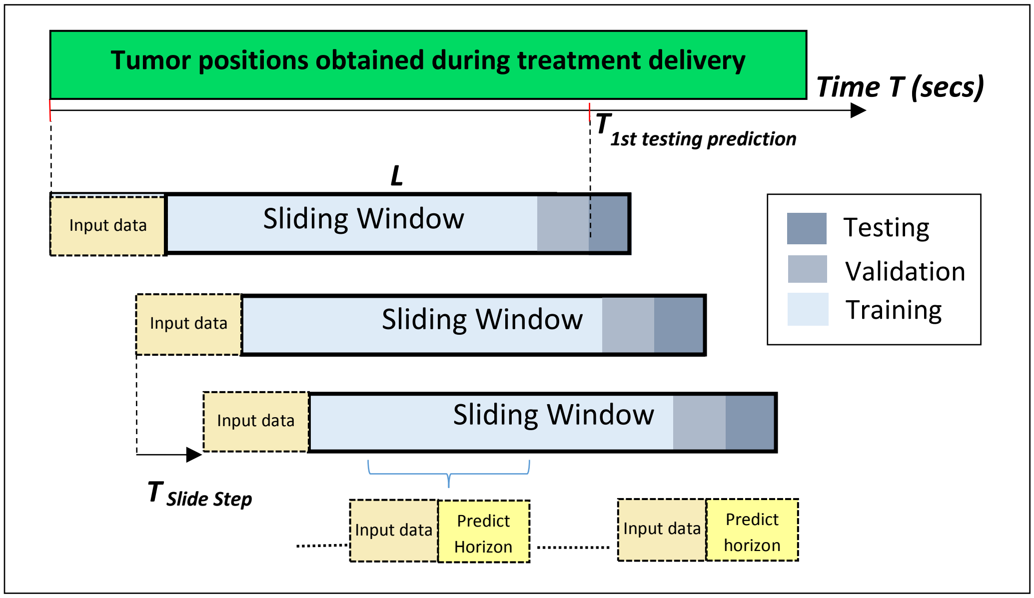

Figure 6.2. : Online learning and prediction using a sliding window scheme with data obtained during treatment delivery. Training in each sliding window will stop when either the maximum number of epochs or the specified MSE is reached.

6.2.5 Establishing the values of the parameters (number of hidden neurons, sliding window and input data size) for the model

The length of the sliding window corresponds to the number of training batches required to optimize the weights of the neural network model. Each training batch is comprised of multiple samples of input-output data pairs grouped as a vector (or feature) for learning. The input data, a finite length of immediate past data prior to the predicted data, provides the minimal information that is needed to support the predicted outcome. The presentation of the input and corresponding output pair of data to the neural network enables the model to learn to predict with the required prediction horizon. A prediction horizon of 650 ms corresponding to approximately five samples (tumor positions acquired at 0.133 s interval) of delay was simulated to cover the system latencies observed with an EPID-based image-guided radiotherapy system (IGRT) [33, 34], as well as for other IGRT systems where the latencies are smaller than 650 ms [35], since prediction error often only increases with the prediction horizon. The iterative learning in each sliding window will terminate when either the maximum number of training epochs or the desired mean square error (MSE) was reached. Both sliding window and input data size could be optimized to improve the accuracy of the prediction [31 32].

A common practice when training the model is to partition the data in the sliding window into training, testing and validation datasets [32]. During implementation, the training, testing, and validation were divided into 80%, 10% and 10% of the size of the sliding window. In other words, within the training dataset (i.e., 80% of the sliding window data), there would be vectors comprising finite lengths of input data and their corresponding output data.

Due to the large combinations of sliding window length, input data size and number of hidden neurons, a 2-stage process was used to determine the optimal combination of parameters. Firstly, the sliding window length was determined using the 1st period of the detected tumor trajectory of each patient. The rationale for selecting the 1st period is to expose the neural network to the full inhale and exhale trends observed in one period. Although different periodicity might occur for the remaining treatment, selecting the 1st period for the sliding window would allow the determination of the neural network parameters to be established early so that the first prediction would be available as early as possible (vs. selecting other periods). A summary of the 1st period detected from the seven tumor trajectories and the corresponding sliding window sizes used for the neural network is shown in table 6.2. Secondly, a parametric study (by sweeping the values of the parameters in a fixed step size) was implemented to identify the possible combinations of input data size and number of hidden neurons. Specifically, by sweeping the input data size from 10 to 100 in steps of 10 data samples, while the number of hidden neurons was increased from

10 to 100 in steps of 10 neurons, an array of neural network models were used to predict the tumor trajectories of each patient. An additional parametric study with five input data and five hidden neurons was included. A 2D array of MSE with the two parameters as variables was obtained from the predictions for each of the seven trajectories along with an average 2D array of MSE. From this average MSE surface, regions with low MSE, which are less sensitive to the parameter changes, were identified. Within the low sensitivity region, one pair of input data size and number of hidden neurons was selected as the parameter for the generalized neural network model following the principle of parsimony. Applying the selected pair of parameters to the generalized neural network model, the prediction responses for the seven trajectories were determined. A summary of the whole process is given in figure 6.3. This approach is similar to selecting an average model from an ensemble of neural networks and using the average model to make individual predictions [13-15], except that instead of obtaining a combined prediction from multiple models a generalized set of parameters was obtained from the results of multiple models.

Table 6.2 : Summary of 1st period detected from the tumor trajectory and the sliding window length used in the neural network for each patient trace prediction.

	Lung tumor trajectories							
	P1	**P2**	**P3**	**P4**	**P5**	**P6**	**P7**	**Average**
1st period of tumor trajectory (s)	3.1	2.7	2.3	3.6	2.9	4.8	6.4	3.69
Sliding window size* (data samples)	25	22	19	29	22	36	50	29

*Data samples were chosen with two extra samples in addition to the 1st period of the tumor trajectory

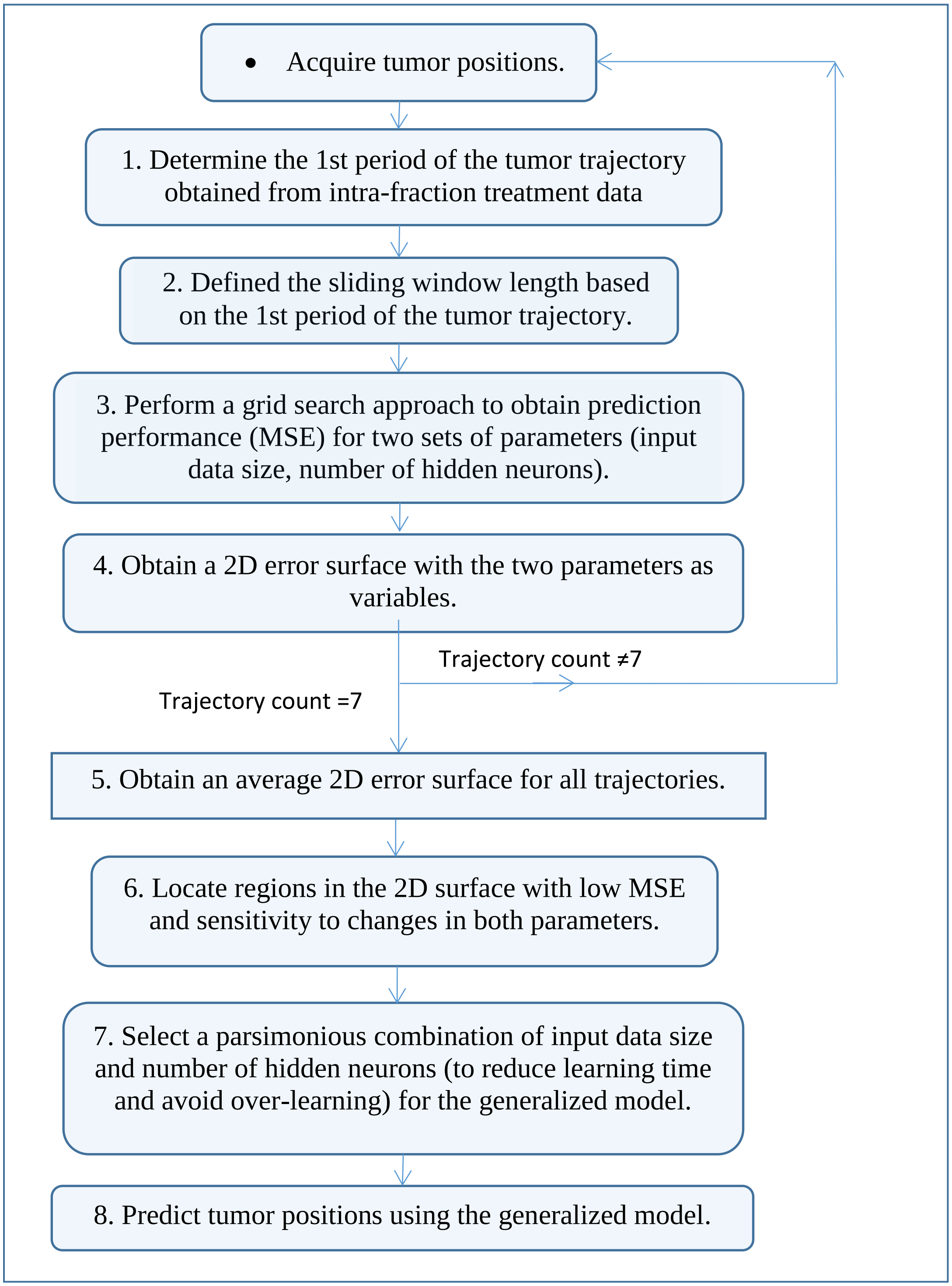

Figure 6.3 : The process involved in building a generalized neural network model for the prediction of tumor position.

6.2.6 Weight inheritance

Two methods were used to establish the initial weights for each training batch (i.e. sliding window, as described in Section II. D). Method 1 uses randomly initialized weights to re-train the network while Method 2 uses inherited weights for each training batch. The inherited weights would act as regularization for the model and would allow subsequent trainings to converge faster [36]. A summary of the two methods is given in table 6.3 and their performances (accuracy and computation time) were compared.

Table 6.3 : A summary of the two methods used for weight initialization.

Methods	Training Epochs	Learning Rate	Weights initialization
Mtd. 1	800	0.02	Weights initialized for each training batch
Mtd. 2	800	0.02	Inherited weights from the previous batch

6.2.7 Evaluation of prediction performance

With $\widehat{y_i}\ and\ y_i$ being the predicted and actual tumor position respectively, the performance of the neural network was evaluated using the mean error, mean absolute error (MAE), mean square error (MSE) and root mean square error (RMSE) is given by

$$Mean\ error\ = \frac{1}{N}\sum_{i=1}^{N}(\widehat{y_i} - y_i) \tag{6.16}$$

$$MAE\ = \frac{1}{N}\sum_{i=1}^{N}|\widehat{y_i} - y_i| \tag{6.17}$$

$$MSE = \frac{1}{N}\sum_{i=1}^{N}(\widehat{y_i} - y_i)^2 \tag{6.18}$$

$$RMSE = \sqrt{\frac{1}{N}\sum_{i=1}^{N}(\widehat{y_i} - y_i)^2} \tag{6.19}$$

where N is the number of data samples in each training batch. The mean error determines if the prediction under- or over-estimates the actual tumor position (i.e., the sign of the error) while the MAE is an estimate of the magnitude of the error. The MAE assigns equal weights to the error terms while the MSE emphasizes the outliers. As a result, the MSE was used during training iterations since it penalizes extreme errors [37]. For radiotherapy applications where safety is emphasized, it is essential to have a small maximum prediction error to avoid irradiating healthy tissue. Hence the maximum absolute error was included as one of the evaluation metrics. The performance of methods 1 and 2 were compared using the above metrics.

To show that the proposed neural network can be used as a plug-and-play prediction module and to evaluate its capability to generalize and make predictions on unseen data, a 1-minute tumor trajectory of patient 8 (P8), which has not been used in the determination of the average MSE error surface, was left out of the training data sets and used as a sample for cross-validation. The 1st period of the tumor trajectory of patient 8 was determined at 34 s, leading to a sliding window length of 26 samples.

Finally, differences in the prediction errors between the generalized and personalized neural network will be compared using tumor trajectory P6.

6.3 Results

Figure 6.4 depicts the 2D error (MSE) surfaces as a function of the number of hidden neurons vs. input data size for tumor trajectories P1 (figure 6.4. (a)) to P7 (figure 6.4(g)). For most of the trajectories, similar trends of decreasing errors are observed as the number of hidden neurons increases. The prediction error surface for P6 exhibits a large variation in error magnitude along the x-axis, indicating that it is sensitive to variations in the amount of input data. Figure 6.4(h) plots the average MSE for the seven patients. The MSE is more dependent on the input data size compared to the number of hidden neurons. A relatively stable MSE region is observed when the input data length increases beyond fifty-five.

Figure 6.5 depicts the MSE surfaces for the seven trajectories obtained using method 2. Except for trajectory P6, the error decreases as the input data size increases. For P6, small errors were only observed with input data sizes of less than 15. The errors were sensitive to the parameter selection. Figure 6.5(h) plots the average MSE for the seven trajectories. Compared to the average MSE of method 1 (figure 6.4(h)), a relatively stable error surface is obtained with method 2. With fifteen hidden neurons (figure 6.5), a stable MSE error surface is observed with an input data size of fifteen to one hundred. Beyond thirty-five input data samples, it is observed that the variation of MSE with respect to the number of hidden nodes is relatively insignificant. A combination with thirty-five input data samples and twenty hidden nodes was selected as the optimal set of parameters for the generalized neural network, i.e., (input data size, number of hidden nodes) = (35, 20). Thirty-five samples correspond to an input data length of 4.66 s.

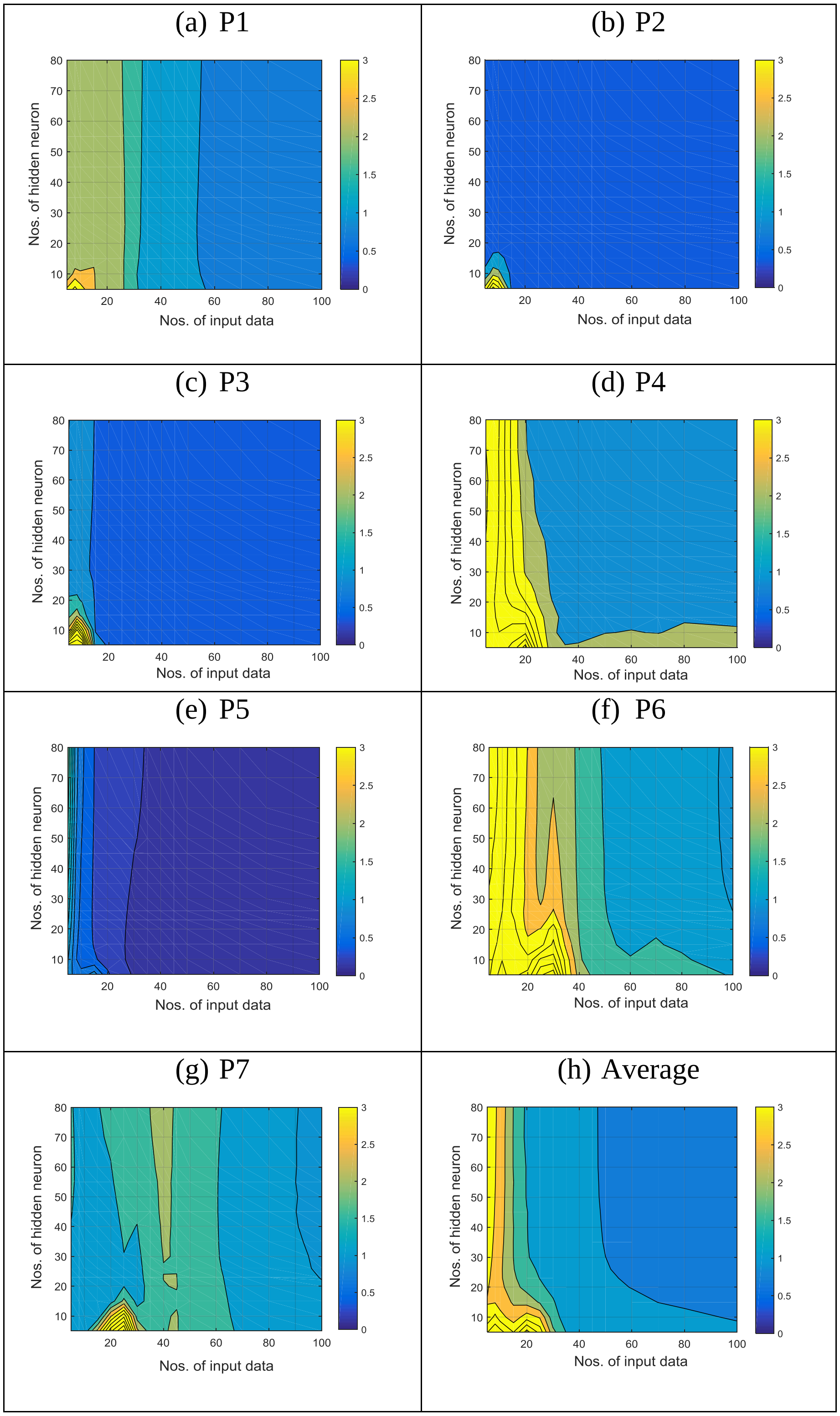
(a) P1

(b) P2

(c) P3

(d) P4

(e) P5

(f) P6

(g) P7

(h) Average

Figure 6.4 : 2D error (MSE) surfaces showing the prediction performance as a function of the number of hidden neurons vs. input data size for trajectories (a) P1 to (g) P7 using method 1. (h) Corresponds to the average error surface obtained from the seven trajectories.

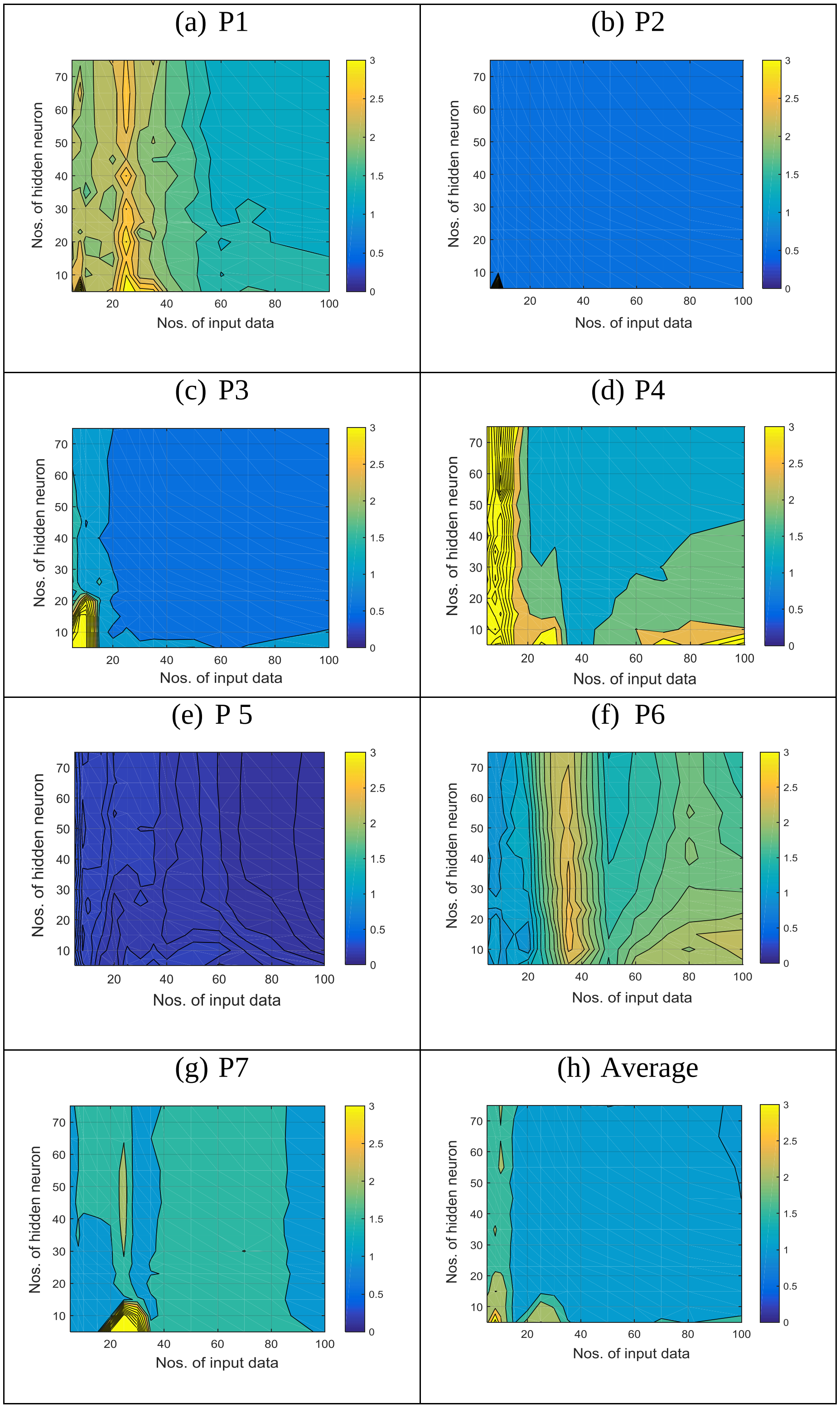

Figure 6.5 : 2D error (MSE) surfaces showing the prediction performance as a function of the number of hidden neurons vs. input data size for trajectories (a) P1 to (g) P7 using method 2. (h) Corresponds to the average error surface obtained from the seven trajectories.

Figure 6.6 plots the actual and predicted tumor trajectories (P1 through P7) obtained using the generalized neural network model trained with method 2. The increase in position is associated with the inhale phase of the patient's respiration. For trajectories P1, P2, P5, and P7, no drastic changes in the prediction errors were observed. Most of the errors occur near the peaks (transition from inhale to exhale) and troughs (transition from exhale to inhale) of the tumor trajectories. For trajectory P3, a deep breath with a peak-to-peak tumor position of around 10 mm, an increase of 3 mm when compared to the previous cycle, was observed between 33 s to 38 s (figure 6.6(c)). The error incurred during this period is -2.1 mm at around 37.2 s. It should be highlighted that the maximum absolute error for P3 was not due to the deep breath encountered between 33 s to 38 s. Maximum error of about 4.85 mm was incurred due to the irregular periods encountered at around 55 s (figure 6.6(c)). Similarly, for trajectories P4 and P6 the increase in the prediction error at around 37 s and 39.5 s respectively was due to an irregular period where the tumor remained in the exhale/resting position over a longer duration compared to previous cycles. For P6, in addition to the spike in error at 39.5 s, the maximum absolute error of 6.09 mm occurs at 10.3 s. The initial learning periods, i.e., time taken prior to making the first prediction, for the seven trajectories are 8.27 s, 7.87 s, 7.60 s, 8.80 s, 8.13s, 9.87 s and 11.4 s for trajectories P1 – P7 respectively (using method 2). This corresponds to an average initial learning period of 8.8 s.

The performances of both method 1 and 2 were summarized in table 6.4 and table 6.5 respectively. Overall, method 2 yields lower errors compared to method 1. Average MAE of 0.73

mm and 0.59 mm were incurred for method 1 and 2 respectively. In both methods, the largest absolute error was incurred by P6 followed by P3.

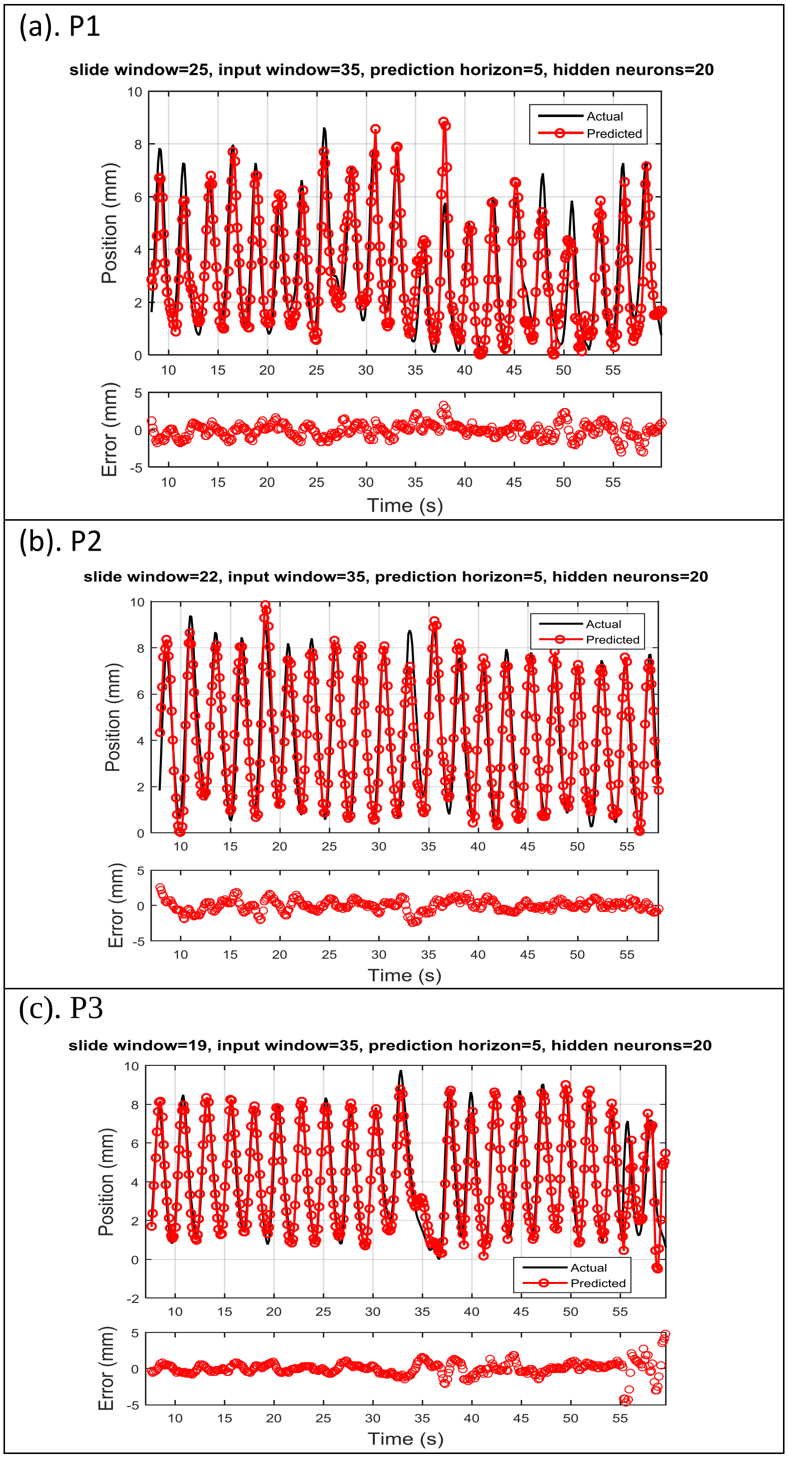

(a). P1

slide window=25, input window=35, prediction horizon=5, hidden neurons=20

(b). P2

slide window=22, input window=35, prediction horizon=5, hidden neurons=20

(c). P3

slide window=19, input window=35, prediction horizon=5, hidden neurons=20

(d) P4

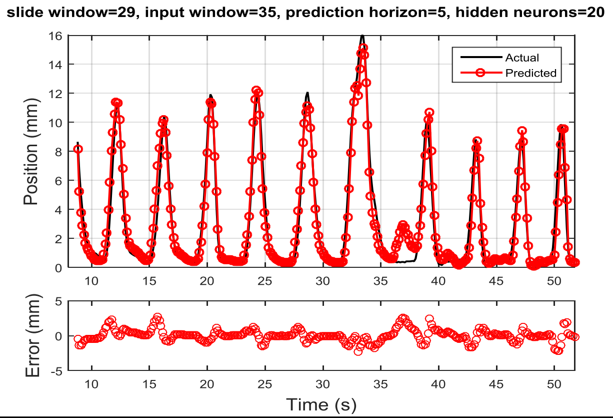
slide window=29, input window=35, prediction horizon=5, hidden neurons=20

(e) P5

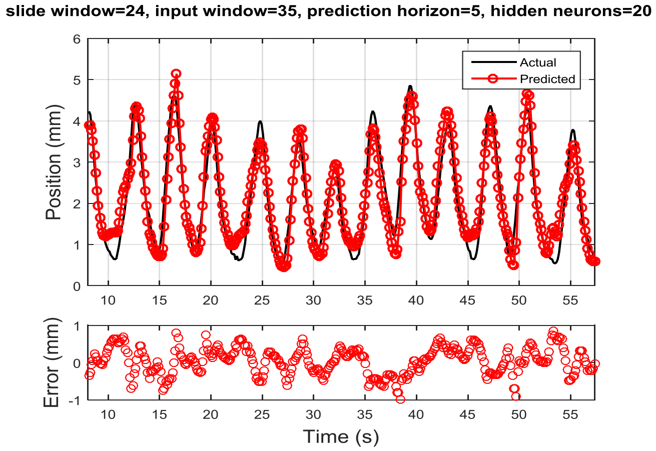
slide window=24, input window=35, prediction horizon=5, hidden neurons=20

(f) P6

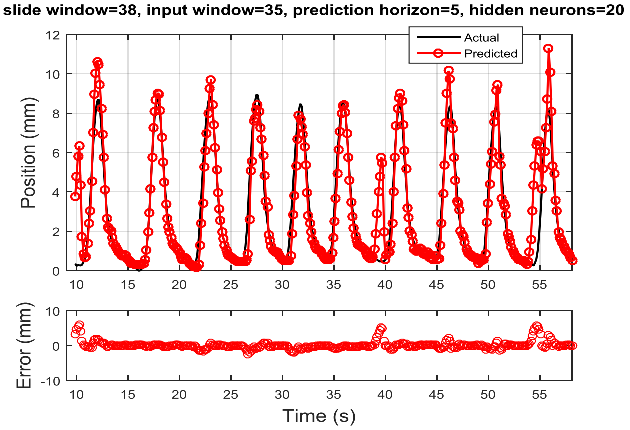
slide window=38, input window=35, prediction horizon=5, hidden neurons=20

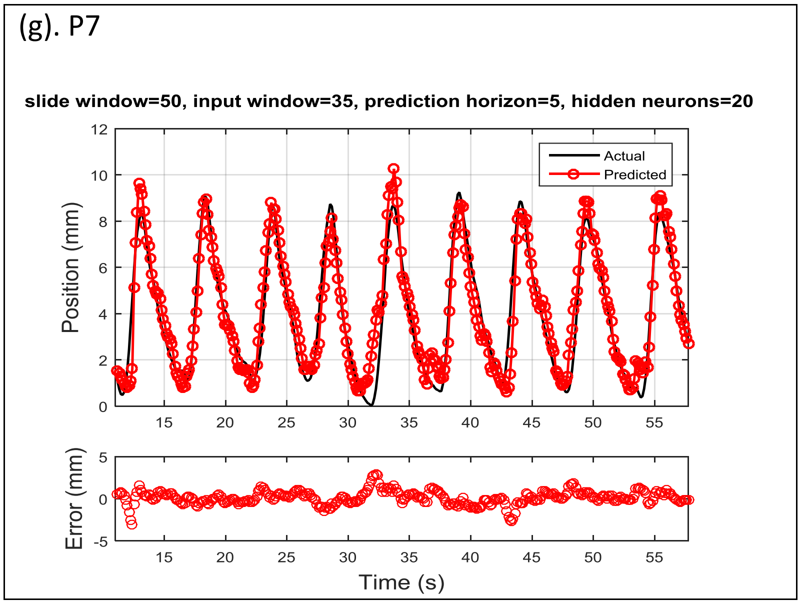

Figure 6.6 : Actual and predicted tumor trajectories (selected from seven patients) using method 2.

Table 6.4 : Errors (predicted – actual position) in predicting patient tumor trajectories P1 through P7 using method 1 with the generalized neural network model.

	Mean error (mm)	**MAE (mm)**	**Max. abs. error (mm)**	**RMSE (mm)**
P 1	-0.04	0.77	3.86	1.04
P2	-0.02	0.61	3.07	0.80
P3	0.06	0.72	5.00	1.10
P4	0.12	0.91	4.82	1.38
P5	0.02	0.37	1.49	0.48
P6	0.26	0.87	7.71	1.58
P7	0.08	0.83	4.18	1.17
Average	0.07	0.73	4.30	1.08

Table 6.5 : Errors (predicted – actual position) in predicting patient tumor trajectories P1 through P7 using method 2 (i.e., inherited weights) with the generalized neural network model.

	Mean error (mm)	**MAE (mm)**	**Max. abs. error (mm)**	**RMSE (mm)**
P1	-0.10	0.73	2.86	0.90
P2	0.00	0.62	2.52	0.79
P3	0.01	0.64	4.85	0.96
P4	0.03	0.60	2.64	0.86
P5	0.05	0.30	0.97	0.36
P6	0.16	0.60	6.09	1.17
P7	0.13	0.60	3.03	0.80
Average	0.04	0.59	3.28	0.83

The boxplot in figure 6.7 depicts the distributions of prediction errors amongst the individual trajectories for methods 1 and 2. For all the trajectories, the mean of their error distributions are close to zero. This indicates a symmetrical distribution of errors due to the under- and over-estimations of tumor positions. Although P5 and P6 demonstrate the smallest spread of error measured by the 1.5 inter-quartile range (1.5IQR), the error distribution of P6 is marred by a large maximum error.

Figure 6.8 plots the distributions of the prediction errors for methods 1 and 2 for all the trajectories and table 6.6 shows the accuracy (mean prediction errors ± standard deviation of the position errors of all the trajectories) and precision (the width of the central 68% of the distribution, after normalizing each distribution with the mean error). Method 2 yields better performance with an accuracy and precision of 0.04 ± 0.86 mm and 1.29 mm respectively. Method 2 requires an average computation time of 0.018 s to make a prediction on the tumor position.

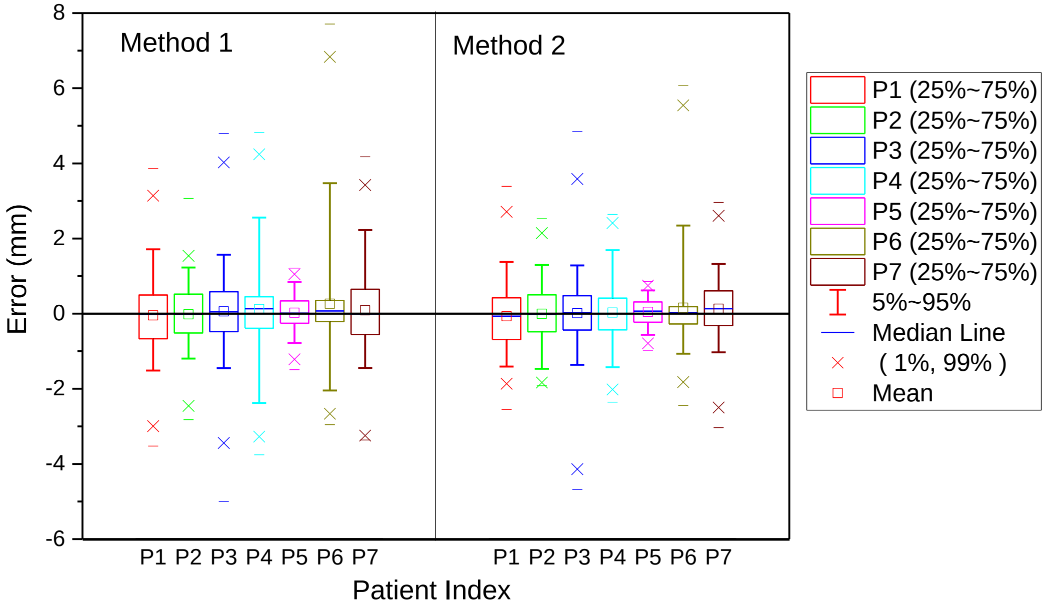

Figure 6.7 : Boxplot showing the distributions of mean prediction errors amongst individual trajectories using Methods 1 and 2.

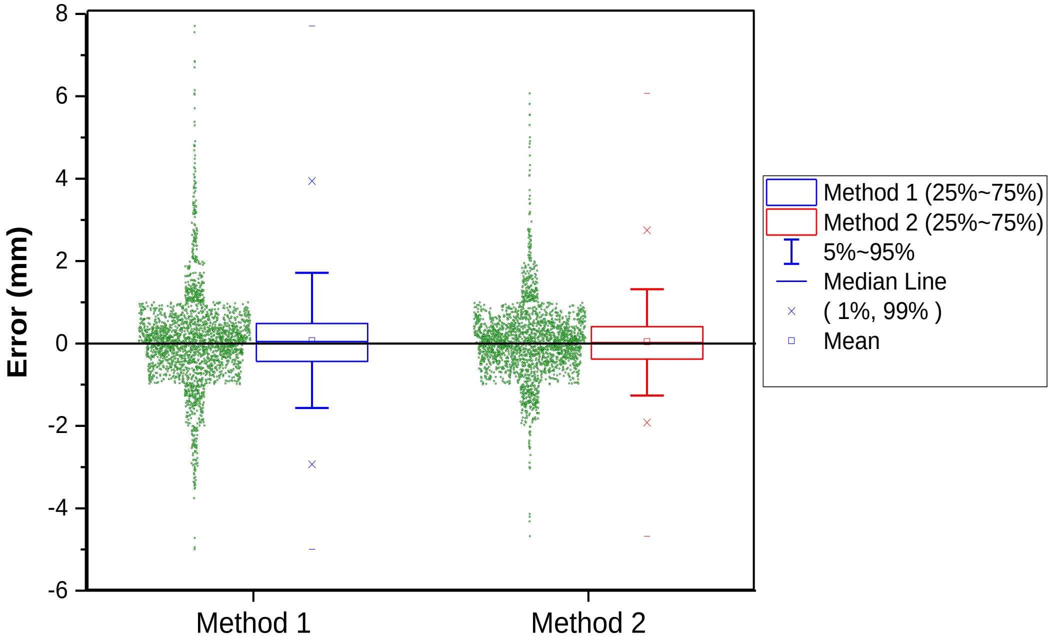

Figure 6.8 : Boxplot showing the distributions of mean prediction errors of all trajectories using Methods 1 and 2.

Table 6.6 : Performance of the two prediction methods quantified by the computation time, accuracy (mean prediction errors ± standard deviation of the position errors of all the patients) and precision (the width of the central 68% of the distribution, after normalizing each distribution with the mean error) of the prediction against the actual tumor position.

	Error Statistics		**Computation Time* (s)**
	Accuracy (mm)	**Precision (mm)**	
Method 1	0.07 ± 1.12	1.54	0.04
Method 2	0.04 ± 0.86	1.29	0.02

* Average computation time for the prediction of a new tumor position on an Intel i5-2520M 2.56GHz CPU.

Figure 6.9 plots the actual and predicted tumor trajectories of patient 8. The errors, summarized in table 6.7, are within the range of errors observed from the other patients shown in table 6.5. Results imply that the neural network is capable of predicting tumor trajectories that were not used as part of the data samples to establish the parameters for the generalized neural network.

Figure 6.10 plots the actual and predicted tumor trajectory P6 obtained using a personalized neural network trained with a smaller input window size (i.e., five) and number of hidden neurons (i.e., five) compared to the generalized neural network. Method 2 was used for the training. Table 6.8 provides a summary of the prediction performance for P6 obtained using the generalized and personalized neural networks. The improvement in the prediction performance acquired with a smaller input data size and hidden neurons is in agreement with the trend observed in the error surface plot shown in figure 6.5(f) where lower MSE error are observed in the regions with input data size smaller than 20.

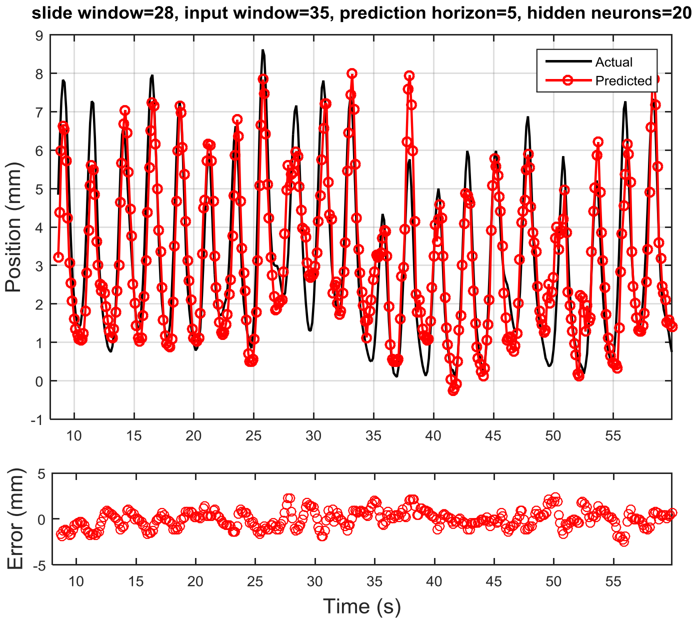

Figure 6.9 : Actual and predicted tumor trajectories of patient 8(P8). P8 serves as the leave-one-out sample to evaluate the performance of the generalized neural network (trained with method 2) on unseen data.

Table 6.7 : Errors (predicted – actual position) in predicting tumor trajectory P 8 using method 2 with the generalized neural network model.

	Mean error (mm)	**MAE (mm)**	**Max. abs. error (mm)**	**RMSE (mm)**
P8	-0.04	0.74	2.53	0.93

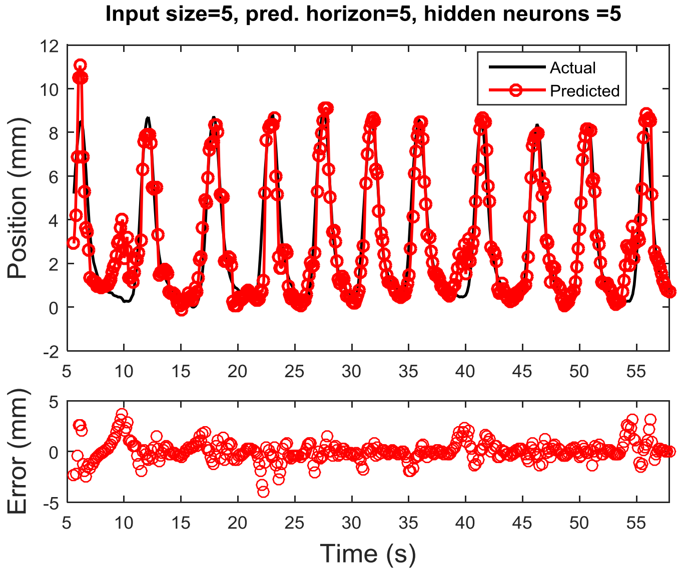

Figure 6.10 : Actual and predicted tumor trajectory of P6 using a personalized neural network model with a smaller input window size (i.e., five) and a smaller number of hidden neurons (i.e. five). Compared to using a generalized neural network with thirty-five input data and twenty hidden neurons (figure 6(f)), the error at around 40 s in figure 6(f) was reduced as shown in this figure.

Table 6.8 : A comparison of the prediction performances of P6 using a generalized vs. a personalized neural network model, both trained with method 2.

	(Input data size, Nos. of hidden neurons)	**Mean error (mm)**	**MAE (mm)**	**Max. abs. error (mm)**	**RMSE (mm^2)**
Generalized model	(35, 20)	0.16	0.60	6.09	1.08
Personalized model	(5, 5)	0.05	0.65	3.94	0.97

6.4 Discussion

It was observed that prediction error peaks during the initial period (at 10.27 s) and at 39.5 s for the tumor trajectory of P6 (figure 6.6(f)), Analysis of the signal before 10.27 s (i.e. from the learning data prior to making the first prediction) and just prior to 39.5 s indicated that both errors occurred when the tumor remains in the exhale / resting position for a prolonged duration compared to previous cycles. In both cases, the prediction errors were allowed to accumulate without any intervention, i.e., the error increases from -0.02 mm at 38.8s to 5.3 mm at 39.6 s over a span of six predicted data samples. In practice, since each of these errors was determined after each treatment delivery, contingency plans to either activate gating or stop the treatment would have been imposed when the error exceeds a certain threshold after treatment deliveries. Since prediction errors can only be determined after treatment delivery, i.e., at the prediction horizon, any remedy to minimize the impact of the error can only be performed in subsequent delivery.

Similarly, with a large prediction error detected at the beginning (i.e., 10.27 s) of trajectory P6, subsequent deliveries can be delayed until a more favorable motion profile is established by an alternative monitoring device (e.g. kV imaging) instead of using EPID images. The above strategy aims to minimize the impact and possibility of large prediction errors. With step-and-shoot intensity modulated radiation therapy (IMRT) techniques, the effect of the prediction errors could potentially be averaged out.

Using a personalized neural network with a smaller input data size and number of hidden neurons reduces the errors observed at 10.27 s and 39.5 s of trajectory P6 (figure 6.10). This could be due to the fact that the smaller window is more robust in handling changes in the periodicity of the tumor trajectory since the smaller window prevents the model from retaining memories associated with the longer periodicity of previous breathing cycles. As a result, it is able to recognize the change more quickly when the period shortens. For future work, an ensemble/ committee [5], [13-15] of neural networks using different input data sizes can be used to make parallel predictions of the tumor positions. Based on the errors of prediction and pattern of the observed trajectory, the most suitable network could be automatically selected for subsequent predictions. Alternatively, dynamic weightings based on the errors amongst the prediction models can be used to provide an average prediction from the ensemble of networks.

6.4.1 Factors affecting prediction accuracy

Comparing the characteristics of trajectories in table 6.1 with the prediction results, changes in frequency within the trajectories tend to incur higher prediction errors. This is in agreement with the observations made by other groups [1] as well as observed in the trajectories of P4 and P6. Both trajectories are characterized by abrupt changes in the transition between exhale and inhale, i.e., the tumor would change direction rapidly after remaining in the exhale position for a long period of time. As a result, a larger proportion of the data points were being presented to the network when the tumor was near the exhale positions (refer to figures. 6.6(d) and 6.6(f)). Overlearning of the previous trend in which the tumor was near the exhale positions could have deteriorated the capability of the neural network to accurately predict the tumor position when the length of subsequent periods changes. With the smallest range of motion amplitudes and maximum acceleration, trajectory P5 incurred the lowest maximum absolute error, MAE, and MSE. The effects of the same characteristics on the other patients are inconclusive since the trajectories are associated with other confounding traits (e.g., irregular frequencies). Although the prediction performance of trajectory P3 shows that our model is robust against random deep breaths, an anomaly detection mechanism could be incorporated to either adapt the method of prediction or to provide weightings that are associated with the level of uncertainty in the predicted results. A larger treatment margin could potentially be used to compensate for the uncertainty in the predicted tumor position. The impact of the other characteristics of the trajectory such as the trend, stationarity, autocorrelation function and seasonality [5, 38] on the prediction performance of this model will be studied in future work. In the current work, the prediction horizon was fixed at five EPID image samples (665 ms). This is in between the range of latencies (50 ms to 1400 ms) observed in some image-guided adaptive radiotherapy systems [35]. It is well-known that prediction accuracy deteriorates as the prediction horizon increases [35].

The ability for the neural network to generalize and predict on unseen data is crucial in ensuring that the model does not memorize the training pattern. By partitioning the data into training, validation and testing datasets, it ensures that predictions were made on unseen data partitioned under the test set. In addition, using the tumor trajectory of patient 8 as a leave-one-out sample for cross-validation, the results show that our models can generalized and be used to predict on unseen data. Instead of using random initial weights for the training of different data batches, the use of inherited weights improves the prediction accuracy and computation time.

6.4.2 Personalized vs. generalized model

Although a personalized neural network has shown smaller error compared to a generalized model for patient 6 (figure 6.10), extra time and resources are needed to train and optimize different networks when applied to different patients. The generalized neural network model proposed in this work does not require separate optimization and synchronization; the only data needed from the treatment delivery is the first period of the tumor trajectory. In addition, a shorter initial learning period was observed using the generalized neural network model proposed this study. Although potential errors could arise in adapting the generalized network for specific patients, errors could exist in synchronizing and adapting the individualized neural network to the tumor motions observed in subsequent treatment fractions. In addition to some of the published work that compares the performance between a generalized and a specialized neural network [39, 40], the difference in performance as well as the pros and cons of using a personal vs. a generalized neural network designed using our approach should be further examined in future work. In addition, trajectories can be classified into different groups according to the characteristics of the trajectories described earlier. A group-based neural network could then be used to predict tumor trajectories having the same characteristics.

6.4.3 Impact of prediction accuracy on treatment outcome

It has been shown that using a tumor tracking method with an error of 0.9 ± 0.5 mm (tracking and prediction applied), a reduction of gamma failure rate (dose difference at 3%/ 3mm) from 22.5% to 0.2% was still achieved in a DMLC system [34]. The benefits of prediction and tracking in IGRT will outweigh the prediction errors observed. Underexposure of the tumor and over exposure of the surrounding tissues due to the lag between the beam and the tumor position can be prevented [34, 41]. Since safety concerns are paramount in radiotherapy, gating and termination of treatments in progress are possible options when a large prediction error is encountered.

6.4.4 Comparison of performance with other neural network models

With an average RMSE of 0.83mm for a prediction horizon of 665 ms, our results are within the same range of accuracies compared to a RMSE of 1.2 ± 0.9 mm for a system latency of 600 ms [35], 0.97 mm for a latency of 400 ms [42] and 0.9 mm for system latency of 520 ms [43]. Our results are also within the range of accuracies when compared with the extensive list of prediction studies surveyed in [44].

The average duration of the initial learning periods, i.e., the time taken prior to making the first prediction, is 8.8 s for the seven trajectories. This is shorter than 12 s [45], 25 s [4], 31s [46] and 40 s [47] reported previously. The generalized input data length of 35 samples (i.e., 4.66 s), is within the range of input data length (3 – 7.7 s) used in the other studies [4, 47-49]. In this study, an average of 29 input-output data pairs was used for each training batch (i.e., sliding window length). This is smaller than the number of data pairs required in the other studies that uses the same amount of training epochs (i.e., 800 per batch) for a static neural network [50].

As with any data-driven approach, our proposed method of using the average MSE error surface of different patients' tumor trajectories to obtain an optimal value for the two variables (i.e., input data size and number of hidden neurons) requires more data samples to validate the model design. In the present work seven trajectories, each with approximately 60 s of data sampled at an interval of 0.133 s, provided a total of 5000 data samples for this study. Additional data with diverse motion patterns are required to yield a more robust generalized neural network and to further validate our approach. The sensitivities of the parameters with respect to the calculated errors would require further study. With irregular tumor trajectories, an ensemble of neural networks can be used to predict the mean and uncertainty of the predicted tumor positions. The uncertainties could potentially be factored into the design of margins for adaptive radiotherapy treatments.

6.5 Conclusions

Based on current published literature, this work presents the first attempt to use the averaged MSE error surface obtained from the prediction of different patients' tumor trajectories to determine the parameters of a generalized neural network. Adhering to the design rule of model parsimony, an input data length of 35 data samples and 20 hidden neurons were selected for the generalized model. Using the 1st period of the tumor trajectory as a sliding window length, a systematic approach of establishing the values for the parameters of a MLP neural network has been demonstrated for the prediction of tumor motion. Instead of initializing the weights for every training batch (method 1), inheriting weights from previous training (method 2) improves the prediction accuracy and computation time on average. Average MAE and MSE of 0.59 mm and 0.83 mm are achieved with the model trained using method 2. The prediction performance on the leave-one-out data sample indicates that the model is able to generalize when tested on unseen data. By using the generalized model with the 1st period of the tumor trajectory as the sliding window data length, the initial training period prior to making the first prediction was reduced to an average of 8.8 s. This is the shortest waiting time compared to the other previous studies. This neural network model could potentially be deployed as a plug-and-play model for prediction of tumor trajectory during treatment delivery, eliminating the need for optimizing individual neural networks with pre-treatment data of patients.

References

1. D. Ruan, J. A. Fessler, J. M. Balter and P. J. Keall, “Real-time profiling of respiratory motion: baseline drift, frequency variation and fundamental pattern change”, Phys. Med. Biol. 54, 4777-4792 (2009).
2. M. Murphy, J. Jalden, M. Isaksson, “Adaptive filtering to predict lung tumor breathing motion during image-guided radiation therapy”, Proc. 16th Int. Congress on Computer-assisted Radiology Surgery (CARS 2002), 539-544 (2002).
3. J. Schuster, M. Myers, M. Rosu, N. Mukhopadhyay, and E. Weiss, “Variations of the tumor position in frameless lung sbrt: assessment of predictive factors including tumor volume changes”, J Nucl Med Radiat Ther 4(147), Article ID 1000147 (2013).
4. J. Rottmann and R. Berbeco, “Using an external surrogate for predictor model training in real-time motion management of lung tumors”, Med. Phys. 41, 121706 (2014).
5. G. P. Zhang and V. L. Berardi, “Time series forecasting with neural network ensembles: an application for exchange rate prediction”, J. Operational Res. Soc. 52 (6), 652-664 (2001).
6. L. Breiman, “Stacked regressions”, Machine Learning, 24, 49-64 (1996).
7. G. Bontempi, “Combination of two estimators” in Handbook Statistical Foundations of Machine Learning. OTexts: Melbourne, Australia. Chap 3.10. https://www.otexts.org/1443 Accessed on 10 April 2016.
8. G. Bontempi, “Model Averaging Approach” in Handbook Statistical Foundations of Machine Learning. OTexts: Melbourne, Australia. Chap 9, https://www.otexts.org/1413 Accessed on 10 April 2016.
9. D. K. Chaturvedi, “Factors affecting the performance of artificial neural network models”, Soft Computing - Techniques and its Applications in Electrical Engineering, 103 (Springer Berlin Heidelberg), 51-85 (2008).
10. J. T. Yao, C. L. Tan, “Guidelines for financial forecasting with neural networks”, Proc. Int. Conf. Neural Information Processing, Shanghai, China, 757-761, (2001).
11. R. Erenshteyn, R. Foulds, S. Galuska, “Is designing a neural network application an art or a science?”, SIGCHI Bulletin, ACM Press. New York, (July 1994).
12. N. Kourentzes and S. F. Crone, “Automatic modelling of neural networks for time series prediction – in search of a uniform methodology across varying time frequencies”, Proc. 2nd European Symp. on Time Series Prediction, ESTSP’08, Helsinki, Finland.
13. S. Chaigusin, C. Chirathamjaree, and J. Clayden, “The use of neural networks in the prediction of the stock exchange of Thailand (SET) index”, Proc. IEEE Int. Conf. Computational Intelligence for Modelling, Control and Automation. Austria. 670-673 (2008).

14. U. Naftaly, N. Intrator, and D. Horn, "Optimal ensemble averaging of neural networks", Network: Computation in Neural Systems 8 (3), 283–296 (1997).

15. S. Kulkarni, N. Reddy and S. Hariharan, “Facial expression (mood) recognition from facial images using committee neural networks”, BioMedical Engineering OnLine, 8(16), (2009).

16. R. Adhikari and R. K. Agrawal, “Model Parsimony” in An Introductory Study on Time Series Modeling and Forecasting. LAP LAMBERT Academic Publishing (January 29, 2013), Chapter 2.7.

17. F. Liu, C. Quek and G. S. Ng, “Neural network model for time series prediction by reinforcement learning”, IEEE Proc. Int. Joint Conf. on Neural Networks, IJCNN '05, 2, 809-814 (2005).

18. R. Rojas, “The Backpropagation Algorithms”, in Neural Networks (Springer-Verlag, Berlin, 1996), Chapter 7.

19. N. J. Nilsson, “Training Feedforward Networks by Backpropagation”, in Introduction to Machine Learning - An Early Draft of a Proposed Textbook (2005) Chapter 4. (http://ai.stanford.edu/~nilsson/MLBOOK.pdf,) Accessed on March 14 2016.

20. D. Stansbury, “A gentle introduction to artificial neural networks”, https://theclevermachine.wordpress.com/2014/09/11/a-gentle-introduction-to-artificial-neural-networks/. Accessed on March 14 2016.

21. ML:Neural Networks: Learning. https://share.coursera.org/wiki/index.php/ML:Neural_Networks:_Learning. Accessed on Dec 14 2015.

22. T. Nishida, S. Kurogi and T. Saeki, “An analysis of competitive and re-initialization learning for adaptive vector quantization”, Proc. Int. Joint Conf. on Neural Networks, IJCNN '01. 2, 978-983 (2001).

23. G. Bontempi, “Backpropagation”, in Handbook Statistical Foundations of Machine Learning. OTexts: Melbourne, Australia. Chap 8.1.1.2, https://www.otexts.org/1510 Accessed on 10 April 2016.

24. Y. Suh, S. Dieterich, B. Cho B, and P. Keall, “An analysis of thoracic and abdominal tumor motion for stereotactic body radiotherapy patients”, Phys. Med. Biol. 53, 3623–3640 (2008).

25. S. Romano, H. ElAarag, “A neural network proxy cache replacement strategy and its implementation in the Squid proxy server”, Neural Comput & Application 20, 59-78 (2011).

26. H. ElAarag and S. Romano, “Training of NNPCR-2: An improved neural network proxy cache replacement strategy”, IEEE Int Symp. Performance Evaluation of Computer & Telecommunication Systems, SPECTS 2009. 41, 260 – 267 (2009).

27. H. Cheng, P.-N. Tan, J. Gao and J. Scripps, "Multistep-ahead time series prediction", Advances in Knowledge Discovery and Data Mining, in Lecture Notes in Computer Science 3918, 765-774 (2006).

28. J. Rodrigues, A. Nogueira and P Salvador, "Improving the traffic prediction capability of neural networks using sliding window and multitask learning mechanisms", Proc. 2nd Int. Conf. Evolving Internet, Valencia, Spain (2010).

29. L. Mozaffari, A. Mozaffari and N. Azad, "Vehicle speed prediction via a sliding-window time series analysis and an evolutionary least learning machine: A case study on San Francisco urban roads", Engineering Science and Technology 18, 150-162 (2015).

30. Z. Telec, B. Trawiński, T. Lasota, and G. Trawiński, "Evaluation of Neural Network Ensemble Approach to Predict from a Data Stream", 6th Int. Conf. Computational Collective Intelligence. Technologies and Applications, ICCCI 2014, LNAI 8733, 472-482 (2014).

31. G. P. Zhang, B. E. Patuwo and M. Y. Hu, "Simulation study of artificial neural networks for nonlinear time-series forecasting", Computers & Operations Research 28, 381-396 (2001).

32. I. Kaastra and M. Boyd, "Designing a neural network for forecasting financial economic time series", Neurocomputing 10 (3), 215-236 (1996).

33. P. R. Poulsen, B. Cho, A. Sawant, D. Ruan, P. Keall, "Detailed analysis of latencies in image-based dynamic MLC tracking", Med Phys. 37, 4998-5005 (2010).

34. B. Cho, P. R. Roulsen, A. Sloutsky, A. Sawant and P. Keall, "First demonstration of combined KV/MV image-guided real-time dynamic multileaf-collimator target tracking", Int. J. Radiat. Oncol. Biol. Phys. 74 859-67 (2009).

35. R. S. Neville, "Inheritance of information in multi-layer sigma-pi neural networks", Proc. Int Joint Conf. Neural Networks 2, 1120-1125 (2003).

36. R. Adhikari and R. K. Agrawal, "Forecast Performance Measures", in An Introductory Study on Time Series Modeling and Forecasting. LAP LAMBERT Academic Publishing (January 29, 2013) Chapter 6.

37. D. Ruan, J. A. Fessler, J. M. Balter, and J.-J. Sonke, "Exploring breathing pattern irregularity with projection-based method", Med. Phys. 33, 2491-2499 (2006).

38. S. Pollock, D. Lee, P. Keall and T. Kima, "Audiovisual biofeedback improves motion prediction accuracy", Med. Phys. 40 (4), 041705, (2013).

39. M. J. Murphy and D. Pokhrel, "Optimization of an adaptive neural network to predict breathing", Med. Phys. 36(1), 40-47 (2009).

40. S. S Kulkarni, N. P. Reddy and S. Hariharan, "Facial expression (mood) recognition from facial images using committee neural networks", BioMedical Engineering OnLine 8 (16), (2009).

41. E. Colvill et. al., “A dosimetric comparison of real-time adaptive and non-adaptive radiotherapy: A multi-institutional study encompassing robotic, gimbaled, multileaf collimator and couch tracking”, Radiother Oncol. Available online Mar 22 2016.

42. J. H. Goodband, O.C. Haas, and J. A. Mills, “A comparison of neural network approaches for online prediction in IGRT”, Med. Phys. 35(3), 1113-1122 (2008).

43. J. Yun, M. Mackenzie, S. Rathee, D. Robinson and B. G. Fallone, “An artificial neural network (ANN)-based lung-tumor motion predictor for intrafractional MR tumor tracking”, Med. Phys. 39 (7), 4423-4433 (2012).

44. P. Verma, J. Wu, M. Langer, I. Das and G. Sandison, “Survey: real-time tumor motion prediction for image-guided radiation treatment”, Computing in Sci. & Engine. 13 (5), 24-35, (2011).

45. J. Rottmann, P. Keall and R. Berbeco, “Markerless EPID image guided dynamic multi-leaf collimator tracking for lung tumors”, Phys. Med. Biol. 58, 4195–4204 (2013).

46. M. J. Menten, et. al., “Comparison of a multileaf collimator tracking system and a robotic treatment couch tracking system for organ motion compensation during radiotherapy”, Med. Phys. 39, 7032 (2012).

47. A. Krauss, S. Nill and U. Oelfke, “The comparative performance of four respiratory motion predictors for real-time tumor tracking”, Phys. Med. Biol. 56, 5303-5317 (2011).

48. G. C. Sharp, S. B. Jiang, S. Shimizu, and H. Shirato, “Prediction of respiratory tumor motion for real-time image-guided radiotherapy”, Phys. Med. Biol. 49(3), 425-440, (2004).

49. R. Ernst, A. Drichen, A. Schlaefer, and A. Schweikard, “Evaluating and comparing algorithms for respiratory motion prediction”, Phys. Med. Biol. 58(11), 3911–3929 (2013).

50. I. Bukovsky, N. Homma, K. Ichiji, M. Cejnek, M. Slama, P. M. Benes, and J. Bila, “A fast neural network approach to predict lung tumor motion during respiration for radiation therapy applications”, BioMed Research Int. vol. 2015, Article ID 489679, 13 pages (2015).

Chapter 7 Conclusions of Dissertation

7.1 Restatement of Hypothesis

Based on previous studies examining the current status and challenges associated with image-guided adaptive radiotherapy system, it is hypothesized that:

i. by using a computer/robotic vision approach such as the optical flow algorithm, the motion of an uncontoured tumor can be tracked automatically with an accuracy of 0.5 mm [1, 2] in order to adapt treatment delivery;
ii. motions and intrusions of critical structure at the edges of the treatment field can be detected and tracked automatically;
iii. system latencies of typical radiotherapy systems can be compensated with a prediction model that is efficient and accurate compared to existing techniques available for tumor motion prediction [3-10].

7.2 Conclusions

This dissertation sought to examine some of the issues and challenges pertaining to the realization of image-guided adaptive radiotherapy. Solutions and proof-of-concept studies were implemented to track the tumor and its surrounding structures, to predict and update the treatment aperture. The conclusions that can be drawn from this dissertation are as follows:

1) **Uncontoured tumor motions can be tracked with a weighted optical flow algorithm.** By comparing the tracking of our algorithm with a potentiometer measurement, average position errors of 0.6 ± 0.2 mm, 0.2 ± 0.2 mm and 0.1 ± 0.1 mm are obtained for 6, 12

and 16 breaths/min motions, respectively. Evaluation was performed with a phantom tumor programmed to move according to an asymmetrical cosine function representing average clinical tumor motion. When the algorithm was used to track a tumor on patient DRR images, the tracking performance of our algorithm was statistically similar to that of both a manual delineation process and a centroid tracking algorithm. Although the accuracy of our approach is similar to that of other methods, the benefit is that it does not require manual delineation of the target or prior knowledge of the tumor features from a training data set and can, therefore, provide automatic motion estimation during treatment.

2) **INI method which uses the initial BEV as a fixed reference image is the least prone to accumulation of position errors.** Using a virtual DMLC and a printed 3D tumor as a control for this study, the performance of three implementations of the optical flow algorithm were compared. Results demonstrated the accumulation of position errors during the tracking of target that moves with realistic tumor motions and on MV EPID images. The INI method which uses the initial BEV as a fixed reference image is the least prone to accumulation of position errors. This is followed by the SEQ method (updates the reference image sequentially), and the PERD method (updates the reference image periodically). The accumulation of position errors was due to (1) isolated, (2) accumulation of small inter-frame displacement errors in a similar direction. Potential causes for the inter-displacement errors are (1) motions that are smaller than the image or tracking resolution and (2) under-estimation of high displacements, a common limitation of algorithms that are optimized prior to online tracking. Tracking accuracies of -0.06 ± 0.23 mm, 0.04 ± 0.35 mm and -0.14 ± 0.63 mm and precisions of 0.32 mm, 0.68 mm and

0.79 mm for the INI, SEQ and PERD methods were achieved, respectively (position errors of INI < SEQ < PERD).

3) **Motions and intrusions of a critical structure at the edge of the treatment field can be detected and tracked using local optical flow analysis with an adaptive field edge.**

   Through the use of (i) an optimized optical flow algorithm with a 3-by-3 pixel regularization, (ii) an optimal cluster of 9 rows by 10 columns of local vectors (resulting in the smallest position errors) and (iii) a control algorithm with one-frame prediction and buffers incorporated, the feasibility to adapt MLC leaves based on the motions tracked at the edges of a treatment field have been successfully demonstrated. A mean positional error of -0.4 ± 0.3 mm and a precision of 1.06 mm were obtained for tracking an external object intruding with motions similar to the tumor trajectory of five lung cancer patients. A strong correlation between the computed position of the OAR and the motion of the MLC leaves was achieved. The results provide motivation to combine global adaptation of the treatment field (due to the motion of the main target) with local adjustments at the edges to account for unplanned intrusions.

4) **A generalized neural network can be used to predict tumor motion with performance comparable to, if not better than, previously proposed solutions.**

   This is the first attempt to use the average MSE error surface obtained from the prediction of different patients' tumor trajectories to determine the parameters of a generalized neural network. With an average RMSE of 0.83 mm for a prediction horizon of 665 ms, the results of this study are within the same range of accuracies compared with other studies. The average duration of the initial learning period is 8.8 s for the seven patients. This is the shortest compared to 12 s [7], 25 s [8], 31s [10] and 40 s [9] reported previously. The input data length of 35 samples (4.66 s), is within the range of input data length (3 – 7.7 s) used in other studies [3, 8, 9, 11, 12]. Similar to other studies, the prediction performance is sensitive to irregularities in the frequency of the tumor trajectory. For safety reasons, treatment could be terminated or gated when the MAE exceeds a certain threshold. Inheriting weights from previous training improves the average prediction accuracy and computation time. Without the need to either optimize for individual patients or to assess pre-treatment data, coupled with a reduction in the initial learning period, the neural network can potentially be used as a plug-and-play predictor for tumor motions. This would allow adaptation of treatment to commence earlier.

In summary, the results from these proof-of-concept studies support the hypotheses of this thesis. It is envisioned that the work developed here will contribute positively towards the advancement of image guided adaptive radiotherapy.

7. 3 Future Work

The current work sets the stage for further verification with realistic patient data. This includes clinical images of tumor and critical structures. More specifically, the following topics await further work and development:

- On tracking uncontoured tumor using weighted optical flow algorithm, although the tracking accuracy on MV images with different CNR have been studied, and patient DRR images have been used to evaluate the tracking accuracy, the inherent low contrast of MV images could potentially pose a challenge to the weighted optical flow tracking algorithm. It would be desirable to further validate these results with clinical MV images having different image qualities. It is envisioned that a refinement of the algorithm could be applied to offset any limitations. With arc therapy, motions due to gantry rotation could result in an apparent motion of the background anatomical structures in addition to the tumor motion. However, since gantry rotation can be quantified, the ability to discriminate optical vectors associated with such rotation can be incorporated into the tracking algorithm. Further testing would be required. To reduce computation time, parallel computation could be used to obtain the vectors at different image resolution levels. For the current work, rigid body translations are assumed. The performance of the algorithm could be evaluated for non-rigid body motions.

- In the comparison of the three different implementations of the optical flow algorithm (chapter 4), additional errors were incurred when determining and updating the reference at the EoE. In the current implementation, a moving window of five data points was used, and the EoE would be detected when the slope of the velocity and acceleration derived from the first two images are different from the subsequent three data points. This implies that any update of the new reference image will only happen two frames after EoE. This update could potentially introduce errors when the adjustment occurs at higher velocities, causing abrupt changes in the inter-frame displacement as observed in our results. Since a prediction algorithm would be employed in practice to compensate for system latency, the EoE could be predicted in advance, and the update of reference image could occur exactly at the EoE of each breathing cycle. Like most studies that use cine mode to acquire EPID images, the memory limitation of the Varian Clinac used for this work limits the maximum number of high-resolution images that can be acquired to about 200

[13, 14]. With a frame rate of 7.5 frame/s, this amounts to about 27 s of treatment time, which is short compared to typical treatment time of around 4 min for SBRT. In view of the possible accumulation of position errors, proposed algorithms should be validated over an extended period of time. With the virtual DMLC developed herein, system latencies can be simulated, and accuracies of the tracking and prediction modules can be tested. Although data for seven patients with diverse motion characteristics was used in this study, further studies using a larger data size with diverse tumor shapes, deformations, motions and image quality are required to confirm our preliminary observations.

- The study on motion detection at the field edges has demonstrated the capability of the algorithm in tracking rigid-body intrusions with different motion profiles through the use of data of five patients. A simplified rectangular treatment field bounded by MLC leaves on a straight edge was used for the simulation. The next logical step would be to track both the global motion of the main target and intrusions at the edges of a clinical BEV instead of the simulated rectangular field. This would require the monitoring and adaptation of all the individual leaves that conform to the target. Since the local adaptations could introduce deviations to the treatment delivery compared to the treatment plans, its dosimetric impact, and treatment outcome of adaptively shielding the OAR would require further detailed studies. The current approach uses local optical flow vectors, to detect and discriminate motions at the edges (due to an intruding object) from the main target motion. Feature-based learning approaches can be incorporated to augment the segregation of the vectors in cases where multiple structures are observed in a treatment field. Traditional approaches of feature learning consist of two parts, a feature detector such as the Scale Invariant Feature Transform (SIFT) detector and a classifier such as the support vector machine. This could further be extended to a deep learning approach where both tasks (detection and classification) can be accomplished simultaneously.

- Despite using doses of < 20 Gy per fraction for tumors in the central lung region of 2-cmperimeter around the proximal bronchial tree (PBT), fatal complications such as bronchial necrosis and stricture, and fatal hemoptysis have been reported for SBRT treatments [15]. The critical structures for lung tumors includes the spinal cord, esophagus, ipsilateral brachial plexus, heart, trachea and ipsilateral main bronchus, right and left lung. Mean (with 1 std. dev.) esophagus motion of 3.5(1.8), 4.0(2.6) and 8.3(3.8) mm has been observed in the lateral, anterior-posterior and superior-inferior directions respectively [16]. Mean spinal cord motion of up to 3 mm has been reported [17]. Mean variations (over an average respiratory cycle) of 3 mm (range 1-10 mm) and 2 mm (1-5 mm) in the distance between the GTV and both esophagus and spinal cord have been observed in the transverse plane respectively [18]. Patients with tumors that are near (< 1 cm) to the proximal bronchial tree (PBT) are reported to be more likely to incur > Grade 3 toxicities than those with tumors > 1cm from the PBT [15]. The ability to detect and avoid these critical structures during treatment delivery is desirable. The dosimetric impact of avoiding these critical structures would depend on a variety of factors. These factors include the treatment technique, duration of exposure of the critical structure, the tolerance of the structures to radiation, and both the position and relative motion of the critical structure with the GTV. The dosimetric impact of OAR avoidance will be studied in future work.

On predicting tumor motion, as with any data-driven approach, our method of using the average prediction response from different patients to design a generalized network needs more patient data to validate. In the present work, tumor trajectories from seven patients provided a total of 5000 positional data samples for our study. Additional data with diverse motion patterns is required to yield a more robust generalized neural network, and to further validate our approach. The sensitivities of the parameters with respect to the errors would require further study. Although a multilayer perceptron network with backpropagation learning has been used for our neural network, other network topologies such as the recurrent network and radial basis function network can be compared for performance improvement. With irregular tumor trajectories, an ensemble of neural networks can be used to predict the mean and uncertainty of the predicted tumor positions. This could potentially be factored into the design of margins for adaptive radiotherapy treatments. Current prediction is performed for a horizon of 665 ms, which is within the range of 50 ms to 1400 ms reported for some of the practical systems [3]. Testing for longer prediction horizons would be performed in the future.

References

1. J. Meyer, A. Richter, K. Baier, J. Wilbert, M. Guckenberger and M. Flentje, “Tracking moving objects with megavoltage portal imaging: A feasibility study”, Med. Phys. 33, 1275-1280 (2006).

2. J. Rottmann, M. Aristophanous, A. Chen, L. Court and R. Berbeco, “A multi-region algorithm for markerless beam’s-eye view lung tumor tracking”, Phys. Med. Biol. 55 5585–5598 (2010).

3. S. Pollock, D. Lee, P. Keall and T. Kima, “Audiovisual biofeedback improves motion prediction accuracy”, Med. Phys. 40 (4), 041705 (2013).

4. J. Rottmann and R. Berbeco, “Using an external surrogate for predictor model training in real-time motion management of lung tumors”, Medical Physics 41, 121706 (2014).

5. J. H. Goodband, O.C. Haas, and J.A. Mills, “A comparison of neural network approaches for online prediction in IGRT”, Med. Phys., 35(3), 1113-1122 (2008).

6. J. Yun, M. Mackenzie, S. Rathee, D. Robinson and B. G. Fallone, “An artificial neural network (ANN)-based lung-tumor motion predictor for intrafractional MR tumor tracking”, Med. Phys. 39 (7), 4423-4433 (2012).

7. P. Verma, J. Wu, M. Langer, I. Das and G. Sandison, “Survey: real-time tumor motion prediction for image-guided radiation treatment”, Computing in Sci. & Engine. 13 (5), 24-35, (2011).

8. J. Rottmann, P. Keall and R. Berbeco, “Markerless EPID image guided dynamic multi-leaf collimator tracking for lung tumors”, Phys. Med. Biol. 58, 4195–4204 (2013).

9. A. Krauss, S. Nill and U. Oelfke, “The comparative performance of four respiratory motion predictors for real-time tumor tracking”, Phys. Med. Biol. 56, 5303-5317 (2011).

10. M. J. Menten, et. al., “Comparison of a multileaf collimator tracking system and a robotic treatment couch tracking system for organ motion compensation during radiotherapy”, Med. Phys. 39, 7032 (2012).

11. G. C. Sharp, S. B. Jiang, S. Shimizu, and H. Shirato, “Prediction of respiratory tumor motion for real-time image-guided radiotherapy”, Phys. Med. Biol. 49(3), 425-440, (2004).

12. F. Ernst, A. Drichen, A. Schlaefer, and A. Schweikard, “Evaluating and comparing algorithms for respiratory motion prediction”, Phys. Med. Biol. 58(11), 3911–3929 (2013).

13. J. Adamson and Q. Wu, “Independent verification of gantry angle for pre-treatment VMAT QA using EPID”, Phys. Med. Biol. 57(20), 6587-6600 (2012).

14. P. M. McCowan, D. Rickey, P. Rowshanfarzad, P. B. Greer, W. Ansbacher, and B. M. McCurdy, “Investigation of gantry angle data accuracy for cine-mode EPID images acquired during arc-IMRT”, J. App. Clin. Med. Phys. 15(1), (2014).
15. J. Haseltine, A. Rimner, D. Gelblum, A. Modh, K. Rosenzweig, A. Jackson, E. Yorke, and A. Wu, “Fatal complications after stereotactic body radiation therapy for central lung tumors abutting the proximal bronchial tree”, Pract Radiat Oncol. 6 e27–e33 (2016).
16. T. Hashimoto, H. Shirato, M. Kato, K. Yamazaki, N. Kurauchi, T. Morikawa, S. Shimizu, Y. Ahn, Y. Akine, K. Miyasaka, “Real-time monitoring of a digestive tract marker to reduce adverse effects of moving organs at risk (OAR) in radiotherapy for thoracic and abdominal tumors”, Int J Radiat Oncol Biol Phys., 61, 1559-1564 (2005).
17. S. Winklhofer, F. Schoth, P. Stolzmann, T. Krings, M. Mull, M. Wiesmann, C. Stracke, “Spinal cord motion: influence of respiration and cardiac cycle”, Rofo. 86, 1016-1021, (2014).
18. E. Weiss, K. Wijesooriya, and P. Keall, “Esophagus and spinal cord motion relative to GTV motion in four dimensional CTs of lung cancer patients”, Radiother Oncol., 87, 44–48, (2008).

Appendix A : Using Mathematical Induction to Formulate the Equations for the Position of Aperture and Targets

In the first method (INI), direct registration with an initial reference frame was performed for every image (figure 4.1). The optical flow algorithm was applied to determine the inter-frame displacements between all images with the initial image. Following the method of induction, the initial position of the aperture $Pos_{aperture}(1)$ and target $Pos_{target}(1)$ are given in equations (A.1) and (A.2). This assumes that the target was positioned at the isocenter verified by the setup procedure. Without prior motion information, the position of the aperture in the second image frame $Pos_{aperture}(2)$ is given by equation (A.3):

Initial Conditions:

$$Pos_{aperture}(1) = 0 \tag{A.1}$$

$$Pos_{target}(1) = 0 \tag{A.2}$$

$$Pos_{aperture}(2) = 0 \tag{A.3}$$

Applying tracking between the first and second image provides the displacement of the target given by the optical flow vector $OF_{DIR}(1)$:

Subsequent Motion Tracking:

$$Pos_{target}(2) = Pos_{aperture}(2) + OF_{INI}(1) = 0 + OF_{INI}(1) = OF_{INI}(1) \tag{A.4}$$

where $OF_{INI}(1)$ = *OF* (*IM*(1), *IM* (2)), is the weighted average value of the optical flow vectors obtained between *IM*(1) and *IM*(2).

To maintain tracking of the object, the aperture position $Pos_{aperture}(3)$ in the subsequent image *IM*(3) was updated following the object motion $OF_{INI}(1)$. The position of the target in that aperture would then be given respectively by:

$$Pos_{aperture}\ (3) = Pos_{aperture}\ (2) + OF_{INI}(1) \tag{A.5}$$

$$= Pos_{aperture}\ (1) + OF_{INI}\ (1)$$

$$Pos_{target}\ (3) = Pos_{aperture}\ (3) + OF_{INI}(2) \tag{A.6}$$

$$= [Pos_{aperture}\ (2) + OF_{INI}\ (1)] + OF_{INI}\ (2)$$

$$= [Pos_{aperture}\ (1) + OF_{INI}\ (1)] + OF_{INI}\ (2)$$

where $Pos_{aperture}(1)$ and $Pos_{aperture}(2)$ are defined in equations. (S1) and (S3) respectively. Similarly, the position of the aperture in the fourth image frame $Pos_{aperture}(4)$ was obtained by updating its position from image *IM* (3) with the computed motion given by $OF_{INI}(2)$ and the target

$$Pos_{aperture}(4)=Pos_{aperture}(3)+OF_{INI}(2) \tag{A.7}$$

$$= [Pos_{aperture}(1) + OF_{INI}(1)] + OF_{INI}(2)$$

Position determined by $OF_{INI}(3)$:

$$Pos_{aperture}(4) = Pos_{aperture}(3) + OF_{INI}(2) \tag{A.8}$$

$$= [Pos_{aperture}(1) + OF_{INI}(1)] + OF_{INI}(2)$$

$$Pos_{target}(4) = Pos_{aperture}(4) + OF_{INI}(3) \tag{A.9}$$

$$= [Pos_{aperture}(2) + OF_{INI}(2) + OF_{INI}(1)] +OF_{INI}(3)$$

$$= Pos_{aperture}(1) + OF_{INI}(1) + OF_{INI}(2) + OF_{INI}(3)$$

For i^{th} image (i.e. *IM*(*i*)), the generalized representation of the position of the aperture and target can be written as:

***For ith* image frame:**

$$Pos_{aperture}(i) = Pos_{aperture}(1) + \sum_{i}^{n} OF_{INI}(i-2)\,; i > 3 \tag{A.10}$$

$$Pos_{target}(i) = Pos_{aperture}(1) + \sum_{i}^{n} OF_{INI}\ (i-1)\,; \qquad i > 2 \tag{A.11}$$

where $OF_{INI}(i) = OF(\ IM(1), IM(i+1)\ )$ was obtained by computing the optical flow of image IM (*i+1*) with the reference image frame *IM*(1). Letting $Pos_{aperture}(1) = P_0$:

$$Pos_{aperture}(i) = \begin{cases} P_0 & i = 1,2 \\ P_0 + \sum_{i}^{n} OF_{INI}(i-2)\,; & i \geq 3 \end{cases} \tag{A.12}$$

$$Pos_{target}(i) = P_0 + \sum_{i}^{n} OF_{INI}(i-1)\,; \qquad i \geq 2 \tag{A.13}$$

Following the motion detected using the INI method, the generalized expression for the position of the aperture and target at IM image (*i*) are provided by equations (A.11) and (A.12) respectively, which are similar to equations (4.1) and (4.2) shown in Chapter 4. A similar approach was used to formulate the expressions for the other two methods, i.e. SEQ and PERD methods.

Appendix B : Determination of the Optical Flow Vector from a Common Region of Two Image Frames Having Different Sizes as a Result of Treatment Field Adaptation

This section provides the details of obtaining the local motion at the edges of a treatment field. The adaptation of the MLC leaves and the sampling region on the two image frames for a single-axis SI motion detected at the edge can be expressed mathematically by letting IM be a treatment image with a pixel in that image defined as $IM_k\,(r(k)_i,\ c(k)_j)$, where r and c are the row and columns with index (i, j) respectively and k being the index of the image sequence. A common region S of image IM_k and IM_{k+1} is defined as

$$S \in (IM_k \cap IM_{k+1}) \tag{B.1}$$

Assuming that the MLC leaves are oriented in the same direction as the tumor motion, and these leaves are perpendicular to the rows of the image matrix, the size of the intersecting region, defined by the rows of pixels $(r_1 \ldots r_n)$ common in both images (refer to figure B.(1)), will vary according to the displacement of the MLC:

$$S = \begin{cases} IM_k\left(r(k+1)_{\,i=1\ldots n}, c(k+1)_{\,j}\right) \cap\ IM_{k+1}\left(r(k+1)_{\,i=1\ldots n}, c(k+1)_{\,j}\right);\ \ MLCdisp(k+1) > 0 \\ IM_k\left(r(k)_{\,i=1\ldots n}, c(k)_{\,j}\right) \cap\ IM_{k+1}\left(r(k)_{\,i=1\ldots n}, c(k)_{\,j}\right);\ \ MLCdisp\,(k+1) \leq 0 \end{cases} \tag{B.2}$$

A set of optical flow vectors OF is derived from the region S.

$$S(r_{i=1\ldots n}, c_j) \vdash OF(r_{i=1\ldots n}, c_j) \tag{B.3}$$

("$\vdash$" is the mathematical symbol for inference, i.e. 'is derived from'). To determine the motion at the edge, a subset $\widehat{OF}_L$ of the optical flow map are sampled with m rows of pixels from the edge

$$\widehat{OF}_L = OF\,(r_{i=(offset+1)\ldots m}\,, c_j) \tag{B.4}$$

where *offset* + 1 < m < *n*, and *offset* is the number of rows of empty vectors at the edges of the optical flow map due to the regularization employed in the optical flow computation. The mean value of the optical flow vectors sampled from this cluster $\widehat{OF}_L$ will be used to determine the motion at the edge. A similar approach of deriving a common region on two images for motion computation can be applied when the MLC leaves are perpendicular to the columns of the image matrix.

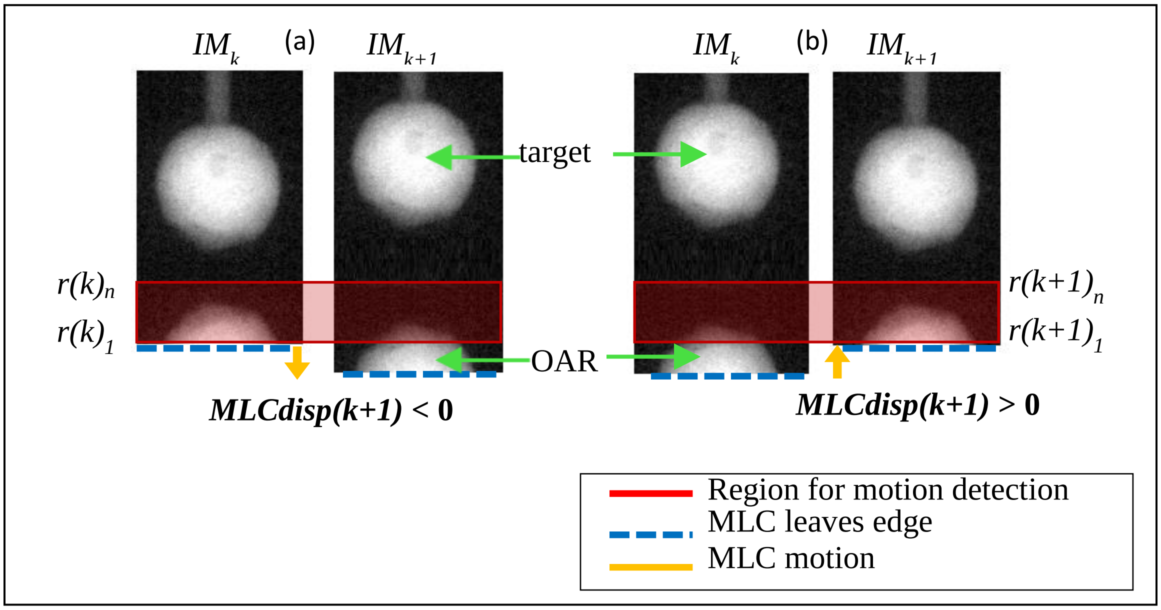

Figure B.1: (a) The common region between the two consecutive images IM_k and IM_{k+1} is limited by $r(k)_1$ of IM_k when the MLC is extending beyond its previous position following the leaving of the OAR from the irradiated field. Hence, the computation and sampling of the optical flow vectors at the edges are determined by the MLC edge in the previous image frame. Figure B.1(b) The common region between the two consecutive images is limited by $r(k+1)_1$ of IM_{k+1} when the MLC is moving in the same direction as the OAR intruding into the irradiated field. Hence, the computation and sampling of the optical flow map would be bounded by the newly adjusted MLC edge as opposed to the previous MLC position.

Appendix C : Detection and Tracking of Multiple Targets on Portal Images during Radiation Therapy using Feature-Based Learning and an Optical Flow Algorithm

This section presents the preliminary work done in using a feature-based learning approach, coupled with the optical flow algorithm, to detect and track a tumor and an intruding structure in a simulated beam's eye field.

Abstract

To adapt for motions observed in radiation treatment images, an algorithm was implemented to track the main tumor target motion and to detect intruding objects at the edges of a treatment field. With the use of a Support Vector Machine (SVM) algorithm, intrusion of targets was learned and recognized from a training dataset. Based on the numbers of objects predicted from the classifier, the k-means algorithm was used to cluster the optical flow motion vectors. The mean velocity for the main target and intruding object were calculated independently.

C.1 Introduction

With the rise of high-dose radiation treatment over a small number of fractions, the ability to detect an unplanned intrusion of critical structures into the beam's eye view (BEV) during treatment delivery is desirable. This section investigates the feasibility of detecting and tracking multiple targets from megavoltage (MV) photon images acquired with an electronic portal imaging device (EPID). In addition to tracking the main target, intrusions into the BEV will be detected and tracked using a feature-based learning and a weighted optical flow algorithm [1].

C.2 Materials & Methods

C.2.1 Learning and detecting multiple objects

MV EPID images of a 3D printed lung tumor were acquired. The printed tumor was attached to an actuator and programmed to move according to (i) the lung tumor motions of five patients and (ii) a mathematical function representing an average tumor motion. Image processing was performed to simulate the intrusion of external structures into the BEV with a motion that is similar in magnitude but in an opposite direction to the main target. A "bag-of-words" representation of images was created and used to recognize two object classes – a tumor (1 object) and a tumor with an intruding organ (2 objects). Four major steps were involved (figure C.1): (1) A Scale-Invariant Feature Transform (SIFT) algorithm [2] was used to extract the features. (2) A visual vocabulary was constructed, and (3) each image was converted into a histogram with frequencies of each visual vocabulary. (4) Histograms and labels were fed into an SVM model. In this study, the number of clusters (k) was limited to either 1 or 2.

C.2.2 Computation and clustering of motion vectors

A multi-resolution optical flow method was used to compute the motion vectors between images [4]. Using unsupervised learning, motion vectors obtained were grouped into k clusters where k is the number of objects detected from the SVM classification. The mean displacement and location of the respective clusters representing the tumor and intruding organ motion were determined.

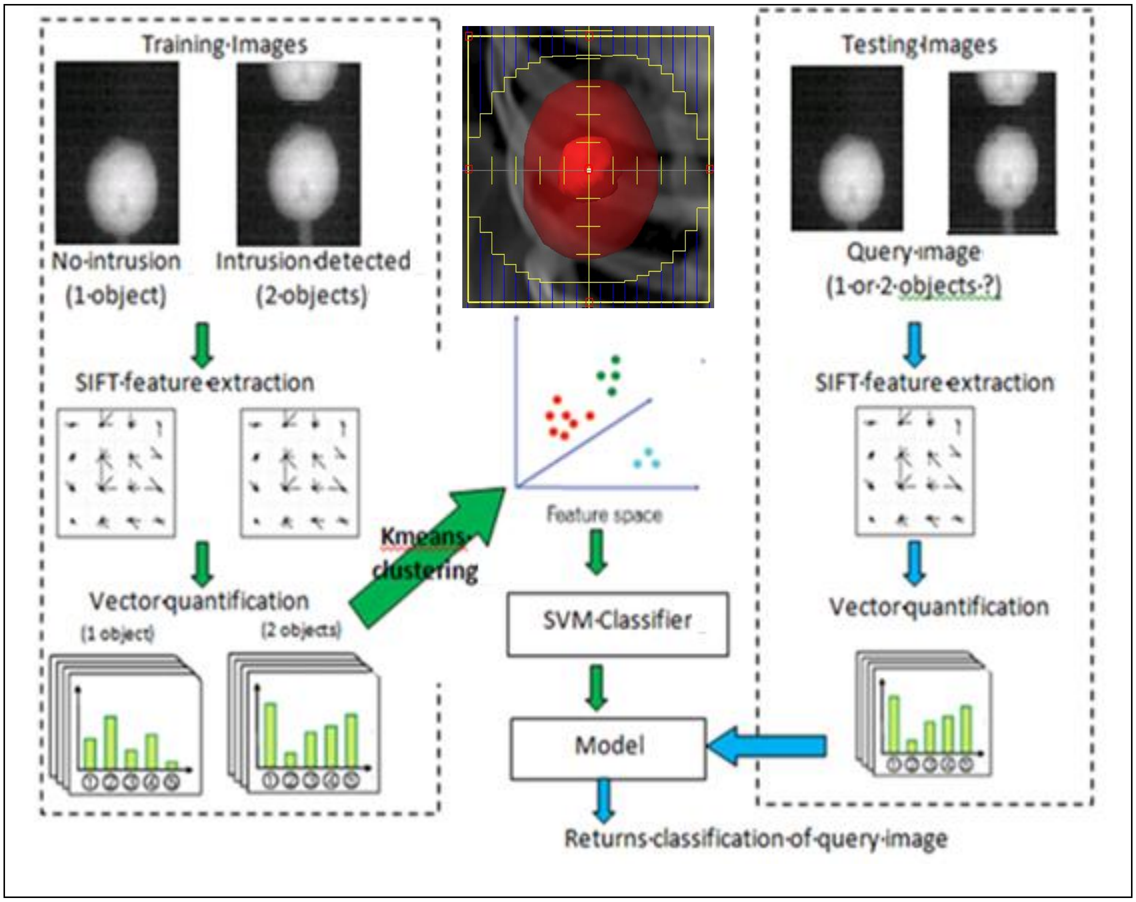

Figure C.1 : SIFT feature-based learning to detect the presence of multiple targets (e.g. main tumor target and an intruding OAR) in the MV EPID images.

C.3 Results

By using the image sequence from patient #1 for training images, an average recognition rate of 93.6% is obtained from the testing images of Patients #2 - #5 (table C.1). A 100% recognition rate was also obtained when detecting an object moving with the average tumor motion function. Figure C.2(a) shows an example of the optical flow map while figure C.2(b) and figure C.2(c) plots the inter-frame displacement for the main target and intruding structure moving with the same mathematical function respectively. A mean inter-frame difference of 0.2 pixels/frame (0.3

mm/s) is obtained between the two motions. This is within the accuracy of 0.4 ± 0.3 mm/s reported previously for tracking the main target [1].

Table C.1 Recognition rate using image sequence from Patient 1 for training. Testing is performed on the image sequence for the other patients.

	Patient	**# of success**	**# of error**	**# of total**	**Recognition Rate**
Training	1	211	0	211	100%
Testing	2	186	25	211	88.2%
	3	202	9	211	95.7%
	4	204	7	211	96.7%
	5	198	13	211	93.8%

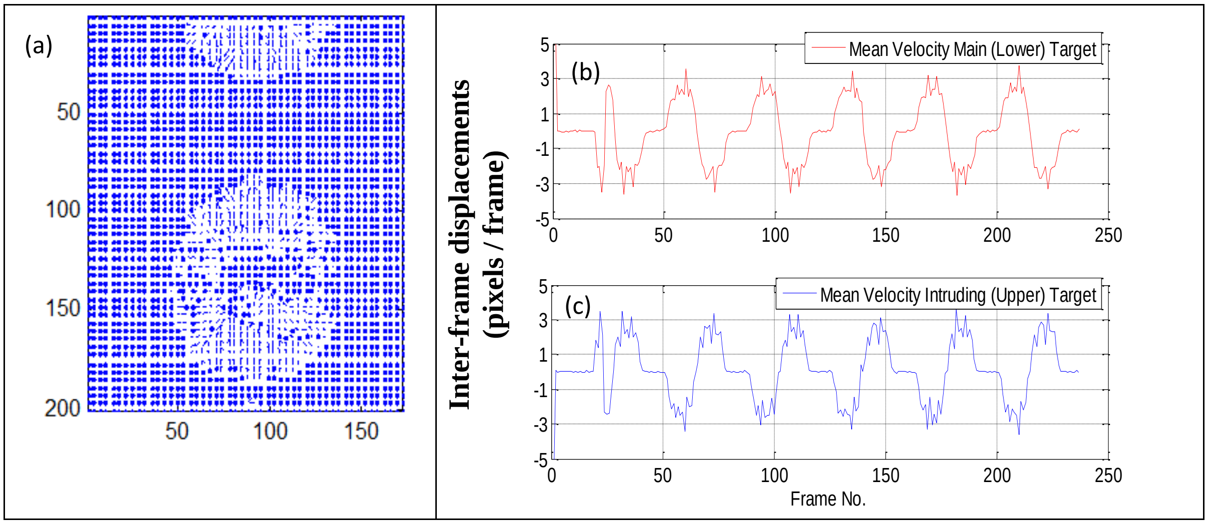

Figure C.2 : (a) An example of the optical flow vector map showing the motion of the main target and an intruding structure, the estimated mean velocity of the (b) main target and (c) intruding structure, simulated to move with the same magnitude but in the opposite direction to each other.

C.4 Conclusions

The ability to detect the presence of a main target and an intruding structure was established with a feature-based learning approach. Based on the number of objects detected, clustering was performed on the vectors, and the average value of each cluster provides a good estimation of the respective motion of the two structures.

References

1. P.T. Teo, R. Crow, S. van Nest, D. Sasaki and S. Pistorius, "Tracking lung tumor motion using a dynamically weighted optical flow algorithm and electronic portal imaging device", Meas. Sci. Technol. **24,** 074012 (15pp) (2013).
2. D. G. Lowe, "Distinctive Image Features from Scale-Invariant Key points", Int. Journal of Computer Vision, 60, 91-110 (2004).

Appendix D : List of Publications and Presentations by the Author of this Dissertation

Manuscripts under Preparations

1. T. Teo, et. al., “Markerless tumor motion tracking with a virtual DMLC: A comparison of three approaches using a weighted optical flow based algorithm”, manuscript to be submitted to Medical Physics journal by September 2016.
2. T. Teo, et. al., “Intrafraction organ-at-risk(OAR) intrusion detection and avoidance – a proof-of-concept study with electronic portal images and local optical flow vectors”, manuscript to be submitted to Medical Physics journal by September 2016.
3. T. Teo**,** et. al., “Prediction of lung tumor motion using a generalized neural network optimized from the average prediction outcome of a group of patients”, manuscript to be submitted to Medical Physics journal by September 2016.

Peer-reviewed Publications

1. T. Teo, et. al., “Drift correction techniques in the tracking of lung tumor motion”, *IFMBE Proceedings*, vol. 51, chapter 141. DOI 10.1007/978-3-319-19387-8_141.
2. T. Teo, et. al., “Application and parametric studies of a sliding window neural network for respiratory motion predictions of lung cancer patients”, *IFMBE Proceedings*, vol. 51, chapter 146. DOI:10.1007/978-3-319-19387-8_146.
3. T. Teo, S. Pistorius, “Tissue motion tracking at the edges of a radiation treatment field using local optical flow analysis”, *Journal of Physics: Conf Series* (Inst. of Physics), 489, 012040, 2014.
4. P T. Teo, et. al., "Tracking lung tumour motion using a dynamically weighted optical flow algorithm and electronic portal imaging device", *J. Measurement Science Technol* (Inst. of Physics), 24, 074012, 2013.

Conference / Presentations

1. T. Teo, et. al., “Evaluating tracking and prediction of tumor motion in a motion-compensating system for adaptive radiotherapy”, *Accepted for* oral presentation at the *IEEE International Conference on Imaging Systems and Techniques (IST 2016)*, Greece, Oct. 4-6 2016.
2. T. Teo, et al., “Prediction of lung tumor motion using a generalized neural network optimized from the average prediction outcome of a group of patients”, *Finalist, Young Investigator Symposium, Canadian Org. of Med Physicist COMP 62th Annual Scientific Meeting,* St Johns, Newfoundland, Canada, July 21 2016.

3. T. Teo, et. al., “Detection and tracking of multiple targets on portal images using feature-based learning and weighted optical flow algorithm”, *accepted (but withdrawn due to funding) for 18th Int. Conf. on the use of Computers in Radiation Therapy*. Sept. 2016.

4. T. Teo, et. al., “Detection and tracking of intrusions at the edges of a treatment field using local Optical Flow”, *Proc. Electronic Patient Imaging EPI2K16,* St Louis, Missouri, May 8, 2016.

5. P. T. Teo, et. al., “Drift correction techniques in the tracking of lung tumor motion”, *World Congress in Medical Physics & Biomedical Engineering*, Toronto, June 2015.

6. P. T. Teo, N. Bruce and S. Pistorius, “Application and parametric studies of a sliding window neural network for respiratory motion predictions of lung cancer patients”, *World Congress in Medical Physics & Biomedical Engineering,* Toronto, June 2015.

7. P. T. Teo and S Pistorius “Tissue motion recognition at the edges of a radiation treatment field using regional histogram of optical flow analysis”, *Int. Conf. on the Use of Computers in Radiation Therapy (ICCR 2013)* Australia, 6 - 9 May 2013.

8. P. T. Teo, et. al., “Tracking a Phantom's Lung Tumour Target Using Optical Flow”, *Proc. IEEE Int. Conf. Imaging Systems &Tech. (IST2012),* Manchester, U.K. July 15 -17, 2012.

9. T. P-T. Teo, et. al., “Evaluation of a Breathing Phantom’s Tumour Motion Using Portal Images and an Optical Flow Tracking Algorithm”, Medical Physics, vol. 37, pp. 3900. *Canadian Organization of Medical Physics Annual Meeting*, Ottawa, Canada. June 16-19, 2010.

10. T. P-T. Teo, et. al. “Detection of tumor and organ motion during radiotherapy”, *Manitoba Health Research Poster Competition*, June 2, 2009 (awarded Prize for Research Excellence).

Appendix E : Copyrights and Permissions

From: Diederich, Christian <Chris.Diederich@ucsf.edu>
Sent: Saturday, April 23, 2016 9:58 PM
To: Peng Teo
Subject: Re: permission to reproduce a figure from your department website.

Yes this is ok. If you can find original website address ref that or better reference jean pouliot. Good luck on your defense. Jean would approve.

Chris

Sent from my iPhone

On Apr 23, 2016, at 4:44 PM, Peng Teo <umteop@myumanitoba.ca> wrote:

Hi Dr Diederich,

I am writing to request for permission to use one of the figures that was previously published in your website for my PhD thesis.

The picture depicting indirect detection mechanism of the EPID, was previously maintained under the EPID tutorial website. But however, due to the sad passing of Dr. Pouliot, it is no longer accessible. I have a copy of the figure that I managed to download quite awhile ago and would like to get your permission for usage in the introduction chapter of my thesis.

Thank you in advance for looking into my request.

Troy Peng Thian Teo

PhD Candidate
Medical Physics,
Uni of Manitoba/ CancerCare Manitoba

<EPID uing indirect detection mechanism.jpg>

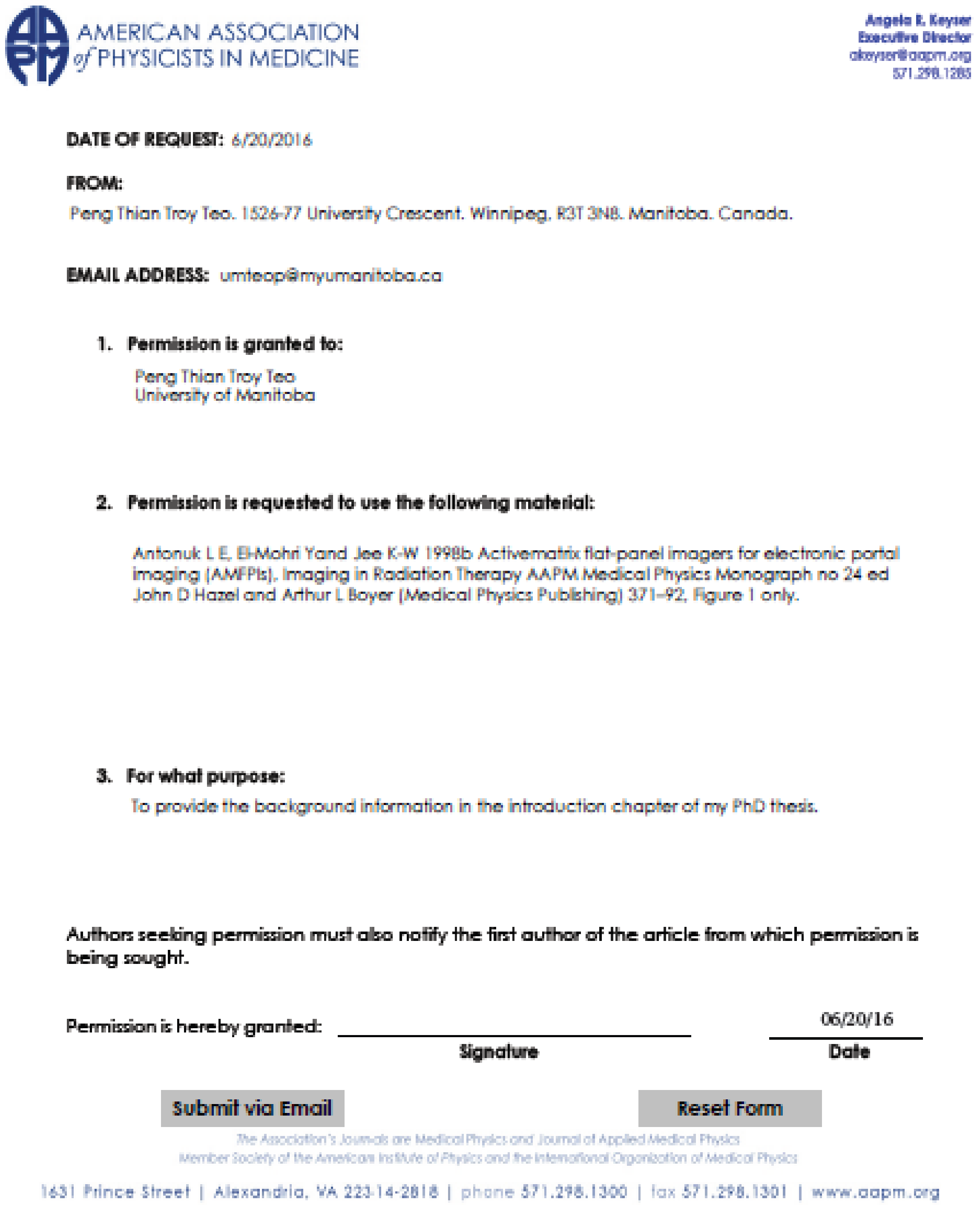

AMERICAN ASSOCIATION of PHYSICISTS IN MEDICINE

Angela R. Keyser
Executive Director
akeyser@aapm.org
571.298.1285

DATE OF REQUEST: 6/20/2016

FROM:

Peng Thian Troy Teo. 1526-77 University Crescent. Winnipeg, R3T 3N8. Manitoba. Canada.

EMAIL ADDRESS: umteop@myumanitoba.ca

1. **Permission is granted to:**

   Peng Thian Troy Teo
   University of Manitoba

2. **Permission is requested to use the following material:**

   Antonuk L E, El-Mohri Yand Jee K-W 1998b Activematrix flat-panel imagers for electronic portal imaging (AMFPIs), Imaging in Radiation Therapy AAPM Medical Physics Monograph no 24 ed John D Hazel and Arthur L Boyer (Medical Physics Publishing) 371–92, Figure 1 only.

3. **For what purpose:**

   To provide the background information in the introduction chapter of my PhD thesis.

Authors seeking permission must also notify the first author of the article from which permission is being sought.

Permission is hereby granted: ______________________ 06/20/16

Signature **Date**

Submit via Email   Reset Form

The Association's Journals are Medical Physics and Journal of Applied Medical Physics
Member Society of the American Institute of Physics and the International Organization of Medical Physics

1631 Prince Street | Alexandria, VA 22314-2818 | phone 571.298.1300 | fax 571.298.1301 | www.aapm.org